



VNIVERSITAT
DE VALÈNCIA

Departamento de Física Atómica, Molecular y Nuclear
Instituto de Física Corpuscular
Doctorado en Física

**Collectivity along $N=50$:
Nuclear Structure studies on the
neutron-magic nuclei ^{92}Mo and ^{94}Ru
with AGATA and VAMOS++**

TESIS DOCTORAL

Rosa María Pérez Vidal

DIRIGIDA POR

Andrés Gadea Raga y César Domingo Pardo

Octubre 2019

Declaration

Dr. Andrés Gadea y **Dr. César Domingo**, Investigadores del Consejo Superior de Investigaciones Científicas (CSIC)

CERTIFICAN:

Que la presente memoria "**Collectivity along N=50: Nuclear Structure studies on the neutron-magic nuclei ^{92}Mo and ^{94}Ru with AGATA and VAMOS++**" ha sido realizada bajo su dirección en el Instituto de Física Corpuscular (Centro-mixto del CSIC y de la Universidad de Valencia) por **Rosa María Pérez Vidal** y constituye su Tesis para optar al grado de Doctor en Física.

Y para que así conste, firman el presente certificado.

Dr. Andrés Gadea Raga

Dr. César Domingo Pardo

V.º B.º del tutor, Dr. Juan Zuñiga Román

*A mi madre, a mi hermano
y, en especial, a mi padre.
Siempre contigo, papá.*

UNIVERSIDAD DE VALENCIA

Abstract

Departamento de Física Atómica, Molecular y Nuclear
Instituto de Física Corpuscular

Doctor of Philosophy

by Rosa María Pérez Vidal

The present Thesis focusses on the experimental study of the evolution of collectivity in the vicinity of the doubly-magic nucleus ^{100}Sn . In particular, the conservation of seniority along the $g_{9/2}$ shell has been investigated. This shell is the first one in which the seniority might not be conserved. Excellent cases for studying the properties of this shell are the the $N = 50$ isotones in the vicinity of ^{100}Sn and the $Z = 28$ isotopes towards ^{78}Ni , which have the same valence nucleons for protons and neutrons, respectively. In the former case, shell model calculations predict the conservation of seniority towards the complete occupation of the $g_{9/2}$ orbital due to an increasing pairing-strength along the $N = 50$ isotones, which differs from what the calculations suggest for the latter case.

To test this phenomenon, the reduced transition probabilities for the $4^+ \rightarrow 2^+$ yrast transitions, in ^{92}Mo and ^{94}Ru nuclei, have been determined experimentally for the first time via lifetime measurements at the GANIL laboratory. The multi-nucleon transfer reaction mechanism was unconventionally used to populate the proton-rich nuclei of interest: a ^{92}Mo beam with an energy of 716.9 MeV impinged on the stretched ^{92}Mo target of the IKP Cologne plunger, while a ^{24}Mg foil was used to degrade the energy of the reaction products to measure the lifetime with the RDDS technique. The reaction products of interest have been identified with the magnetic spectrometer VAMOS++, while the gamma-rays have been measured using AGATA.

From this experiment the reduced transition probabilities for the $4^+ \rightarrow 2^+$ and $2^+ \rightarrow 0^+$ yrast transitions in ^{92}Mo and ^{94}Ru and for the $4^+ \rightarrow 2^+$ and $6^+ \rightarrow 4^+$ yrast transitions in ^{90}Zr have been determined. This made possible a complete study of the seniority scheme in the $\pi g_{9/2}$. The results on the obtained reduced transition probabilities have been interpreted on the basis of realistic shell model predictions in the $f_{5/2}$, $p_{3/2}$, $p_{1/2}$, $g_{9/2}$ proton valence space, allowing also for the comparison of the nuclear structure trends between the valence mirror symmetry partners.

Additionally, part of this Thesis is devoted to the performance of state-of-the art high-resolution gamma-ray spectroscopy detector used in the experiment. The characterization of AGATA is provided based on the analysis of source and in-beam data taken with 23 segmented crystals.

Acknowledgements

La presente Tesis doctoral no es tan sólo el resultado de una ardua labor investigadora sino la consecuencia de la implicación y el compromiso mostrados por todas aquellas personas e instituciones que han hecho posible que esta inolvidable experiencia llegara a buen término (¡por fin!).

Este trabajo ha sido parcialmente financiado por el Ministerio de Ciencia, Innovación y Universidades de España, a través de la beca de Formación de Personal Investigador, FPI (BES-2012-061407) y de las subvenciones de los proyectos SEV-2014-0398, FPA2011-29854-C04, FPA2014-57196-C5 and FPA2017-84756-C4, por los fondos de la Comisión Europea FEDER y por la Generalitat Valenciana, Conselleria d'Educació, Investigació, Cultura i Esport a través de subvención del proyecto PROMETEU/2019/005. Además, la beca FPI me permitió desarrollar la actividad experimental de la Tesis en distintos laboratorios internacionales a través de los programas para Estancias Breves EEBB-I-14-08606 (GSI, Alemania), EEBB-I-15-09671(GANIL, Francia)y EEBB-I-16-11451 (GANIL, Francia). Por todo ello, quiero agradecer especialmente el apoyo recibido durante mi formación académica y labor investigadora a las respectivas Instituciones. También quiero agradecer al IFIC y a la Universidad de Valencia su hospitalidad y apoyo durante el periodo de realización esta Tesis doctoral.

Son muchas las personas que me han acompañado durante el transcurso del doctorado y a todas ellas quiero agradecerles cada momento que me han dedicado.

En particular, a mis directores, Andrés Gadea Raga y César Domingo-Pardo. Este trabajo nunca habria existido si no fuera por ellos. Muchas gracias Andrés y César, por vuestra guía en este largo viaje, por vuestra infinita paciencia, dedicación e implicación en la dirección de la tesis, por vuestros consejos y opiniones que han contribuido a mi desarrollo tanto profesional como personal y por vuestro apoyo y comprensión en los momentos difíciles.

With the following lines, I would like to thank all the people I met during my experience at LNL, GSI and GANIL. This Thesis would not have been finished without their help and advice.

To José Javier Valiente, for providing me with the opportunity to perform data analysis work at LNL, for being available for any discussion, for following constantly my Thesis work and for his friendship.

To Jürgen Gerl for allowing me to be part of the group at GSI during the experimental campaign of 2014. To all the researchers there, for transmitting me their knowledge on AGATA as well as the different detectors present in the PRESPEC installations, and to the PhD students, for the warm welcome at GSI, the kind help during my first long period far from home and the fun moments outside the laboratory.

To Emmanuel Clement for giving me the great opportunity to work in the first and second experimental campaigns at GANIL and acquire a lot of experience in the AGATA and VAMOS++ instruments. This was highly useful for the understanding of my experiment and to develop skills in the analysis. I am really grateful to have been able to work with the group.

To Antoine Lemasson, Maurycy Rejmund, Alahari Navin and Yung Hee Kim, for their huge help

and advice for analysing VAMOS++ data. Again, thanks to Navin, for having expanded and improved my knowledge with his tricky questions. To Bertrand Jacquot, thank you for sharing your knowledge. To Emmanuel Clement, Caterina Michelagnoli, Amel Korichi, Magda Zielinska and Hongjie Li, for the amount of advices and discussions for analysing the AGATA data. To Amel, for his time, infinite help and support. *Merçi pour votre hospitalité et votre affection, je me sentais vraiment comme votre fille.* To Caterina, thank you for teaching me everything you know about AGATA and for your strong support and comprehension in difficult times. To Marco, who was at GANIL during my two stays, for sharing with me so many night-shifts and taking part in my adventures at GANIL (*È Meraviglioso far parte di un team!*). Thank you to the AGATA performance team. To Waely López, Joa Ljungvall and Marc Labiche, for the fruitful discussions about AGATA. To Oliver Stezowski and Jérémie Dudouet, thank you for the continuous help with the data analysis software. To Claus Müller-Gattermann and Christoph Fransen for the discussions about plunger measurements and the DDCM technique. To Suzana Szilner, for her availability for questions and calculations of the cross section, before and after the experiment. To the Naples group, for the great work with the shell-model calculations, especially to Angela Gargano and Luigi Coraggio.

I am also grateful to every single person I have met during schools, conferences and experiments. Thank you for sharing your valuable knowledge.

Finally, thank you very much to all the members of the AGATA, VAMOS++ and IKP plunger collaboration and all the people involved in the experiment of my Thesis. This work would not have been possible without their help.

Volviendo a Valencia, me gustaría empezar dando las gracias a Tayfun y a Mariluz, mis compañeros del grupo *AGATA* en el IFIC y buenos amigos, que han vivido de cerca todo el proceso siempre dispuestos a escuchar, ayudar y animar. Gracias a la *celda 132* (y visitantes) por ser el mejor despacho que pueda existir, donde el buen ambiente nunca falta para animar y motivar a cualquiera que lo necesite. Echaré mucho de menos nuestros intentos de baile los viernes por la mañana, las risas contagiosas y las canciones dedicadas: *“Rosa, Rosa, tan maravillosa...”* Al grupo de *Doctorandoms* que ha ido variando su composición a lo largo de los años pero siendo siempre la mejor vía para recargar energías. Gracias por compartir vuestras experiencias conmigo durante la comida, no perdáis nunca la dulce tradición de los postres. Pese a no formar hoy en día parte de este grupo, merecen un agradecimiento especial Ana, Ane, Damián y Javi por su infinita ayuda y apoyo siempre y, sobre todo, en los momentos más difíciles. A todos vosotros gracias por estar ahí, por las noches de *Benicinos*, ya fuera media hora o hasta que cerraran *Pi-ca-di-lly* (leído como lo diría Carlos).

A mis amigos de Alicante, que tarde lo que tarde en volver siempre me reciben como si nunca pasara el tiempo. En especial, a Laura y Salva, quienes han estado siempre apoyándome, animándome y celebrando cada triunfo desde la distancia. Desde el primer momento en que nos conocimos en el primer año del instituto supe que seríamos mejores amigos para siempre. Muchas gracias por estar siempre orgullosos de mí. Recordando el instituto, me gustaría hacer una mención especial a mi profesor de Física de 2º de Bachillerato, Sanz, a quien estaré eternamente

agradecida por convencerme para introducirme en el fascinante mundo de la Física a través de sus maravillosas clases que hacían del aprendizaje una diversión.

A mis amigos de la carrera y del Rector Peset, con quienes compartí todas mis vivencias universitarias y que, a pesar de que nuestros caminos se han separado desde entonces, siempre han estado pendientes de la evolución de la Tesis. A Esther, Jesús, Patricia y Erica. A Lledó, Ana, Marina y Mapi. Muchas gracias a todos por vuestra amistad incondicional.

A Héctor, gracias por aparecer en los últimos meses del doctorado y no desistir en tu *conquista*. Has sido un grandísimo apoyo en la finalización de este camino. Gracias por creer siempre en mis capacidades, por hacerme ver siempre el lado positivo de todo, por querer que sea feliz y hacer todo lo posible para que lo consiga. *Although pineapples are in your head, you'll make me fly and I'll be happy all the time.*

Por último, y no por ello menos importante, a mi familia, que ha seguido con admiración e interés (y en ocasiones, preocupación) todos mis pasos durante este viaje. A mis abuelos, tíos y primos, muchas gracias por el apoyo incondicional recibido y la fuerza en los momentos difíciles. A mi hermano por aguantar todas mis quejas y lamentos sin importar la hora del día. Por creer siempre en mí. Por darme fuerzas siempre que lo necesito. *Ets el millor*. A mis padres, a quienes se lo debo todo ya que sin ellos nunca habría podido llegar a ser quien soy. A mi madre, gracias por tu ejemplo y valentía, por sacar fuerzas de donde no las hay para conseguir siempre lo mejor para mí. A mi padre, gracias por haberme permitido disfrutar de tu compañía, de tu sabiduría infinita, de tu cariño y de tu amor incondicional durante 27 años. Gracias por enseñarme tu lógica, paciencia y optimismo. Espero poder seguir tu legado como es debido para que siempre te sientas orgulloso de mí. *Te echamos mucho de menos*. A los tres, gracias por vuestra enorme ayuda siempre y, en especial, durante este camino. Os quiero mucho.

A todos vosotros, muchas gracias.

Contents

Declaration	III
Abstract	VII
Acknowledgements	IX
List of Figures	XVII
List of Tables	XXIII
Abbreviations	XXV
1. Introduction	1
1.1. Physics motivation	1
1.1.1. Pairing and Seniority	1
1.1.2. The $g_{9/2}$ shell	2
1.2. AGATA	5
1.3. Thesis outline	7
2. Experimental details	9
2.1. Introduction to the experiment	9
2.2. Reaction Mechanism	12
2.2.1. Kinematics	15
2.2.2. Cross Section	19
2.3. The VAMOS++ Magnetic Spectrometer	21
2.3.1. The optical elements	23
2.3.2. The charged particle detectors and electronics	24
2.3.2.1. The entrance detectors	25
2.3.2.2. The focal plane detectors	27
2.3.2.3. The electronics	29
2.4. The differential plunger	30
2.4.1. Recoil Distance Doppler Shift technique	32

2.4.2.	The target and degrader	35
2.4.3.	Distances	37
2.5.	The AGATA Spectrometer	40
2.5.1.	The gamma-ray detectors and electronics	41
2.5.2.	Pulse Shape Analysis	45
2.5.3.	Tracking	48
2.6.	Data acquisition	50
2.6.1.	AGATA-VAMOS++ trigger on the GTS System	52
2.6.2.	Data flow with NARVAL	53
3.	Data processing	57
3.1.	The AGATA data processing	57
3.1.1.	The Local Level	59
3.1.1.1.	Crystal Producer	60
3.1.1.2.	Preprocessing Filter	61
3.1.1.3.	PSA Filter	70
3.1.1.4.	PostPSA Filter	73
3.1.2.	The Global Level	79
3.1.2.1.	Event Builder and Merger	79
3.1.2.2.	Tracking Filter	79
3.1.3.	GRID computing	82
3.1.3.1.	Example of Local level processing (PSA) on the GRID	85
3.1.3.2.	Example of a full experiment processing (PSA+tracking) on the GRID	87
3.2.	The VAMOS++ data processing	88
3.2.1.	Calibration and event reconstruction	89
3.2.1.1.	Multi-wire entrance detectors (DPS-MWPC)	91
3.2.1.2.	Multi-wire focal plan detector (MWPPAC)	94
3.2.1.3.	Drift Chambers (DC)	95
3.2.1.4.	Ionization Chamber (IC)	97
3.2.2.	The Particle Identification	100
3.2.2.1.	Atomic number	100
3.2.2.2.	Charge state	101
3.2.2.3.	Mass number	103
3.3.	Gamma-ray spectroscopy	104
3.3.1.	Doppler correction	105
3.3.1.1.	Velocity distribution	105
3.3.1.2.	Angle distribution	106
3.3.1.3.	Tracked gamma-rays	108
3.3.2.	Total Kinetic Energy Loss (TKEL) in MNT reactions	111
4.	Lifetime determination	113
4.1.	RDDS data analysis	113
4.1.1.	Decay Curve Method (DCM)	114

4.1.2.	Differential Decay Curve Method (DDCM)	116
4.1.3.	Feeding treatment	118
4.1.4.	Deorientation	120
4.2.	Verification of methodology: lifetime in ^{93}Tc and ^{94}Mo	121
4.2.1.	Verification with ^{93}Tc	122
4.2.2.	Verification with ^{94}Mo	125
4.3.	Analysis of the Inelastic Channel: lifetime in ^{92}Mo	127
4.4.	Analysis of the Two-Proton Transfer Channel: lifetimes in ^{90}Zr and ^{94}Ru	132
4.4.1.	Analysis of ^{90}Zr	132
4.4.2.	Analysis of ^{94}Ru	136
5.	Theoretical interpretation and Conclusions	141
5.1.	The nuclear shell-model	141
5.1.1.	Realistic effective Hamiltonian	142
5.1.2.	Transition operators	144
5.2.	Evolution of collectivity along the $\pi g_{9/2}$	145
5.2.1.	Experimental results	145
5.2.2.	Theoretical calculations	147
5.2.2.1.	Seniority scheme	151
5.3.	Summary and conclusions	153
6.	Performance of AGATA	157
6.1.	AGATA configuration	157
6.2.	Measurement and methodology description	159
6.2.1.	Energy Resolution	161
6.2.2.	Efficiency and Peak-to-Total	164
6.2.2.1.	Methodology of Analysis	165
6.3.	Results	167
6.3.1.	Performance with sources	168
6.3.1.1.	Energy Resolution	170
6.3.1.2.	Efficiency and Peak-to-Total	171
6.3.2.	Discussion on the in-beam performance with the inelastic reaction channel	182
6.3.2.1.	Energy Resolution	186
6.3.2.2.	Efficiency and Peak-to-Total	187
6.4.	Summary	192
7.	Resumen de la Tesis	195
7.1.	Introducción	195
7.2.	Detalles experimentales	196
7.2.1.	El espectrometro magnético VAMOS++	197
7.2.2.	El espectrometro AGATA	198
7.2.3.	El plunger diferencial	198
7.3.	Procesado de datos	199

7.4.	Determinación del tiempo de vida	201
7.4.1.	Técnica RDDS	201
7.4.2.	Verificación de la metodología	203
7.4.3.	Resultados	204
7.5.	Interpretación Teórica y Conclusiones	205
7.5.1.	Evolución de la colectividad en la capa $\pi g_{9/2}$	205
7.5.1.1.	Esquema de <i>seniority</i>	207
7.5.2.	Conclusiones	208
7.6.	Rendimiento de AGATA	209
7.6.1.	Resolución en energía	209
7.6.2.	Eficiencia	210
7.7.	Sumario	210

List of Figures

1.1. Low energy spectra for the N=50 isotones and the Z=28 isotopes $g_{9/2}$ in the shell.	3
1.2. Reduced transition probabilities for the N=50 isotones, the Z=28 isotopes and a seniority conserving interaction in the $g_{9/2}$ shell from a four particle (hole) system.	4
1.3. Reduced transition probabilities for the N=50 isotones and the Z=28 isotopes in the $g_{9/2}$ shell from large-scale shell-model calculations.	5
1.4. AGATA sub-array photograph.	6
2.1. Plan of GANIL facility.	10
2.2. Picture of the experimental setup used at GANIL for the lifetime measurement.	12
2.3. Simplified illustration of the nuclear reactions classification.	13
2.4. Definition of the grazing angle in a binary nuclear reaction.	15
2.5. Scheme of the reaction kinematics in the laboratory frame.	15
2.6. Schematic view of the experimental setup.	17
2.7. Dependency of the cross section with the angle in the center of mass for the $^{92}\text{Mo}+^{92}\text{Mo}$ reaction.	20
2.8. Relative yields for the transfer channels observed in the $^{92}\text{Mo}+^{92}\text{Mo}$ reaction.	20
2.9. Schematic view of the VAMOS++ optical elements.	22
2.10. Schematic view of the VAMOS++ detection system.	24
2.11. Schematic view and pictures of the DPS-MWPC detector assembly.	26
2.12. Picture of the MWPPAC assembly.	27
2.13. Schematic drawing and pictures of the drift chamber assembly.	28
2.14. Drawing of the ionization chamber modular assembly.	29
2.15. Schematic representation of the Plunger device.	31
2.16. Drawing of the Plunger device inside the reaction chamber.	32
2.17. Schematic drawing of the RDDS technique using the differential plunger in grazing reactions.	33
2.18. Picture of the target and degrader used in the experiment.	35
2.19. Picture of the Plunger device inside the reaction chamber.	36
2.20. Plunger distance calibration.	39
2.21. Drawings of AGATA geometries.	42

2.22. AGATA segmentation labelling and AGATA triple cluster photography.	43
2.23. Photography of the AGATA sub-array configuration at GANIL. . .	45
2.24. Net charges and transient signals for one event in an AGATA detector. 46	
2.25. The most probable gamma-ray detection mechanisms at different ranges of E_γ	49
2.26. Schematic layout of the AGATA-VAMOS++ data acquisition system and the near-line analysis.	51
2.27. Illustration of the topology of the GTS tree.	53
3.1. AGATA data processing with a complementary detector: Scheme of the chain of NARVAL actors.	59
3.2. Producer: Segments amplitude signals.	60
3.3. Preprocessing: Segments signals calibrated in energy.	62
3.4. Preprocessing: Segments cross-talk correction.	63
3.5. Preprocessing: Segments correction matrices.	64
3.6. Preprocessing: Dead segments in crystal 03A.	65
3.7. Preprocessing: Broken segment correction in crystal 12B.	66
3.8. Preprocessing: Lost segment correction in crystal 11B.	67
3.9. Preprocessing: Unstable segment correction in crystal 00B.	68
3.10. Preprocessing: Unstable segment correction in crystal 04B.	68
3.11. Preprocessing: Segments time alignment to the core.	69
3.12. Preprocessing: T_0 alignment.	70
3.13. PSA: Traces.	71
3.14. PSA: gamma-ray interaction distributions.	71
3.15. PSA:Gamma-ray interaction position distributions in the XY plane by slices.	72
3.16. PSA: Effect of time position of the experimental trace.	73
3.17. PostPSA: Neutron damage correction.	74
3.18. PostPSA: Segments after the neutron damage correction.	75
3.19. PostPSA: Energy recalibration for the energy sum of segments and the core.	76
3.20. PostPSA: Overlap of all the time combinations between crystals for the global time alignment.	77
3.21. PostPSA: Global time alignment.	78
3.22. Tracking: First Interaction pattern.	80
3.23. Tracking: P_{track} parameter evaluation.	81
3.24. Tracking: σ_θ parameter evaluation.	81
3.25. Tracking: P_{sing} parameter evaluation.	81
3.26. Scheme of the chain of NARVAL actors for the data processing on the GRID.	84
3.27. Test of AGATA data processing on GRID (30 cdat files).	86
3.28. Scheme of the identification principle structure in VAMOS++. . . .	89
3.29. Schematic drawing of the focal plane detectors.	90
3.30. PPS-MWPC:Charge calibration.	92

3.31. DPS-MWPC: Hit positions pattern.	93
3.32. DPS-MWPC:scatering angles determination.	93
3.33. DPS-MWPC: Scattering angle and the interaction point on the target.	94
3.34. MWPPAC: ToF aligment	95
3.35. DC: Charge calibration.	96
3.36. IC: Thresholds first row.	98
3.37. IC: Gain matching.	99
3.38. IC: Energy evolution in time.	100
3.39. Energy loss as a function of the total energy released in the IC for the Z identification.	101
3.40. Charge states q as a function of the A/q ratio.	102
3.41. Total mass distribution for the ions detected in VAMOS++.	103
3.42. Mass distributions for the Zr, Nb, Mo, Tc and Ru isotopes	103
3.43. AGATA-VAMOS++ timestamp difference.	104
3.44. Velocity distributions for the inelastic channel, the $\pm 1p$ and the $\pm 2p$ transfer channels.	106
3.45. Schematic view of the VAMOS++ and AGATA reference frames.	107
3.46. Angular distribution between the recoil direction and the emitted gamma-ray direction.	108
3.47. Comparison of the tracked gamma-ray spectra without and with the Doppler correction for ^{92}Mo	109
3.48. Doppler correction example for ^{92}Mo	109
3.49. Tracked gamma-ray spectra obtained with AGATA in coincidence with VAMOS++ for the nuclei ^{90}Zr , ^{91}Nb , ^{92}Mo , ^{93}Tc and ^{94}Ru	110
3.50. Example of different TKEL cuts in ^{92}Mo for the shortest target-to- degrader distance.	111
4.1. Schematic drawing of the RDDS technique using the differential plunger and the methodology to determine the lifetime.	114
4.2. Schematic level-feeding pattern.	115
4.3. Effect of the long-lived transitions in RDDS technique.	119
4.4. Example of the subtraction method in ^{92}Mo for the shortest target- to-degrader distance.	120
4.5. Measured intensities from the ratio of the unshifted component at 125° and 155° of $4^+ \rightarrow 2^+$ transition in ^{92}Mo (773.0 keV) as a function of several target-to-degrader distances.	121
4.6. Doppler corrected gamma-ray energy spectrum for ^{93}Tc for the shortest target-to-degrader distance.	122
4.8. Doppler corrected spectra of ^{93}Tc in the $25/2^- \rightarrow 21/2^-$ (607.5 keV) transitions region for the seven distances measured.	123
4.7. Simplified level scheme of ^{93}Tc showing the feeders observed.	123
4.9. Decay curve for the ^{93}Tc $25/2^- \rightarrow 21/2^-$	124
4.10. Doppler corrected gamma-ray energy spectrum for ^{94}Mo for the shortest target-to-degrader distance.	125

4.12. Doppler corrected spectra of ^{94}Mo showing the $2^+ \rightarrow 0^+$ (871.1 keV), $4^+ \rightarrow 2^+$ (702.6 keV) and $6^+ \rightarrow 4^+$ (849.7 keV) transitions region for the seven distances measured.	126
4.11. Simplified level scheme of ^{94}Mo showing the feeders observed.	126
4.13. Decay curve for the $4^+ \rightarrow 2^+$ transition in ^{94}Mo	127
4.14. Doppler corrected gamma-ray energy spectrum for ^{92}Mo for the shortest target-to-degrader distance.	128
4.15. Simplified level scheme of ^{92}Mo showing the feeders observed.	129
4.16. Doppler corrected spectra of ^{92}Mo showing the $4^+ \rightarrow 2^+$ (773.09 keV) and $2^+ \rightarrow 0^+$ (1509.5 keV) transitions region for the seven distances measured.	129
4.17. Decay curve for the $4^+ \rightarrow 2^+$ transition in ^{92}Mo	130
4.18. Decay curve for the $2^+ \rightarrow 0^+$ transition in ^{92}Mo	130
4.19. Decay curve for the $4^+ \rightarrow 2^+$ transition in ^{92}Mo	131
4.20. Doppler corrected gamma-ray energy spectrum for ^{90}Zr for the shortest target-to-degrader distance.	132
4.21. Simplified level scheme of ^{90}Zr showing the feeders observed.	133
4.22. Doppler corrected spectra of ^{90}Zr showing the $4^+ \rightarrow 2^+$ (890.7 keV) and $6^+ \rightarrow 5^-$ (1129.2 keV) transitions region for the seven distances measured.	134
4.23. Decay curve for the $4^+ \rightarrow 2^+$ transition in ^{90}Zr	135
4.24. Decay curve for the $6^+ \rightarrow 5^-$ transition in ^{90}Zr	135
4.25. Doppler corrected gamma-ray energy spectrum for ^{94}Ru for the shortest target-to-degrader distance.	136
4.26. Simplified level scheme of ^{94}Ru showing the feeders observed.	137
4.27. Doppler corrected spectra of ^{94}Ru showing the $4^+ \rightarrow 2^+$ (755.5 keV) and $2^+ \rightarrow 0^+$ (1430.7 keV) transitions region for the seven distances measured.	138
4.28. Decay curve for the $4^+ \rightarrow 2^+$ transition in ^{94}Ru	138
4.29. Decay curve for the $2^+ \rightarrow 0^+$ transition in ^{94}Ru	139
5.1. Experimental collectivity along $N = 50$ of the $4^+ \rightarrow 2^+$ transition.	146
5.2. Experimental and theoretical energy spectra and $B(E2)$ strength of ^{90}Zr	148
5.3. Experimental and theoretical energy spectra and $B(E2)$ strength of ^{92}Mo	149
5.4. Experimental and theoretical energy spectra and $B(E2)$ strength of ^{94}Ru	150
5.5. Evolution of collectivity along $N=50$	152
5.6. Evolution of collectivity along the $g_{9/2}$ orbital for the VMS partners with different seniority schemes.	154
6.1. AGATA configuration (24 crystals) as seen from the reaction chamber.	158
6.2. Schematic view of the set-up for the AGATA performance.	160
6.3. Detector resolution.	161
6.4. AGATA counting rates per detector with sources and in-beam.	162

6.5. Efficiency vs Rate	163
6.6. FWHM at 1.332 MeV. MWD-Risetime.	163
6.7. Schematic illustration for the efficiency measurement methodology.	165
6.8. Level scheme for two gamma-rays cascade.	166
6.9. Spectra comparison for different modes of analysis. ^{152}Eu	169
6.10. Comparison between the tracked spectra: Core and Sum of segments energies	169
6.11. FWHM at 1.3 MeV. Neutron damage correction.	170
6.12. FWHM as a function of the energy.	171
6.13. Core common energy spectrum of ^{152}Eu . Background contamination.	172
6.14. Core common energy spectrum and efficiency curve of ^{152}Eu . Background subtraction.	173
6.15. Time window gamma-gamma coincidence.	174
6.16. Relative core efficiency per crystal at 1.3MeV.	175
6.17. Absolute efficiency for 23 capsules using different AGATA analysis modes.	176
6.18. Angular distribution correlated, uncorrelated and normalized. Tracked data with sources.	177
6.19. Angular correlation. Tracked data with sources.	178
6.20. Angular correlation distribution for the data with sources.	179
6.21. Absolute efficiency comparison of the different modes of analysis for 23 capsules.	180
6.22. Scheme of the in-beam measurement used for the performance.	183
6.23. In-beam Doppler corrected spectra (^{92}Mo) comparison for different modes of analysis.	184
6.24. In-beam comparison between the Doppler corrected tracked spectra: Core and Sum of segments energies	185
6.25. In-beam comparison between the non Doppler corrected tracked spectra : Core and Sum of segments energies	185
6.26. In-beam spectra comparison showing the resolution quality of the peaks.	186
6.27. Time window gamma-gamma coincidence.	188
6.28. In-beam (^{92}Mo at 0° with respect to the VAMOS++ axis) spectrum. Background subtraction in coincidence.	189
6.29. In-beam (^{92}Mo at 90° with respect to the VAMOS++ axis) spectrum. Background subtraction in coincidence.	190
6.30. Losses of requests in the trigger processor for high total rates in AGATA	191
6.31. Absolute efficiency comparison of the different modes of analysis with sources and in-beam using 23 capsules.	193
7.1. Dibujo esquemático del montaje experimental.	197
7.2. Espectros de energía experimentales y teóricos para los núcleos ^{90}Zr , ^{92}Mo y ^{94}Ru	206
7.3. Evolución de la colectividad a lo largo de los isótonos con $N = 50$	207

List of Tables

2.1.	Optimum parameters for the reaction mechanism and the transmission of the recoil to be detected in the magnetic spectrometer. . . .	17
2.2.	Kinematic transmissions of reaction products ejected at the grazing angle through the detection system at different stages.	18
2.3.	Q values and expected total cross sections for the proton pickup channels in the reaction $^{92}\text{Mo} + ^{92}\text{Mo}$	19
2.4.	Operational features of VAMOS++.	22
2.5.	Characteristics of the VAMOS++ quadrupoles.	23
2.6.	Characteristics of the VAMOS++ Dipole.	24
2.7.	VAMOS++ detectors characteristics.	25
2.8.	Performance of the DPS-MWPC detector.	26
2.9.	Characteristics of the differential plunger setup.	31
2.10.	Plunger contact points.	39
2.11.	Absolute target-to-degrader distances measured.	40
2.12.	Absolute target-to-degrader distances measured.	40
2.13.	Topology of NARVAL actors for the local and global level processing.	55
3.1.	PostPSA: FWHM of the sum energy of all the segments and the core energy before and after the neutron damage correction	76
3.2.	List of services to access remote sources on the GRID.	83
3.3.	AGATA Storage Elements (SE) and Computing Elements (CE) on the GRID.	83
3.4.	Comparison of different types computing resources in terms of data replay time for AGATA data local level processing (PSA).	85
3.5.	Comparison of different types of AGATA data processing on GRID for the present experiment.	87
3.6.	Velocities of the reaction products before and after de degrader. . .	106
4.1.	Half-life ($t_{1/2}$), lifetime (τ) and reduced transition probability ($B(E2)$) for the ^{92}Mo $4^+ \rightarrow 2^+$ transition at 773 keV.	131
4.2.	Half-life ($t_{1/2}$), lifetime (τ) and reduced transition probability ($B(E2)$) for the ^{92}Mo $2^+ \rightarrow 0^+$ transition at 1510 keV.	131
4.3.	Half-life ($t_{1/2}$), lifetime (τ) and reduced transition probability ($B(E2)$) for the ^{90}Zr $4^+ \rightarrow 2^+$ transition at 890 keV.	136
4.4.	Tentative half-life ($t_{1/2}$), lifetime (τ) for the ^{90}Zr $6^+ \rightarrow 5^-$ transition at 1129 keV and reduced transition probability ($B(E2)$) for the $6^+ \rightarrow 4^+$ transition at 371 keV.	136

4.5.	Half-life ($t_{1/2}$), lifetime (τ) and reduced transition probability ($B(E2)$) for the $^{94}\text{Ru } 4^+ \rightarrow 2^+$ transition at 755 keV.	139
4.6.	Half-life ($t_{1/2}$), lifetime (τ) and reduced transition probability ($B(E2)$) for the $^{94}\text{Ru } 2^+ \rightarrow 0^+$ transition at 1430 keV.	139
5.1.	Adopted lifetimes (τ), half-lives ($t_{1/2}$) and reduced transition probabilities ($B(E2)$) from this experiment.	145
5.2.	Experimental and calculated $B(E2)$ strengths of ^{90}Zr	148
5.3.	Experimental and calculated $B(E2)$ strengths of ^{92}Mo	149
5.4.	Experimental and calculated $B(E2)$ strengths of ^{94}Ru	150
5.5.	VMS partners nuclear structure features comparison in the $g_{9/2}$ mid shell.	155
6.1.	Crystal look up table E682.	158
6.2.	Calibration sources.	159
6.3.	Total internal conversion coefficient α_T	173
6.4.	Angular correlation: A_k coefficients.	174
6.5.	Electronics dead-time estimation.	177
6.6.	Efficiency fit parameters.	181
6.7.	Efficiency and P/T at 1332 keV.	181
6.8.	Raw efficiency at 1510 keV.	189
6.9.	Average efficiency estimation at 1510 keV.	192
7.1.	Vidas medias (τ), períodos de semidesintegración ($t_{1/2}$) y probabilidades de transición reducidas ($B(E2)$) obtenidas en este experimento.	205

Abbreviations

ADC	A nalog to D igital C onverter
ADL	AGATA D ata L ibrary
AGATA	A dvanced G amma T racking A rray
caDSAM	c ontinuous- a ngle D oppler S hift A ttenuation M ethod
CIME	C yclotron pour I ons de M oyenne E nergie
CFD	C onstant F raction D iscriminator
C0	C yclotron compact
CSS	C yclotron à S ecteurs S éparés
DC	D rift C hamber
DCM	D ecay C urve M ethod
DDCM	D ifferential D ecay C urve M ethod
ECR	E lectron C yclotron R esonances
DPS-MWPC	D ual P osition S ensitive M ulti- W ire P roportional C ounter
FoM	F igure of M erit
FWHM	F ull W idth at H alf M aximum
GANIL	G rand A ccelerateur N ational d' I ons L ourds
GTS	G lobal T rigger S ynchronization
HPGe	H igh P urity G ermanium
ISOL	I sotope S eparation O n- L ine
LISE	L igne d' I ons S uper E pluchés
MGT	M ars G amma T racking
MNT	M ulti- N ucleon T ransfer
MWD	M oving W indow D econvolution
MWPPAC	M ulti- W ire P aralel P late A valanche C ounter

Abbreviations

NIM	N uclear I nstrumentation M odule
OFT	O rsay F orward T racking
RDDS	R ecoil D istance D oppler- S hift
RIB	R adioactive I on B eam
SPIRAL	S ystème de P roduction d' I ons R adioactifs en L igné
TAC	T ime-to- A mplitude C onverter
TDC	T ime to D igital C onverter
TKEL	T otal K inetic E nergy L oss
ToF	T ime of F light
VMS	V alence- M irror S immetry

Chapter 1

Introduction

1.1. Physics motivation

The ^{100}Sn nucleus, being the heaviest bound doubly-magic nucleus with equal number of protons and neutrons, has attracted considerable interest from the experimental as well as theoretical point of view [1, 2]. In particular, the structure of this nucleus and its neighbours are excellent benchmark cases to test state-of-the-art shell-model calculations in this emblematic region of the nuclear chart.

1.1.1. Pairing and Seniority

The pairing interaction was introduced by Racah, initially to classify states of n electrons in the atom [3], and latter was extended for the nucleus as a first-order approximation of the strong force between identical nucleons [4]. The eigenstates of a pairing interaction are characterized by a seniority number ν , which corresponds to the number of unpaired nucleons contribution to the total angular momentum J [4]. The seniority is one of the simplest and most powerful approaches in the nuclear shell-model and together with the total spin J classifies the jj-coupling of nucleons in a single j shell.

The conservation of seniority and its properties provide insightful information to identify the shell closures far from stability. While seniority is an approximate symmetry, it is generally is generally conserved up to a large extent (orbital $j \leq$

7/2) and the conditions to preserve it are well known [4–6]. The first shell where seniority violating effects can be observed is the $g_{9/2}$ shell [6].

Excellent cases for studying the properties of the $g_{9/2}$ shell are the $N = 50$ isotopes in the vicinity of the double magic ^{100}Sn and the $Z = 28$ isotopes towards the double magic ^{78}Ni which have the same valence nucleons and where the $g_{9/2}$ orbital first appears for protons and neutrons, respectively. In addition, as a consequence of having the same valence nucleons for protons and neutrons they are expected to present similarities in their structure. This situation is named Valence-Mirror symmetry (VMS).

1.1.2. The $g_{9/2}$ shell

Although the first shell in which the seniority might not be conserved is $g_{9/2}$, it can be occasionally conserved for a subset of solvable eigenstates [5]. This property can be viewed as a partial dynamic symmetry [4]. In particular, Van Isacker [4] showed that in a purely algebraic analysis of levels in nuclei with four identical valence $g_{9/2}$ nucleons (either neutrons or protons) two special states with good seniority $v = 4$ and total spins $J = 4$ and 6 are found as eigenstates of any two-body interaction. This leads to a structure that exhibit both $v = 2$ and $v = 4$ levels. Those levels have been calculated and compared with the observed yrast states in the valence mirror symmetry partners ($N = 50$ isotones and Ni isotopes towards the double-magic closure shell, top and bottom panels respectively) as depicted in Fig. 1.1 from Ref. [5]. Of particular interest are the nuclei with valence-mirror symmetry in the middle of the shell which have four particles or holes for protons (^{94}Ru and ^{96}Pd) and neutrons (^{72}Ni and ^{74}Ni).

There is a remarkable difference in the nuclear structure features between these VMS partners. The solvable $J = 4, 6$ states (thick lines in Fig. 1.1) with seniority $v = 4$ are a few hundred of keV above the yrast states with the same J and seniority $v = 2$ in the ^{94}Ru and ^{96}Pd , at variance with the ^{72}Ni and ^{74}Ni cases, where they are yrast states.

This unique feature has significant effects on the $E2$ decay pattern as illustrated in Fig. 1.2. In the left part, the decay between yrast states is shown in the mid shell of the $N = 50$ isotones and the Ni isotopes as expected from the calculations in a $(9/2)^4$ system. A enhancement in the $B(E2)$ values is observed in the $Z = 28$

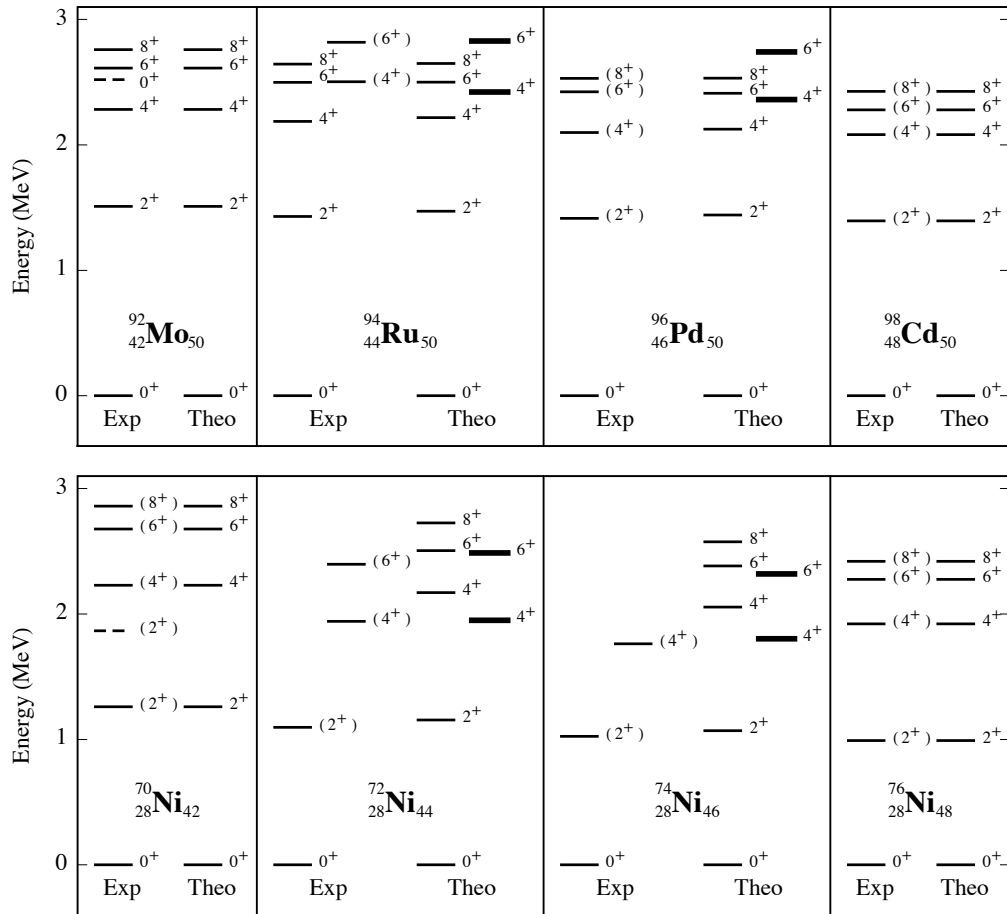


FIGURE 1.1: Top panel: Yrast level schemes for the $N=50$ isotones ^{92}Mo , ^{94}Ru , ^{96}Pd , ^{96}Cd from Ref. [4]. Bottom panel: Yrast level schemes for the Ni isotopes ^{70}Ni , ^{72}Ni , ^{74}Ni , ^{76}Ni from Ref. [4]. Experimental levels on the right side and calculated levels on left side. The thick lines indicate the solvable states with $v = 4$ and the dashed lines are referred to the intruder levels (see Ref. [4] for more details).

isotopes in comparison of the reduced values found in the $N = 50$ isotones for the yrast band. In the right panel of Fig. 1.2, the $E2$ decay pattern is illustrated for a seniority conserving interaction in a four-particle (hole) system. The transition probabilities $B(E2)$ are very small between states with $v = 2$ which are yrast as the seniority classification of the nuclei in the middle of the shell suggests, and as an explanation of seniority isomers [4]. On the other hand, the $B(E2)$ s are an order of magnitude higher for the solvable states with $v = 4$. The $B(E2)$ pattern calculated for the yrast states in ^{94}Ru and ^{96}Pd agrees with seniority conservation.

The same unique feature is still present in the large-scale shell-model calculations of Lisetskiy [8], where a $f_{5/2}$, $p_{3/2}$, $p_{1/2}$, $g_{9/2}$ model space and effective quadrupole charges of $e_p = 2$ for protons and $e_n = 1$ for neutrons are used. Although this calculations show that the nuclear structure towards ^{100}Sn , from $A = 92$ to $A = 98$, is similar to the nuclear structure between ^{70}Ni and ^{76}Ni [8], the two-body

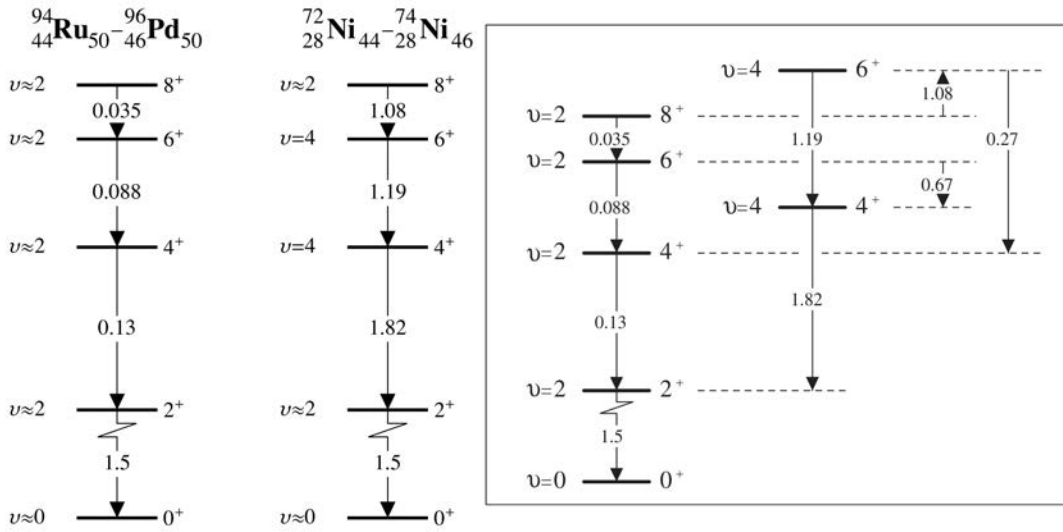


FIGURE 1.2: Left panel: Calculated $B(E2)$ of the $(9/2)^4$ system for the $N = 50$ isotones and the $Z = 28$ isotopes around the middle shell from Ref. [7]. Right panel: E2 decay in $(9/2)^4$ system as obtained with a seniority conserving interaction, from Ref. [5]. In both cases the numbers between the levels denote $B(E2)$ values expressed in units of $B(E2; 2^+ \rightarrow 0^+)$ the two-particle system.

interaction seems to be completely different in the two regions, with the consequent change of seniority in the middle of the shell and of the E2 strength systematics, as illustrated in Fig. 1.3 (solid symbols). The red symbols are what one expects from shell-model calculations if there is seniority conservation and correspond to the $N = 50$ isotones. Independent shell-model calculations [9] using a more conventional effective charge of $e_p = 1.55$ predict slightly lower values for the reduced transition probabilities (see empty symbols in Fig. 1.3), but the same inverted trend for $4^+ \rightarrow 2^+$ transitions toward the fill-up of the $g_{9/2}$ orbital along $N = 50$ is maintained.

The experimental studies performed along the $N=50$ isotones in the $g_{9/2}$ shell corroborates that the yrast $J=2,6,8$ states in this region can be classified by seniority $\nu = 2$ [11, 12]. With the present knowledge of the evolution of collectivity in the $g_{9/2}$ shell towards ^{100}Sn for the $4^+ \rightarrow 2^+$ transition [11] (blue symbols in Fig. 1.3) it is not possible to arrive to a conclusion on the seniority conservation. Therefore, the aim of this Thesis is to explore the seniority conservation for the $N=50$ isotones in the $g_{9/2}$ shell via lifetime measurement of the yrast transitions $4^+ \rightarrow 2^+$ of ^{92}Mo and ^{94}Ru (and ^{90}Zr for a complete systematics of the collectivity). This measurement will allow for a detailed comparison of the nuclear structure between the valence mirror symmetry partners $Z = 28$ isotopes and $N = 50$ isotones.

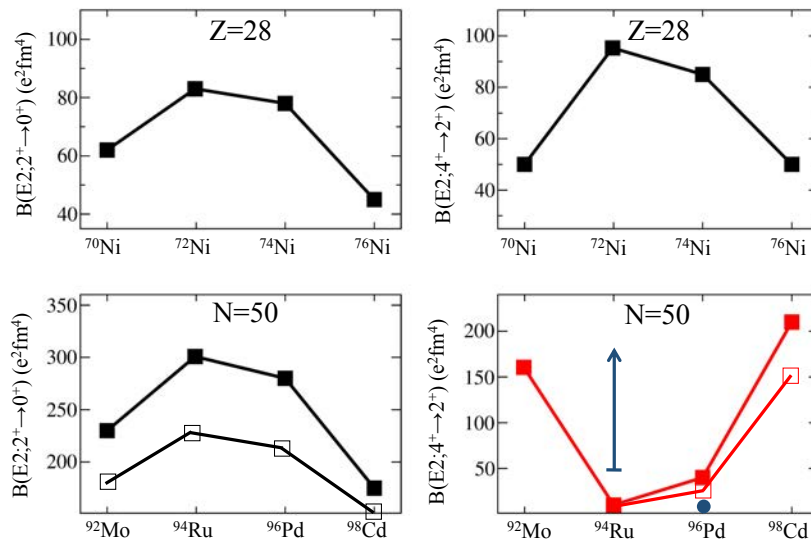


FIGURE 1.3: Calculated $B(E2; 2^+ \rightarrow 0^+)$ (left) and $B(E2; 4^+ \rightarrow 2^+)$ (right) values for $Z = 28$ isotopes with $A = 70 - 76$ (upper part) and $N = 50$ isotones with $A = 92 - 98$ (lower part). Solid squares correspond to the shell-model calculation reported in Ref. [10]. Empty squares correspond to another shell-model calculation made with an effective charge of $e_p = 1.55$. Blue symbols are the experimental $B(E2)$ in that region[11]. See text for details.

1.2. AGATA

High-resolution gamma-ray spectroscopy is a fundamental tool in nuclear physics to investigate the structure of the atomic nucleus. With the inception of the new generation of Radioactive-Ion Beam (RIB) facilities, where a much wider range of unstable proton- and neutron-rich nuclei will become accessible, new gamma-ray detection systems, which provide high efficiency and sensitivity, are required. The Advanced Gamma Tracking Array (AGATA) [13] is a new generation detector based on the technique of gamma-ray tracking in electrically segmented high-purity germanium crystals (Fig. 1.4). Each detector is 36-fold segmented with six-fold azimuthal and six-fold longitudinal segmentation. This allows to obtain the position of the gamma-ray interaction within the detector with high accuracy (5 mm) by means of Pulse Shape Analysis (PSA) techniques. Knowing with accuracy the energy, time and position of every interaction permits to reconstruct the path of the gamma-ray interaction with tracking algorithms. The combination of these two techniques improves the position sensitivity, the photo-peak efficiency, the peak to total ratio and the resolution in the Doppler corrected spectra. As a result of these innovative approaches, AGATA is a position sensitive high-resolution gamma spectrometer capable of operating in extreme measuring conditions (high

counting rates and high background) in combination of complementary detectors and devices, for example to measure charged particles or neutrons. Moreover these techniques improve the peak to total ratio and the resolution in the Doppler corrected spectra, which is crucial for the success of the measurement performed in this Thesis.



FIGURE 1.4: AGATA sub-array with 32 crystals arranged in 10-triple clusters and 1-double cluster installed at GANIL in France.

In order to ensure that the energy resolution, detection efficiency and peak-to-total ratio expected after the PSA and tracking techniques are achieved, dedicated source measurements have been performed before and after each experimental campaign. The first experimental campaign of AGATA was at INFN-LNL (Legnaro) with 15 crystals [14], then at GSI (Darmstadt) with up to 24 crystals [15] and finally at GANIL (Caen) with currently 41 crystals [16]. The latter facility is where the experiment of this Thesis was performed, being the AGATA sub-array composed only of 24 detectors at that time. In some cases, a test with sources is not enough to provide a complete evaluation of the setup and a test using typical reactions is required to validate and ensure the correct performance of the AGATA sub-array. Therefore, in this Thesis, an evaluation of the AGATA sub-array performance figures under the extreme experimental conditions of our measurement will be presented in comparison with dedicated source measurements using the same setup conditions. In addition, a significant part of this PhD Thesis work has been devoted to the study of the AGATA sub-array performance figures with calibrated sources at GSI [17] and GANIL [18].

1.3. Thesis outline

This Thesis will investigate the seniority conservation along the $N = 50$ isotones towards ^{100}Sn via lifetime measurements of the $4^+ \rightarrow 2^+$ and $2^+ \rightarrow 0^+$ yrast transitions in ^{94}Ru , ^{92}Mo and ^{90}Zr nuclei. In addition, the AGATA tracking array performance will be detailed by comparing the figures obtained in measurements using calibrated radioactive sources and measurements in-beam. The details of the forthcoming chapters are outlined in the following.

- Chapter 2 will describe the details of the experiment that was performed to obtain the data analysed in this Thesis. The experimental setup using the AGATA gamma tracking array plus the VAMOS++ magnetic spectrometer in combination with the IKP Cologne Plunger and its constituent parts will be discussed, as well as the reaction mechanisms to produce the nuclei of interest.
- Chapter 3 will be devoted to the data analysis processing of the complex AGATA-VAMOS++ system.
- Chapter 4 will discuss the lifetime determination through the Recoil Doppler Shift technique (RDDS) with the differential Plunger. With that purpose, two methods of analysis, Decay Curve Method (DCM) and Differential Decay Curve Method (DDCM), will be described and applied. Moreover the results on the obtained lifetimes and reduced transition probabilities for the $4^+ \rightarrow 2^+$ and $2^+ \rightarrow 0^+$ yrast transitions in ^{94}Ru , ^{92}Mo and ^{90}Zr will be presented.
- Chapter 5 will interpret the obtained results on the basis of Shell Model predictions, allowing also for the comparison of the nuclear structure trends between the valence mirror symmetry partners ^{56}Ni - ^{78}Ni $Z = 28$ isotopes and ^{78}Ni - ^{100}Sn $N = 50$ isotonic chain. A summary on the main findings in this Thesis and outline future work will be presented.
- Chapter 6 will discuss the AGATA performance with gamma-ray sources and in-beam measurements.

Chapter 2

Experimental details

To test experimentally the phenomenon described in Section 1.1.2 the reduced transition probabilities for the $4^+ \rightarrow 2^+$ yrast transitions in ^{94}Ru and ^{92}Mo nuclei have been determined experimentally via lifetime measurements at the GANIL laboratory. In this chapter, the instruments employed, the methodology and the details of the experiment will be described.

2.1. Introduction to the experiment

The present experiment was carried out at Grand Accélérateur d'Ions Lourds (GANIL), in Caen (France), which is one of the most important large scale facilities for experimental Nuclear Physics in Europe. The GANIL facility produces and accelerates stable ion beams since 1982 for nuclear physics, atomic physics, radiobiology and material irradiation [19]. Nowadays, intense exotic beams [20] are produced by the ISOL method at the SPIRAL1 facility (which is being upgraded to extend the range of post-accelerated radioactive ions, SPIRAL2) or by fragmentation using the LISE spectrometer [21]. Nevertheless, the nature of our study requires intense stable beams. The accelerators and the experimental areas with their devices are schematically depicted in Fig. 2.1.

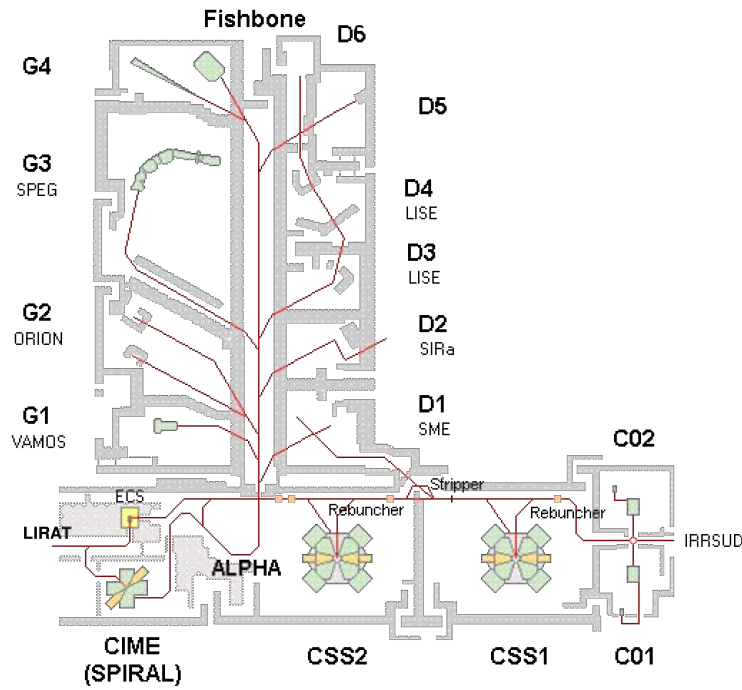


FIGURE 2.1: Schematic drawing of the GANIL installations from [21].

The GANIL acceleration system consists of two ECR (Electron Cyclotron Resonance type) ion sources with their Compact Cyclotron units (C01 and C02, $E/A < 1$ MeV) for the beam production and pre-acceleration; two cascaded identical accelerators, separated-sector cyclotrons type (CSS1 and CSS2); and the CIME cyclotron at the SPIRAL1 for the post-acceleration and production of radioactive ions beams selected by the ISOL method [22]. After acceleration, the beam is directed through the “fishbone” (beam transport and distribution system) towards the different experimental rooms (D1 to D6 and G1 to G4 in Fig. 2.1) depending on the experimental requirements, where the targets and detection apparatus are installed.

The goal of the present experimental work was the study of the collectivity along the $N=50$ isotones towards ^{100}Sn through lifetime measurements. In particular, the measurement of the reduced transition probabilities of $4^+ \rightarrow 2^+$ in ^{92}Mo and ^{94}Ru nuclei. Typically these nuclei would be produced by fusion evaporation but such measurements cannot be tackled due to the presence of low excitation energy isomeric states with lifetimes between hundreds of nanoseconds to tens of microseconds. Therefore, the multi-nucleon transfer reaction was unconventionally used for the production of proton-rich nuclei [23] employing both a beam and a target of ^{92}Mo .

The stable beam of ^{92}Mo was accelerated through the following steps: the ions generated from the neutral atoms of ^{92}Mo in an ECR ion source [24] were injected (after the selection of a single charge state, 16+) into the first cyclotron (C01) and pre-accelerated. From there the beam was accelerated in the CSS1¹ cyclotron up to the final energy of 7.8 MeV/u for a charge state 37+ (the cyclotrons use the same RF frequency of 10.29 Mhz).

After the energy selection (using the magnetic rigidity) the accelerated beam of ^{92}Mo was directed to the experimental room G1 where it impinged in a ^{92}Mo foil of 0.775 mg/cm² to populate the excited states of the nuclei of interest via multi-nucleon transfer reactions. The target was mounted in the IKP Cologne Plunger device for lifetime measurements with the Differential RDDS technique. A 1.9 mg/cm² Mg degrader foil was used to slow down the reaction products in the Plunger, as required by the technique. For the reaction products of interest for this work, in this particular Multi-Nucleon transfer reaction, the cross sections are in the range of the mb. Moreover, since we are dealing with quasi-elastic binary reactions, the differential cross section varies strongly with the angle of the ejectile relative to the beam direction, having a maximum at the Grazing angle. In addition, Multi-nucleon transfer reactions aren't very selective, producing a large number of reaction products. Therefore, high efficiency and very selective detection systems are required. In the present experiment the AGATA array was coupled to the VAMOS++ spectrometer allowing the detection selectivity of the reaction products of interest and high sensitivity on the measurement of the gamma-rays in coincidence with the detected reaction products. A picture of the setup is shown in Fig. 2.2.

The VAMOS++ spectrometer was positioned at the grazing angle (23° with respect to the beam axis) where the production cross section for the quasi-elastic channels is largest. The detector system gives all the necessary information for the complete ion identification, which is performed via an event-by-event reconstruction of the trajectory inside the magnetic elements of the spectrometer.

The AGATA array was composed of 8 triple clusters (with 23 functioning detectors), located at 22.8 cm distance from the target and setted at backward angles.

¹Only CSS1 was used. The CSS2 cyclotron is used only to accelerate beams beyond 10 MeV/A. For beams with energies around the Coulomb barrier, as in this experiment, CSS1 is sufficient.

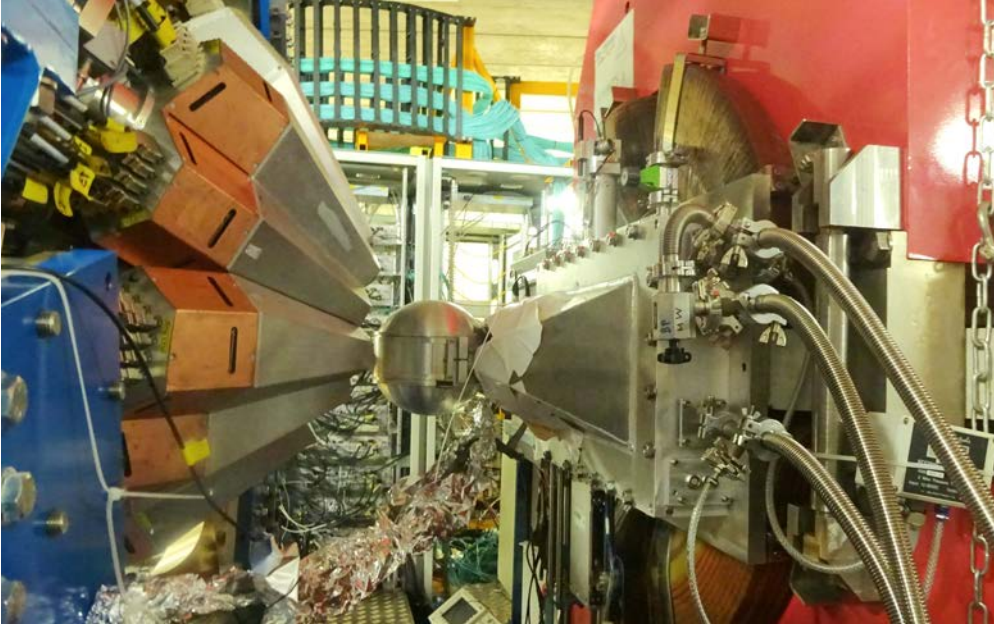


FIGURE 2.2: Picture of the experimental setup used at GANIL for the lifetime measurement: the AGATA tracking array for gamma-ray detection (left), the differential Cologne Plunger for the lifetime measurement inside the reaction chamber (middle) and the VAMOS++ magnetic spectrometer for the reaction products identification (right).

The backward angles subtended by AGATA are most sensitive to the Doppler-shift variations and thus, to the lifetime effect.

The Plunger device was placed in the geometrical centre of the reaction chamber and perpendicular to the optical axis of the spectrometer. The degrader was positioned at different distances in order to determine the lifetime using the RDDS technique. In order to cover the full lifetime range expected for the isotones of interest (from 1 ps up to hundreds of ps) seven different distances were measured at 19, 25, 100, 500, 1000, 2000 and 4000 μm .

Seven days of beam time (24 UT) were used to measure the seven target-degrader distances. In the following sections a more detailed description of the production and the main characteristics of the various components of the detection system are given.

2.2. Reaction Mechanism

The reactions taking place when nuclei collide can be classified according to the impact parameter, as it is schematically depicted in Fig. 2.3. The impact parameter, b , is the distance between the trajectory of a projectile and the target.

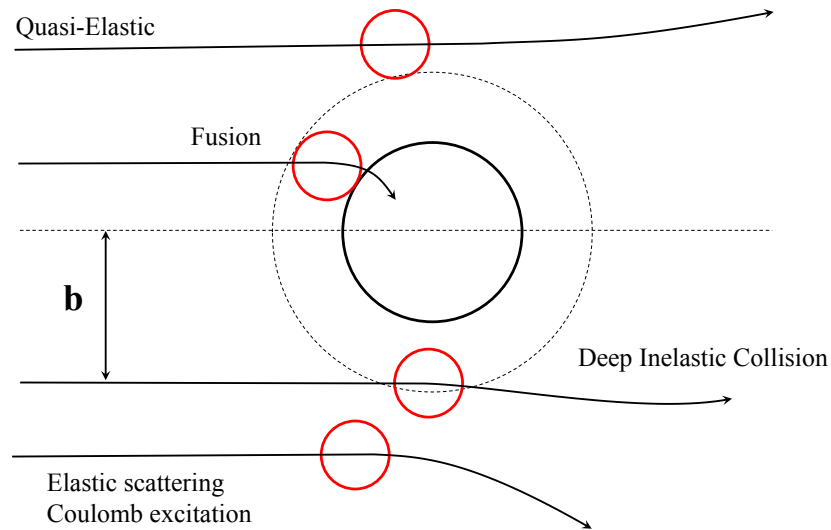


FIGURE 2.3: Simplified illustration of the heavy-ion nuclear reactions classification by parameter impact.

The minimum distance between the projectile and target, d , is given by the sum of both nuclear radii involved in the reaction. Comparing both distances the main reactions that can occur are:

- **Distant reactions** ($b \gg d$). The colliding nuclei scatter without transference of nucleons. In this group are included the processes of elastic scattering or at most Coulomb excitation. In the latter case the two nuclei excite themselves through the electromagnetic fields generated.
- **Quasi-Elastic (QE) to Deep Inelastic Collision (DIC) reactions** ($b \sim d$). The colliding nuclei can exchange a certain number of nucleons and nonetheless maintain their target-like or beam-like character. The *Multi-Nucleon Transfer* (MNT) reaction, which is the one exploited in our experiment, belongs to this group. These processes populate a small number of selected states which decay by single gamma transitions or low multiplicity gamma cascades.
- **Fusion reactions** ($b < d$). The colliding nuclei merge forming a compound nucleus. In this situation, all the beam energy is transformed into excitation energy of the resulting nucleus. As a consequence, high-spin states at extremes of angular momentum can be obtained. Depending on the excitation energy and momentum transferred, the compound nucleus can emit few

light particles (fusion-evaporation reactions) or, at extreme values of angular momentum, fission (fusion-fission reactions).

The nuclei of interest in the present experiment (^{92}Mo , ^{94}Ru) belong to the proton-rich region of the nuclide chart. Typically the proton-rich nuclei are populated via fusion-evaporation reactions, while multi-nucleon transfer reactions have demonstrated to be a very useful tool to populate neutron-rich nuclei. In fusion-evaporation reactions the compound nucleus is produced with high angular momentum and well-defined high excitation energy released by subsequent evaporation of particles and high multiplicity cascades of gamma rays. As a consequence, medium to high-spin states are usually populated, which hinder the direct lifetime measurement of the yrast transitions due to the presence of isomeric states in the nuclei of interest. On the contrary, the MNT reaction populates medium to low angular momentum states, which decay by single gamma transitions or low multiplicity gamma cascades. Therefore, the MNT reaction has been unconventionally used in this work to populate the proton-rich nuclei of interest following the approach described in Ref. [23].

The MNT processes in heavy ions are extensively discussed in Ref. [25]. In the following the main features of the transfer reactions will be described. In such reactions the scattering angle for the direction of the reaction products (ejectiles) where the reaction cross section is maximum is called grazing angle [26]. This will be illustrated in Section 2.2.2. This angle is defined as the angle, θ_g , corresponding the closest distance between the projectile and target when the nuclei “touch” each other (Fig. 2.4),

$$d = 1.2 \left(A_b^{1/3} + A_t^{1/3} \right) = \left(\frac{Z_b Z_t e^2}{4\pi\epsilon_0 E_k} \right) \cdot \left(1 + \csc \frac{\theta_g}{2} \right) \quad (2.1)$$

where A_b is the nuclear mass number for the beam, A_t is the nuclear mass number for the target, Z_b is the proton number for the beam, Z_t is the proton number for the target and d is expressed in femtómetros (fermis). For the experiment performed, the grazing angle is around 23° in the laboratory reference frame. It is important to know this angle since our products of interest in the MNT reaction have relatively low cross section and detectors such as those for ion identification, like VAMOS++, should be placed at this angle to reach the highest possible statistics.

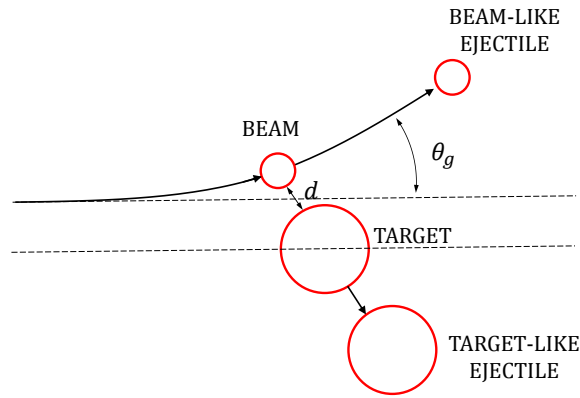


FIGURE 2.4: Schematic drawing of the definition of the grazing angle in a binary nuclear reaction.

Other feature of these reactions is the preservation of the binary character of the system. Since the ejectiles are similar to the initial nuclei (having exchanged a few nucleons), they can always be identified as beam-like and target-like constituents.

2.2.1. Kinematics

Fig. 2.5 shows schematically the kinematics of a moving projectile and a stationary target nucleus and the notation used for its description. The initial state before the reaction is defined by the mass (m_b), kinetic energy (T_b), the momentum of the beam (p_b) and the mass of the target (m_t).

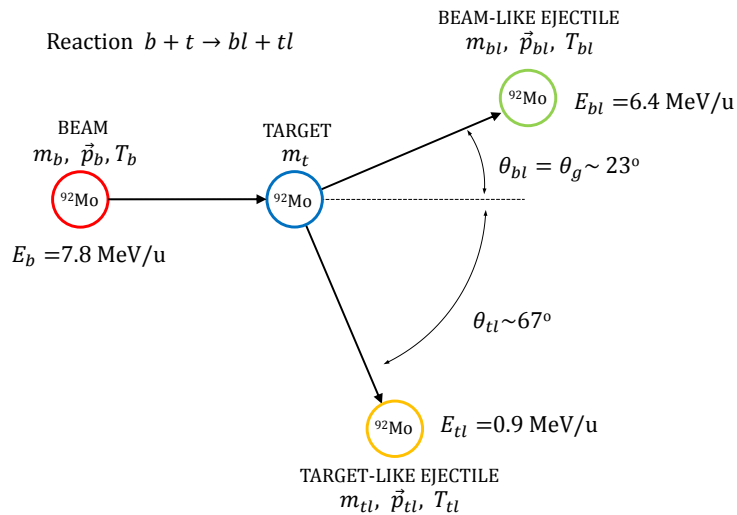


FIGURE 2.5: Scheme of the reaction kinematics in the laboratory frame.

The final state after the reaction is characterized by the mass (m_i), the kinetic energy (T_i), the momentum (p_i) and the angles (θ_i) of ejection with respect the beam axis of the beam-like and target-like reaction products ($i = bl$ and tl respectively).

The Q -value of the reaction is defined as the difference between the initial mass energy and final mass energy [27],

$$Q = (m_{initial} - m_{final})c^2 = (m_b + m_t - m_{bl} - m_{tl})c^2 \quad (2.2)$$

which is the same as the excess of kinetic energy of the final products,

$$Q = (T_{final} - T_{initial})c^2 = (T_{bl} + T_{tl} - T_b - T_t)c^2 \quad (2.3)$$

The Q -value determines the exothermic or endothermic nature of the reaction. If $Q > 0$, the nuclear mass energy or binding energy is released as kinetic energy to ejectiles. If, on the contrary, $Q < 0$ then the initial kinetic energy of the system is converted into the binding energy of reaction products. The yield of the MNT reaction is strongly dependent on the Q -value of the reaction [28].

The reaction used in the experiment was $^{92}\text{Mo}+^{92}\text{Mo}$. As depicted in Fig. 2.5, the ^{92}Mo beam impinges on the ^{92}Mo target with a energy of 7.8MeV/u (717 MeV in the laboratory frame, 352 MeV in the center of mass frame). The grazing angle of the reaction in the laboratory frame is around 23° (around 42° in the center of mass frame). In this reaction the kinematics of both reaction partners is exchangeable: the beam-like (target-like) reaction products are ejected at that angle with an energy of 6.4 MeV/u, while the target-like (beam-like) products are emitted at almost 67° with an energy of 0.9 MeV/u (see the basic geometry of the reaction plane in Fig. 2.5). Then, in order to perform the experiment with the optimum detection configuration, the setup is arranged as shown in Fig. 2.6. AGATA is positioned at backward angles with respect the axis of the VAMOS++ spectrometer, to maximize the Doppler effect, necessary for the RDDS measurement. VAMOS++ is oriented at 23° . The plunger device sits in the geometrical center of the reaction chamber but rotated 23° to have the target and degrading assembly facing the entrance of the spectrometer.

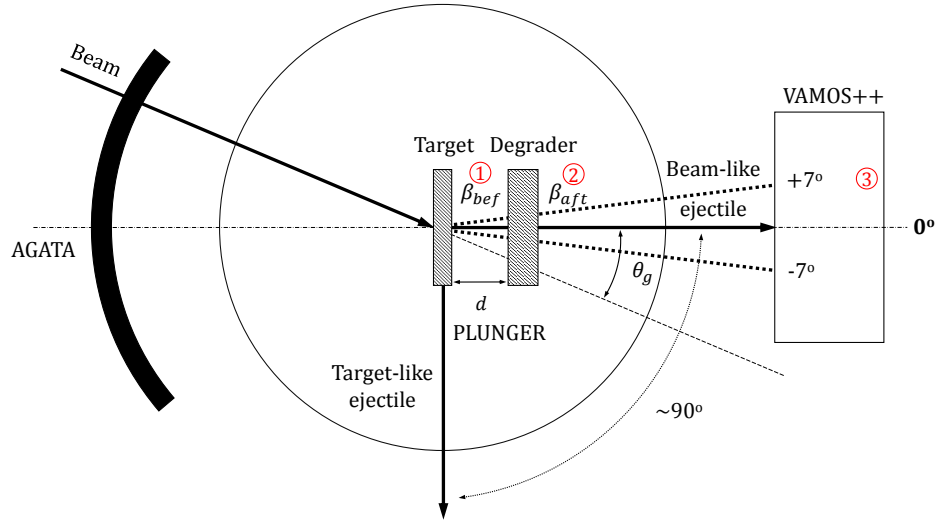


FIGURE 2.6: Schematic view of the experimental setup. The grazing angle, θ_g , is around 23° . The different stages of the recoil transmission are labelled with numbers (see text and Table 2.2 for details).

The kinematics of the $^{92}\text{Mo}+^{92}\text{Mo}$ reaction was calculated before the experiment using LISE⁺⁺ [29–31]. This code allows to simulate an experiment from the parameters of the reaction mechanism up to the registration of products selected by a spectrometer.

TABLE 2.1: Optimum parameters for the reaction mechanism and the transmission of the recoil to be detected in the magnetic spectrometer.

	Material	^{92}Mo
Beam	Energy	7.8 MeV/u
	Energy CM	352 MeV ($1.5V_c$)
	Intensity	1 pA at 37+
Target	Material	^{92}Mo
	Thickness ²	0.775 mg/cm ²
Degrader	Material	^{24}Mg
	Thickness	1.9 mg/cm ²

²Since the plunger device was placed at 23° with respect the beam axis (direction of the ejectiles of interest) the effective thickness of the target becomes 0.842 mg/cm² and has to be included in the initial parameters of the LISE⁺⁺ program. For the degrader case, no effective thickness needs to be considered as it is set parallel to the target, i.e., at 0° with respect the reaction products axis direction.

The parameters of the reaction are selected taking into account several aspects. First of all the beam energy is selected in order to optimize the reaction dynamics. In addition, the beam energy should be adjusted as well, accordingly to the target-degrader thickness, to have sufficient energy on the ejectile/beam-like reaction products that ensures a good Z resolution in the Ionization Chamber of the magnetic spectrometer. To this aim, the recoil ions should arrive to the ionization chamber with a higher energy than the Bragg peak within the first or second section. Apart from that, energy losses in the degrader have to be considered attending to the minimum separation between the two components observed in the gamma-ray spectra due to the different velocities. The minimum separation to disentangle the two peaks is crucial to perform a good lifetime determination in the analysis (as it will be discussed latter). The main task of choosing the optimum parameters is to find the best compromise between producing a high yield ①, obtaining a minimum separation acceptable for the gamma-ray energy components before and after the degrader ② and achieving the highest possible Z resolution ③. The different stages of transmission for the reaction parameters selected (Table 2.1) are depicted in Fig. 2.5. In Table 2.2 the corresponding values are shown for each stage of the nuclei transmission through the detection system:

- ① Energy, E_{bef} , and velocity, β_{bef} , of the recoils after the reaction is produced (before the recoils pass through the degrader).
- ② Energy, E_{aft} , and velocity, β_{aft} , of the recoils after passing through the degrader.
- ③ Energy of the recoils before entering in the ionization chamber, E_{IC} .

TABLE 2.2: Kinematic transmissions of reaction products ejected at the grazing angle through the detection system at different stages for the VAMOS++ angular acceptance (see text and Fig. 2.5 for details).

Reaction: $^{92}\text{Mo}+^{92}\text{Mo}\rightarrow^{92}\text{Mo}+^{92}\text{Mo}$				
		$\theta_g=23^\circ$	$\theta_g - 7^\circ$	$\theta_g + 7^\circ$
①	E_{bef} (MeV/u)	6.35	6.95	5.59
	β_{bef} (%)	11.61	11.97	10.90
②	E_{aft} (MeV/u)	5.41	6.03	4.62
	β_{aft} (%)	10.73	11.3 2	9.92
③	E_{IC} (MeV/u)	4.16	4.82	3.32

2.2.2. Cross Section

The cross sections for the reaction channels of interest have been calculated with the GRAZING program [32], which is based in the semiclassical model of few nucleon transfers with low energy dissipation developed by A. Winther [33, 34]. The GRAZING model calculates the evolution of the reaction by taking into account, besides the relative motion variables, the intrinsic degrees of freedom of projectile and target. These are the surface degrees of freedom and the one-nucleon transfer channels. The relative motion of the system is calculated in a nuclear plus Coulomb field [35]. The exchange of many nucleons proceeds via a multistep mechanism of single nucleons (both protons and neutrons, via stripping and pickup processes). So far, this model has been successfully applied in the description of multi-nucleon transfer reactions as well as of fusion reactions and barrier distributions [35].

In order to study the collective properties of the $N = 50$ isotones, towards ^{100}Sn , we are interested in, one should investigate the lifetimes of the low-lying states of the ^{92}Mo , ^{94}Ru , ^{96}Pd and ^{98}Cd nuclei as depicted in Fig. 1.3. However, the lifetimes of interest in ^{96}Pd are sufficiently long that could be already measured in beta-decay studies and ^{98}Cd is an extremely difficult case. With the present reaction only the measurements in ^{92}Mo and ^{94}Ru are possible, as the cross section is drastically reduced with increasing number of transferred protons (Table 2.3). In spite of this, studying only the ^{92}Mo and ^{94}Ru nuclei is enough to observe the trend and confirm or deny the existence of the expected behaviour of the $B(E2; 4^+ \rightarrow 2^+)$ transition probability.

TABLE 2.3: Q values and expected total cross sections for some of the transfer channels involved in the reaction $^{92}\text{Mo}+^{92}\text{Mo}$ using the GRAZING code.

Reaction	Products	Q-value (MeV)	Total Cross Section (mb)
$^{92}\text{Mo}+^{92}\text{Mo}$	^{92}Mo (0p)	0	531.95
	^{94}Ru (2p)	-2.27	5.00
	^{96}Pd (4p)	-9.46	0.089
	^{98}Cd (6p)	-22.71	0.0011

The differential cross section for the $^{92}\text{Mo}+^{92}\text{Mo}$ reaction is depicted as a function of the angle of the reaction in the center of mass reference frame in Fig. 2.7. The elastic, the one proton pick up and the two proton pick up channels are indicated revealing that the cross section is maximum nearby the grazing angle of the reaction (around 42° in the center of mass).

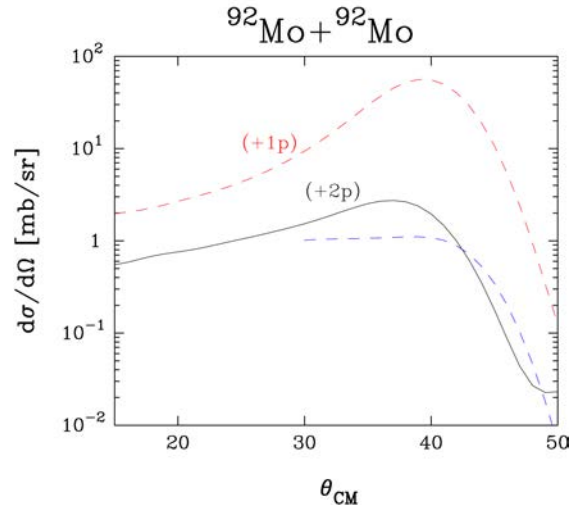


FIGURE 2.7: Dependency of the cross section with the angle in the center of mass for the $^{92}\text{Mo}+^{92}\text{Mo}$ reaction [36]. The blue, red and black lines indicate the elastic, the one proton pick up and the two proton pick up channels, respectively.

Fig. 2.8 shows the relative cross sections normalized to the one proton stripping channel (^{91}Nb) for the indicated channels. The reaction yields for the different channels in this experiment were measured with the VAMOS++ magnetic spectrometer. The energy of the $^{92}\text{Mo}+^{92}\text{Mo}$ reaction in the laboratory frame was $E_{lab}=717$ MeV. The experimental values (black circles) are obtained by integrating the mass distributions via Gaussian fits. In addition, the data are compared with the GRAZING predictions [37]. The red and blue histograms in Fig. 2.8 are the calculation obtained with the model before and after the neutron evaporation, respectively.

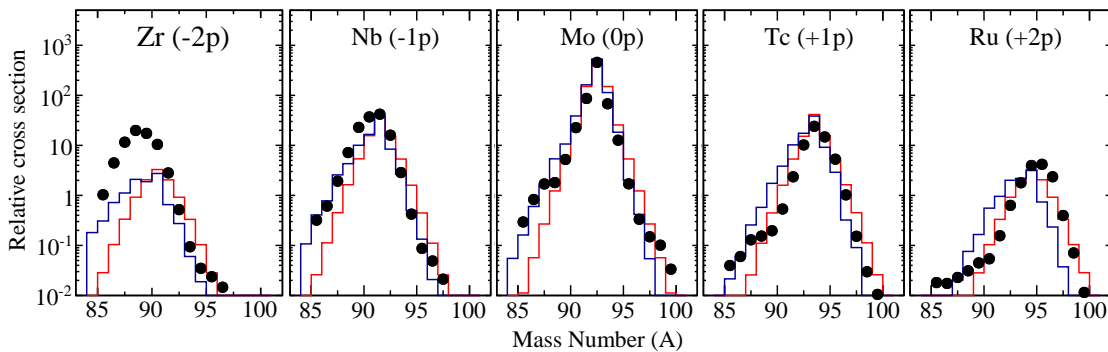


FIGURE 2.8: Relative cross sections for the transfer channels observed in the $^{92}\text{Mo}+^{92}\text{Mo}$ reaction normalized to one proton stripping channel. The points are the experimental data from this experiment while the histograms are the results of calculations using the GRAZING code [37]. The red line is before the neutron evaporation and the blue one after it.

From the comparison, the agreement in the inelastic channel as well as in the $\pm 1p$ channels can be appreciated. Also, the fluttering observed in the Tc and Ru isotopes, for the neutron stripping channels, indicate a stronger evaporation than included in GRAZING. In addition, the deviations in Zr and Ru isotopes suggest the presence of deep-inelastic components which are selected in a very specific way by the VAMOS++ magnetic spectrometer as observed in Ref. [38]. The distribution for +1p and +2p channels are quite similar to the grazing ones without evaporation, while in the -1p and -2p channels the agreement seems to be better with the products after evaporation. Similar problems have been found before in Ref. [35], where the energy of the beam is well above the Coulomb barrier.

It should be pointed out that proton transfer processes in heavy-ion collisions are much less understood than neutron reactions, because there is a large modification in the trajectories of entrance and exit channels due to the Coulomb field [35].

The state-of-the-art, high efficiency and very selective detection systems, used in this measurement, will be described in the following sections.

2.3. The VAMOS++ Magnetic Spectrometer

The VAMOS++ (VARIABLE MOde Spectrometer) magnetic spectrometer [39–41] is a large acceptance device that can operate in different optical modes. It has been built to obtain sensitivity and selectivity for experiments using the stable and radioactive ion beams provided by the GANIL facility. It allows the complete identification of the reaction products in terms of A (mass number) and Z (proton number) to identify their trajectories inside the spectrometer and to measure their velocities. In addition, it allows the possibility of coupling it with a large gamma-array, like AGATA. This opens the possibility to perform spectroscopic studies using multi-nucleon transfer reactions with heavy stable beams, in coincidence with the reaction products.

The spectrometer, as shown schematically in Fig. 2.9, consists of two large aperture magnetic quadrupoles at the entrance, followed by a Wien filter and a large magnetic dipole. The spectrometer can be rotated around the target from 0° to 46° . The main operational features of the VAMOS++ spectrometer are summarized in Table 2.4. The detection system is formed by two-dimensional position sensitive

tracking detectors with good resolution at the entrance position. This improvement was developed to be able to work with the superior angular resolution of the AGATA gamma-ray tracking array [41]. The tracking detectors provide the start time information, a measurement of the scattering angle (θ) and the interaction point on the target. In the focal plane, the multi-wire parallel plate avalanche counter measures the stop time for the time of flight (*TOF*). The drift chambers provide the position (x, y). And the ionization chamber yields the energy loss (ΔE) and the total energy (E) of the recoil ions.

TABLE 2.4: Operational characteristics of the VAMOS++ magnetic spectrometer coupled with AGATA [42]. For the present experiment the rigidity, $B\rho$, for the central trajectory was 0.91 Tm and the angular rotation was 23° with respect the beam axis (i.e. θ_g for this particular reaction and energy).

Horizontal acceptance	± 122 mrad ($\pm 7^\circ$)
Vertical acceptance	± 160 mrad ($\pm 10^\circ$)
Momentum acceptance	$\pm 5\%$ (at 25 msr)
$M = q$ resolution	1/160%
Z resolution	1/66%
Maximum rigidity $B\rho$	1.6 Tm
Flight path length	760 cm
Angular rotation	0-46° (variable)

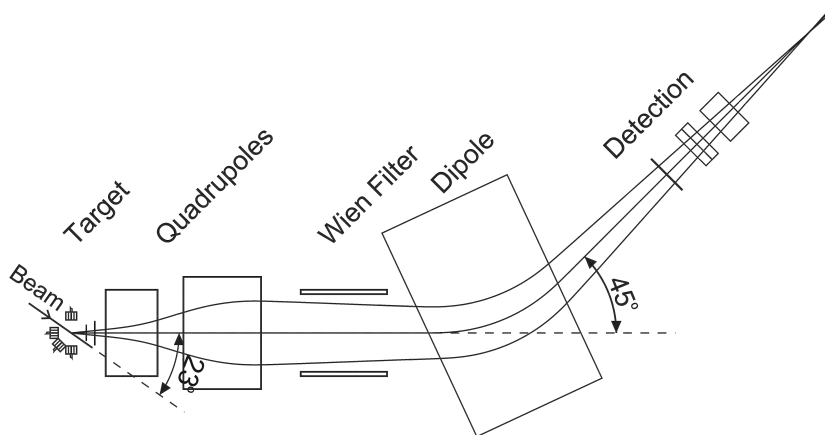


FIGURE 2.9: Schematic view of the VAMOS++ showing the optical elements (adapted from [42]). The spectrometer is shown rotated 23° with respect to the beam direction and the charged particle detection system placed at 45° .

In the following the different optical elements and the detectors will be described in detail. The description of the trajectory reconstruction and identification method will be presented in Chapter 3.

2.3.1. The optical elements

In the dispersive mode, VAMOS++ operates as a traditional magnetic spectrometer without using the Wien filter. The optical elements of the spectrometer consist of two large aperture magnetic quadrupoles and a dipole for focusing and dispersing the charged particles respectively.

Quadrupole magnets

The quadrupole magnets are used to focus the ions. In order to achieve a high angular acceptance of the spectrometer both quadrupoles have large aperture gaps. The first quadrupole (*Q1*) focuses in the vertical plane (*y*-direction) having a magnetic length of 60 cm and an aperture diameter of 30 cm. The second quadrupole (*Q2*) focuses in the horizontal plane (*x*-direction i.e. in the dispersion plane) and owns 90 cm of magnetic length being elliptical in shape with its major axis of 100 cm. *Q1* is placed 1 m away from the entrance detector position and the drift between the quadrupoles is 30 cm. The main features of the quadrupoles are summarized in Table 2.5.

TABLE 2.5: Main characteristics of the VAMOS++ Quadrupole Magnets [43].

	<i>Q1</i>	<i>Q2</i>
Focussing plane	vertical	horizontal
Max. Field gradient	7.1 T/m	2.3 T/m
Max. pole tip field	1.05 T	1.0 T
Magnetic length	60 cm	90 cm
Aperture diameter	30 cm	100 cm

Dipole magnet

Following the quadrupoles a Wien filter (not used) is set at 35 cm downstream. The filter is followed by a large dipole magnet (see Fig. 2.9). The drift between the Wien Filter and the dipole is 70 cm. The magnetic dipole is used to bend the ion trajectories according to their magnetic rigidity. Its bending angle varies between 0° and 60° and it has a nominal radius of deflection of $\rho = 1.5$ m. The magnetic field required for the maximum magnetic rigidity of 1.6 Tm and the maximum deflection angle of 60° is $B = 1.1$ T. The entrance and exit surfaces of the dipole magnet are at an angle of 20° and 30° respectively, with respect to the optical axis

having a curvature of 5 m and 3 m to reduce second order image aberrations. The pole gap for the magnet is 15 cm. The main features of the dipole are detailed in Table 2.6.

TABLE 2.6: Main characteristics of the VAMOS++ Dipole [44] [43].

Max. field	1.1 T
Deflecting radius	1.5 m
Deflecting angle	0-60°
Entrance angle	20°
Entrance curvature	5 m
Exit angle	30°
Exit curvature	3 m
Pole gap	15 cm

2.3.2. The charged particle detectors and electronics

A schematic view of the VAMOS++ detection system is shown in Fig. 2.10. This figure illustrates the setup used in the experiment, where the focal plane detectors are organized in modules. The main characteristics of each detector are summarized in Table 2.7.

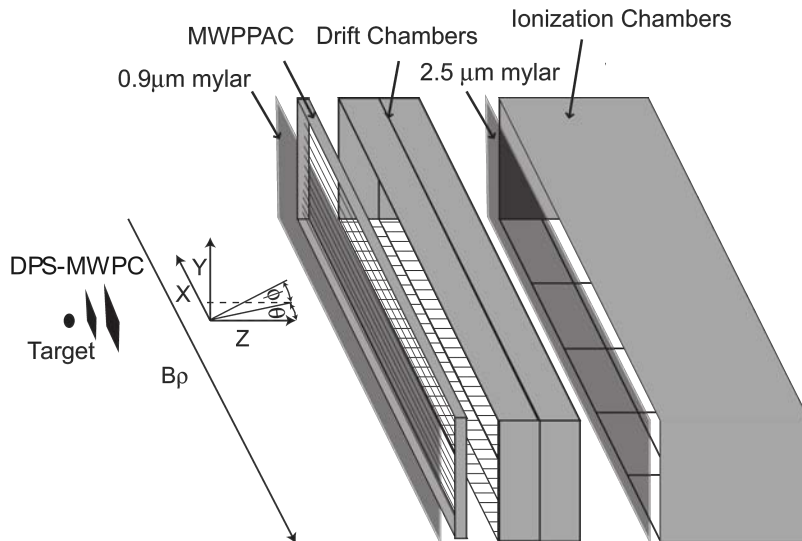


FIGURE 2.10: Schematic view of the VAMOS++ detection system adapted from [40]. The coordinate system for the trajectory description and the direction of the $B\rho$ increasing values are shown.

TABLE 2.7: VAMOS++ detectors characteristics. The gas used in all the detectors was Isobutane at the pressure marked in the table.

Detector	Active area or volume	Gas pressure	Quantity measured
MWPC1	$40 \times 61 \text{ mm}^2$	6 mbar	$X_1, Y_1, t_1 = t_{start}$
MWPC2	$65 \times 93 \text{ mm}^2$	6 mbar	X_2, Y_2, t_2
MWPPAC	$1000 \times 150 \text{ mm}^2$	6 mbar	t_{stop}
DC1	$1000 \times 150 \times 100 \text{ mm}^3$	6 mbar	$X_{1,2}, Y_{1,2}$
DC2	$1000 \times 150 \times 100 \text{ mm}^3$	6 mbar	$X_{3,4}, Y_{3,4}$
IC1-IC4	$1000 \times 150 \times 120 \text{ mm}^3$	60 mbar	$\Delta E, E$

2.3.2.1. The entrance detectors

Dual Position Sensitive Multi-Wire Proportional Counter (DPS-MWPC)

The entrance detectors consist of a pair of Position Sensitive Multi-Wire Proportional Counters (DPS-MWPC) placed 174 mm downstream of the target and separated by 105 mm. They cover the full angular acceptance of VAMOS++ ($\Delta\theta_V = \pm 7^\circ$ and $\Delta\phi_V = \pm 11^\circ$). The MWPCs provide a direct and precise measurement of the position of the reaction products on the X and Y axis ($X_{1,2}$ and $Y_{1,2}$) and a pair of fast timing signals ($t_{1,2}$) for the start of the time-of-flight measurements. The MWPCs operate in a common volume gas of isobutane (C_4H_{10}) at a low pressure of 6 mbar and isolated by two Mylar windows of 0.9 μm thickness. Fig. 2.11 shows the detector assembly. The first and second MWPCs have active areas (width \times height) of $40 \times 61 \text{ mm}^2$ and $65 \times 93 \text{ mm}^2$ respectively. Fig. 2.11(a) shows schematically the composition of each detector, a central cathode that provides a time signal and two orthogonally oriented anodes of wire planes for the 2 dimensional position measurement. The cathodes and anodes are composed of 20 μm diameter gold plated tungsten wires with a spacing of 0.5 mm and 1.0 mm respectively for obtaining the required avalanche amplification gain. The distance between the electrodes is 2.4 mm. Two 100 μm diameter gold plated tungsten wires are set diagonally on the front of the first MWPC and the back of the second MWPC as a reference to align the detector and get the position resolution. The typical values for the voltages on the cathode range between -415 V and -475 V.

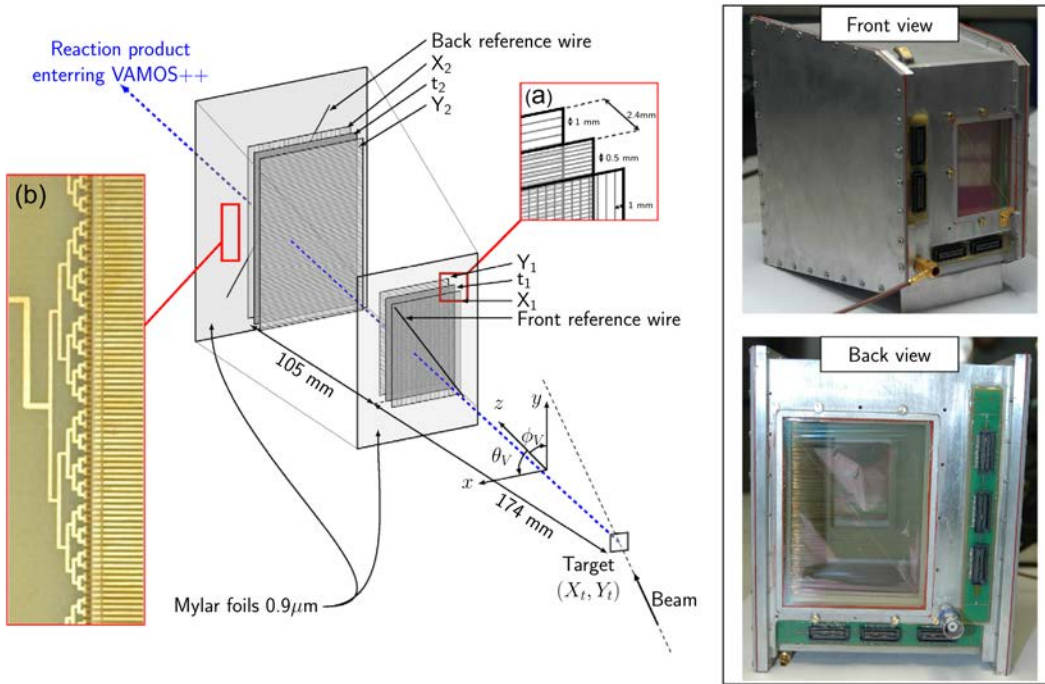


FIGURE 2.11: Left: Schematic view of the DPS-MWPC detector assembly. The detector is composed of a pair of position sensitive MWPCs. Inset (a): Expansion of the three wire planes illustrating the wire plane orientation and spacings. Inset (b): Picture of the equivalent path length routing of a time plane signal. Right: Front and back views of the detector assembly. Picture from [41]

Fig. 2.11 (b) shows the equivalence path-length PCB routings of a time plane signal made for avoiding a dispersion in the time signal measurement in the Y position. The dispersion in the X position is corrected by means of software on an event-by-event basis. The time-of-flight, position and angular resolutions of the DPS-MWPC detector at VAMOS++ are shown in Table 2.8.

TABLE 2.8: Performance of the DPS-MWPC detector [41].

Quantity	Description	Unit	σ
t_1	Time-of-flight	ps	130(5)
X_1, Y_1	Front MWPC	μm	130(5)
X_2, Y_2	Back MWPC	μm	84(11)
θ_V, ϕ_V	Scattering angles	mrad	1.1(1)
X_t, Y_t	Interaction position on the target	ps μm	239(30)

2.3.2.2. The focal plane detectors

Multi-Wire Parallel Plate Avalanche Counter (MWPPAC)

The first detector in the Focal Plane is the Multi-Wire Parallel Plate Avalanche Counter (MWPPAC) which consists of an active area of $1000 \times 150 \text{ mm}^2$ divided into 20 equal independent sections in the horizontal plane. It is structured with three electrodes: a central cathode with polarized wires (-500 V), for timing and two anodes at distance of 2.2 mm from it with grounded wires, for position. The wires are made of gold coated tungsten, have $20 \text{ }\mu\text{m}$ diameter and are distributed with a step of $500 \text{ }\mu\text{m}$ and 1 mm for the central and external planes, respectively. A fast time signal is provided by each section of the cathode used as a stop signal for time-of-flight measurements performed between the first MWPC at the entrance and the MWPPAC at the focal plane.



FIGURE 2.12: Picture of the MWPPAC assembly taken from Ref. [45].

Fig. 2.12 shows the MWPPAC assembly with the 20 time-signals readout. To isolate the beam line vacuum a Mylar window of $0.9 \text{ }\mu\text{m}$ is mounted at the entrance of the focal plane. The window is reinforced by 100 mm diameter nylon wires placed every 50 mm. The MWPPAC operates with isobutane ($\text{i}(\text{C}_4\text{H}_{10})$) at a low pressure of 6 mbar.

Drift Chambers (DC)

The MWPPAC is followed by the two Drift Chambers (DC) which measure the horizontal (X) and vertical (Y) positions to reconstruct the trajectories of the ions. Each DC has an active volume of $1000 \times 150 \times 100 \text{ mm}^3$ (width \times height \times depth respectively) and consists of a drift region of 150 mm and an amplification region of 20 mm separated by a Frisch wire grid as schematically shown in Fig. 2.13 (a).

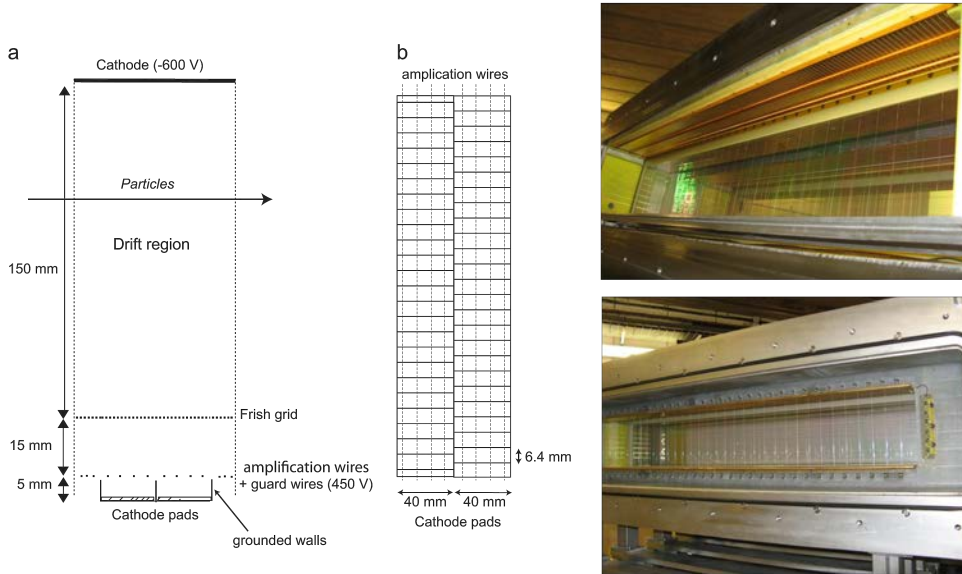


FIGURE 2.13: Left: Schematic drawing of the drift chamber, figure taken from [40]. (a) Drift chamber in the $Y - Z$ plane. (b) Segmented cathode showing individual pads in $X - Z$ plane. Right: Pictures of a modular mechanical setup containing the drift chamber from [45].

The grid is made of $50 \mu\text{m}$ diameter gold plated tungsten wires spaced 2.54 mm . The amplification wires are set at 15 mm from the Frish grid and are $20 \mu\text{m}$ in diameter with a spacing of 10 mm . The cathode plane is divided in two rows, each one containing 160 pads and having four wires in front. Fig. 2.13 (b) shows an example for a few pads. The pads are made from gold plated strips of 6.02 mm with a step of 6.4 mm in the dispersive direction and the two cathode rows are offset by half strip for improving the position measurement between pads.

The detector operates at common gas (isobutane) together with the MWPPAC at a pressure of 6 mbar . The drift cathode is polarized with a voltage of -600 V , the amplification wires with $+450 \text{ V}$ and the Frish grid and pads are grounded. The position resolutions are measured to be $\sim 270 \mu\text{m}$ in the dispersive plane (X) and $\sim 350 \mu\text{m}$ in the drift direction (Y) [40].

Ionization Chamber (IC)

The last detector in the focal plane is the Ionization Chamber (IC). It is set-up downstream of the DCs and used to measure the energy deposited by the ions in the gas. The IC is divided in four sections along the beam direction and each section is segmented in 5 pads providing the energy loss ΔE and the total energy

E for the determination the atomic number Z of the ion. Fig. 2.14 depicts the IC assembly in the modular setup. The active volume per IC section is $1000 \times 150 \times 120$ mm³. The IC consists of cathode and anode. A gap of 150 mm and a Frisch grid are placed at 30 mm from the anode. The material of the Frisch grid wires is gold plated tungsten with a diameter is 50 μ m and separated 1 mm. An acceleration grid with the same characteristics is placed at a distance of 10 mm from the anode.

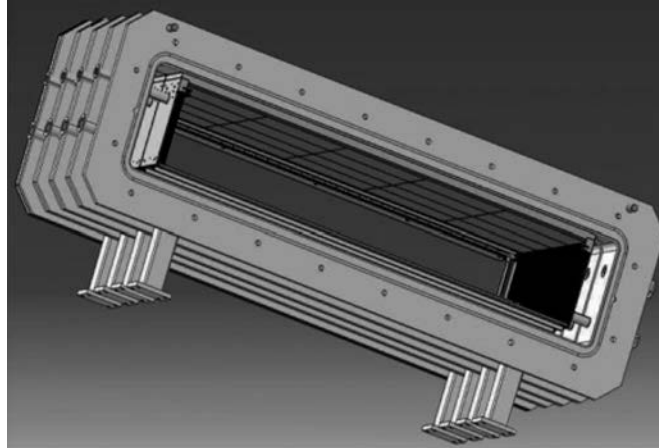


FIGURE 2.14: Drawing of a single module containing the ionization [40].

The energy loss, ΔE , can be measured from the energy deposited only in the first section or in the two first sections depending on the energy release profile, in order to optimize the Z resolution. The sum of the energy loss in each section is the total energy measured, E . The resolution achieved on the atomic number (Z) is around $\Delta Z/Z \sim 1/66$. The IC operates with isobutane at a pressure of 60 mbar. At the entrance of the IC a Mylar window of 2.5 μ m is placed to separate the different gas pressures in the DC and the IC. The window is reinforced by 32 vertical nylon wires to avoid any deformation arising due to different operating pressure. Another Mylar window can be set-up between the third and fourth section of the IC to increase -if required- the gas pressure of the fourth IC in order to stop the ions completely. This feature was not used in the present experiment.

2.3.2.3. The electronics

The electronic chain for the processing of the analog signals in the VAMOS++ detection system is briefly described in this section. The start timing signal is provided by the MWPC signals amplified by fast timing amplifiers (FTA) and treated by constant fraction discriminators (CFD). The stop signal given by the

MWPPAC is processed analogously and the ToF is measured using a time to amplitude converter (TAC) [41]. The charge collection in the MWPCs and DCs is based on GAS Silicon multiPLEXing (GASSIPLEX) chips. For each channel the collected charge is converted into voltage which is multiplexed in the output and fed to a fast analog to digital converter (ADC)[42]. The IC analog signals are processed with standard NIM electronics consisting of pre-amplifiers, amplifiers and discriminators and digitized by ADCs.

All digitized signals are collected event-by-event by standard VME modules or dedicated CAEN CRAMS modules (CAEN Readout for Analog Multiplexed Signals). For data acquisition, the master event trigger is provided by the start-stop signals, i.e., VAMOS++ detecting a particle. The trigger decision coupled to the AGATA detector will be briefly indicated in Section 2.6.

2.4. The differential plunger

The differential plunger is a complex device, developed by the IKP University of Cologne, that allows to measure the lifetime of the excited nuclei in the range of picoseconds by means of the Recoil Distance Doppler Shift technique (RDDS). Note that the RDDS technique always requires a high-resolution (Ge) detection system. The plunger has been designed to regulate the distance between the target and the degrader in the micrometer range. The usage of a degrader instead of a stopper, as in the standard plunger devices, allows the detection of recoiling nuclei downstream of the device. This is essential for experiments such as the present one, where the nuclei of interest need to be identified with a magnetic spectrometer, like VAMOS++ in this experiment.

The plunger device consists of target and degrader foils placed in their respective frames. The target foil is fixed while the degrader is displaced to different distances. A drawing of the plunger device showing the different components is depicted in Fig. 2.15. The IKP-University of Cologne Plunger is equipped with a piezo-electric linear motor to displace the degrader up to 1 cm. The distance measuring system utilizes inductive transducers, which cover the distance range from contact to 5 mm. A feedback system uses a piezo-electric crystal for the short range corrections (in the range between 0-50 μm) and allows to keep the target-degrader

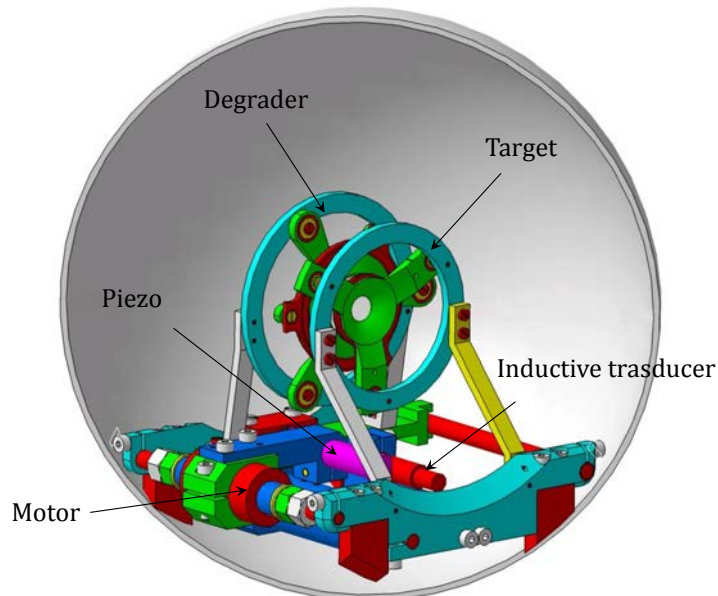


FIGURE 2.15: Schematic representation of the Plunger device for deep inelastic and transfer reactions from [46].

separation constant during experiment. The main specifications of the differential plunger components are summarized in Table 2.9.

TABLE 2.9: Characteristics of the differential plunger setup for grazing reactions [46, 47].

	Range	Accuracy
Motor system	0-10 mm	1 μm
Measuring distance system	0-5mm	0.01 μm
Feedback system	0-50 μm	0.05 μm
Rotation around the beam axis	0-45°	0.5°

For the present measurements, the plunger device is placed with all the mechanical components in dedicated reaction chambers. Fig. 2.16 shows the differential plunger device placed inside the scattering chamber of the AGATA-VAMOS++ experimental setup. Moreover, in the multi-nucleon transfer and deep-inelastic reactions the plunger symmetry axis, which is the axis perpendicular to the target plane going through the center of the target, has to be tilted with respect to the beam axis following the grazing angle direction. It should coincide with the entrance axis of the magnetic spectrometer, in forward position, and the symmetry axis of the gamma-ray spectrometer, positioned in backward direction. The design of the plunger enables the rotation of the device with respect to the beam axis up

to a maximum angle of 55° . In addition, its supporting structure allows to easily (dis-)mounting for keeping the axis alignment (ring support in Fig. 2.16)

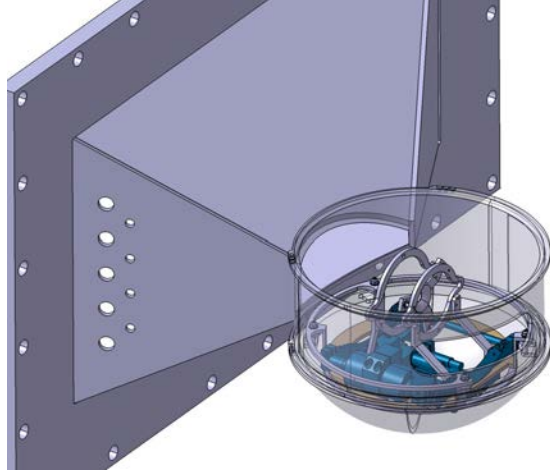


FIGURE 2.16: Drawing of the Plunger device inside the reaction chamber [46].

2.4.1. Recoil Distance Doppler Shift technique

The lifetimes of the excited states of interest are expected to range from few picoseconds to hundreds of picoseconds. One of the best techniques for the determination of such lifetimes in excited nuclear states is the Recoil Distance Doppler Shift (RDDS) method [47]. Conventional RDDS is performed with a target and a stopper foil that fully absorbed the reaction product energy. In our case, in order to allow identification of the reaction products with VAMOS++, this technique has been implemented by means of the differential plunger setup [47]. As described previously, it essentially consists of a thin target at a fixed position and a degrader to slow down the velocity of the ions.

The RDDS technique and its principle are illustrated schematically in Fig. 2.17. After the nuclear reaction in a thin target, the excited nucleus leaves the target with a velocity v_{bef} , which is reduced after passing the degrader foil to v_{aft} and detected in the mass spectrometer (VAMOS++). The excited nucleus can de-excite via gamma-ray transitions down to the ground state. These gamma-ray transitions, emitted before or after the nucleus passing the degrader, are measured in the gamma-ray spectrometer (AGATA). Since they are emitted in flight, the measured radiation is affected by the Doppler effect and the observed emitted

energy is given by,

$$E = E_0 \frac{\sqrt{1 - \beta^2}}{1 - \beta \cos\theta} \approx E_0(1 + \beta \cos\theta) \quad (2.4)$$

where E_0 is the energy of the transition measured at rest, θ is the angle between the direction of the emitting nucleus and the direction of the emitted gamma-ray and $\beta = v/c$ is the velocity of the emitting nucleus. Since the velocity of the emitting nucleus changes after passing the degrader, the energy of the gamma-ray emitted will be observed at two different energies (E_{bef} , E_{aft}) following the Eq. (2.4) for each velocity.

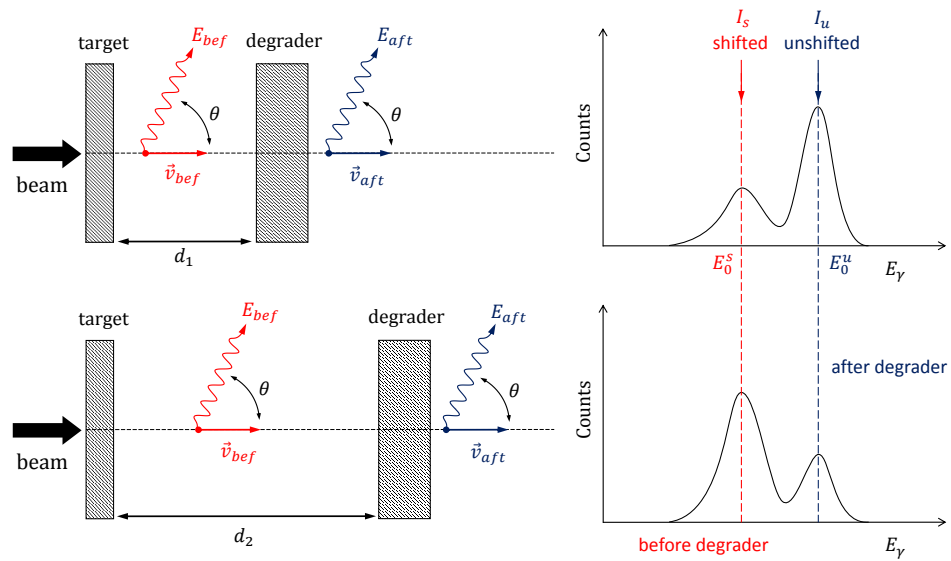


FIGURE 2.17: Schematic drawing of the RDDS technique using the differential plunger in grazing reactions. The recoil velocity after the degrader (v_{aft}) is measured with the magnetic spectrometer. This allows the Doppler correction of the gamma-rays emitted after the ions passing the degrader and its peaks appear at the correct energy (unshifted). The variation of the unshifted (u) and shifted (s) components are shown in the corresponding measured spectrum for different distances. For the grazing reactions setup the gamma-rays are observed at backward angles, thus the peak of the gamma emitted before the degrader is lowered in energy. For simplicity the setup and recoil direction have been drawn in the same direction as the beam, but notice that the setup should be tilted with respect to the beam axis following the grazing angle direction (where the cross section of the recoil is higher), as depicted in Fig. 2.6.

The momentum information about the excited nucleus for the Doppler correction is provided by the mass spectrometer (after being slowed down by the degrader, v_{aft}). Therefore, the right Doppler correction is obtained for the gamma-rays emitted by the nucleus after passing the degrader. The latter appear at the correct energy

position E_0^u (unshifted), which is given by

$$E_0^u = E_0 = E_{aft}/(1 + \beta_{aft} \cos\theta). \quad (2.5)$$

On the other hand, the gamma-rays emitted by the nucleus before passing the degrader appear at lower energy E_0^s (shifted) due to the insufficient Doppler correction using the velocity of the nucleus after de degrader,

$$E_0^s = E_{bef}/(1 + \beta_{aft} \cos\theta). \quad (2.6)$$

In this way in the gamma-ray spectrum one obtains on each gamma transition a shifted (emitted before the degrader, red in Fig. 2.17) $I_s(t)$ and an unshifted (emitted after the degrader, blue in Fig. 2.17) $I_u(t)$ component. Their intensities correspond to the decay probability during the time of flight before and after the degrader, respectively. This decay probability is directly related to the lifetime of the excited state that one wants to determine. Thus, by measuring the intensity of the gamma-rays emitted before or/and after the degrader by the nucleus of interest as a function of the target-degrader distance, one can extract accurate information about the lifetime of the corresponding excited nuclear states.

The traditional analysis method to extract the lifetime of excited nuclear states is the so-called Decay Curve Method (DCM). It is based on the application of the Bateman equations to the curve resulting from the ratio of the intensities of the two components, shifted and unshifted, as a function of the distance. For this method, absolute distances are needed. Therefore the zero point of the plunger belongs to the quantities to be determined [47], along with the common parameters such as lifetime, initial populations or branching ratios.

An alternative method, which helps to overcome the problems of the standard analysis is the Differential Decay Curve Method (DDCM) developed by A. Dewald and co-workers in Colongne [47]. An advantage of this method is that it is insensitive to the absolute distance between target and degrader. Systematic errors are kept well under control too.

A common difficulty in this kind of experiments arises from side-feeding. This is the level feeding for which no discrete feeding transitions are observed. If the feeding of a state is not well determined, unrealistic lifetime values may be obtained. The advantage of using the differential RDDS technique in a setup with

a magnetic spectrometer is that using specific gates on the kinetic energy of the reaction products permits to gain valuable information on the feeding.

The detailed information regarding the extraction of the lifetime of the de-exciting state will be described in Chapter 4 together with the line-shape analysis of the fast and degraded components.

2.4.2. The target and degrader

In the present experiment, the differential plunger setup includes a target of 0.775 mg/cm^2 of ^{92}Mo enriched to 97.01% and a 1.9 mg/cm^2 ^{24}Mg foil used as an energy degrader. Fig. 2.18 shows a picture of the target and degrader foils. Both foils were produced with the rolling technique [48], which uses polished stainless steel plates for the lamination of the foils. With this technique a small quantity of material is required and the risk of getting small protruding solid particles more than $10 \text{ }\mu\text{m}$ is very reduced. However, the total surface roughness can be larger compared to other techniques due to surface structure of the rolling, which can be imprinted onto the produced foil if the rolling plates are not well polished when rolling the foil to the final thickness [47].



FIGURE 2.18: Picture of the ^{92}Mo target (right) and ^{24}Mg degrader (left) used in the experiment.

The target and the degrader are aligned parallel in the plunger device with their support frames. Both foils should be stretched in order to make the surface as regular as possible and avoid changes in the distances due to the heating of the foils when the beam hits them. To stretch the thin foils they are glued onto aluminium rings (Fig. 2.18) and after, pressure is applied with conically-shaped frames for

stretching. In Fig. 2.19, the target and the degrader are shown stretched and ready for the experiment.

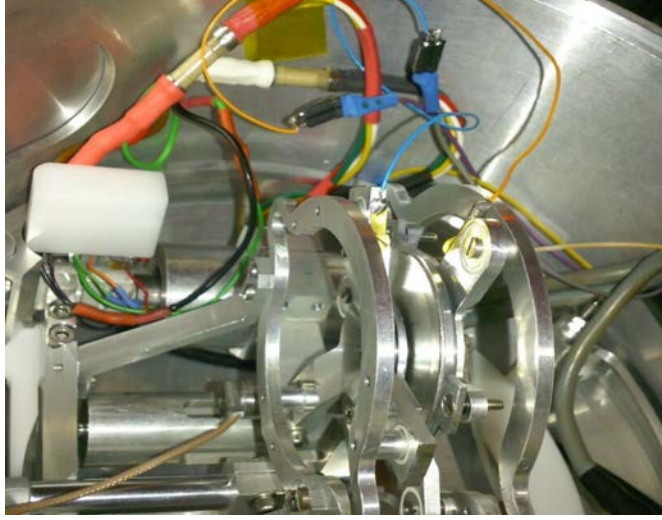


FIGURE 2.19: Picture of the Plunger device inside the reaction chamber.

The diameter of the target and degrader are different as seen in Fig. 2.18. The diameter of the frame and the inner cone are 27 mm and 10 mm respectively for the target, and 40 mm and 20 mm for the degrader [46]. This fact avoids that the supports collide at the closest possible target-to-degrader distance and permits to push the target a bit into the degrader foil without damage, thereby enabling an effective closer distance between the foils [47].

The selection of target and degrader was based on the yield of the reaction and the transmission of its products through the system. The target should be thin enough to allow most of the reaction products to get out of the target and reach the mass spectrometer passing through the degrader. At the same time, it should be thick enough to provide sufficient yield, of the reaction products of interest, which is - within reason- proportional to the target thickness. For the degrader, the optimum thickness is found when there is a sufficient thickness that the velocity change allows a separation of the shifted and unshifted components greater than the energy resolution of the gamma spectrometer and a minimal loss of transmission through mass spectrometer. The separation of the peaks can be estimated from the following relation derived from the equations in Section 2.4.1,

$$\frac{E_0^u - E_0^s}{E_0^u} = (\beta_{aft} - \beta_{bef})\cos\theta + \vartheta(2) \quad (2.7)$$

where E_0^u is the Doppler corrected energy after the degrader, E_0^s is the wrong Doppler corrected energy before the degrader, and β_{aft} and β_{bef} are the corresponding velocities. The angle θ is the angle between the recoil trajectory and the gamma detector. $\vartheta(2)$ represents a second-order term, which generally can be neglected [49].

In order to test the suitability of the chosen target and degrader characteristics, the kinematics of the reaction have been calculated using the LISE⁺⁺ program [29–31] (see Table 2.2). After the $^{92}\text{Mo}+^{92}\text{Mo}$ reaction, the beam-like reaction products exit the target foil with an average energy of 6.35 MeV/u (583.61 MeV) and a velocity of 34.82 $\mu\text{m}/\text{ps}$ ($\beta \sim 11.6\%$). The Mg foil degrades the energy of the ions to 5.41 MeV/u (497.22 MeV) and the velocity to 32.17 $\mu\text{m}/\text{ps}$ ($\beta \sim 10.7\%$), resulting an average difference of velocities of $\Delta\beta \sim 0.90\%$. Considering an average angle of 145° between the beam-like direction and the gamma detectors for the AGATA setup in this experiment and a gamma-ray energy of 800 keV (representative for the energy of the transitions of interest), the energy separation obtained, through Eq. (2.7), is around 6 keV ($\Delta E_0/E_0^u \sim 0.74\%$). Taking into account the AGATA resolution at that energy (see 6.12), the estimated separation is large enough to distinguish gamma-rays emitted before and after the degrader foil by their different Doppler shifts.

2.4.3. Distances

During the experiment several target-to-degrader distances, ranging from 20 to 4000 μm , were measured. The displacement of the mechanical components, to change the distances, is done by means of a piezo-electric displacement motor and a high accuracy distance sensor [47].

As mentioned before, the knowledge of the zero point of the plunger (minimum distance target-to-degrader) is crucial for the RDDS technique via DCM, especially for very short lifetimes (below 2 ps). The first mechanical contact (before any electrical contact can be measured) determines the effective minimum distance between target and degrader. This depends on the surface roughness of the foils and on the precision of the parallel alignment of the target and the degrader foils.

The minimum target-to-degrader separation can be measured with the capacitance method [47]. This method helps to monitor and correct possible deviations of the selected distances which are mostly caused by heating up of the system due to the impact of the beam during the experiment. The electrically insulated target and degrader foils act as a parallel plate capacitor with a capacitance given by,

$$C(x) = \epsilon_0 \frac{A}{x} \quad (2.8)$$

where A is the area of the stretched foil, x the separation between the target and degrader and ϵ_0 the vacuum permittivity. The minimal distance is determined by plotting the $C(x)^{-1}$ values as a function of the target-to-degrader distance and intersecting the extrapolated linear curve when $C(x)^{-1}=0$. In this way the absolute distance between the target and the degrader can be accurately obtained.

Various distance calibrations were performed before the experiment to check the stability of the plunger by measuring the target-to-degrader capacitance as a function of the separation. The measurements were taken without beam, with the plunger being in thermal equilibrium and in place for the experiment. Afterwards, the calibration was used to determine the actual target-to-degrader distance when measuring in-beam. However, after the first short distance measurement, some instabilities were detected in the plunger due to oscillations in the intensity of the beam. This fact required the examination of stretched foil status and the alignment between them. For this reason, another distance calibration was performed and used for the rest of the distances measured in the experiment. In Fig. 2.20 an example of the calibration curve is shown. In the insert of the figure the zero point is defined by the extrapolation of the linear part of the curve (at short distances) when $V(x)^{-1} = 0$.

The obtained values for the effective minimum distance and the minimum distance are presented in Table 2.10 for the calibration measurements done before and during the experiment. The zero offset is obtained from the difference between the effective minimum distance at the mechanical contact position and the minimum distance at the zero point position. This quantity has to be added to the effective distance in order to determine the absolute distance, which is very important for the correct application of the DCM in the RDDS technique. The effective distance is obtained by subtracting the mechanical contact position to the average actual distance measured.

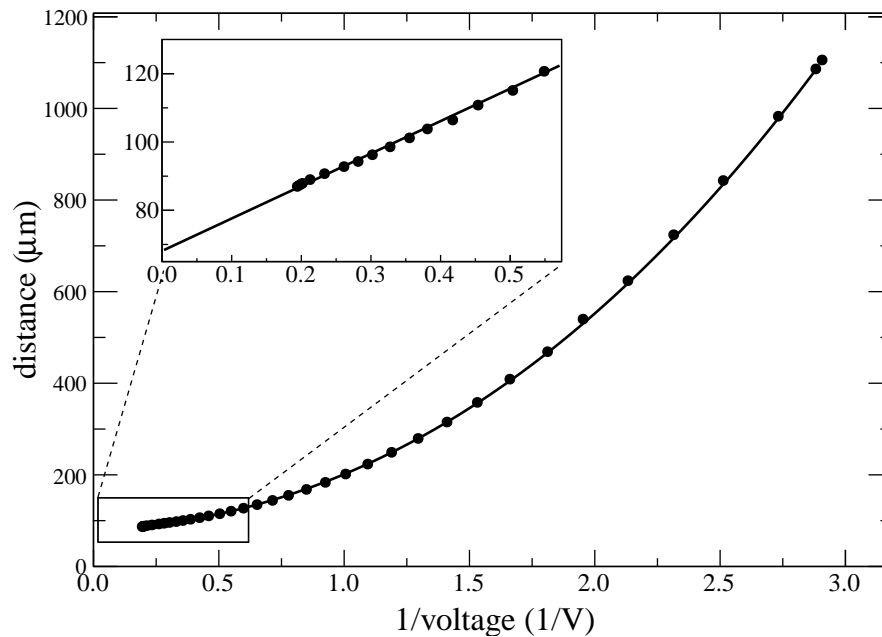


FIGURE 2.20: Example of a plunger distance calibration for the present experiment. Distance vs. $1/\text{voltages}$ for a calibration measured with distance-feedback control at short distances. The insert illustrates the linearity of the plot at short distances and the zero point from intersection of the extrapolated linear curve with the vertical axis.

TABLE 2.10: Effective minimum distance (mechanical contact) and minimum distance (zero point) between the target and the degrader determined with the capacitance method.

Measurement	Mechanical contact (μm)	Zero point (μm)	Zero offset (μm)
Before exp	83.4	69.1(8)	14.3(8)
During exp	87.0	71.8(11)	15.2(11)

The aforementioned quantities are shown in Table 2.11. The first row of the table (first short distance before the plunger instabilities) has been obtained with the calibrations performed before the experiment. For the rest, the calibration during the experiment has been used. The zero offset correction has been applied to the short distances range, where the feedback was sensitive.

TABLE 2.11: Average actual distance (d_{aver}), effective distance (d_{eff}) and absolute distance (d_{abs}) measured with the differential plunger setup.

d_{aver} (μm)	d_{eff} (μm)	d_{abs} (μm)
88.4(4)	5.0(4)	19.3(9)
97.0(10)	10.0(10)	25.2(15)
177.0(8)	90.0(8)	105.2(14)
576.9(19)	489.9(19)	505.1(22)

The final absolute distances considered for the analysis are summarized in Table 2.12. In total seven different distances were measured to cover the ranges of lifetimes expected for the nuclei of interest. For the short distances (19, 25, 105 and 505 μm) the plunger position is affected by the error on the zero offset and the fluctuations due to the beam (included in the average actual distance). For the long distances (1, 2 and 4 mm) the feedback does not work and the error assumed corresponds to the sensitivity of the piezo-motor [46]. The 2 mm distance was performed initially before the plunger instabilities and another measurement with the same distance was done after the examination of stretched foil status in order to check that the instabilities didn't affect the measurement. In addition, it should be remarked that the time of measurement of the distance of 505 μm was the shortest one with only 3 hours of measurement.

TABLE 2.12: Absolute target-to-degrader distances measured with the differential plunger setup.

Distances (μm)	Time of measurement (h)	Mean beam Intensity (pnA)
19.3(9)	13.54	0.97
25.2(15)	20.87	0.56
105.2(14)	23.46	0.65
505.1(22)	2.98	0.81
1000(1)	25.48	0.91
2000(1)	17.87	0.65
2000(1)	15.18	0.72
4000(1)	23.45	0.86

2.5. The AGATA Spectrometer

The Advanced Gamma Tracking Array (AGATA) [13] is a new generation detector based on the technique of gamma-ray tracking in electrically segmented high-purity

germanium crystals. It has been built to be used in the nuclear research facilities operating presently in Europe and will be especially important for the experimental conditions at the future facilities for intense unstable and high-intensity stable ions.

The European experimental gamma-ray spectroscopy community, since the early nineties, coordinated efforts to build large scale high-energy resolution arrays, e.g. the escape-suppressed spectrometer EUROBALL (1995-2004). The escape-suppression technique provides excellent peak-to-total (signal to background) ratios but, in turn, limits the solid angle covered by the Ge detectors, thus limiting the sensitivity of the arrays.

AGATA is the result of the early European Commission financed initiative, the TMR network "Development of gamma-ray tracking detectors" [50], with the participation of more than 40 institutes in 12 countries. The inception of the Ge position sensitive detectors technology has opened the possibility to build arrays of detectors based on the gamma-ray tracking concept, providing an unprecedented level of sensitivity and efficiency. Only two arrays with such technology are being built in the world, the European implementation of the tracking array is realized in the AGATA project. The second one, as well under construction at U.S., is the GRETA array [51].

AGATA consists of high-fold segmented Ge detectors and a front-end electronics, based on advanced digital signal processing techniques, which allows to extract energy, timing and spatial information for a gamma-ray by pulse shape analysis of the Ge detector signals. Utilizing the information on the positions of the interaction points and the energies released at each point the tracks of the gamma-rays in a Ge shell can be reconstructed in three dimensions. All these concepts and its constituents will be explained in the following sections.

2.5.1. The gamma-ray detectors and electronics

The AGATA detectors are highly segmented, encapsulated coaxial n-type high purity germanium (HPGe) crystals. The crystals have a tapered hexagonal geometry with an asymmetric shape to fit into the 4π detector geometry (see left panel in Fig. 2.21).

This geometry using 180 crystals was optimized by extensive Monte-Carlo simulations in order to minimize the solid angle not covered by detector and to

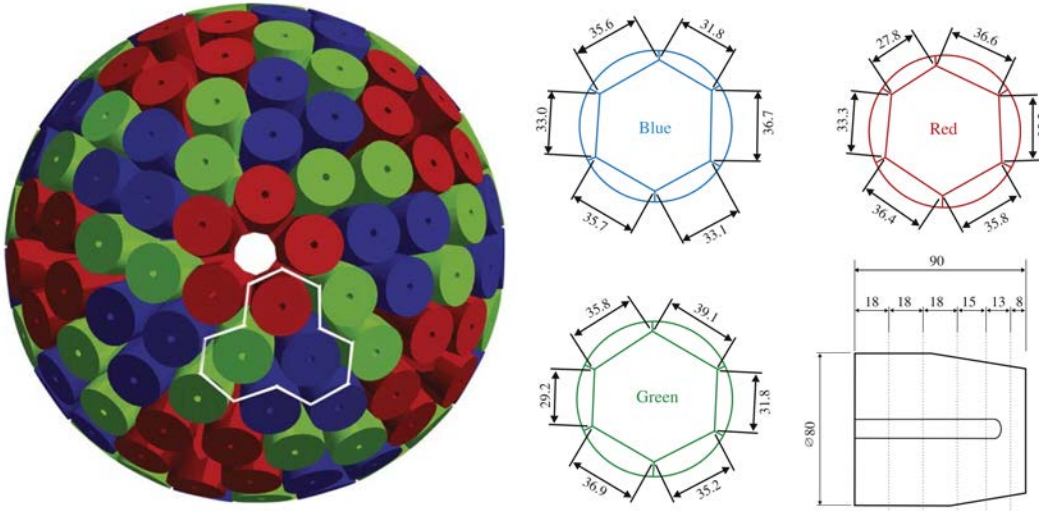


FIGURE 2.21: Left: Complete geometry of the AGATA 4π s.r. array with 180 crystals generated in GEANT4 simulations. The white line indicates a triple cluster. Right: Drawing of the crystals geometries for the different shapes in a cluster associated to different colours (red, green and blue). A schematic drawing of the position of the segmentation lines is shown on the lower right part. The dimensions are given in mm. Both figures were taken from Ref. [13].

maximize the overall detection efficiency by using different shapes in the cluster of detectors [52]. For this geometry, the expected solid angle coverage of the array is 82%. The conceptual design expected performance figures achieve a photopeak efficiency of 43% and a peak-to-total of 60% for single 1 MeV photons. For a cascade of 30 photons of 1 MeV the figures are reduced to 28 % and 52% respectively. To achieve this configuration, the AGATA crystals are grouped in clusters of three different shape HPGe crystals arranged in one cryostat [13]. As illustrated in Fig. 2.21, each crystal in an AGATA Triple Cluster (ATC) has a colour assigned to differentiate the shapes: type A (red), type B (green), type C (blue). They have also assigned a serial number (A001, A002, etc) and a position number (00A, 01A, etc) which indicates the crystal position in the holding structure of AGATA.

The crystals dimensions are 90 mm length and 80 mm of diameter before shaping. The inner radius of the AGATA sphere is 22.5 mm. The external surfaces of the HPGe detectors and in particular of the AGATA ones, are extremely delicate, in order to be able to manipulate, mount and maintain the detectors, the single crystals are encapsulated following the technique developed for the EUROBALL Cluster Detectors. The crystals encapsulated in the sealed, vacuum proof, thin aluminum enclosure, are finally accurately mounted in the ATC (see Fig. 2.22).

Each AGATA crystal is 36-fold electronically segmented, six azimuthal and six

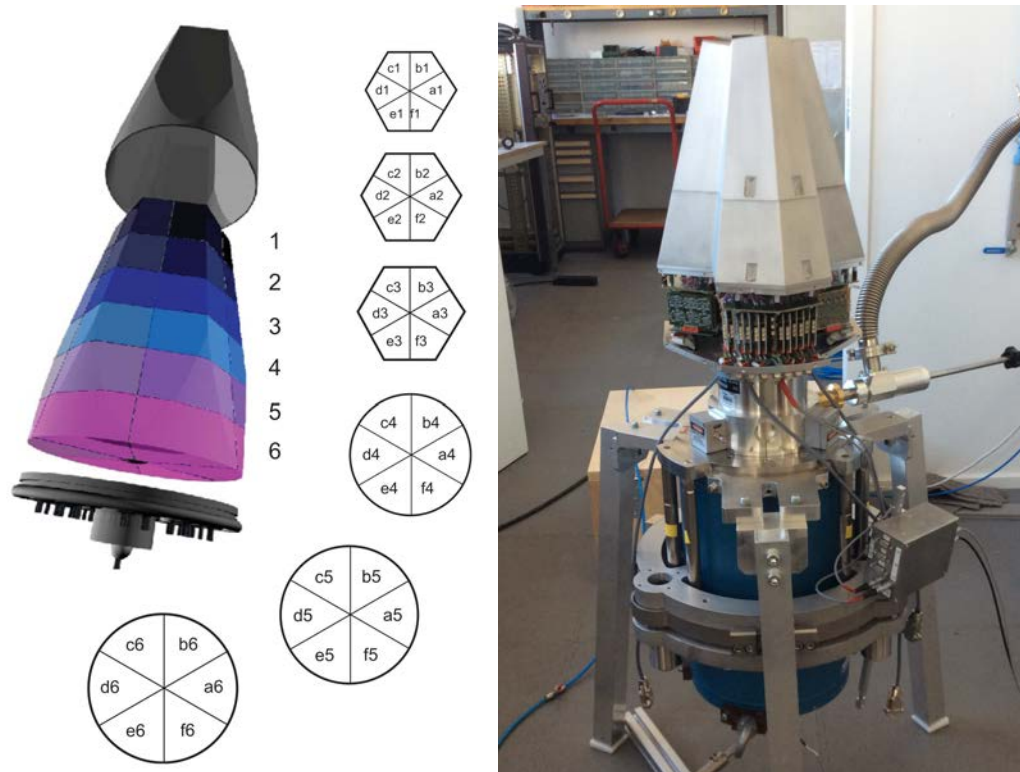


FIGURE 2.22: Left: Scheme of the segments labelling of one AGATA crystal. Is divided in six rings labelled 1-6. Each ring is subdivided into six sector labelled a-f. Figure taken from Ref. [13]. Right: Picture of an AGATA triple cluster with its pre-amplifiers uncovered and the Dewar.

longitudinal segments providing 36 electronically independent outputs. The segments are labelled per rings and sectors as schematically depicted in the left panel of Fig. 2.22. The total energy deposited in each crystal is measured in the central contact that collects the negative charges (electrons) produced in the ionization process. In the segments, the positive charges (holes) are collected from the ionizations produced locally. Each of the AGATA crystals provides 38 signals, 36 for the segments and two for the core, which correspond to a 5 MeV and a 30 MeV full range. The signals of the Ge detectors are processed first by the front-end electronics. They comprise preamplifiers and digitisers. AGATA uses charge preamplifiers specially which have been specially designed to fulfil the requirements needed for good timing properties, PSA, and high counting rate capability (more than 50 kHz per crystal).

The output of the respective preamplifier is digitised by means of a 100-MHz 14-bit ADC (12 ENOB). These sampled data are then sent via optical links to preprocessing electronics, where the energy and time information for each waveform are extracted. The energy is obtained by applying a digital trapezoidal filter or Moving

Window Deconvolution (MWD) technique [53, 54] by using the response function of the pre-amplifier. The trapezoidal filter risetime or MWD-risetime is constant and must be calibrated for the pole-zero cancellation. Long MWD-risetimes gives a better resolution but has higher probability of pile-up, which reduces the efficiency in high counting rates conditions [55]. In the preprocessing as well, a rough time information, mainly for triggering purposes, is determined with a CFD. The outputs of this stage are transmitted to a computer farm where further data processing, such as the PSA is performed.

Each detector is treated independently up to the reconstruction of interaction points inside de detectors (PSA), and the post-PSA corrections, as the neutron-damage. The synchronization among the different elements and time tagging is performed by the Global Trigger Synchronization (GTS) system. Two type of triggers are used in the AGATA readout. A local trigger which generates a request signal per detector if there is a pulse registered in the core and a global trigger which validates the signal through the central trigger processor before sending the traces of the segment and core to the computers farm. The GTS system and the data acquisition with the complementary detectors at GANIL will be explained in Section 2.6.

For this experiment, the AGATA device was composed of 24 crystals, i.e. about 2 sr (Fig. 2.23). The configuration of the crystals was chosen to maximize the separation between shifted and non-shifted components produced in the plunger measurement. In addition, AGATA was placed at a backward position (see the detectors arrangement in Fig. 2.6) and the target-array distance was 22.8 cm, to maintain a good separation of the two components. Since the experiment produced around 50kHz per crystal a short MWD-risetime of 2.5 μ s was selected. This election is based on the efficiency losses encountered at high counting rates as described in Ref. [55] and reviewed in Chapter 6. More details on the detectors used for this experiment, such as their position and serial numbers are given in Chapter 6. This chapter includes as well an evaluation of the AGATA performance is reported using calibrated gamma-ray sources and in-beam measurements. For this work, the calibrations and optimizations described in Chapter 3 have been taken into account. The AGATA data analysis will be presented in Chapter 3.

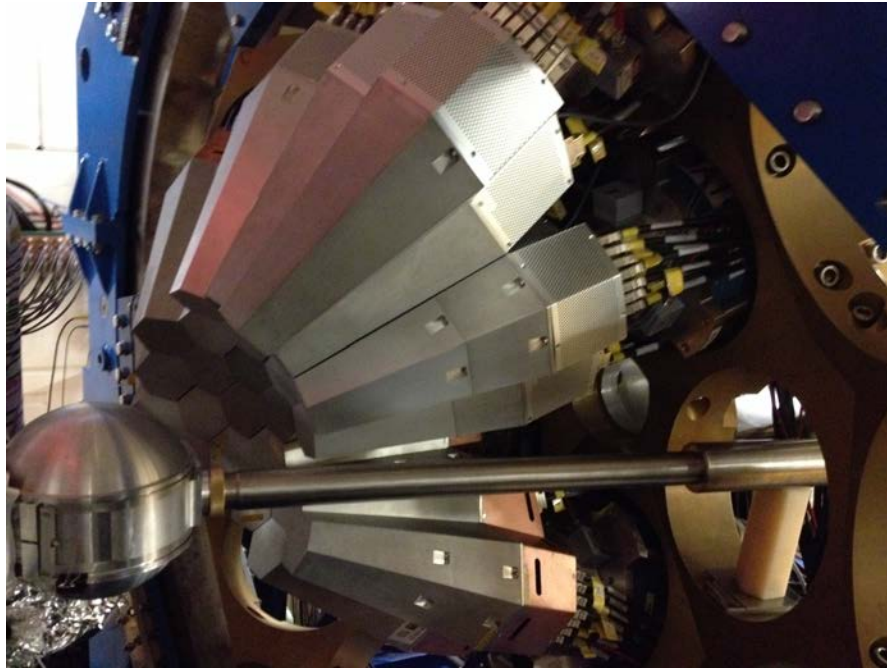


FIGURE 2.23: Photography of the AGATA sub-array configuration at GANIL. It was composed of 24 detectors and placed at mm from the reaction chamber.

2.5.2. Pulse Shape Analysis

The reconstruction of the gamma-ray trajectories inside the detector requires the knowledge of the position, time and energy information of each interaction point of the gamma-rays. The Pulse Shape Analysis (PSA) [13] algorithm provides this information with accuracy for the tracking task. To this aim, the PSA evaluates the shape of the measured, charge and induced, signals traces by comparing them to a library of traces that have been predetermined for different positions in the segments. The AGATA data library (ADL), also known as basis, contains simulated pulses of every segment and core for every possible interaction in the detector[56]. The combination of the basis which fits better the measured traces is used to assign where the interaction of the gamma-ray took place along with the associated deposited energy and the time at which it happened [57]. A comprehensive understanding of the signal shape is necessary in order to obtain three-dimensional interaction position accurately. A signal is shaped when electrons and holes are collected on the electrodes producing induced charges of opposite sign. Electrical signals are not only produced in the segments where interactions have taken place,

but transient signals in the neighbouring segments as well. The difference between both signals is that the signal obtained in the hit segment is a net-charge signal with a non-vanishing integrated current, while for the transient signals the integral of the current over the collecting time is zero. The analysis of both net charge signals and transient signals enables us to determine the position of the interactions with a higher resolution than the segment size which is about few millimeters [58]. For coaxial detectors, the radial position is derived from the charge collection time, named drift time. The latter depends on the distance to the electrode. The integral of the current gives the charge which provides the energy measurement.

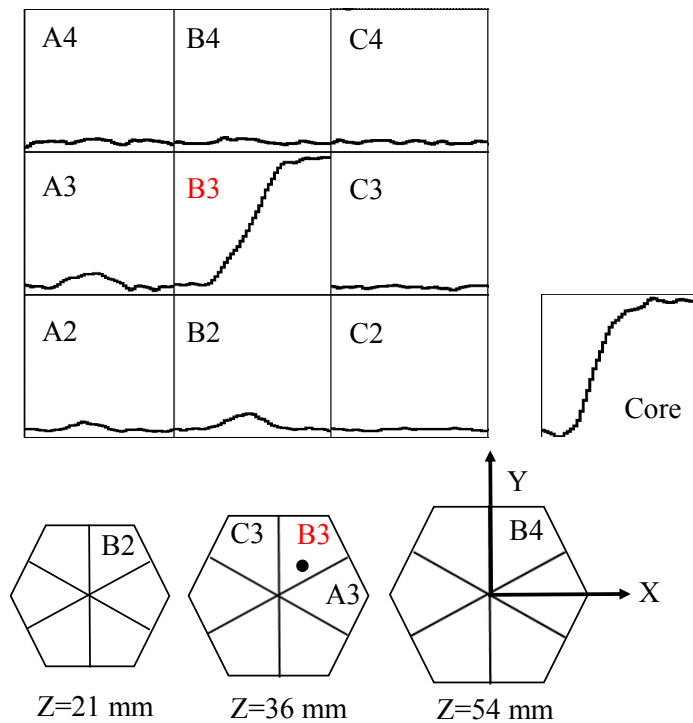


FIGURE 2.24: Net charges and transient signals for one event in an AGATA detector. The net charges are registered in the core and segment B3, where the interaction took place (black dot). The induced mirror charges are seen in the neighbouring segments and indicate the position of the interaction inside the segment.

Different PSA algorithms have been developed for AGATA. A number of tests with several of them have been performed within the AGATA collaboration revealing a similar performance among them [17]. Hence, in this Thesis the standard PSA algorithm, the so-called Adaptive Grid Search [59], has been used due to its shorter processing time than the others.

The Adaptive Grid Search compares in two steps the measured signals with the calculated signals from a grid of points in the crystal. Firstly, a three dimensional

search in a coarse grid of 6 mm is conducted to find a rough value for the position of the interaction. Afterwards, a more accurate search with a fine grid of 2 mm is repeated around the initial position. The evaluation of the measured signals is done by minimizing the following figure of merit (FoM)[60]:

$$FoM = \sum_{j,t_i} |A_{j,m}(t_i) - A_{j,s}(t_i)|^p, \quad (2.9)$$

where $A_{j,m}(t_i)$ and $A_{j,s}(t_i)$ are the measured and calculated signals, respectively, in a segment j at the time t_i . The exponent p is a positive number which is chosen. For the comparison, the net and transient signals of the segments and the core signal are considered (Fig. 2.24). This algorithm considers only a single interaction per detector segment. The PSA is an essential and crucial step for the good accomplishment of the tracking algorithm. Thus, a good quality of the signal basis calculation and the PSA algorithm performance is needed. Apart from this, the preparation of the data, which will be sent to the PSA, is very important. The energy and time signals have to be properly calibrated and aligned, respectively. The effects of the electronic couplings among channels should be corrected, such as the differential crosstalk phenomenon.

Additionally the PSA provides the information for the correction of the effects produced by the damage of the crystal structure caused by the interaction of fast neutrons in the germanium medium.

Crosstalk

The crosstalk is a phenomenon which appears in any electrically segmented detector due to the electronic coupling among channels. It consists of two components: one proportional to the net charge signal, proportional crosstalk, and another which is proportional to the derivative of that signal, differential crosstalk, [61]. The crosstalk produces false signals yielding amplitude losses and fold-dependent shifts on the reconstructed energies. This generates a worsening of the energy resolution because the sum of the amplitudes of the segments fired by a multiple interaction event depends on the hit pattern. Consequently, the spectroscopic performance of the detector is partially spoiled. Therefore, the segments amplitude signal has to be corrected. The calculations for the correction of the crosstalk effect are exhaustively reported in Refs. [61, 62]. They are made according to a

linear combination of the signal amplitudes of the other segments. The crosstalk effects and their correction will be illustrated in Chapter 3 (Fig. 3.4).

Neutron Damage

During experiments, the HPGe detectors are exposed to a continuous flux of fast neutrons that come from deep inelastic collisions, fission and fusion evaporation reactions. Fast neutrons are well known to produce specific lattice defects in germanium crystals which act as efficient hole traps. This leads to a reduction in the charge collection efficiency of the detectors observable by a low energy tailing on the energy line shape [63]. The AGATA crystals are n-type HPGe detectors, which are found to be less sensitive to the neutron radiation than the p-type ones [64], in terms of central contact signals. However, in tracking arrays, the segment signals of the outer contact are also used and they appear to be very sensitive to neutron induced traps than the core electrode [63].

The lattice defects in the detectors can be removed by the annealing of the crystals, but this treatment cannot be applied between each experiment. Fortunately, trapping effects can be corrected on-line/off-line thanks to the high position sensitivity of AGATA. The fraction of charge carriers lost in the collection process depends mainly on their travel path, the details of which can be easily obtained from the position of the interaction given by the PSA. The collection efficiency of the charge carriers is evaluated for each position in a particular electrode of the detector. Using the position information given by the PSA and the detector specific trapping sensitivity (based on collection efficiencies for electrons and holes) the energy deficit can be corrected. The effects of the neutron damage and its correction based on these principles will be illustrated in Chapter 3 (Fig. 3.17).

2.5.3. Tracking

The principle of gamma-ray tracking is based on the identification of the individual gamma-ray energies and the reconstruction of its trajectory inside the active volume of detector by using the interaction points and energy releases extracted by the PSA algorithm. Several methods have been developed to track gamma-rays by knowing the PSA information and the details of the interaction mechanisms at the energies relevant for gamma-ray spectroscopy. Each mechanism has a different hit

pattern as is illustrated in Fig. 2.25 for the main interactions of gamma-radiation with matter. These are the photoelectric effect, the Compton scattering and the pair production.

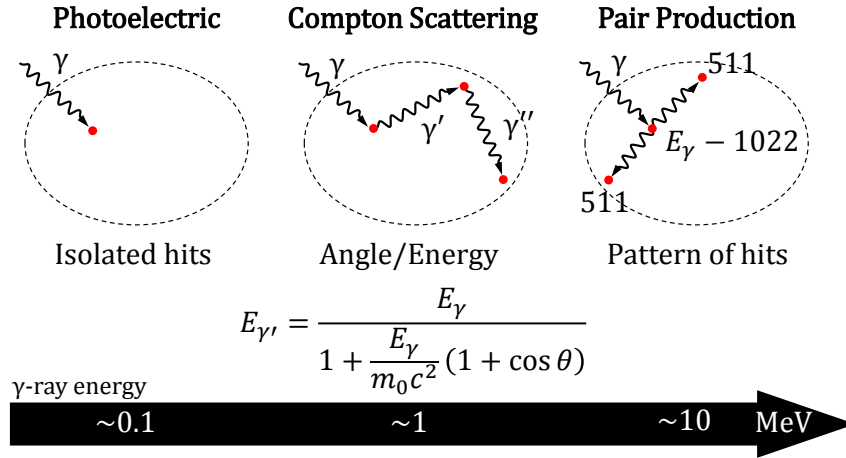


FIGURE 2.25: The most probable gamma-ray detection mechanisms at different ranges of E_γ .

The photoelectric effect is dominant at energies below 150 keV and the full photon energy is deposited in a single isolated interaction point. The Compton scattering consists of a scattering sequence of the photon before the remaining full-energy of the photon is deposited by photoelectric effect and is dominant at between 100 keV and 10 MeV. The pair production becomes possible above 1.022 MeV. In this mechanism the first interaction point releases the total gamma-ray energy except the mass needed to create the electron-positron pair and the emitted two photons from the annihilation generate their own clusters of interaction points close by the initial interaction point. For more details about the interaction mechanisms see Ref. [64].

The main mechanism for most of the energy range of interest in gamma-ray spectroscopy, is the Compton scattering and is the process which the tracking algorithms are mainly based on. There are two types of tracking algorithms regarding the starting point procedure for the reconstruction of the gamma-ray path. These are classified in forward-tracking algorithms [65], if they start by recognizing clusters of interaction points or backward tracking algorithms [66], if they start from the final interaction point. The former algorithm is considered more reliable than the latter [67]. Other tracking algorithms are reviewed in Ref. [57]. Currently, there are two codes based on the forward tracking algorithm used by the AGATA

community: the Orsay Forward Tracking (OFT) [67] and the Mars Gamma Tracking (MGT)[68]. In this work the OFT algorithm is used. As in all forward-tracking algorithms, the OFT groups the interaction points deduced by the PSA into clusters that may belong to the same physical event. The clusters of interaction points in the 3-dimensional space, defined by the polar θ and azimuth ϕ angles, are evaluated according to their relative angular separation. The maximum separation depends on the total number of interaction points detected in AGATA [67].

In the process, all the permutations of interaction points within a cluster are compared with a χ^2 test [67]:

$$FoM \propto \exp\left(\frac{E_{s,C} - E_s}{\sigma_E^2}\right), \quad (2.10)$$

where E_s is the scattered energy measured from the interaction point energy, $E_{s,C}$ is the scattered energy obtained from the Compton scattering formula and σ_E^2 is the uncertainty in the determination of the scattered energies. The latter depends on the energy resolution and position resolution, σ_θ , of the interaction points from the PSA. The Figure of Merit (FoM) is an indicator of goodness of how the scattering angles and energies from the interaction positions satisfy the Compton formula. The position uncertainties are controlled by the parameter σ_θ which reflects the average interaction-point position resolution in the experiment. Moreover, clusters for which the FoM is smaller than a minimum probability of having multiple-interaction-points, P_{track} , are rejected. The single-interaction-points are evaluated with the parameter P_{sing} which is the minimum probability for a gamma-ray to have penetrated a given depth and been absorbed via the photo electric effect. Finally, in order to obtain the best tracking performance the aforementioned parameters (σ_θ , P_{track} and P_{sing}) are tuned to maximize the FoM in Eq. (2.10). The optimization of the these parameters will be discussed in Chapter 3.

2.6. Data acquisition

The Data Acquisition System (DAQ) is in charge of processing the signals provided by the detectors into several steps up to their storage for subsequent data analysis. The AGATA DAQ is performed in such a way that the complete array is considered as an aggregation of individual crystals which pass through several stages (as

illustrated in the left part of Fig. 2.26). The data is stored with common clock and timestamp tags by the Global Trigger Synchronization (GTS) system.

The AGATA readout is composed by a local trigger signal generated by the already mentioned Leading Edge algorithm applied to the signal of the central contact of each crystal and an external global trigger for the validation of the trigger processor.

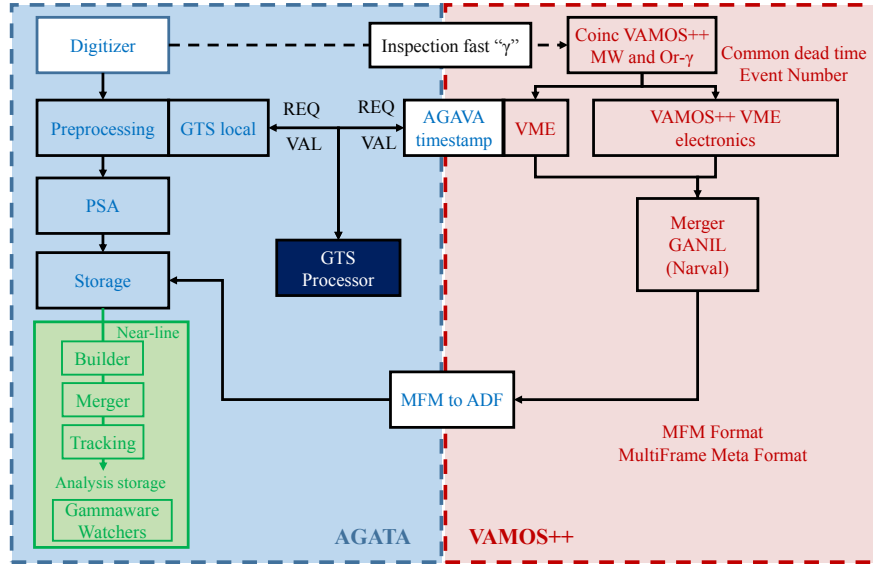


FIGURE 2.26: Schematic layout of the AGATA-VAMOS++ data acquisition system and the near-line analysis adapted from Ref. [45].

The VAMOS++ readout signals are collected using conventional VME electronics working in common dead-time. Its synchronization is based on the distribution of a 32-bit event number given by a Clock Event Number Transmitter Receiver Universal Module (CENTRUM)[69]. The tagged events sent by the various sub-systems on the network are correlated using the GANIL NARVAL data flow. A program called MERGER correlates and builds the individual events in a final event for the analysis and storage [69].

The coupling of the AGATA data flow with the ancillary detector (VAMOS++) is performed by a dedicated VME module, called AGAVA (AGATA VME Adapter)[13]. The AGAVA interface merge the AGATA timestamp-based system with conventional readout based on VME allowing complementary detectors to participate in the GTS trigger decisions. The trigger decision on the GTS and the data flow management between AGATA and VAMOS++ are illustrated in Fig. 2.26. They will be described in more detail the following subsections.

2.6.1. AGATA-VAMOS++ trigger on the GTS System

AGATA, as most of the detection systems, has a limited capability to process and store events, therefore, it is necessary to select the relevant events reducing as much as possible the amount of taken data. Two trigger levels, one local and one global are defined in this experiment. For lifetime measurement employing MNT reactions, the recorded gamma-rays in AGATA must be in coincidence with an identified heavy ion in VAMOS++. The synchronization among the different elements is essential for the optimum operation of the trigger and read-out systems, as well as to reconstruct properly the events in the data analysis process. This task is carried out by the Global Trigger and Synchronization (GTS) system.

The GTS system is organized in a tree layers topology, as illustrated in Fig. 2.27. The GTS tree has by several nodes. In the figure, the root node (in blue), the fan-in-fan-out nodes (in yellow) and the detector nodes or leaves (in green) are shown schematically. The root node is connected to the trigger processor (in purple). In this node all the trigger requests are collected and at the same time a central clock signal and timestamps are distributed. The last action allows to assemble the data of the different elements fired in a particular event into a global event. Each detector (Germanium crystal or ancillary) is connected to a leaf. Any time that any detector leaf produces a trigger request, this is tagged with the clock and forwarded upwards in the tree, through the fan-in-fan-out architecture to the GTS root connected to the trigger processor. The trigger processor validates or rejects the trigger request and broadcasts the decision downwards in the tree. Finally the corresponding event is either sent to the computer farm or discarded.

The decision made on the GTS systems depends on the trigger processor configuration. For the measurement performed in this Thesis, using the coupled system AGATA-VAMOS++, the standard configuration of two partitions was used. As indicated in Figs. 2.26 and 2.27, one partition contained all the Germanium detectors and the other one, the complementary instruments (VAMOS++). The trigger request signals for each partition to perform the gamma-particle coincidence was:

- **The gamma-ray trigger request.** A Digital Constant Fraction Discriminator (DCFD) or Leading Edge (DLE) is applied to the stream of ADC sampled data of the encapsulated detectors core signal. When the signal amplitude is larger that the threshold of the DCFD or DLE, a Trigger Request, for the corresponding AGATA detector, is generated.

- **The particle trigger request.** An ion event detected in VAMOS++ was enabled if the CFD outputs of both the MWPC1 at the entrance position and the MWPPAC at the focal plane were triggered. The VME electronics, in this case, has a long reset time after starting the ADC conversion. Therefore, a coincidence with the gamma-ray (obtained from the inspection signals) was also included in the coincidence conditions. This allows to start the VAMOS++ ADC conversion to be almost certain that the event will not be rejected.

In the trigger processor it is possible to set detector multiplicity threshold conditions within each partition and coincidence conditions between different partitions. Since MNT reactions generally populates the products with a limited angular momentum, the multiplicity threshold for bot partitions was set to 1 and the decision of Validation was taken when for the leafs that produced the requested trigger were inside a time coincidence window defined between the two partitions, i.e., AGATA and VAMOS++ participated in the event with an *AND* in the decision of the trigger.

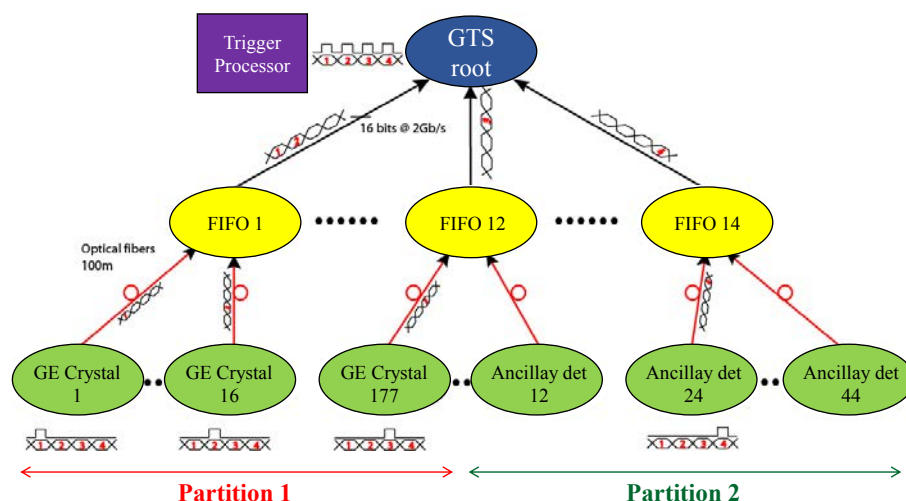


FIGURE 2.27: Illustration of the topology of the GTS tree. Figure taken from Ref. [70].

2.6.2. Data flow with NARVAL

The acquisition and processing of AGATA data is done through the Nouvelle Acquisition temps-Réel Version 1.2 Avec Linux (NARVAL) software [71]. NARVAL

is a modular data acquisition system, developed in the object-oriented language Ada, that manages the data flow and synchronization of many processes in which AGATA is divided: read, process and store. As in the case of the digital signal processing, each AGATA detector is processed individually in parallel (local level processing) until the data is built into a global event (global level processing). NARVAL is comprised of separate blocks of actions that receive and send out data at any stage of the data flow chain. These blocks of actions are called actors and each of them can be of the following type [71]:

- **Producers:** Read data from the electronics or disk, first stage of the data flow.
- **Intermediaries:** Receive the data from the previous stage, conduct operations on it and pass it to the next stage (filters, builders or dispatchers).
 - **Filters:** Process the data locally or globally.
 - **Dispatchers:** Take the data locally or globally and send it to the builders.
 - **Builders:** Build the data to the global level or merge the data with the ancillary data.
- **Consumers:** Write data to disk files, final stage of the data flow.

The chain of actors, called topology, for the AGATA data flow processing coupled to an ancillary detector is summarized in Table 2.13. A schematic view of the topology was already given in Fig. 2.26. Each topology should start with a Producer actor and finish with a Consumer actor. Then, each actor is used sequentially from the first one to the last one. The data written on disk by the Consumer actor is encoded with the AGATA Data Flow (ADF) format [13]. It is also possible to write data at the level of the Producer actor (raw traces data) in the so-called cdat files for post-experiment calibrations and corrections in each stage of the data flow. This can be done through an off-line replay performed with the femul NARVAL emulator, which is written in C++ to allow the users the manipulation of the outputs into the desired format.

During the experiment, only the local level processing was performed in real time (on-line processing). The global level processing was instead replayed near-line, and hence the Intermediate actors received the data from a Producer actor reading

the data from the previous saved files in the local level processing through the Consumer actor (as specified in Table 2.13). Moreover, it should be remarked that the PostPSA Filter, even if it is at the local level, was applied in the global level processing chain, before building the events together. This is typically done in order to reprocess and add the final corrections per detector independently avoiding the large time consuming of the PSA algorithm application. Regarding the merging with the ancillaries, a Producer actor is also used to read out the ancillary data that should be written in ADF format. The GANIL buffers are collected in the MultiFrame Metaformat by a dedicated Narval actor (MFM2ADF) which converts into ADF format and writes the time tagged by the GTS timestamp to allow the event merging correctly. The NARVAL topology for the ancillaries before the conversion into ADF format requires the participation of several actors and all the steps are explained in Ref. [16].

In Chapter 3 a detailed analysis through the data flow analysis steps will be presented.

TABLE 2.13: Topology of NARVAL actors for the local and global level processing.

Actor type	Actor name	Description
Local level		
Producer	Crystal Producer	Reads the data from the front-end electronics or disk.
Filter	Preprocessing Filter	Energy calibrations and time alignments on the traces.
Filter	PSA Filter	Extraction of the position of the interaction points from the calibrated data.
Consumer	BasicAFC	Saves the PSA output to disk files (PSA.adf).
Global level		
Producer	BasicAFP	Reads the data from PSA.adf files.
Filter	PostPSA Filter	Refinement processing on the interaction points (local level, see text for details).
Builder	Event Builder	Builds the events sent by the Dispatcher actor into a global event according to the related timestamps.
Builder	Event Merger	Merges the AGATA and VAMOS++ events sent by the Dispatcher actor according to the related timestamps. The ancillary events are read with a Producer actor before the merging.
Filter	Tracking Filter	Reconstruction of the gamma-ray trajectories from all the associated interaction points of a Compton scattering.
Consumer	Basic AFC	Saves the tracking output disk files (Tracking.adf) for the final analysis.

Chapter 3

Data processing

The AGATA-VAMOS++ combination is an ideal tool for the study of exotic nuclei, which makes possible the complete identification of a particular nucleus -on an event-by-event basis- in coincidence with the excitation spectrum provided by the gamma-rays detected.

The present chapter deals with the preliminary data treatment in the complex AGATA-VAMOS++-Plunger system. Firstly, each detector is treated separately. The VAMOS++ data treatment comprises the calibrations of the detectors for the ion-identification analysis aiming at the highest possible Z and A resolution. Moreover the ion trajectories are reconstructed event-by-event allowing the full determination of the velocity vector. The AGATA data treatment is described in its replay and sorting stages in order to achieve the best performance for the experimental conditions (more information about the AGATA performance is given in Chapter 6). Finally, using the information of the velocity vector provided by VAMOS++ in combination with the information provided by the gamma-ray tracking of the AGATA sub-array, the reconstructed gamma-rays in coincidence can be Doppler corrected event-by-event. The lifetime analysis will be the subject of Chapter 4.

3.1. The AGATA data processing

The AGATA data processing is carried out in two levels: the Local level, where all crystals are handled separately; and the Global level where the streams of

processed data from individually treated crystals are assembled on the basis of timestamp and further processed as events to be merged with complementary detector data. A schematic overview of both Local and Global level processing is presented in Fig. 3.1. The processing of the AGATA data starts from the recorded traces of the core and segments signals of each of the 23 crystals present in the AGATA sub-array during the experiment, i.e. the raw data. From this information the position and energy of each interaction is deduced via a pulse shape analysis at the Local level. The obtained hits in the detector volume are passed to the tracking algorithm, which provides a list containing the reconstructed gamma-rays and the merged complementary data at the Global level.

All the operations on the data are carried out with the chain of NARVAL actors depicted in Fig. 3.1. Each actor is performed sequentially from the first one, to the last one in the data-flow path as defined in a topology file [72]. This procedure is performed on-line for the monitoring of the experiments (on-line data processing) but also performed as a part of data analysis (off-line data processing or replay) starting from the raw traces (cdat files) or from the interaction points given by the on-line pulse-shape analysis (psa.adf files) to finally obtain the tracked gamma-rays combined with the complementary data (VAMOS.adf) in a list mode file (Tracking.adf). Afterwards, a *ROOT* tree [73] is generated from this file using the *GammaWare* software [74]. The *ROOT* tree contains all the necessary information stored in its branches in order to perform the VAMOS++ data processing and the final analysis.

The details of the NARVAL actors and acquisition system during the experiments were given in Chapter 2. For the off-line processing the femul NARVAL emulator is used [72]. This program implements the same actor classes and user-libraries employed in the on-line system via C++ classes.

In the following subsections the different actors will be described in the order that are applied on the data flow together with their most representative spectra. For a more detailed description of the AGATA data processing see Ref. [72]. The data replay has been done using the GRID computing resources as detailed in Section 3.1.3.

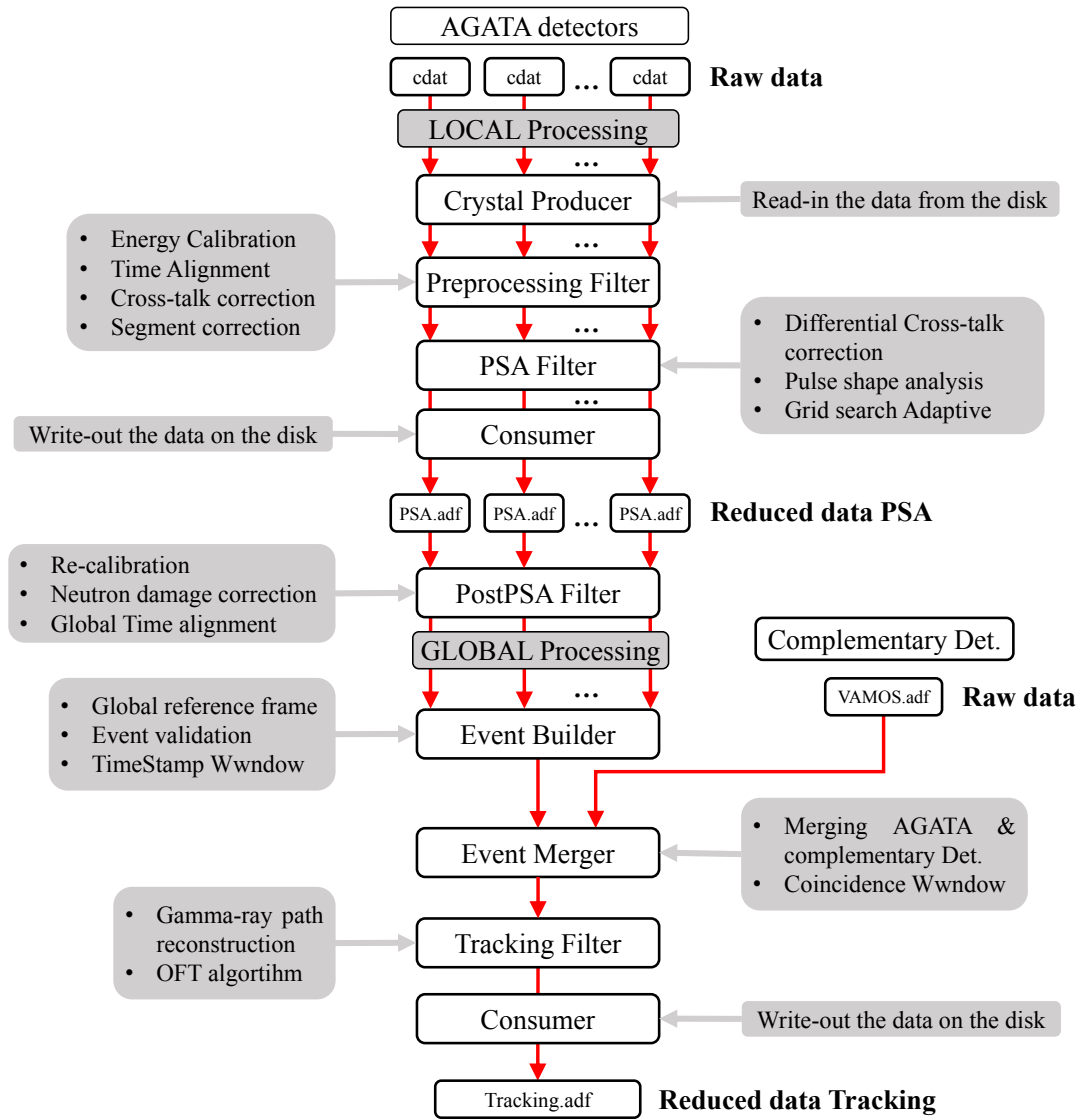


FIGURE 3.1: Structure of the AGATA data processing with a complementary detector. The data is processed in two differentiated steps: the Local and the Global levels (see text for details). The involved NARVAL actors in each level are indicated in boxes with a brief description of their tasks pointed with the grey arrows. The red arrows indicates the direction of the data flow.

3.1.1. The Local Level

As previously mentioned, the signals from each AGATA crystal are processed individually in order to obtain the interaction points using the PSA technique [13]. To this aim, the chain of NARVAL actors reported in Fig. 3.1 is used up to the reconstruction of the PSA hits in the detector reference frame. After the PSA Filter actor further adjustments on the energies of segments and central contact are performed, and the Local level processing chain is closed with a PostPSA Filter actor.

3.1.1.1. Crystal Producer

The first stage of the AGATA data processing is performed by the *Crystal Producer* actor (see Fig. 3.1). At this stage, the libraries needed to perform the data sort are read together with the raw data (event-by-event amplitude, timestamp and traces for segments and central contact). The decoding of the input channels is performed to obtain energy and time signals for all the channels involved. As mentioned in Section 2.5, each AGATA crystal gives 36 signals for the segments and 2 signals for the core contact due to the two different gain outputs from its pre-amplifier. Therefore, for the AGATA detectors involved in the present experiment, $(36 + 1 + 1) \times 23 = 874$ channels are present. The energy spectra written to disk at this level, when measuring with calibration sources, are the ones used to extract the energy calibration coefficients for each channel, segments and central contacts. For that purpose a calibration source is placed in proximity of the reaction chamber. In Fig. 3.2 the spectra of the energy amplitudes are shown for a measurement with a ^{60}Co radioactive source.

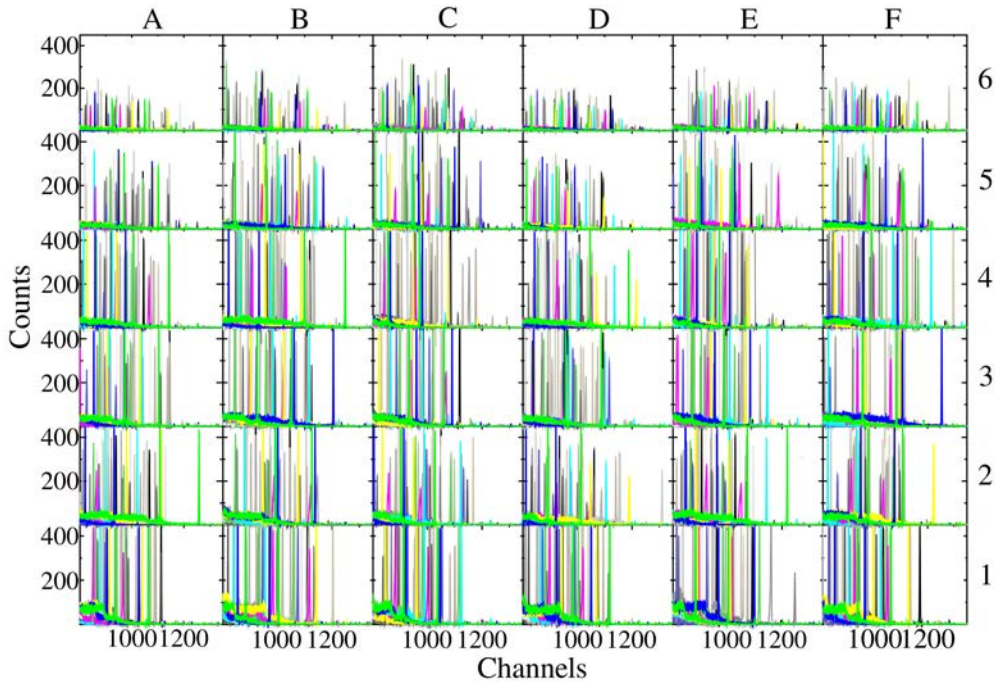


FIGURE 3.2: *Producer: Segments amplitude signals.* Spectra excerpt of the 1.3 MeV gamma-ray transition in ^{60}Co for all AGATA detectors between the channels 800 and 1400 at the producer level. The labels for columns and rows correspond to the nomenclature used in Fig. 2.22, where 1 and 6 means front and back segments of the crystal, respectively.

3.1.1.2. Preprocessing Filter

After the signals are decoded at the producer level the data is sent to the preprocessing stage for the preparation before doing the PSA. The proper preparation of the data is crucial for the correct performance of the PSA algorithm. To this aim the raw signal amplitude needs to be calibrated, the traces of the segments have to be properly aligned in time and all segments should be properly working.

All these tasks are carried out by the *Preprocessing Filter* actor as indicated in Fig. 3.1.

Energy calibration

A good energy calibration is essential in order to obtain a good performance of the PSA and tracking algorithms. In addition, in our case this aspect is crucial for disentangling the two components of a gamma-ray transition caused by the plunger.

The calibration measurement was done using ^{60}Co and ^{152}Eu sources. As the AGATA crystals are segmented, the duration of the measurement was as long as possible in order to have enough statistics in the back segments. The calibration coefficients are deduced from the most intense transitions recorded in the amplitude spectra (an example of this spectra is shown in Fig. 3.2 for the ^{60}Co). The intensities of those transitions are automatically fitted with the program *RecalEnergy* [72] using a linear fit with no offset for each segment and core signals. It should be remarked that the producer data used for the calibration is sorted with the condition that just one segment per crystal fires. This condition allows to treat each segment as an individual detector, thus avoiding the incorrect determination of the calibration coefficient due to the crosstalk effect at higher multiplicities of segments (see next action in the Preprocessing Filter).

The calibration coefficients are applied to the energy information and also to scale the recorded traces used for PSA, since the relative amplitude of the mirror/induced signals is a crucial ingredient in the PSA process. An example of the calibrated spectra is shown in Fig. 3.3 for the segment signals of the 23 detectors present in our setup. By comparing the row 1 (front segments of the crystal) with the row 6 (back segments of the crystal) one can appreciate that the number of counts decreases with the depth of the detector. This is due to the absorption

length in germanium, which for 1 MeV gamma-rays is of 3.5 cm. Moreover, in this figure is clearly seen that some of the detectors have a long tail on the left side of the full absorption peak. This effect occurs due to the uncompleted charge collection due to the charge trapping on the crystal defects produce by fast neutron radiation damage. It can be corrected at the post-psa level (Section 3.1.1.4).

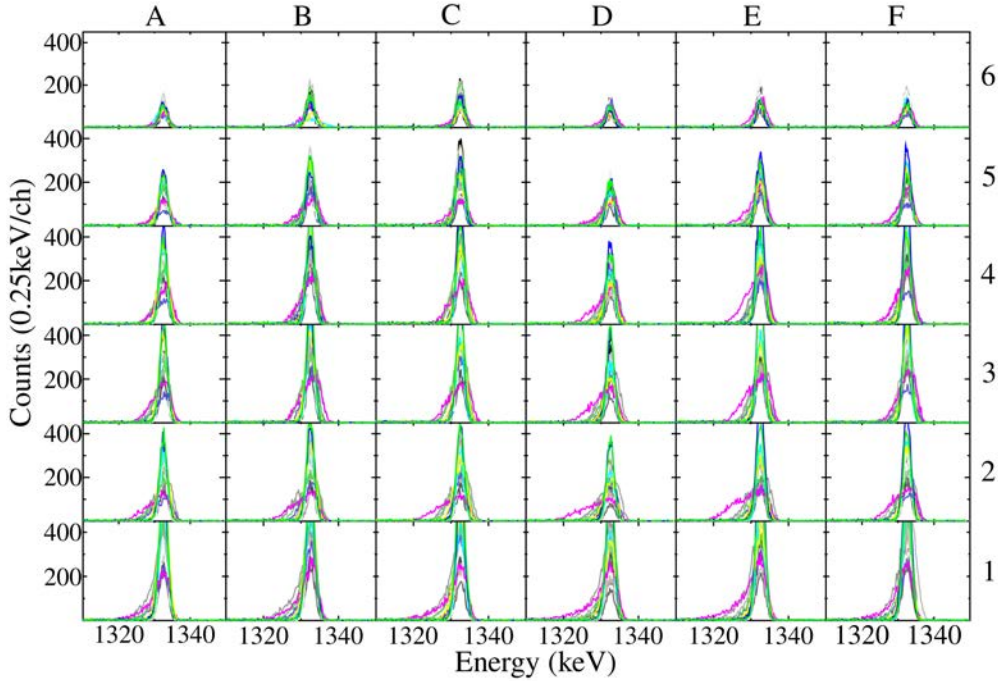


FIGURE 3.3: *Preprocessing: Segments calibration.* Spectra of the 1.3 MeV gamma-ray transition in ^{60}Co for all AGATA detectors after the energy calibration. The spectra with long tail on the left of the peak correspond to the detectors which have suffered the neutron damage effect.

Crosstalk correction

As introduced in Section 2.5.2, in electrically segmented detectors the crosstalk effects are observed if the gamma-ray energy is deposited in more than one segment in the same crystal. This effect has to be considered and corrected in order to properly reconstruct the amplitudes recorded in the segments. If not corrected, one would observe a deficit in the sum energy of the segments when the event involves more than one segment, which increases with the segment multiplicity. This is the so called proportional cross-talk. Nevertheless, the induced/mirror signal are also affected by the cross-talk between segments, this is called differential cross talk, and its correction is necessary to perform properly the Pulse Shape Analysis.

A ^{60}Co source was used in order to obtain the parameters for the cross-talk correction. By an automatic procedure the energies recorded in the segments are sorted

according to the segment multiplicity (i.e. number of firing segments). From that the shift from the nominal energy of the two strong transitions of the ^{60}Co source is deduced to build the cross-talk matrix of coefficients. The software *xTalkSort* [72] is used for that purpose. These matrices are used for the correction of the measured energies and the restoration of the baseline. Additionally, the inverse matrices are included in the calculated signals, used for the Pulse Shape Analysis, in order to take into account the cross-talk effects.

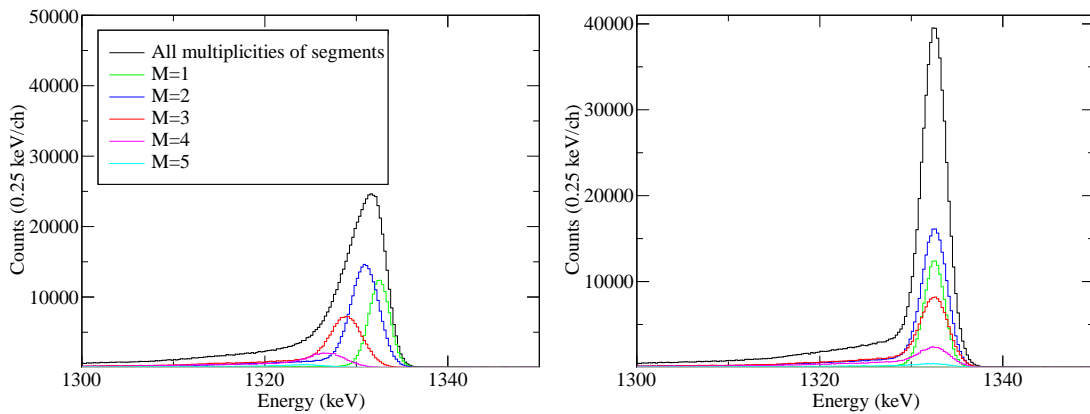


FIGURE 3.4: *Preprocessing: Segments cross-talk correction.* Spectra of the 1.3 MeV gamma-ray transition in ^{60}Co for different multiplicities of segments (coloured lines) and for all the multiplicities of segments together (black line). The left panel shows the spectra before the cross-talk correction and the right one after the correction.

The crosstalk effect between segments is illustrated in Fig. 3.4. In this figure, the spectra of the 1.3 MeV gamma-ray transition of ^{60}Co is shown for different multiplicities of segments. It can be appreciated a centroid shift towards lower energies with increasing segment multiplicity (left panel in Fig. 3.4). Thus, the centroid of the sum energy of the segments (black line) is laying at smaller energy than in case of a single firing segment (green line). After the crosstalk correction (right panel in Fig. 3.4) the centroids appear at the correct energy and the resolution is recovered for the sum of the segments.

Segment corrections

Sometimes the AGATA crystals can present some problematic segments, that can be regarded as *dead* or *unstable* segments. This classification depends on the type of issue present in the segment. When a problematic segment exits in a crystal it

is possible to recover its correct information and the complete performance of the crystal only if all other segments in the detector work correctly.

A *dead segment* is a segment without any or extremely noisy signal and can be further classified into *broken* or *lost* segment. The first case occurs when the net charge is not properly collected but flows to the neighbouring segments, i.e. the net charge is missing or extremely noisy while the transient signals are present. This effect is a result of a problem at the FET level and is manifested with the presence of ghost peaks in the energy spectra of the neighbouring segments and of a strong step-like tail in the spectrum of the core. In the case of a lost segment, although the net charge is correctly collected, no information is present inside the data flow. This could be due to, e.g., a broken wire or a faulty warm part of the pre-amplifier or digitizer channel.

An *unstable segment* is a segment with a energy signal varying in time while the time signal is preserved. Such malfunctioning segments lead to the occurrence of multiple peaks in the segment energy spectrum or in a broad peak.

To recover the signals of a dead segment, a correction to the crosstalk matrix elements is done considering that the sum of the energies released in the segments should be equal to the one observed in the core with the software *xTalkSort* previously mentioned. The correlation between the energy seen by the energy measured by the core and the sum-energy of all segments is shown in Fig. 3.5. In

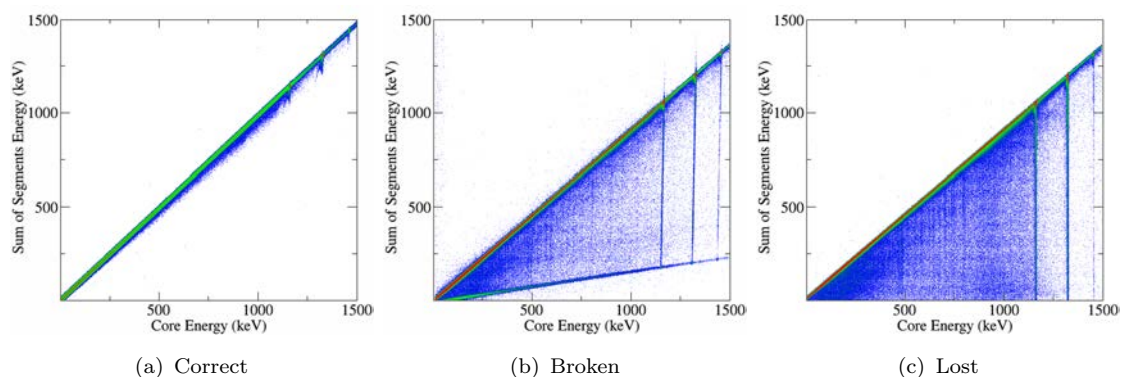


FIGURE 3.5: *Preprocessing: Segments correction matrices.* Correlation between the energy measured by the core and the sum-energy of all segments.

the case of a crystal with all the segments functioning correctly the correlation between the energies should appear as in Fig. 3.5(a). In a broken segment case (Fig. 3.5(b)), the main diagonal is not at 45° and there is a lower limit line for the energy lost in the sum of segment. This structure appears because of the energy

collected by the close neighbouring segments. Additionally, the lines coming from the ^{60}Co peaks are slightly tilted due to the loss in core energy. In a lost segment case (Fig. 3.5(c)) the energy lost in the sum of segment is seen below the diagonal. The lines coming down from the ^{60}Co peaks perfectly vertical in this case.

After the correction, all the information (energy and time) of the segment is recovered and in the broken segment cases, the neighbouring segments and core are restored. Similarly, one can correct for unstable segments the energy signal keeping the time signal. In this case the correction is done treating the segment as for the lost segment case. The steps of the procedure are detailed in Ref. [72] for the dead segment cases. Examples of the procedure application for the dead and unstable segments cases of this Thesis are illustrated and explained in Ref. [75].

A good example for the broken and lost cases is shown in Fig. 3.6. The figure shows the energy calibrated signals for the segments and the central contact of the detector 03A. The problematic segments, its neighbouring segments and the central contact are marked in colours to illustrate the effect produced in each case. Segment 3A (blue) is a lost segment and therefore no effect is appreciated in its neighbours or core contact. Contrary to what is seen for the segment 1C (red),

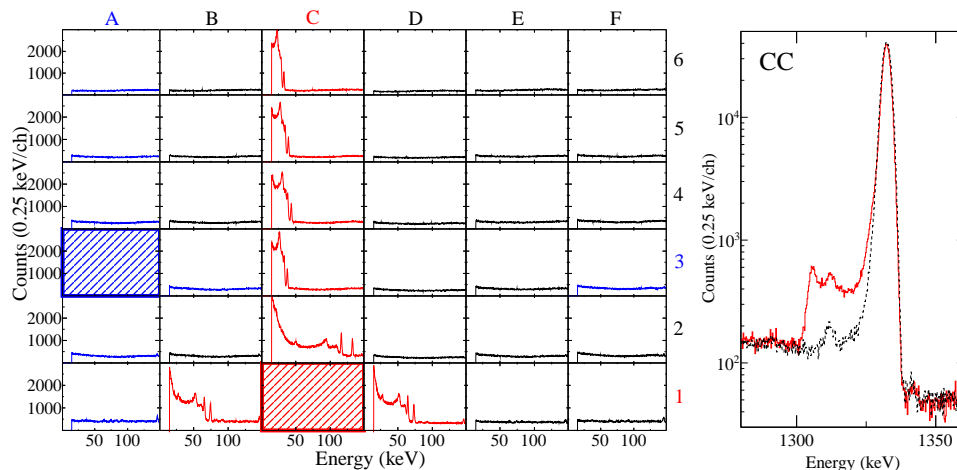


FIGURE 3.6: *Preprocessing: Dead segments in crystal 03A.* Left panel: Low energy spectra of ^{60}Co for the AGATA crystal 03A to illustrate the differences in the neighbouring segments of two types of dead segment: a lost segment (in blue) and a broken segment (in red). The boxes with strips indicate that the signal is missing. Right panel: effect of the broken segment in the energy signal of the central contact (red line) compared with how the signal should look like (black dashed line, signal taken from detector 03C). It is worth remarking that in the cases where the detector has more than one problematic segment the correction can not be performed (see text for more details).

which is a broken segment. In this case, the wrong collection of the net charge is

clearly seen in the effect produced on the neighbouring segments (ghost peaks) and the core (step-like left tail) spectra. Unfortunately since more than one segment are not working correctly the recovery procedure cannot be performed for this detector.

In the case of crystal 12B, there were also two segments with problems, 6A (broken segment) and 1B (unstable segment leading to broad peak and gain shift) as seen in Fig. 3.7. As mentioned above, the restoration of a segment is possible only if the rest of segments work correctly. Then, different crosstalk matrix elements have been built and applied over the time for the broken segment restoration taking into account the energy gain variation as a function of time for the unstable segment.

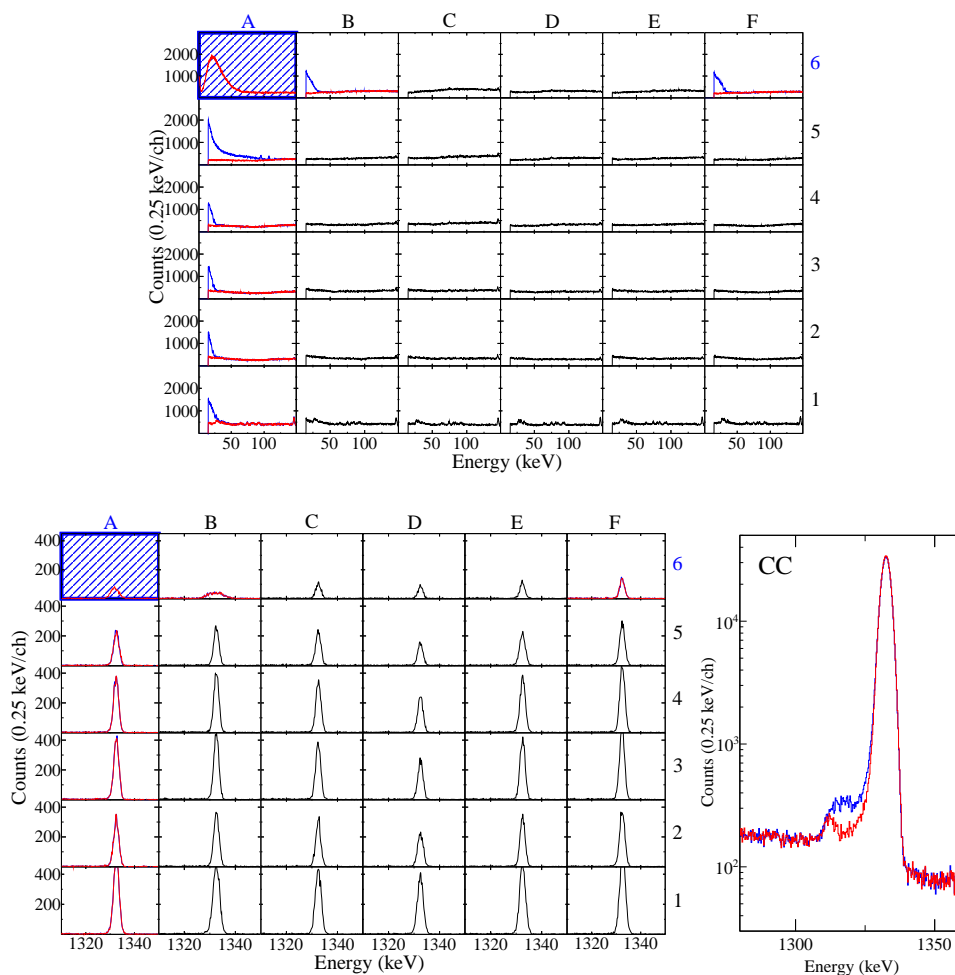


FIGURE 3.7: *Preprocessing: Broken segment correction in crystal 12B.* Low energy spectra and the 1.3 MeV gamma-ray transition of ^{60}Co for the AGATA crystal 12B in the top and bottom-left panel respectively. The strips indicate that the signal is missing before the correction. The bottom-right panel shows the energy signal of the central contact. The blue spectra is before the broken segment correction and the read one after it.

In Fig. 3.7 the recovery of the broken segment 6A is illustrated. The energy signals before the correction are shown in blue. After the correction the satellite peaks disappear, as well as the step-like tail in the central contact spectrum (red lines).

In crystal 11B the segment 1F lost synchronization in the middle of the experiment. Since energy and time information of this segment needed to be recovered and no effect was appreciated in the neighbouring segments and central contact, the lost segment procedure was applied to this segment. Fig. 3.8 shows the energy spectra of the segment with issues before and after the correction in blue and red respectively.

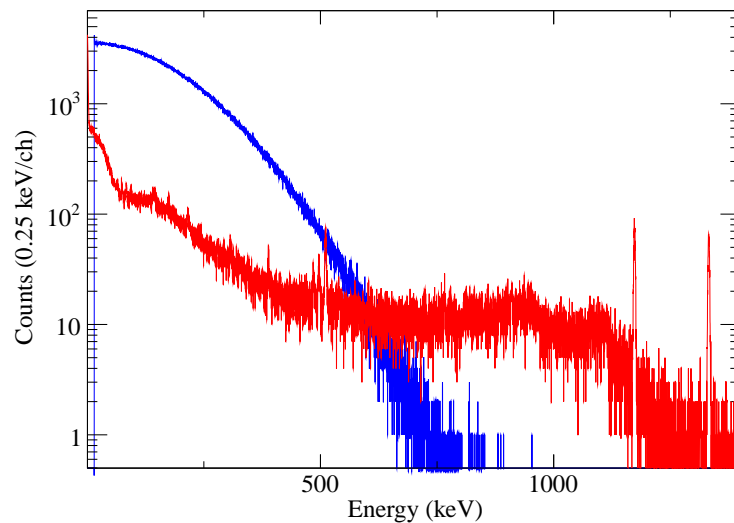


FIGURE 3.8: *Preprocessing: Lost segment correction in crystal 11B.* Spectra of the 1.3 MeV gamma-ray transition in ^{60}Co for the AGATA crystal 11B. Segment 1F lost synchronisation (peak-line blue). After the lost segment type correction the correct shape of the line has been recovered (peak-line in red).

Regarding the unstable segments in the setup of the experiment, the gain instabilities in segment 2B of crystal 00B lead to the occurrence of double peaks on the peak transitions in the full spectrum range (blue peak-line in Fig. 3.9). In the same figure the signal corrected by the unstable segment method is represented in red. Another case corrected as unstable segment is 1F in crystal 04B. In this case the signal showed a right tail on the peak-line transitions over the entire energy range. The malfunctioning of the segment 1F is displayed in blue in Fig. 3.10. The centroid of the peak (marked with the dashed line) clearly shows the right tail structure of the segment before the correction. After the correction the proper shape of peak transition is recovered (read peak-line).

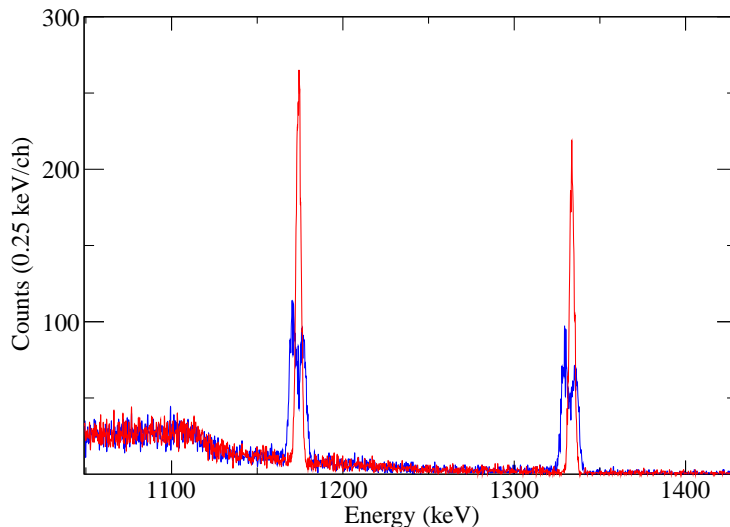


FIGURE 3.9: *Preprocessing: Unstable segment correction in crystal 00B.* Spectra of the 1.3 MeV gamma-ray transition in ^{60}Co for the AGATA crystal 00B. Segment 2B presented a double peak structure for each gamma-ray transition in the energy spectrum (peak-line blue). After the unstable type correction the correct shape of the line has been recovered (peak-line in red).

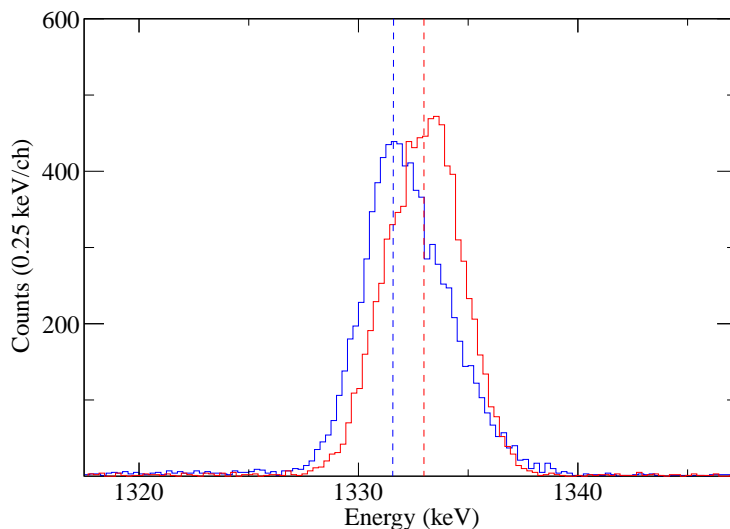


FIGURE 3.10: *Preprocessing: Unstable segment correction in crystal 04B.* Spectra of the 1.3 MeV gamma-ray transition in ^{60}Co for the AGATA crystal 04A. The left tail existing in the energy signal of the segment 1F (peak-line in blue) has been corrected using the unstable segment correction (peak-line in red). The dashed lines guide the eye to find the centroid of the peak before and after de correction.

In summary, five AGATA crystals (00B, 03A, 04B, 11B, 12B) presented problematic segments, which were corrected using the common dead and unstable segment procedures. This ensured the optimal performance of the array. Although 03A could not be corrected, it was kept in the analysis since we needed as much statistics as possible for the two proton channel.

Time alignment

The signals in the database used for the PSA have been calculated [56] for an ideal detector and hence are well aligned in time. Time differences between measured signals can lead to a misinterpretation of the interaction point. Therefore, a good performance of the PSA algorithm requires that traces corresponding to the different segments are aligned in time, which in addition improves the time resolution. For the time alignment a set of shift coefficients for the segments is obtained per detector from the timing spectra when using the core as trigger. With that information, the signals of the segments relative to the core are aligned to each other and also among the different detectors.

The comparison of the time signals of the segments with respect the core before and after the alignment in time is shown in Fig. 3.11.

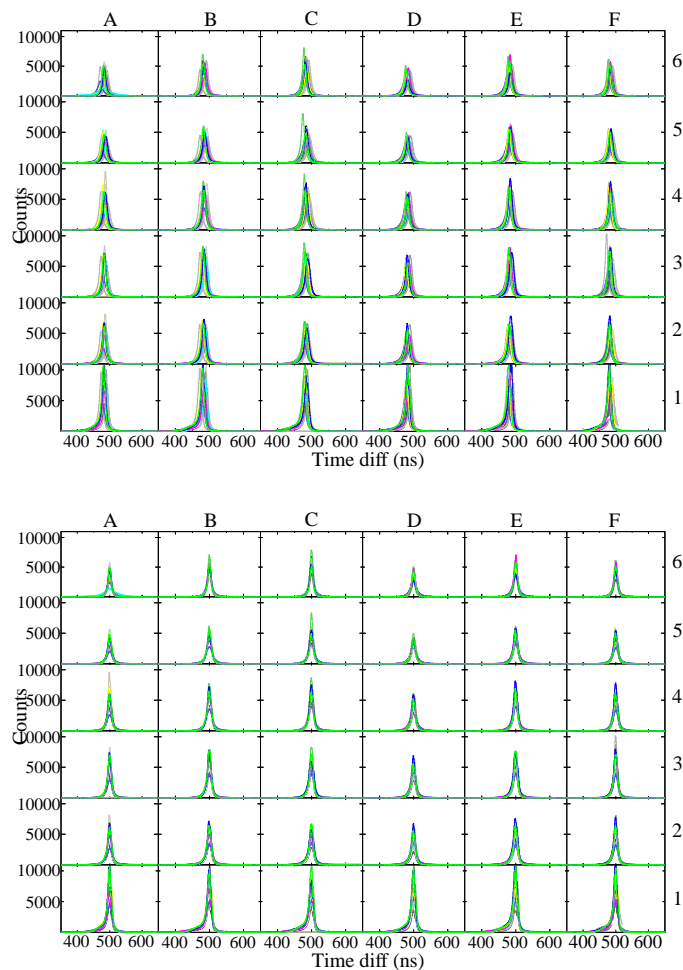


FIGURE 3.11: *Preprocessing: Segments time alignment to the core.* Time spectra of the segments relative to the core for 23 AGATA crystals, before (top panel) and after (bottom panel) the time alignment.

In order to determine the most accurate interaction position the PSA algorithm uses different time shifts of the traces around a time reference called T_{zero} . This time reference is chosen as the sum of the net charge time (previously aligned) and the core time. Then, the crystal time references need to be aligned to each other too in order to have the same starting time reference. The T_{zero} spectra after the time alignment correction for the 23 AGATA crystals is shown in Fig. 3.12.

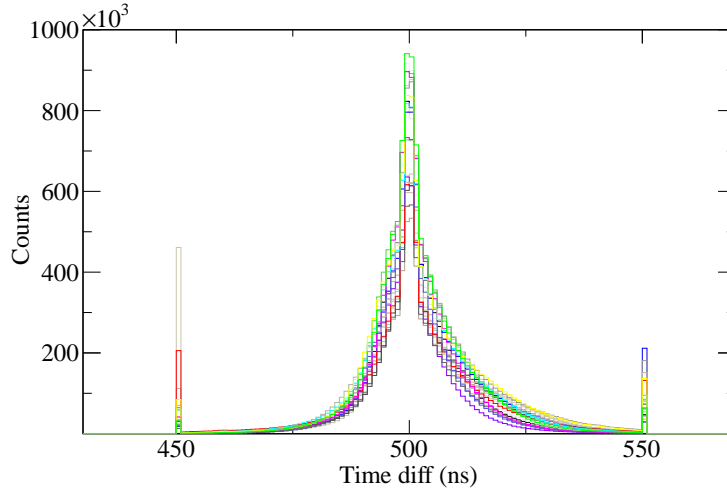


FIGURE 3.12: *Preprocessing: T_0 alignment for the 23 detectors.* T_{zero} spectra after the time alignment of the segments and core signals.

These two steps in the time alignment have a direct impact on the distribution of hits reconstructed by the PSA as it will be shown in the following section.

3.1.1.3. PSA Filter

The Pulse-Shape Analysis is implemented by the *PSA Filter* actor. As introduced in Section 2.5.2, the PSA finds the interaction positions of the gamma-rays by means of a χ^2 minimization between the basis datasets and the experimental data. The energy, time and position information of the interaction points are obtained for the subsequent trajectory reconstruction of the gamma-ray by the tracking algorithms. In addition, it also provides the parameters for the correction of neutron damage to recover the energy resolution of the segments. For this Thesis the Adaptive Grid Search algorithm [59], which considers only a single interaction in a segment, has been used. An example of the comparison of experimental and calculated waveforms is shown in Fig. 3.13.

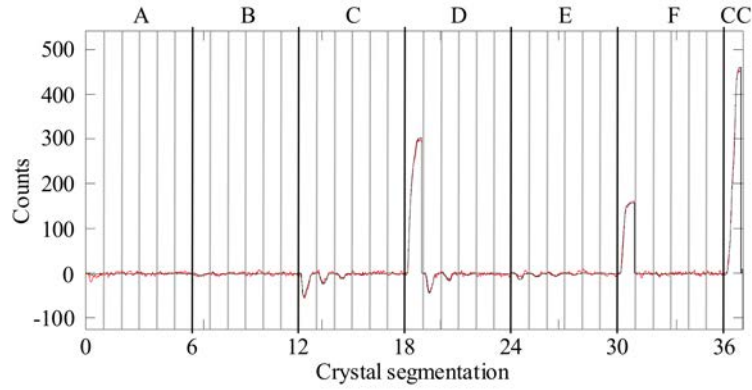


FIGURE 3.13: *PSA: Traces.* Comparison between experimental (red) and calculated (black) traces by the pulse shape analysis of the AGATA crystal 00A.

Examples of the spatial distributions of hits determined by the PSA are presented in Fig. 3.14 for different projection planes. The different sectors of segmentation (A-F) of the projection in the XY plane (Fig. 3.14(a)) as a function of the depth of each ring of segments (1-6) are represented in detail in Fig. 3.15. In these subfigures, the six fold structure of the segments is marked with dashed lines although in some cases is already visible without them. These distributions of hits show that the PSA seems to be biased towards the center of the segments.

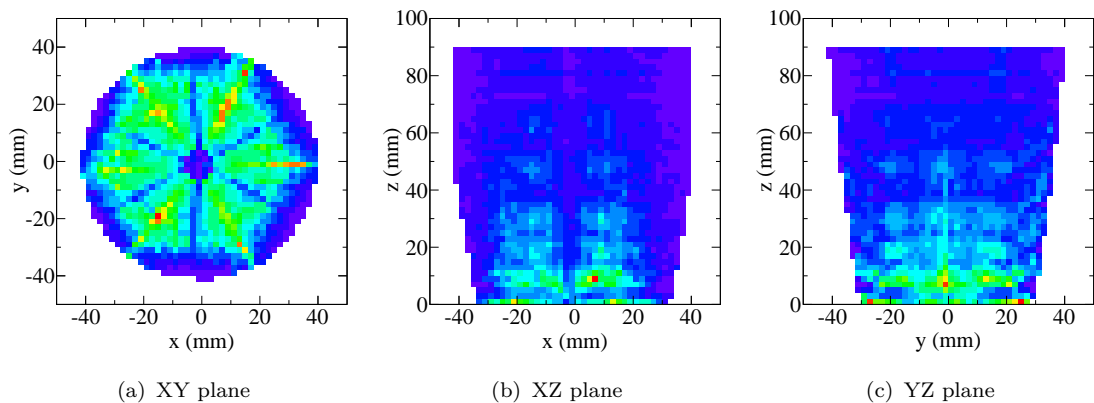


FIGURE 3.14: *PSA: gamma-ray interaction distributions.* XY, XZ and YZ projection planes of the PSA hit pattern for the AGATA crystal 00A.

In principle for a given crystal depth, the distribution of the hits inside a crystal should be homogeneous with statistical fluctuation. However, a clustering of positions inside crystal occurs, even if there is no physical reason for that. This can be ascribed to a limitation of the PSA algorithm or of the calculated pulse bases. This effect is under investigation within the AGATA collaboration. Recent works in order to understand the clustering of interaction points and to optimize the PSA performance can be found in Ref. [60]. The difficulty of getting better results

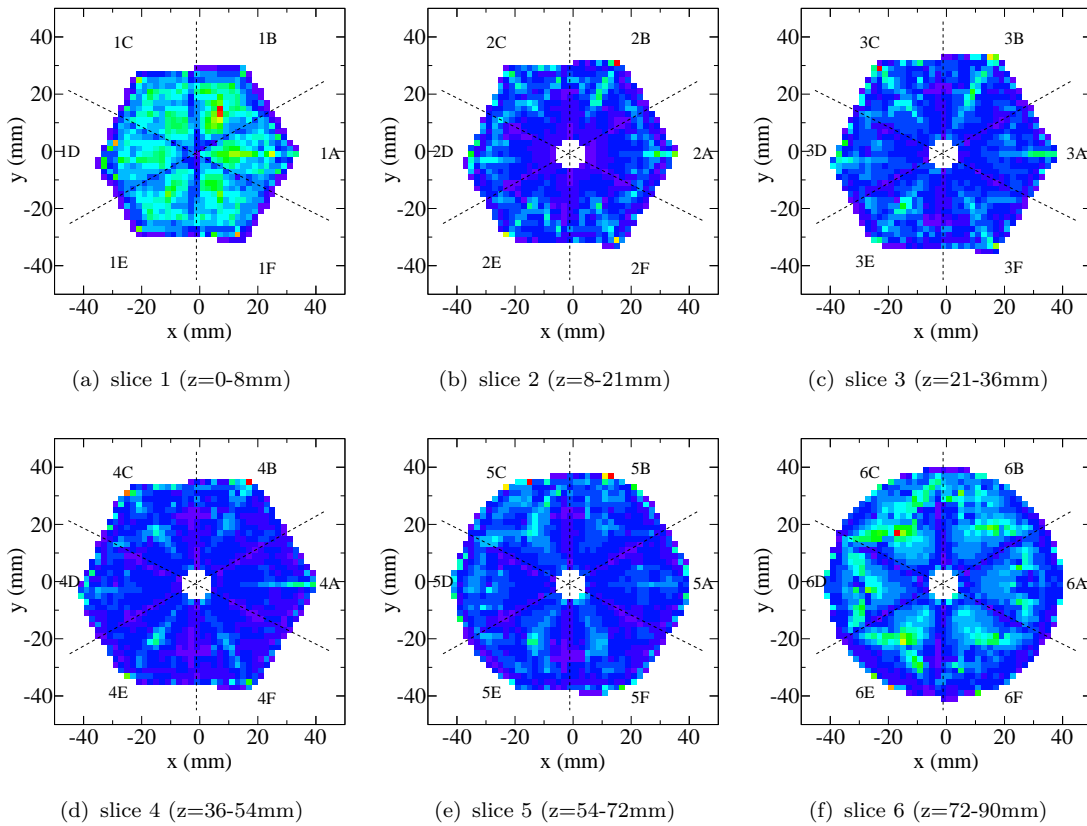


FIGURE 3.15: *PSA: Gamma-ray interaction distributions by slices.* XY projection plane of the PSA hit pattern as a function of the depth of the AGATA crystal 00A following the nomenclature used in Fig. 2.22. The slice 1 corresponds to the front ring of the crystal and the slice 6 to the back ring of the crystal. The dashed lines mark the six fold structure of the segments.

could come from the algorithm, the calculated basis or even the data preparation. The latter point has a direct impact in the performance of the PSA algorithm since it depends on both energy calibration of the traces and on their TZero alignment of the traces. An example of the effect of the time position of the experimental trace is illustrated in Fig. 3.16. Before the TZero alignment (top panel, red line), the shift of the real time compared with the measured time makes that the PSA distributes hits randomly in the passive part of the center of the detector (left bottom panel). After the TZero alignment (top panel, black line) the distribution of hits is recovered (right bottom panel). Therefore, one should follow carefully all the steps of data preparation in the preprocessing level in order to avoid position points randomly distributed by the PSA.

From the comparison of the hit pattern in the XY plane (looking at the front face of the crystal) in Figs. 3.14(a) and 3.16 (right bottom panel) one can easily

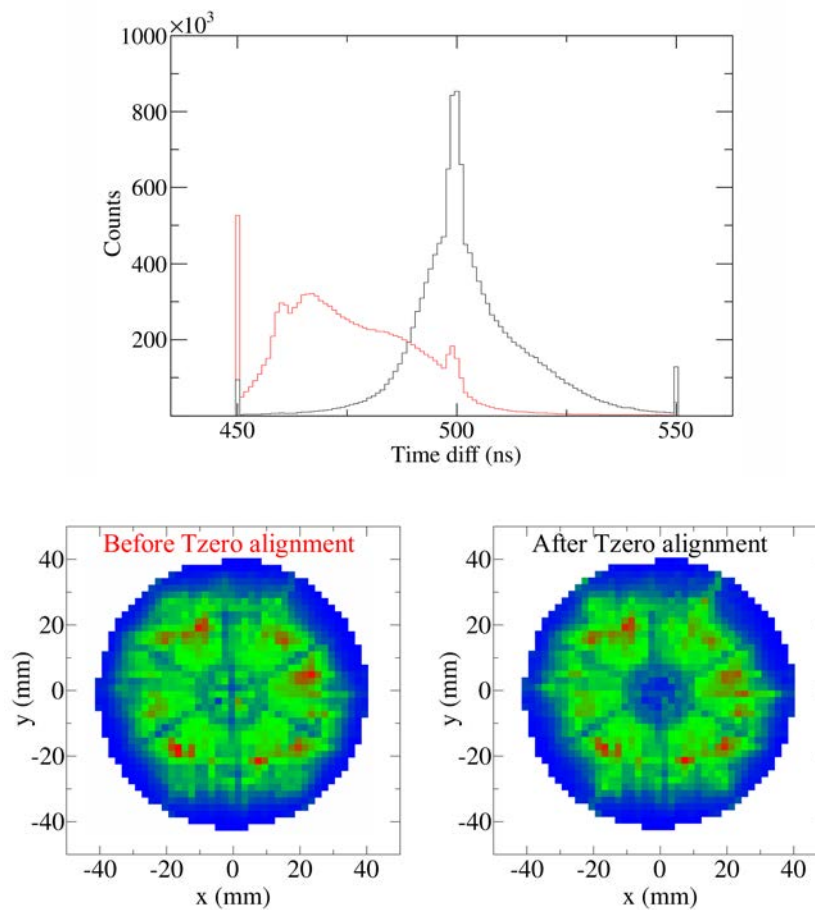


FIGURE 3.16: *PSA: Effect of time position of the experimental trace.* Top: Tzero signal before and after the time alignment for the AGATA crystal 00B, in red and black, respectively. Bottom: The corresponding gamma-ray interaction distributions in the XY plane before (left) and after (right) the alignment.

observe that the pattern shape is not identical due to the different geometry of the detectors.

3.1.1.4. PostPSA Filter

After the PSA analysis a series of refinements can be implemented, if necessary. The latter include the final energy calibration, the global time alignment and the (partial) recovery of neutron damage effects using the PSA hits information. The *PostPSA Filter* actor allows such refinements, which will be described in the following.

Neutron damage correction

AGATA is basically an instrument for high resolution spectroscopy and, therefore, good energy resolution is a fundamental aim of the instrument. Moreover, a good energy resolution is of great importance to clearly disentangle the two components of a gamma-ray transition caused by the Plunger. First of all a precise energy calibration was provided in the preprocessing stage. However several detectors presented in their segments a significant tail on the lower energy part of the gamma-ray peak as a consequence of the detectors exposition to fast neutrons during the previous experiments (see Fig. 3.3 and the impact discussion in Section 2.5.2). Thus spoiling the resolution of affected detectors and the global resolution when the detector are summed up. At this stage, the energy deficit (that is basically a charge collection deficit in the integration time) can be corrected using the position information obtained by the PSA [63]. For that the program *SortPsaHits* [72] is used. This program applies to the PSA hits a grid of correction parameters for the electron and hole trapping, determining the optimum set parameters for all the detector channels that minimizes the FWHM and the tail on the left side of the energy peaks in the spectra. For this experiment, crystals in positions 04B, 04C, 11A, 11C, 12A, 12C, 13A have been corrected. The

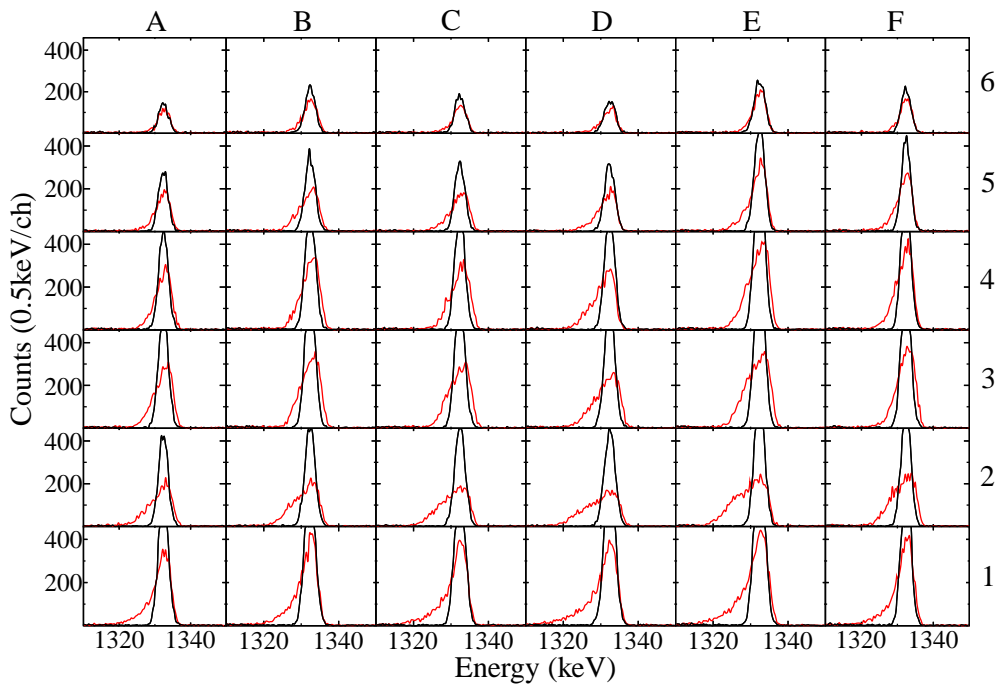


FIGURE 3.17: *PostPSA: Neutron damage correction.* Spectra of the 1.3 MeV gamma-ray transition in ^{60}Co for the segments of crystal 12A before (red) and after (black) the correction of the neutron damage effects.

correction was derived from the ^{60}Co calibration runs performed before the experiment. An example of the correction for one of the detectors is shown in Fig. 3.17. The correction is shown for the segment signals, but it is also done for the signals from the central contact. Nevertheless, the effect of the charge trapping on the electrons collected at the central contact is much less than on the holes collected in the segment contacts.

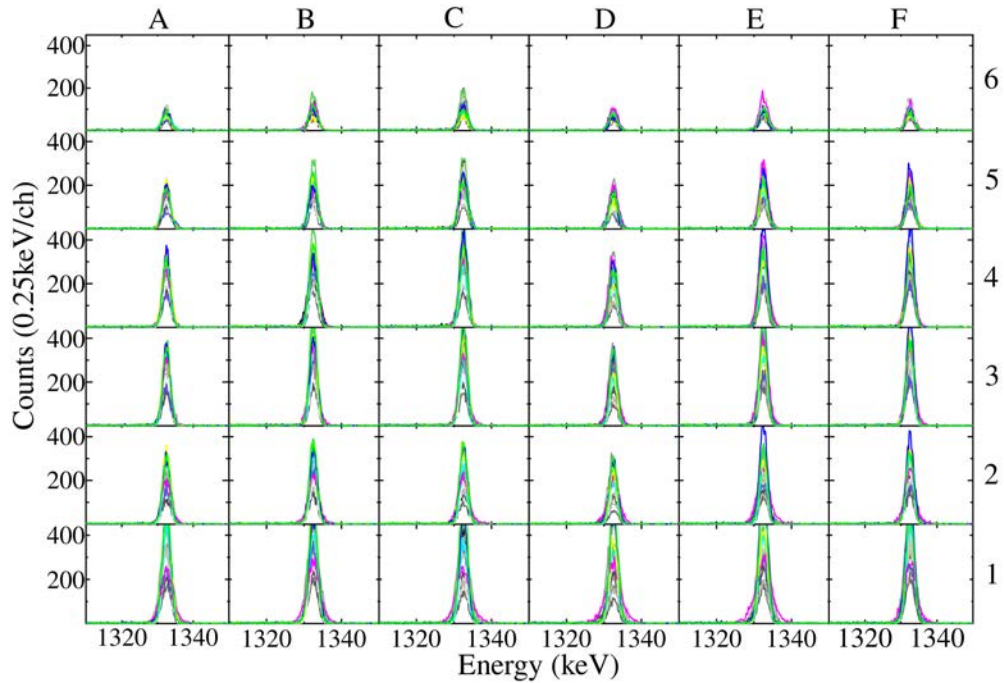


FIGURE 3.18: *PostPSA: Segments after the neutron damage correction.* Spectra of the 1.3 MeV gamma-ray transition in ^{60}Co for all AGATA detectors after the neutron damage correction of the affected detectors.

The line shape of the segments for the 23 detectors after the correction of the damaged ones is depicted in Fig. 3.18. One can appreciate the improvement of the energy resolution by comparing this figure with Fig. 3.3. The original energy resolution can be recovered up to a certain level due to statistical fluctuations caused by the trapping effects [63]. The average FWHM of the energy sum of segments in the affected detectors improved by around 33% becoming 3.4 keV. In the case of the cores, which are less sensitive to neutron-induced traps, the improvement of the average FWHM (4.1 keV) for the damaged detectors is about the 16%. The FWHM before and after the neutron damage correction for both cases are reported in Table 3.1. In addition, detector 11C had electronic noise, which can be appreciated from the broad resolution measured, especially for the core energy. In the latter case not improved after the correction due to electronic noise. An evaluation of the resolution for the sum energy of segments and the energy of the

central contact for each crystal is presented in Chapter 6.

TABLE 3.1: FWHM of the sum energy of all the segments and the core energy before (SumSeg, Core) and after (SumSeg_{NC}, Core_{NC}) the neutron damage correction, measured at 1.3 MeV peak of ⁶⁰Co. Only those detectors that needed the correction are reported in the table. *The broad resolution in detector 11C is ascribed to electronic noise.

Crystal Position	FWHM (keV)			
	SumSeg	SumSeg _{NC}	Core	Core _{NC}
04B	4.297	3.244	4.208	3.527
04C	4.656	3.299	4.029	3.304
11A	4.344	3.207	4.005	3.661
11C *	4.936	4.006	8.429	8.142
12A	3.978	3.096	3.839	3.221
12C	6.017	3.803	4.139	3.157
13A	3.536	3.126	3.719	3.378
Average	4.538	3.397	4.624	4.056

Energy recalibration

The calibration coefficients for the energy sum of segments and the central contacts can be refined in the PostPSA level. This is very important in our experiment to ensure a good energy resolution when all crystals are summed up. The final energy recalibration is shown in Fig. 3.19. Detector 11C showed a resolution problem, in both core and segments, which was ascribed to electronic noise. Another action

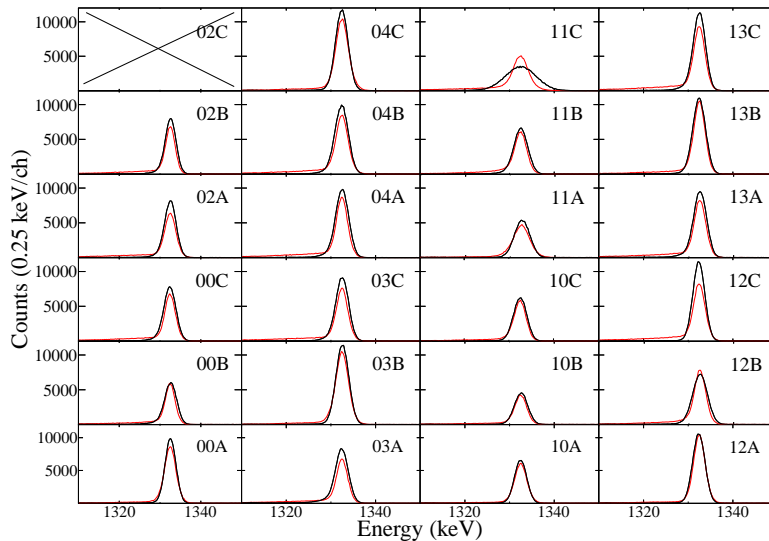


FIGURE 3.19: *PostPSA: Energy recalibration for the energy sum of segments and the core.* Spectra of the 1.3 MeV gamma-ray transition in ⁶⁰Co for all AGATA detectors. The black lines are the energy signals from the cores and the red ones, the energy signals from the sum energy of segments. The detector in position 02C was physically present but not operational.

that can be (optionally) performed at this level is the renormalisation of the sum energy of all segments to the energy measured in the core contact with the option `ForceSegtoCore`. This action reduces effects of not proper functioning of some of the segments. Additionally, it helps to mitigate the impact of neutron damage in cases where the correction can be only partially applied. However, the disadvantage is that at high counting rates the core signal suffers more pile-up than the segments. In our case the usage of the sum of the segments is the suitable option since clearly it improves the FWHM of the peaks in comparison with the cores in the source measurements. This effect is observed in the measurements with beam too. For more details about the comparison of the performance see Chapter 6.

Global time alignment

The alignment of crystals and other detectors is important to reduce random coincidences. This is the last step in the AGATA time alignment and, although it is performed in the global level where all the crystal data are put together, the alignment coefficients are given in the PostPSA level. For the global alignment a time matrix is built with the time difference between each combination of detectors. After getting the time position of all the pairs of time peaks, the optimal time shift for each detector is calculated by the program `SolveTT.py` [72]. The overlap of all time combinations between detectors is presented in Fig. 3.20, where the improvement in the FWHM after the alignment can be appreciated.

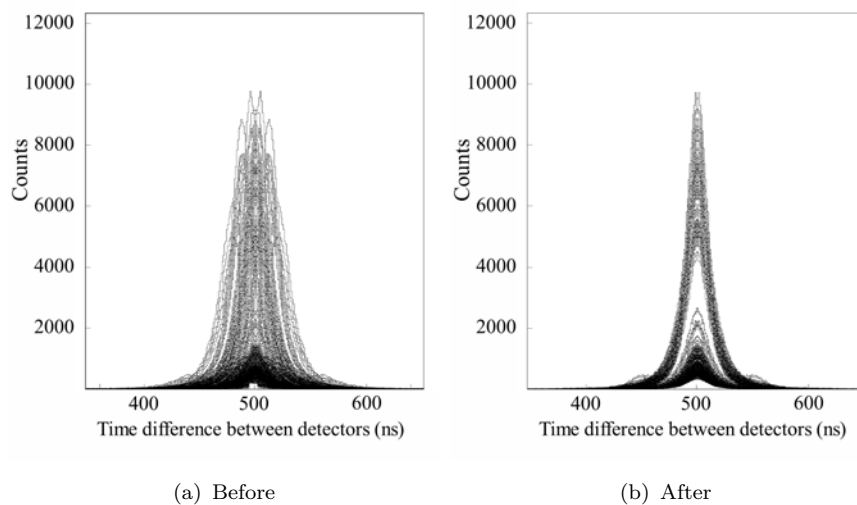


FIGURE 3.20: *PostPSA: Overlap of all the time combinations between crystals for the global time alignment.* The FWHM of the common time spectrum before the alignment 43 ns (a) and after the alignment 28 ns (b).

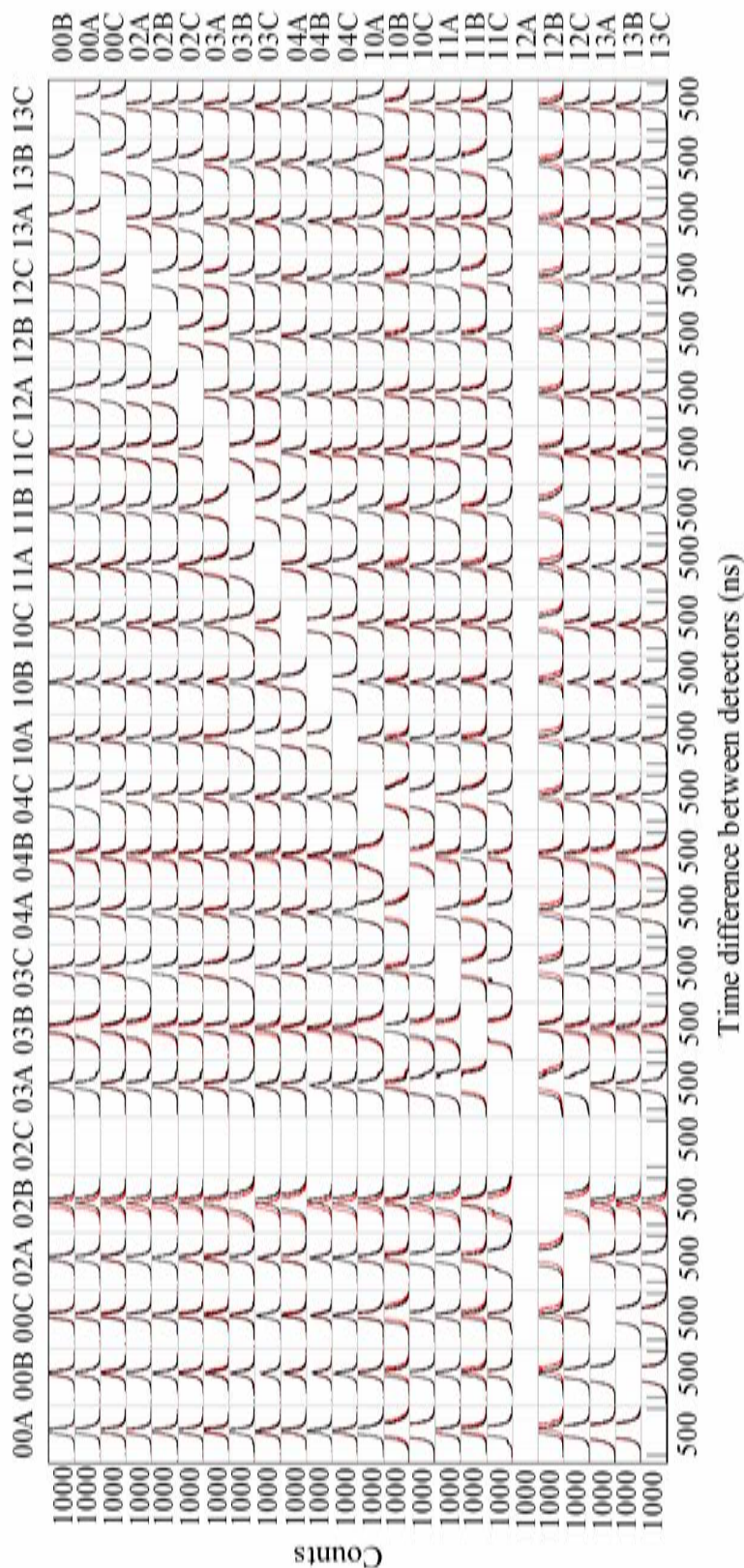


FIGURE 3.21: *PostPSA: Global time alignment.* Time dispersion matrix of the time difference between each combination of detectors. The empty diagonal corresponds to the time difference of a detector between itself. The empty “cross” corresponds to the detector in position 02C, which was physically present but not operational. The red and black spectra are before and after the global time alignment, respectively.

Fig. 3.21 shows the time matrix with the time difference between each pair of crystals before (red) and after (black) the global time alignment.

3.1.2. The Global Level

As illustrated in Fig. 3.1 the Global level actors for a setup with complementary detectors are the Event Builder, Event Merger and the Tracking Filter.

3.1.2.1. Event Builder and Merger

All the information processed independently in the Local level is built together for the final step, which is the reconstruction of the gamma-ray trajectories using a tracking algorithm. The first step is to assemble the event fragments from the AGATA crystals participating to the same event. This action is carried out by the *Event Builder* actor. The output is merged with the complementary detectors events (in this case, VAMOS++) by the *Event Merger* actor into complete events for further processing.

In both cases, builder and merger, the data are selected by the actor according to the timestamps. The events can be selected within a window of timestamp differences in order to eliminate uncorrelated events. In the builder case, events have been constructed using all the data from the crystals within a time window of 1 μs . In the merger case, events are build forcing the coincide between AGATA and the ancillary detector within a 2.5 μs window.

3.1.2.2. Tracking Filter

The reconstruction of the gamma-ray path inside the AGATA array is performed by the *tracking* filter actor. Fig. 3.22 shows the first reconstructed interaction point for each event. The information of the first interaction position inside the AGATA sub-array will be used for the Doppler correction.

The principles of gamma-ray tracking were introduced in Chapter 2 as well as the different tracking algorithms available. In this Thesis the Orsay Forward Tracking (OFT) code has been used. This code implements the forward tracking algorithm and depends on three empirical parameters σ_θ , P_{sing} and P_{track} . Their description

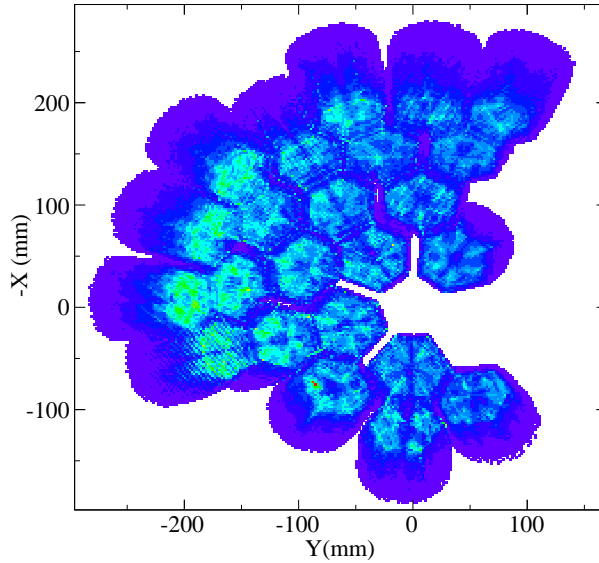


FIGURE 3.22: *Tracking: First Interaction pattern.* First interaction position of the gamma-rays inside the AGATA sub-array. The configuration of the 8 triple AGATA clusters (23 detectors) present in the setup of this experiment can be appreciated from the reaction chamber point of view. Axis in the AGATA laboratory frame. See AGATA coordinates in Fig. 3.45.

was given in Section 2.5.3. In order to enhance the peak-to-total ratio and the efficiency performances a series of tests have been done in order to choose the optimum combination of those parameters according to the goal of the experiment. The test analysis of the tracking capabilities have been applied to the 1332 keV transition of the ^{60}Co source.

The evaluation of the OFT parameters has been done varying each one within its typical ranges [18] and keeping the other two parameters fixed to standard values ($\sigma_{\theta}=0.8, P_{track}=0.05, P_{sing}=0.05$).

In Fig. 3.24 the σ_{θ} parameter has been varied in the range 0.3-3. The maximum in efficiency is found at 0.8 mm while the P/T shows a smooth positive trend with increasing σ_{θ} . In Fig. 3.23 the P_{track} parameter has been varied in the range 0.02-0.05. The efficiency decreases moderately while the P/T increases. The parameter that affects most the efficiency and the P/T is P_{sing} , as it can be seen in Fig. 3.25. This parameter has been varied in the range 0.02-0.15. In this range one can observe that, as expected, a more restrictive singles-interaction acceptance leads to stable efficiency and increasing the P/T ratios.

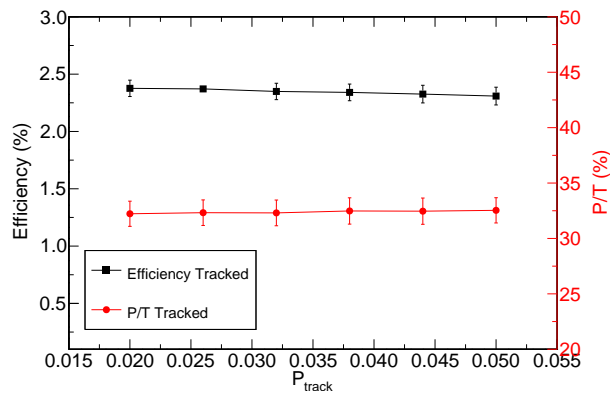


FIGURE 3.23: *Tracking: P_{track} parameter evaluation.* Influence of the P_{track} parameter on the efficiency and P/T in the range 0.02-0.05 ($\sigma_\theta=0.8$, $P_{sing}=0.05$). The black squares (red circles) show the trend of the efficiency (P/T) with the parameter variation.

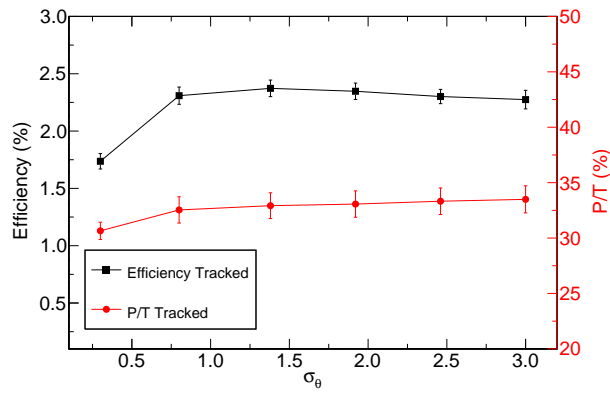


FIGURE 3.24: *Tracking: σ_θ parameter evaluation.* Influence of the σ_θ parameter on the efficiency and P/T in the range 0.3-0.3 ($P_{track}=0.05$, $P_{sing}=0.05$). The black squares (red circles) show how the efficiency (P/T) behaves with the change of the parameter.

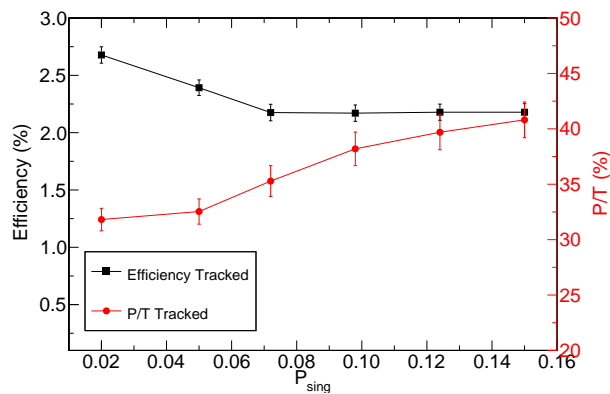


FIGURE 3.25: *Tracking: P_{sing} parameter evaluation.* Influence of the P_{sing} parameter on the efficiency and P/T in the range 0.02-0.15 ($\sigma_\theta=0.8$, $P_{track}=0.05$). The black squares (red circles) show how the efficiency (P/T) is affected by the parameter.

The final set of parameters selected in order to achieve the highest possible efficiency of 2.84(12)% maintaining a reasonable P/T ratio of 31.8(3)%. This choice corresponds to $\sigma_\theta=0.8, P_{track}=0.02$ and $P_{sing}=0.05$.

The tracking gamma-ray spectra and performance figures obtained with the final values for the OFT parameters in comparison with the different methods of data treating in AGATA are presented in Chapter 6.

3.1.3. GRID computing

GRID technologies allow that computers share through Internet or other telecommunication networks not only information, but also processing resources (GRID Computing) and storage capacity (GRID Data) [76].

In the early 21st century, the Large Hadron Collider (LHC) at CERN developed GRID technologies and infrastructures for high energy physics experiments in order to provide a resource to store, distribute and analyse the 15 petabytes (15 million gigabytes) of data generated every year. Such project has been extended to other disciplines and its infrastructures are becoming more stable and robust in the last years. This grid-based infrastructure is the most effective solution to the data-analysis challenge posed by experiments with huge amount of data production, offering many advantages over a centralized system[77].

The new generation gamma-ray detectors as AGATA produces a huge amount of data per experiment making difficult the data storage and slowing down the analysis in home institutes. Therefore the AGATA collaboration has adopted GRID as final storage and backup for the data and benefited from the GRID computing platform [78] for the AGATA data processing.

The AGATA GRID Computing uses the LHC layers or tiers structure [79] (Tiers-1 and Tiers-2). Tiers-1 provide permanent storage for the data reprocessing and analysis and Tiers-2 is used for simulations and end-users analysis. The two layers have similar roles in AGATA, but the Tiers-1 provide Tape Storage.

The GRID architecture is based on the gLite middleware [76], which provides a framework for the interaction between users and the resources. It is a set of components that provides the user with high-level services for scheduling and running computational jobs, accessing and transferring data, obtaining information on the

TABLE 3.2: List of services to access remote sources on the GRID.

Security	Authentication: Valid GRID certificate (CA) Authorization: Be registered in a Virtual Organization (VO)
User Interface (UI)	Access point to the to the remote computing resources through the certificate and the proxy created with the VO. Each user has its personal account.
Computing Element (CE)	Set of computing resources localized at a site (i.e. a cluster, a computing farm). It includes a collection of Worker Nodes (WNs), where the jobs are run.
Storage Element (SE)	Access to data storage resources. Controls simple disk servers, large disk arrays or tape-based Mass Storage Systems (MSS)
Information service (IS)	Information about the resources and their status.
Workload Management System (WMS)	Orchestrates the Job management on the GRID. It accepts user jobs, assigns them to the most appropriate CE, records their status and retrieves their output.

available resources, etc. The set of services to access remote sources is listed in Table 3.2. The AGATA Storage Elements (SE) and Computing Elements (CE) are distributed per tiers as shown in Table 3.3.

When an experiment is performed the AGATA data is placed at the storage sites of INFN-CNAF Tier-1 in Bologna and CC-IN2P3 Tier-1 in Lyon. The data can be also transferred to the storage sites of Tiers-2, keeping the original copy in the Tiers-1. To access and download data a certificate issued by a GRID Certification Authority (CA) is required. Furthermore the user must be a member of the AGATA virtual organisation (security requirements listed in Table 3.2) and should have its personal account in the User Interface (UI). All the information needed for obtaining the access to the AGATA GRID resources is contained in [76, 81].

TABLE 3.3: AGATA Storage Elements (SE) and Computing Elements (CE) on the GRID. The full path link for accessing the data can be found in Refs.[76, 80]

AGATA Storage Elements (SE)	
Tier-1	CC-IN2P3 (Lyon, France) INFN-CNAF (Bologna, Italy)
Tier-2	IPNL (Lyon, France) PNO (Orsay, France) IPHC (Strasbourg, France) IFIC (Valencia, Spain)
AGATA Computing Elements (CE)	
Tier-2	IPNL (Lyon, France) PNO (Orsay, France) IPHC (Strasbourg, France) IFIC (Valencia, Spain)

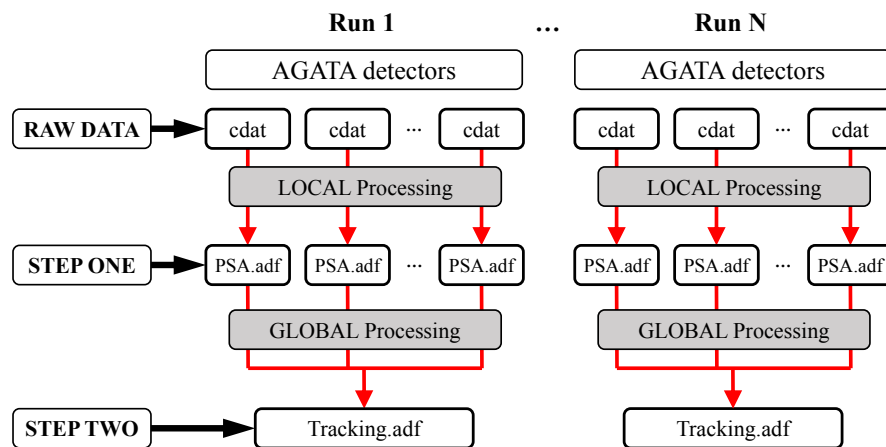


FIGURE 3.26: Scheme of the chain of NARVAL actors. Step one: local processing file by file to decompose recorded waves, PSA Algorithm. Step two: Global processing run by run to reconstruct the gamma-ray path ,Tracking Algorithm

The off-line data replay and processing on GRID proceeds similarly to the off-line data processing performed in a local computer. Nevertheless, the creation of additional bash scripts as well as small changes in the original source codes are required to directly interact with the GRID components. Once all the files are ready as specified in Ref. [81], the reprocessing is performed in two steps, PSA processing (Local level) and then gamma-ray Tracking processing (Global level). As depicted schematically in Fig. 3.26, the raw data are organized in a number of data sets, each data set corresponding to one run of the experiment, and contains (as a minimum) as much as data files as the number of the current Ge crystals used in AGATA. In the step one, each file of each detector of each experiment run is analysed in parallel in a computational job, making shorter the execution time of the pulse shape analysis. When this is done, from each original raw data file, one obtains a psa.adf file with reduced data. Step two (Fig. 3.26) will build and merge all the psa.adf files for each run into the tracking.adf file. In this step each run is analysed in parallel and the tracking algorithm is applied.

The data from the present experiment have been analysed using the GRID computing resources at IFIC (CE-IFIC). Before sending each bunch of jobs the data have always been transferred to the SE at IFIC, Lustre [82]. This provides direct access to them using the Lustre file system and improves the efficiency and the execution time of the jobs [76].

The AGATA data processing and jobs management are described in detail in [76, 80]. Indications and file examples of how to run a replay on the GRID are presented in [81].

3.1.3.1. Example of Local level processing (PSA) on the GRID

Several tests up to the PSA stage (which is the most demanding part of data replay, first step in Fig. 3.26) have been done in order to compare the GRID processing with a normal computer in terms of data replay time. The data set used was a calibration run of ^{60}Co with the data acquisition time of 15 hours and a total number of raw data files (cdats) of 246. The original data files were stored on tape at the Tiers-1 INFN-CNAF and CC-IN2P3 sites. The ^{60}Co data set was transferred to the SE at IFIC, Lustre.

TABLE 3.4: Comparison of different types computing resources in terms of data replay time for AGATA data local level processing (PSA). The set of ^{60}Co calibration data used for this test contained 246 cdat files with a total size of 842Gb for an acquisition time of 15 hours. On the GRID, the data access (SE) was Lustre and the site (CE) IFIC.

Computing	Time of execution
Desktop machine 1 job (1 core)	~2.5 d
Server 23 jobs (20 cores)	~5.5 h
GRID 246 jobs (~100 cores available)	~1-2 h

The same data sorting (replay) was performed with three different computing resources, as described in the following. The first replay was done in one job in one single CPU or core. The second replay was made, distributing the same data into 23 jobs (one per detector) spread over 20 cores in a larger CPU workstation. Finally, the third replay was performed distributing the same data over 246 jobs (one job per cdat file) in a total number of 100 cores available in the GRID infrastructure at IFIC at the moment of the execution. The time execution in each case is shown in Table 3.4. The results of the test clearly indicate that running a Local level replay on the GRID is much more efficient in terms of execution time than running sequentially on a desktop computer, particularly when a large amount of data needs to be processed.

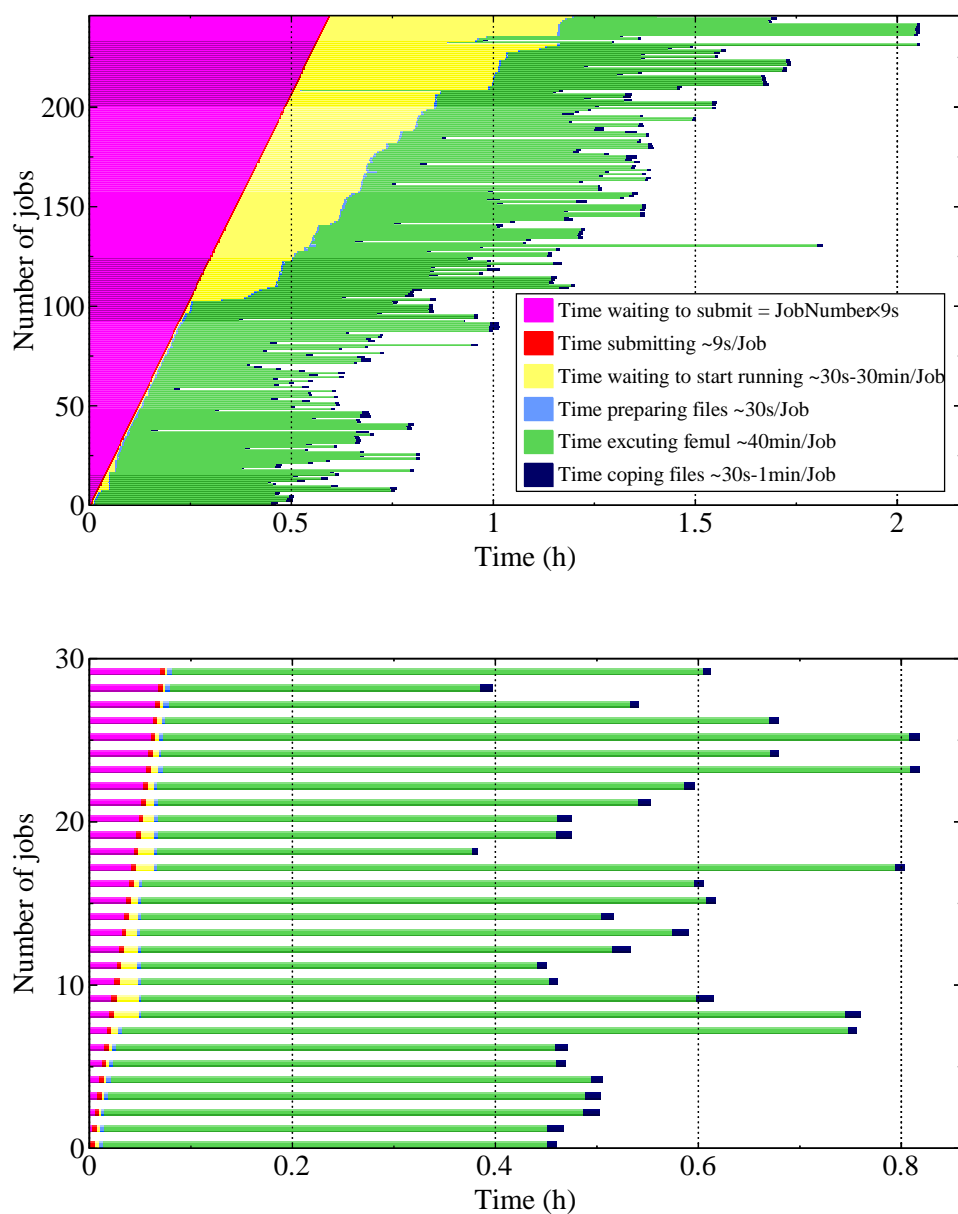


FIGURE 3.27: Test of AGATA data processing on GRID using a set of ^{60}Co calibration data with an acquisition time of 15 hours (246 cdat files with a total size of 842Gb). Top panel: Evolution of the execution of jobs with the time for the 246 jobs submitted. Bottom panel: Zoom of the top panel showing jobs status at a given time of the 30 first jobs submitted. In the legend the average timing estimation for each status of the job is given.

Fig. 3.27 shows the evolution with time of the number of completed GRID jobs. The 246 jobs are submitted sequentially. It takes 9s to submit a job on the GRID (red colour) and thus, the next job has to wait 9s multiplied by the number of jobs already submitted to be submitted (see evolution of the pink colour). After the job is submitted, the time for starting to run the jobs depends on the numbers of

available cores on the GRID. This waiting time is coloured in yellow. In the top panel of Fig. 3.27, one can appreciate that for the first hundred jobs the yellow part is very small, but increases after them. This is due to the number of available cores was around 100 and the remaining jobs are queued until any core becomes free again. The light blue, green and dark blue colours indicate the running time of execution of the job. The more time consuming part of the running status of the job is the PSA analysis performed in the replay with the femul NARVAL emulator, which lasts around 40 minutes per file.

3.1.3.2. Example of a full experiment processing (PSA+tracking) on the GRID

The AGATA data from the present experiment have been fully processed on the GRID. A total amount of 3.9 Tb raw data was collected and stored on tape at the Tiers1 INFN-CNAF and CC-IN2P3 site. From there the data was copied to the SE, Lustre, located at IFIC to perform the data processing in the CE IFIC. The data replay was carried out in two steps as depicted in Fig. 3.26. For the Local level processing (up to the PSA stage) 1651 jobs were submitted. Using the Adaptive Grid Search algorithm each raw data file was processed individually in less than 12 hours. Few jobs were found in error and had to be relaunched, being finished in 1.5 hours. For the next step, the Global level processing (OFT tracking algorithm used) 44 jobs were submitted and executed without errors in short time. A summary of the GRID processing is presented in Table 3.5.

TABLE 3.5: Comparison of different types of AGATA data processing on GRID in terms of data replay time for the present experiment (3.9 Tb). AGATA was composed of 23 crystals and the counting rate per crystal was around 50 kHz. The data access on GRID (SE) was Lustre and the site (CE) IFIC.

Process	PSA	Tracking
Jobs submitted	1651	44
Cores available	~100	~200
Jobs failed	78	0
Time of execution	~10 h	~1h 33m

Running the complete experiment data set (PSA+tracking) on GRID lasted less than 2 days. This procedure allows the reprocessing of the raw data at any time in case of new processing conditions (new or updated algorithm or version for example) faster and more efficiently than the local computers, without losses in the original information [76].

3.2. The VAMOS++ data processing

The VAMOS++ spectrometer is used for the identification of the reaction products in terms of atomic number (Z), mass number (A) and charge state (q) on an event-by-event basis. The VAMOS++ detection system was described in detail in Chapter 2. The measured information for each detected particle in the VAMOS++ spectrometer is the following:

- Ion transversal positions at the entrance of the spectrometer (DPS-MWPC): $X_{1,2}, Y_{1,2}$.
- Time-of-flight of the ions between the first MWPC at the entrance position (t_{start}) and the MWPPAC in the focal plane (t_{stop}): ToF .
- Ion positions at the focal plane (DC): $X_{1,2,3,4}, Y_{1,2,3,4}$.
- Partial and total energy loss in the IC: $\Delta E, E$.

With this information an event-by-event particle identification based on the reconstruction of its trajectory [42] is obtained through the steps schematically illustrated in Fig. 3.28.

The positions measured in the DPS-MWPC allow one to determine the vertical and horizontal positions, X_t and Y_t , and the angles, θ_t and ϕ_t . These parameters define the ion trajectory at the target position. With the vertical and horizontal positions measured in the drift chambers, X_f and Y_f , and the angles, θ_f and ϕ_f , the ion trajectory in the focal plane is determined. This information, in combination with the angular information at the target position, permit the reconstruction of each ion trajectory. The latter is defined by the magnetic rigidity, $B\rho$, and the path length, D (parameters in the boxes with dashed lines in Fig. 3.28). After this, the velocity v of the ions after the degrader can be calculated from the measured ToF and the reconstructed D , using $v = D/ToF$. On the other side, the energy deposited in the ionization chamber gives the partial energy loss, ΔE , and the total energy, E , of the ion which allows the Z number identification. The A_{raw} number is obtained from the measured parameters E and v . The mass over charge ratio, A/q , is derived from trajectory information using the equations of the motion of the charged particle in the magnetic field of the dipole to deduce the charge state, q . Finally, knowing the integer charge state, the A number is determined.

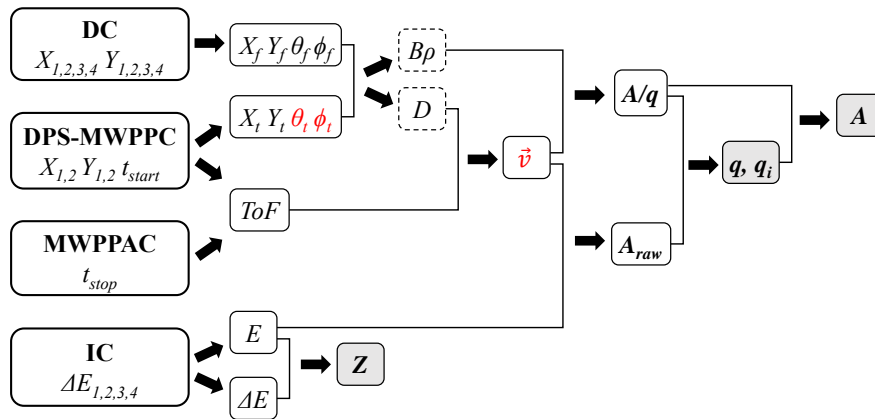


FIGURE 3.28: Scheme of the identification procedure in VAMOS++. The detectors and the steps along the identification procedure correlating measured quantities and reconstructed parameters are shown. The measured and calculated parameters are presented in solid line boxes; the reconstructed ones in dashed line boxes; and the parameters for the complete identification of the ion are given in the grey filled boxes. The parameters marked in red are used for the Doppler correction of the gamma-rays detected in AGATA.

These parameters uniquely identify the reaction products and are indicated in grey filled boxes Fig. 3.28. Moreover, the velocity and the angles at the target position (in red in Fig. 3.28) allow the Doppler correction of the gamma-rays detected in coincidence. Finally, the usage of the VAMOS++ magnetic spectrometer in combination with the RDDS technique allows to partially control the feeding from higher-lying states by setting conditions in the total kinetic energy loss or Q-value (see Section 3.3).

Next subsections discuss the calibration of the entrance and of the focal plane detectors of the VAMOS++ spectrometer, the procedure used for the trajectory reconstruction and the identification and characterization of the ions produced in the $^{92}\text{Mo}+^{92}\text{Mo}$ reaction of this experiment.

3.2.1. Calibration and event reconstruction

The first and probably most important step in the reconstruction of the trajectories and the determination of Z and mass A is the calibration of the VAMOS++ detectors. Electronic calibrations and pedestal corrections are done for each detector before the experiment starts using a Pulser Generator (Pulser) signal. These actions are useful for the on-line analysis and monitoring during the experiment.

well as volumes with different pressure in the gas detectors. This is schematically depicted in Fig. 3.29 for the focal plane detectors.

The individual calibrations for the entrance and focal plane detectors and the reconstruction of events will be shown in the next subsections.

3.2.1.1. Multi-wire entrance detectors (DPS-MWPC)

At the entrance position of the spectrometer the two position-sensitive MWPCs were placed providing the start time information and the $X_{1,2}$, $Y_{1,2}$ positions ($Z_{1,2}$ is the axis of the spectrometer) from which, knowing the relative positions of the two MWPCs and the target, it is possible to deduce the scattering angle and the interaction point on the target. This information is crucial for reconstructing the ion trajectory on an event-by-event basis (explained in Section 3.2.1.3) and for applying the Doppler correction (described in Section 3.3.1).

Firstly a calibration of the MWPCs channels has to be done in order to determine the ion entrance positions in the spectrometer. In (Fig. 3.30) the charge deposited in each channel of the MWPC1 and MCPC2 in X and Y position is depicted before and after the channel calibration. The MWPC1 contains 39 and 60 channels in X and Y wire planes respectively. The MWPC2 has 64 channels in X and 92 channels in Y . The channel 51 in Y plane of MWPC2 was broken during all the experiment.

The hit pattern of the ion entrance positions are shown in (Fig. 3.31) for each MWPC. The difference in the size of the two detectors can be appreciated in the figure. The broken channel is also visible in the right panel.

The next step is the determination of the scattering angles and the target position, which can be easily calculated as schematically shown in Fig. 3.32, using the relationship between the tangent and the sides of the triangle formed:

$$\tan\theta_t = \frac{X_2 - X_1}{Z_2 - Z_1}, \quad \tan\phi_t = \frac{Y_2 - Y_1}{Z_2 - Z_1}. \quad (3.1)$$

However, the detectors efficiency working together dropped along the time due to the increase of events with signal absence in one of the two detectors with the time. This fact, affected considerably the statistics of the ions after the trajectory reconstruction towards the end of the experiment. Therefore, in order to improve

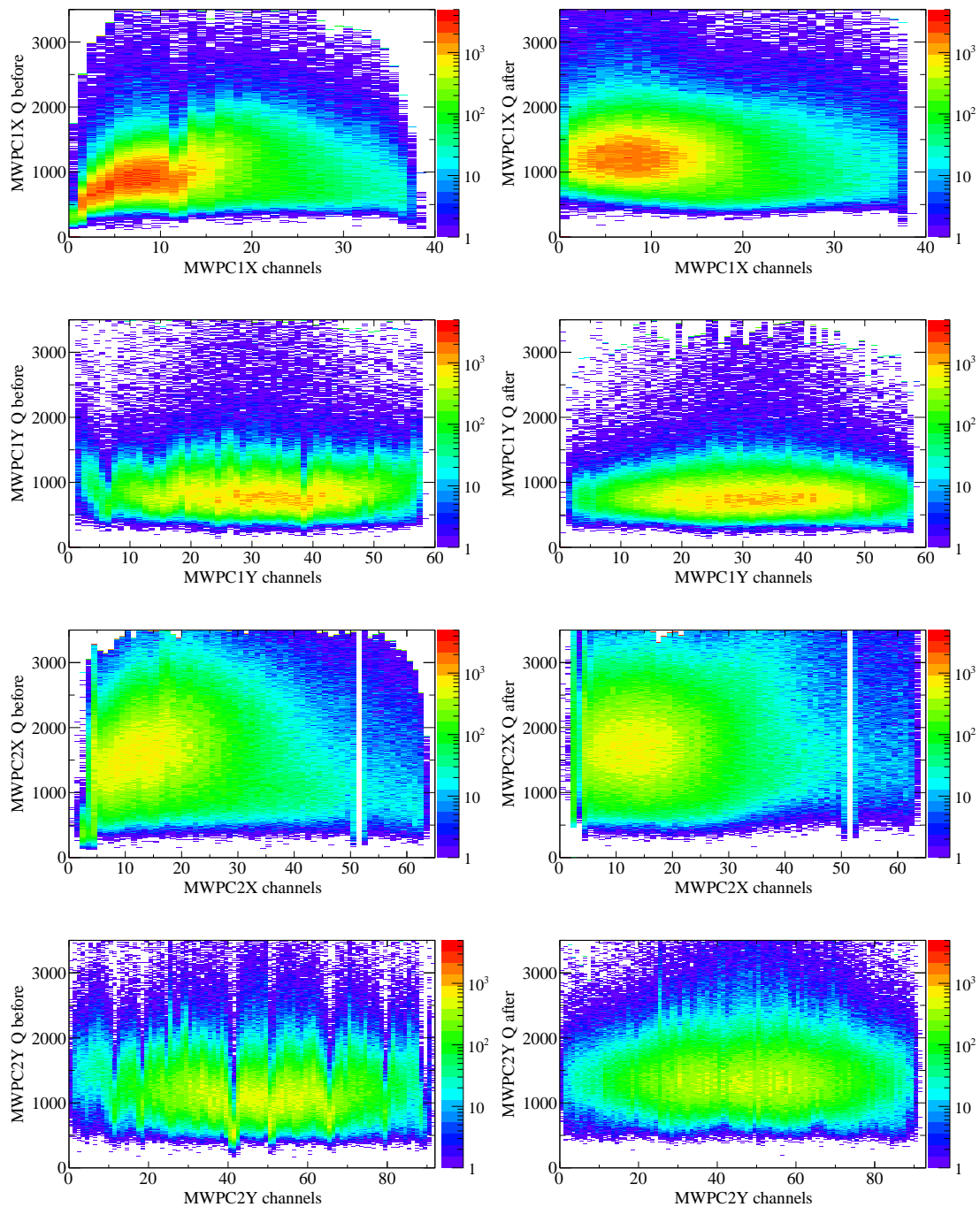


FIGURE 3.30: *DPS-MWPC: Charge calibration.* Gain matching of the charges for all the channels of the X and Y wire planes in the first (four top panels) and second (four bottom panels) MWPC. Left panels are before the calibration and right panels after.

the situation, events for ions arriving at the focal plane of the spectrometer when there were no signals coming from one of the detectors have been taken into account by means of average values at the target position. For signals missing in MWPC1

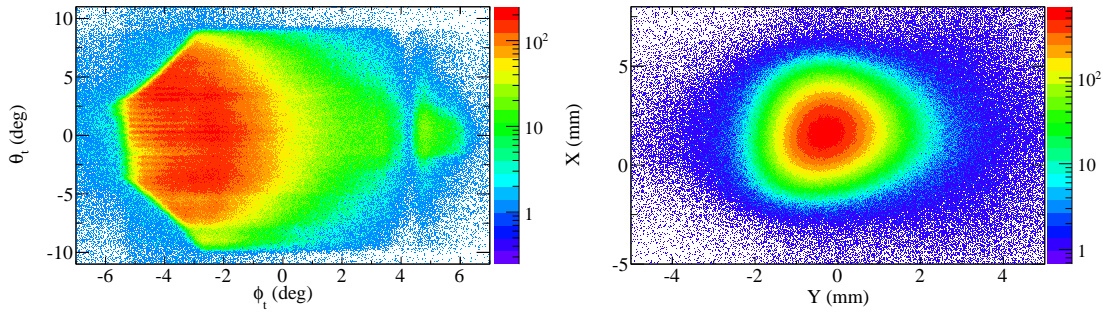


FIGURE 3.33: *DPS-MWPC: Scattering angle and the interaction point on the target.*

3.2.1.2. Multi-wire focal plan detector (MWPPAC)

As described in Chapter 2 the MWPPAC detector is divided into 20 sections (distributed as illustrated in 3.28) on the X-plane giving time signals individually. These signals are used for the ToF measurement of the ions detected in VAMOS++. The ToF is the difference between the time measured in the first MWPC and the MWPPAC time signals. The signal of each section may be affected by an offset of few ns, which is enough to introduce a systematic error in ToF and consequently in the mass identification. Therefore, an offset has been added to the ToF measured at each section using the mass number over the charge state (A/q) ratio, which is more sensitive to small shifts in the ToF. The ratio is given in detail in Ref. [42],

$$\frac{A}{q} = \frac{B\rho c}{3.105D\gamma}ToF, \quad (3.4)$$

where the radius ρ and the trajectory length D are reconstructed from the information provided by the DPS-MWPC (mentioned before) and the position in the focal plane provided by the DC (see next section), while B is the dipole magnetic field set in the spectrometer.

In addition, to reach the maximum mass resolution further corrections were performed to avoid aberrations in the ion trajectories produced by the magnetic multipole or fringe fields. These corrections are based on a complex dependency of several parameters ($Y_f, \theta_f, \phi_f, \theta_t, \phi_t$) and were applied following the recipe established at GANIL based on many previous similar experiments with VAMOS++. In Fig. 3.34, the A/q ratio as a function of the focal plane is depicted before and after the ToF alignment.

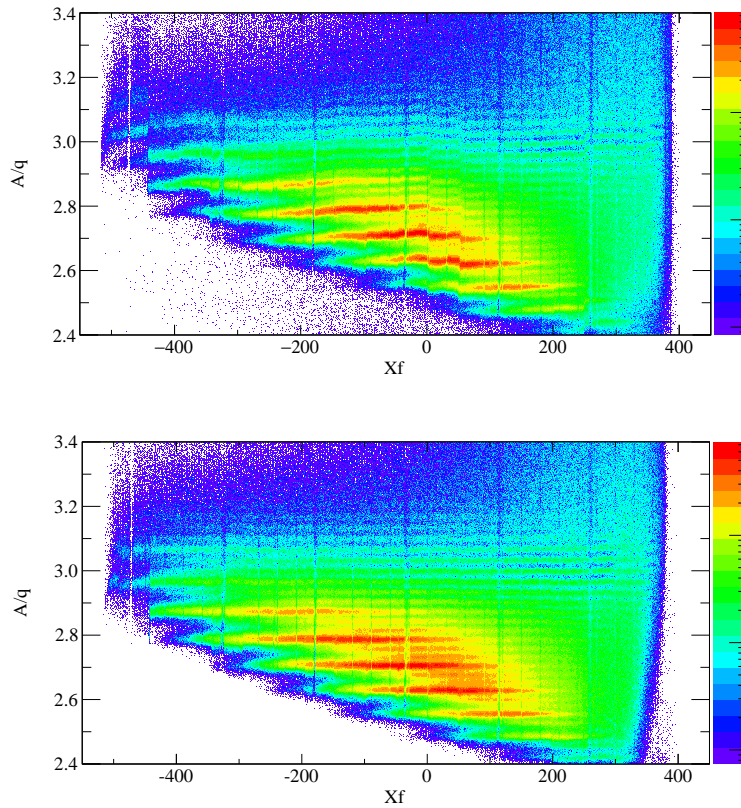


FIGURE 3.34: *MWPPAC: ToF alignment.* A/q ratio as a function of the X focal plane position for the ToF alignment. Top panel: Before the ToF alignment and aberrations corrections. Bottom panel: after the ToF alignment and aberration corrections.

3.2.1.3. Drift Chambers (DC)

The focal plane Drift Chambers contribute to the reconstruction of the ion trajectory by means of the measured coordinates $X_f, Y_f, \theta_f, \phi_f$. This is crucial for the mass identification and therefore it is very important to avoid the gain misalignment for any channel, which will affect the trajectory reconstruction. As explained in Chapter 2, two DCs divided in two were present in the setup with 160 pads per division (see the scheme in 3.28), each providing a position measurement. On one hand, the vertical positions ($Y_{1,2,3,4}$) are determined from the drift time of the electrons, which are converted into distances using the drift velocity of the electrons inside the gas. On the other hand, the horizontal positions ($X_{1,2,3,4}$) are determined according to the charge deposited on each pad. In order to have the same deposited charge for creating always a signal of equal amplitude, it is necessary to align the gain of all the channels.

In Fig. 3.35, the charge deposition is shown before (left) and after (right) the gain matching, as a function of the DC pad identifier, for the four DCs.

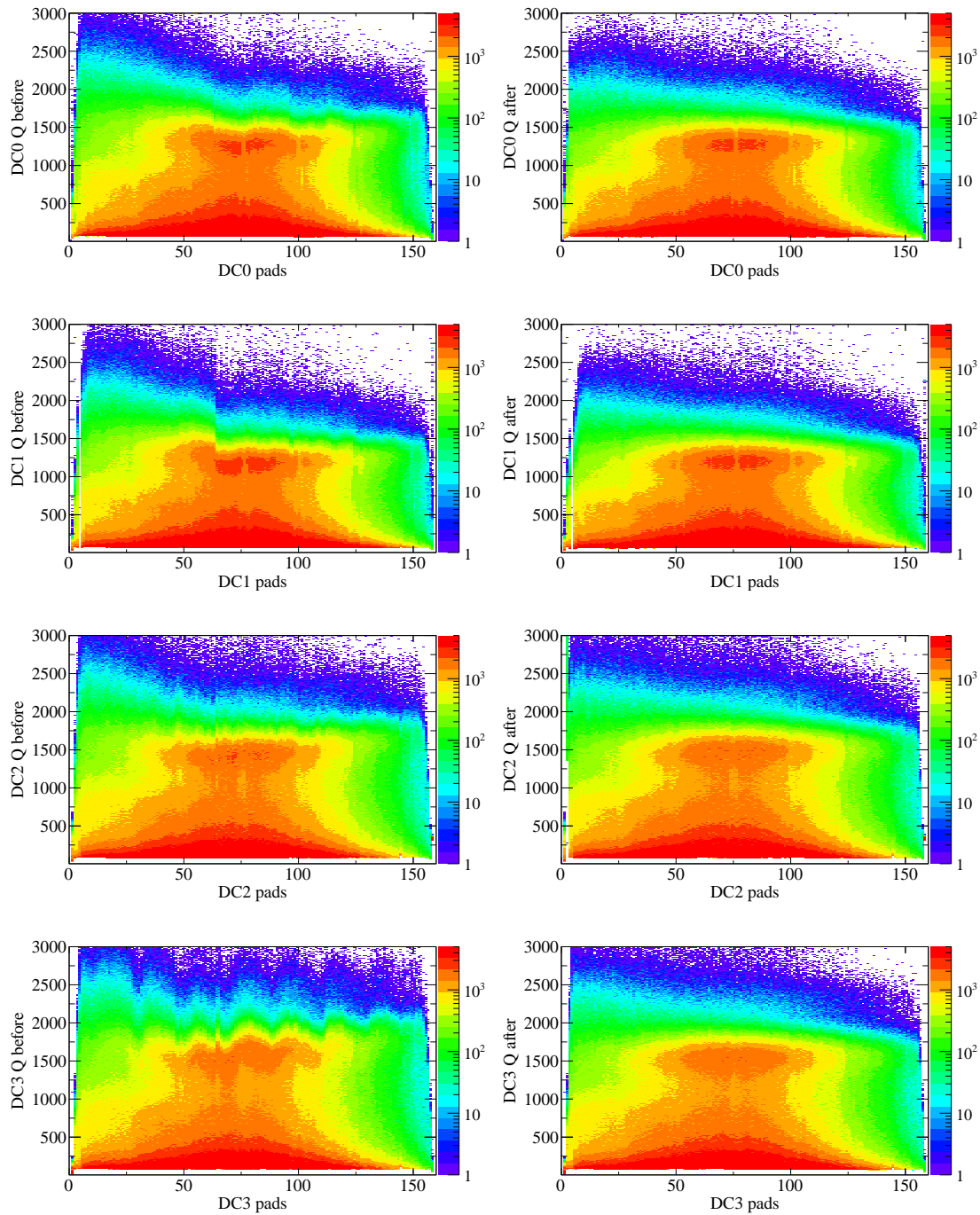


FIGURE 3.35: *DC: Charge calibration.* Gain matching of the charges for all the channels of the 160 pads in the four drift chambers. Left panels are before the calibration and right panels after.

After doing the gain matching for every channel, the algorithm for reconstructing the trajectories inside VAMOS++ has been applied. This algorithm requires a

precise measurement of the final position and angle to retroactively reconstruct the full trajectory of the particles through the electric and magnetic fields using a transformation matrix [42]. When the trajectory of the ions is reconstructed it is possible to obtain the magnetic rigidity $B\rho$ and the length of the trajectories l . Using the reconstructed information the angles at the entrance position and focal plane, the distance for the ToF measured is given by:

$$D = l - \frac{17.40}{\cos(\phi_t)/\cos(\theta_t)} + \frac{764.52 - 760}{\cos(\phi_f)/\cos(\theta_f)}, \quad (3.5)$$

where 17.40 cm is the distance between the target and the first MWPC and 4.52 cm is the distance between the focal plane and the MWPPAC.

3.2.1.4. Ionization Chamber (IC)

The Ionization Chamber provides two fundamental informations, the total energy of the ions (after the losses in the previous detectors and windows) and, taking advantage of its segmentation, it provides as well the $\Delta E/E$ information that allows to obtain the atomic number Z of the ion. While to have good Z resolution is important that the Bragg peak of the arriving ions is mostly covered by the IC, for both, the measurement of the total energy (E) and the energy loss (for the ΔE determination) of the ions, a good energy calibration and alignment among the 20 pads is necessary (schematic view of the IC sections and rows in 3.28).

Firstly, a series of thresholds per IC section are setted in order avoid events triggered by the noise. Low thresholds have been applied to remove the pedestal of the ADCs. High thresholds have been used to avoid pile up and contaminations in the element identification. Moreover, a cut as a function of the focal plane has been performed to reject the pile up of beam or target/degrader ions. This is exemplified in 3.36 for the sections in the first row of the IC.

Once the thresholds are established, the gain matching in energy can be done. The gain matching between sections of the same row as a function of the energy is shown in the right part of Fig. 3.37.

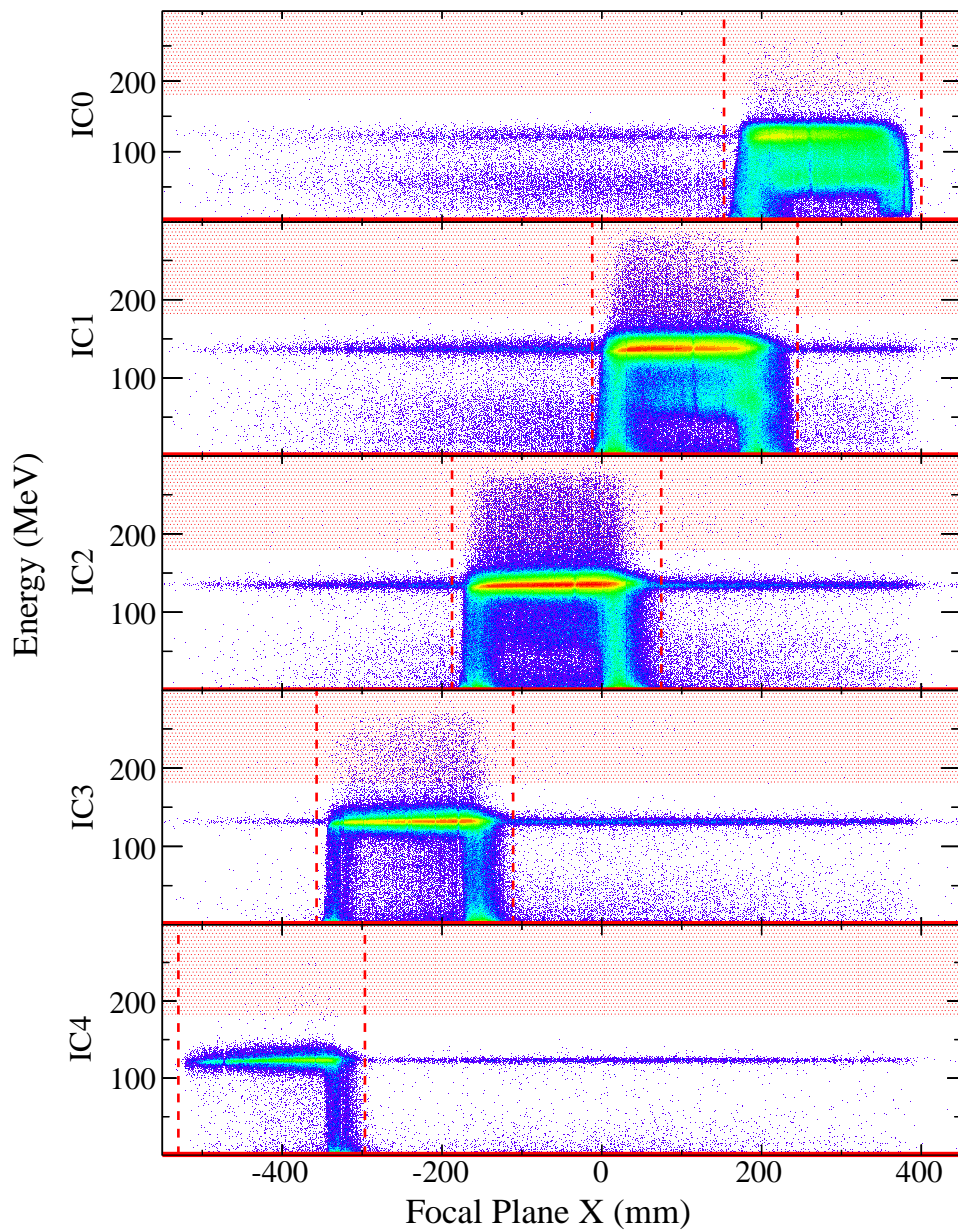


FIGURE 3.36: *IC: Thresholds first row.* Example of the threshold setting using the energy spectra for the first row of the IC versus the X-focal plane position. The red area are the low (pedestal) and high thresholds. The dashed lines delimit the lower and upper limits of the good events.

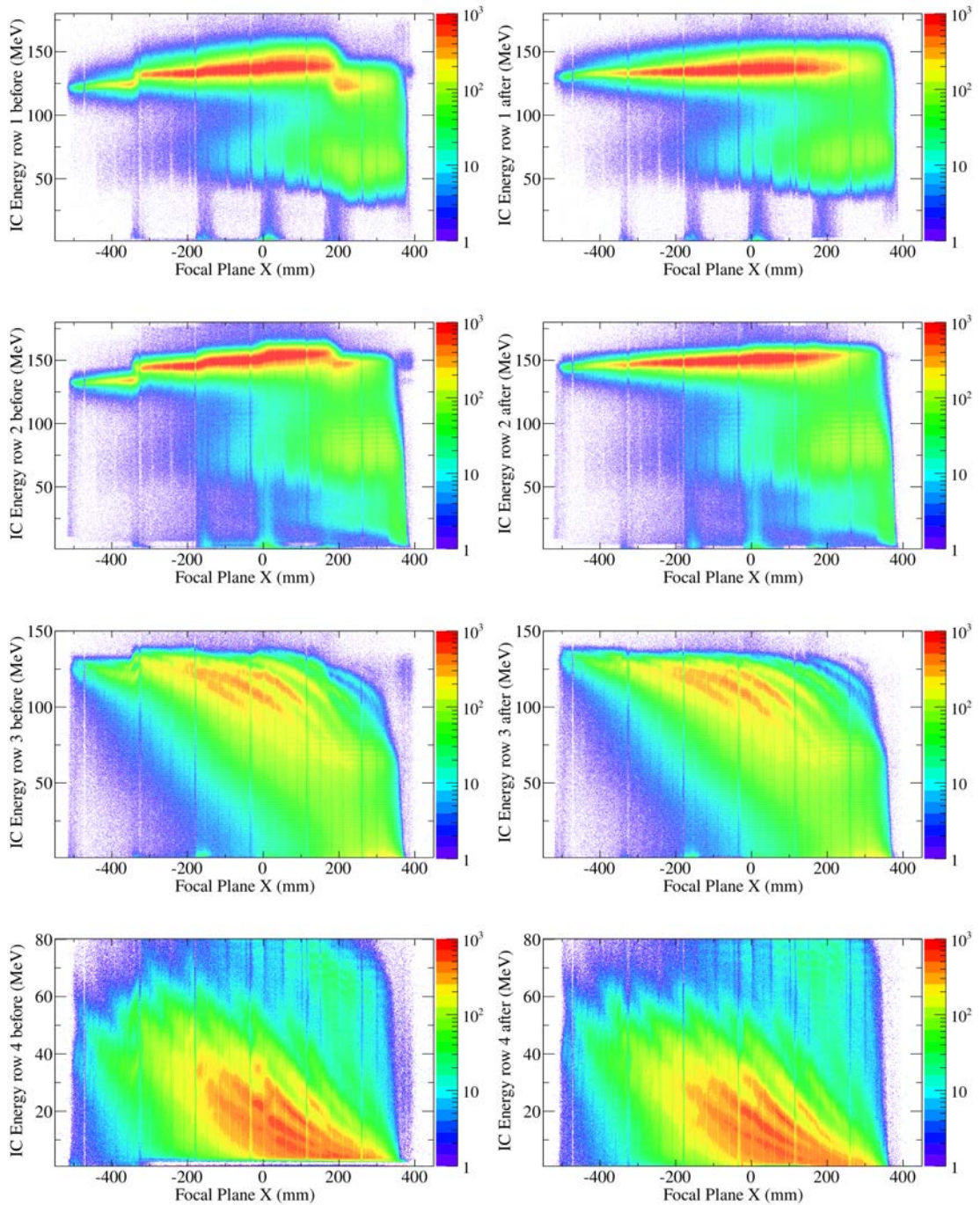


FIGURE 3.37: *IC: Gain matching.* Gain matching of the energy of the IC sections per row after applying the thresholds (see text for details). Left panels are before the calibration and right panels after.

After the alignment and calibration is possible to extract a meaningful Energy loss ΔE and Total Energy E , that as mentioned before provides information for the ion identification. The identification of the atomic number Z and charge states will be discussed in Section 3.2.2.

Additionally, a gain correction as a function of time had to be introduced, since the energy signal of each IC section was fluctuating from the beginning up to the end of the experiment as illustrated in Fig. 3.38. This fact could deteriorate the atomic number resolution.

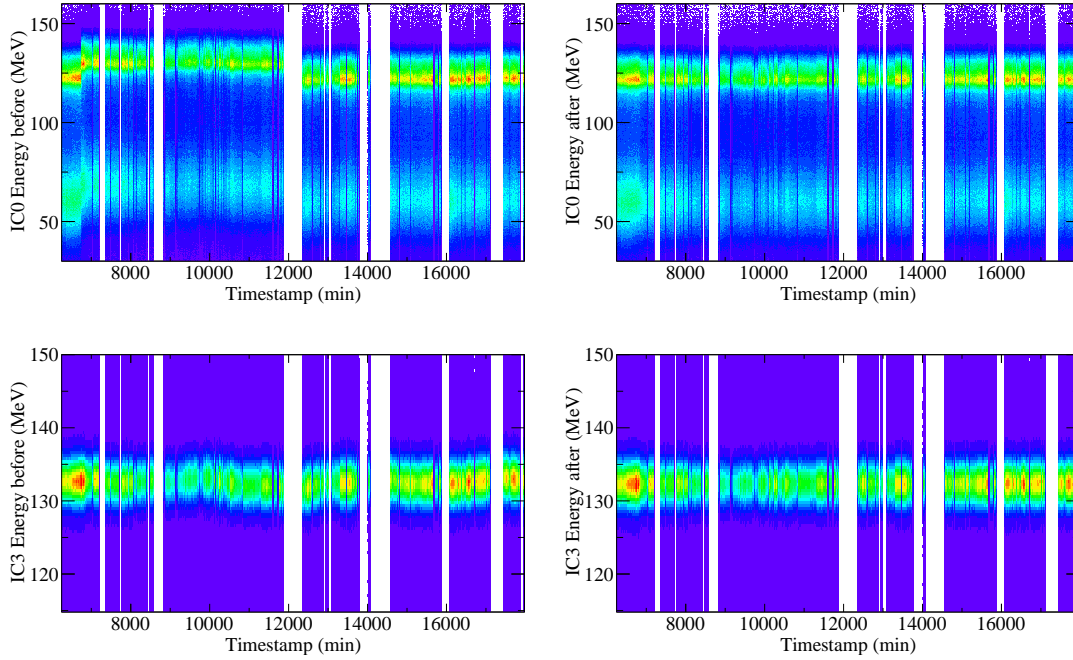


FIGURE 3.38: *IC: Energy evolution in time.* Left panels are before the alignment of the energy as a function of the time of measurement and right panels after.

3.2.2. The Particle Identification

The measured and reconstructed information previously described is used in a second step to identify the ion in terms of Z number, A number and charge state q (parameters inside the grey boxes in Fig. 3.28).

3.2.2.1. Atomic number

The Z number identification is done by means of the energy released inside the IC. The energy loss of a charged particle inside a matter is defined by the Bethe-Bloch equation [64] and to first order approximation is proportional to square of the atomic number Z :

$$\Delta E \propto \frac{Z^2}{E}, \quad (3.6)$$

where ΔE is the energy loss and E the total energy released in the IC detectors.

Different plots can be performed in order to identify the atomic number Z in the IC. Fig. 3.39 shows the energy loss (ΔE) vs. the total energy released in the IC. In the left panel of the figure the energy loss released in the two first rows of the IC is used while in the right panel only the energy loss released in the first row is used. In both plots, separated line structures corresponding to the reaction products can be seen. The Mo isotopes, $Z=42$, can be easily identified from the most intense line due to the elastic events. The other channels of interest, Zr and Ru isotopes ($Z=40$ and 44 respectively) are identified knowing that the release of energy ΔE increases with Z . In the left panel of Fig. 3.39 it can be appreciated that the separation of the two proton pick up becomes difficult because its energy is close to the Bragg-peak (left structure in the matrix), which is the maximum stopping power of the reaction products in the gas. Therefore, the configuration using only the energy released in the first row (right panel) which has a better separation of the Z lines structure has been used (see Fig. 3.29 for the IC sections configuration). The Z identification is done applying the mentioned condition on the 2D plot mentioned.

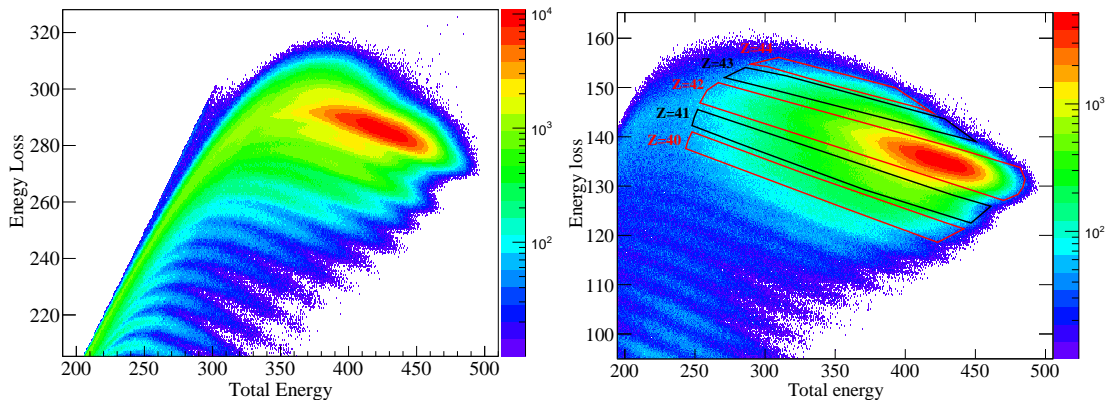


FIGURE 3.39: Energy loss as a function of the total energy released in the IC for the Z identification. Left panel uses the energy loss in the two first row of the IC while the right panel uses the only first one. The conditions selected in the latter case correspond to the Zr, Nb, Mo, Tc and Ru isotopes (from bottom to top, respectively). The isotopes of interested are marked in red. The relative intensity (which is proportional to the counts) is shown on the side bar in both panels.

3.2.2.2. Charge state

Once all isotopes have been determined by their atomic number (Z), the charge state identification can be done. Due to the presence of ions in several charge

states, different A/q values can be obtained for each reaction product with a defined A and Z . The A/q ratio is computed based on the relation given by:

$$\frac{A}{q} = \frac{B\rho}{3.105\beta\gamma}. \quad (3.7)$$

To evaluate the mass A_{raw} the total kinetic energy E and the velocity β are used,

$$A_{raw} = \frac{2E}{931.5(\gamma - 1)}. \quad (3.8)$$

And the charge state q is obtained from the relation,

$$q = \frac{A_{raw}}{A/q}. \quad (3.9)$$

By comparing the charge state q as a function of the A/q ratio, exact values for the charge states can be obtained for each element. In Fig. 3.40 shows the separation of the individual charge states in circular structures. The most intense blobs correspond to the inelastic channel (Mo). From that matrix one can extract the charge state information for each element by gating on each structure and assigning to it a integer value $int(q)$. This procedure has been done for each section of the MWPPAC. Fig. 3.40 shows one example for the section 7 (see Fig. 3.29 for the MWPPAC sections configuration).

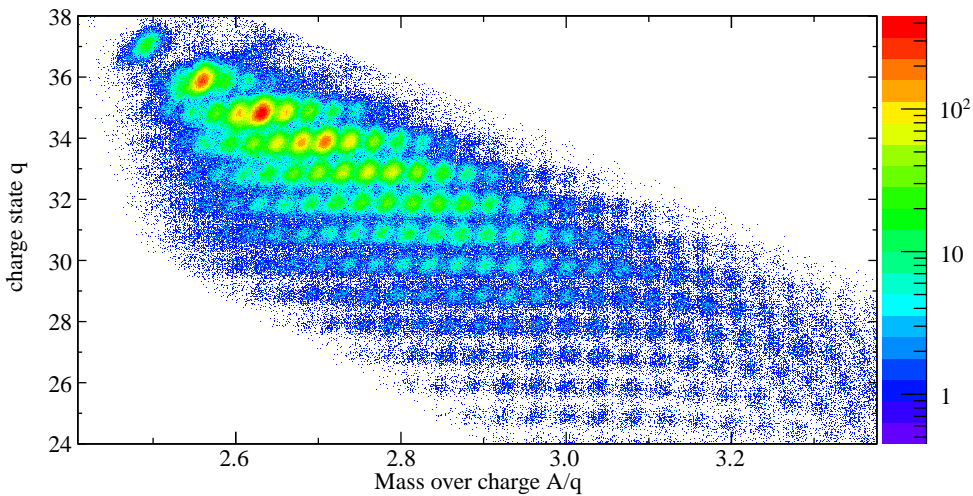


FIGURE 3.40: Charge states q as a function of the A/q ratio for the section 7 of the MWPPAC detector. A gate on each charge state have been performed on each section of the MWPPAC detector for the integer assignation of the charge state. The relative intensity (which is proportional to the counts) is shown on the side bar. The most intense spots correspond to the inelastic reaction channel ^{92}Mo .

3.2.2.3. Mass number

The conditions on individual charge states allow one to build the corresponding mass spectra by simply multiplying the A/q ratio by the integer charge state q :

$$A = A/q \times \text{int}(q), \quad (3.10)$$

The final mass distribution for the ions detected in the VAMOS++ focal plane is shown in Fig. 3.41. The mass resolution achieved in $A = 92$ after the corrections for aberrations is around 0.6%.

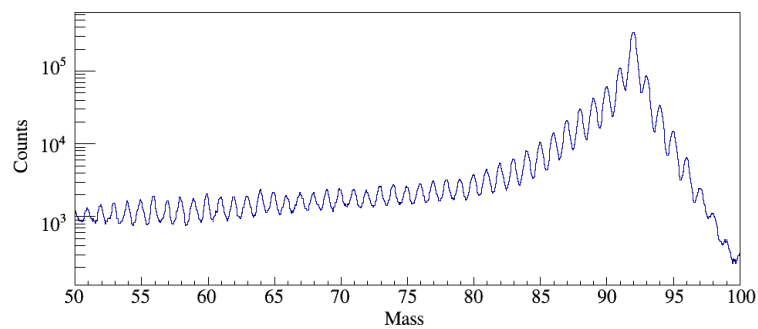


FIGURE 3.41: Total mass distribution for the ions detected in VAMOS++.

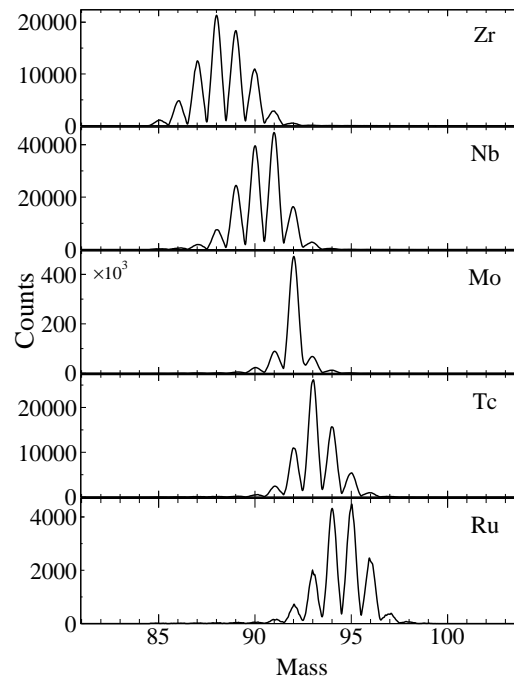


FIGURE 3.42: Mass distributions for the inelastic channel up to the $\pm 2p$ transfer channels.

By selecting the atomic number the mass distributions for each group of isotopes can be studied. The yield distributions for Zr, Nb, Mo, Tc and Ru isotopes is shown in Fig. 3.42.

3.3. Gamma-ray spectroscopy

Finally, after all refined data treatment for AGATA and VAMOS++, the tracked gamma-rays in coincidence with reaction products can be identified and prepared for the lifetime determination via the RDDS technique (Chapter 4). As it will be explained in the next subsections, first of all, the tracked gamma-rays need to be Doppler corrected with the information provided by VAMOS++ (red parameters in Fig. 3.28). Afterwards, the population of the highest excited states can be constrained to avoid totally or partially the undesirable feeding from high lying states. This is possible thanks to the usage of a magnetic spectrometer such as VAMOS++, as it will be explained in Section 3.3.2.

For the correct gamma-ray identification during the experiment, the AGATA events were only acquired with a trigger condition that required coincidence with VAMOS++. Thus, all gamma-rays measured by AGATA were unequivocally assigned to a product nucleus. In order to avoid random coincidences between the gamma-rays and the identified particles one should select the prompt events in the coincidence window between AGATA and VAMOS++. With that purpose a condition has been set in the timestamp difference between both detectors, as it is

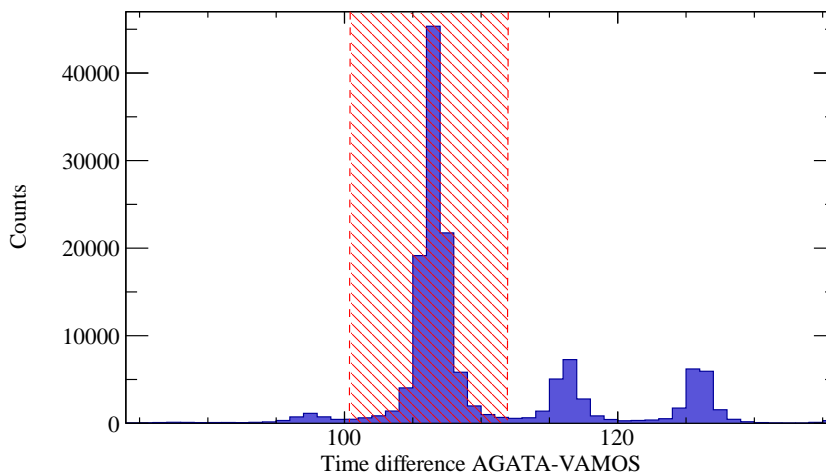


FIGURE 3.43: AGATA-VAMOS++ timestamp difference. The condition of coincidence in the prompt events is marked in red.

shown in Fig. 3.43. The small distributions outside the prompt peak, observed in the time spectrum, are random coincidences with reactions produced by the ions of previous or latter accelerator bunches and they have to be avoided. These bunches are separated by about 90 ns, which corresponds to the GANIL cyclotron High Frequency (HF) period.

3.3.1. Doppler correction

Gamma-rays are emitted by the reaction products in movement and hence, the detected energy of the photon is affected by the Doppler effect. As previously mentioned, the Doppler correction of gamma-rays emitted by the reaction products is performed on an event-by-event basis, hereby using the information from VAMOS++ and AGATA after their calibration and optimization. As already seen in Section 2.4.1, the observed energy of a photon emitted by a moving reaction product is given by,

$$E = E_0 \frac{\sqrt{1 - \beta^2}}{1 - \beta \cos\theta}, \quad (3.11)$$

where E_0 is the energy of the transition measured at rest, β is the velocity of the ions determined by VAMOS++, i.e. the velocity after the degrader, and θ is the angle between the direction of the detected ions (determined by the DPS-MWPC at the entrance position in VAMOS++) and the direction of the emitted gamma-rays (determined by the position of the first interaction of the gamma-ray in AGATA). In the following subsections, the methodology followed to apply the Eq. (3.11) and the final spectra after the correction are presented.

3.3.1.1. Velocity distribution

The velocity information, β , needed for the Doppler correction (Eq. (3.11)) is provided directly by the VAMOS++ spectrometer as presented in Section 3.2.1. This is the velocity after being slowed down by the degrader $\beta = \beta_{aft} = v_{aft}/c$. However, in order to obtain the optimum Doppler correction a small rectification in the velocity distribution had to be done in order to take into account the energy losses inside VAMOS++ during the measurement of the *ToF* due to the gas volume inside the detectors and Mylar foils. This correction enlarges the velocity around 2.5%.

The final velocity distributions after the degrader are represented in Fig. 3.44 for different Z numbers: 40, 41, 42, 43 and 44.

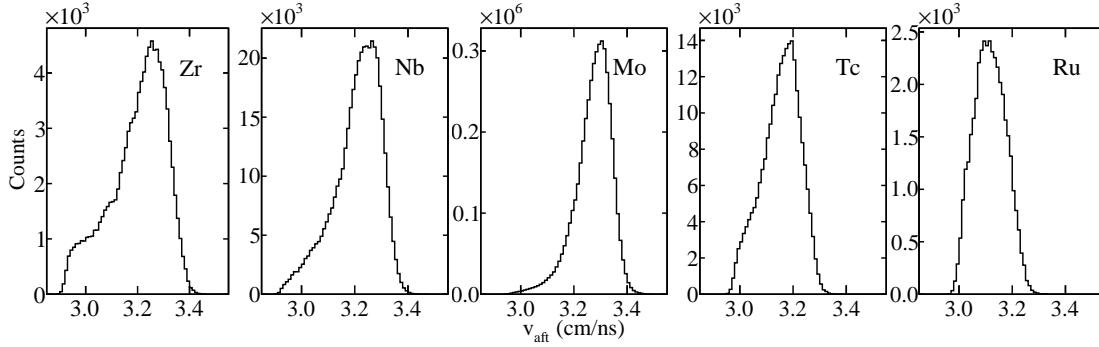


FIGURE 3.44: Velocity distributions for the inelastic channel, the $\pm 1p$ and the $\pm 2p$ transfer channels.

Moreover, the velocity before the degrader v_{bef} , needed for the lifetime determination (Chapter 4) with the RDDS technique, can be derived using the Eq. (2.7), which relates the two velocities before and after the degrader and the measured angle θ with the centroids of the shifted, E_0^s , and unshifted, E_0^u , energies present in the gamma ray spectra after the Doppler correction.

The velocity before the degrader together with the parameters used for its calculation are listed in Table 3.6 for the different nuclei of interest. The angle used is an average of the angle measured (see Section 3.3.1.2). The uncertainties of v_{aft} are given by the FWHM of the distribution. The uncertainty of the energy centroids, $\Delta E = E_0^u - E_0^s$, is negligible in comparison with the velocity value.

TABLE 3.6: Velocities of the reaction products before and after de degrader.

Nucleus	Transition	E_γ (keV)	ΔE (keV)	v_{aft} ($\mu\text{m}/\text{ps}$)	v_{bef} ($\mu\text{m}/\text{ps}$)
^{90}Zr	$2^+ \rightarrow 0^+$	2186.2	-15.9	32.6(9)	35.3 (12)
^{91}Nb	$1/2^- \rightarrow 9/2^+$	1082.3	-8.9	32.5(10)	35.5 (13)
^{92}Mo	$4^+ \rightarrow 2^+$	773	-5.5	32.9(7)	35.5 (10)
^{93}Tc	$25/2^- \rightarrow 21/2^-$	607.2	-4.7	31.6(7)	34.6 (10)
^{94}Ru	$4^+ \rightarrow 2^+$	756	-6.0	31.0(6)	33.9 (9)

3.3.1.2. Angle distribution

The angle θ between the direction of the excited reaction products, $\vec{\beta}$, and its corresponding emitted gamma-ray direction, $\vec{\gamma}$, is derived as follows,

$$\vec{\beta} \cdot \vec{\gamma} = |\beta||\gamma|\cos\theta. \quad (3.12)$$

The direction position of the excited reaction products is calculated with high accuracy on an event-by-event basis from the measured quantities in the DPS-MWPC at the entrance of VAMOS++ as previously explained in Section 3.2.1.1. This direction is defined by the horizontal and vertical angles, θ_t and ϕ_t respectively, which are in the VAMOS++ reference frame.

$$\vec{\beta}_V = \{X_V(\theta_t, \phi_t), Y_V(\theta_t, \phi_t), Z_V(\theta_t, \phi_t)\}. \quad (3.13)$$

The emission direction of the gamma-ray is calculated from the reconstructed first interaction point of the gamma-ray in AGATA (X, Y, Z) and distance of the detector from the nominal target position (X_0, Y_0, Z_0) = (0, 0, 7) (the detector was shifted 7mm towards from the nominal target position towards the target). This direction is expressed in the reference frame of the AGATA.

$$\vec{\gamma}_A = \{X + X_0, Y + Y_0, Z + Z_0\}. \quad (3.14)$$

For the correct determination of the angle the two direction positions must be given in the same reference frame. The axes defining each reference frame are illustrated

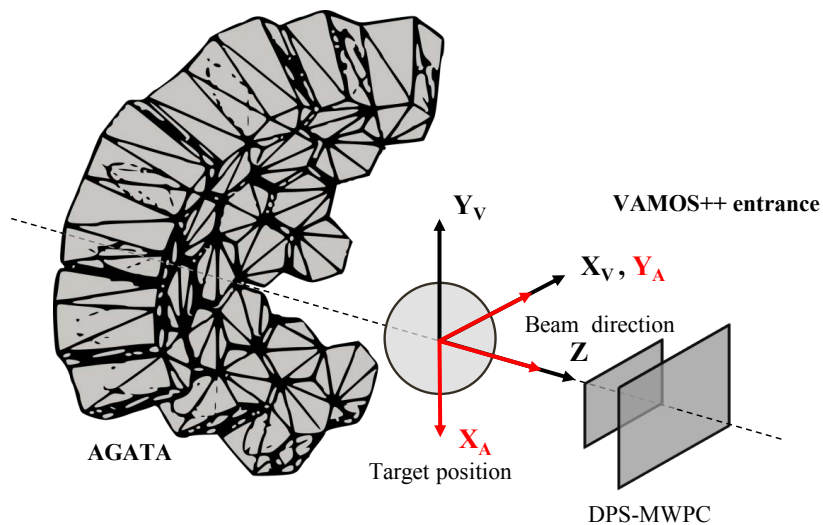


FIGURE 3.45: Schematic view of the reference frames used in the experimental setup. The VAMOS++ reference frame is indicated in black and the AGATA reference frame in red. The Z-axis coincides with the beam direction in both cases. The origin is centred at the nominal target position.

in Fig. 3.45. Following this scheme, the direction position of the emitted gamma-ray given by Eq. (3.14) can be easily transformed with a rotation along the Z-axis to the VAMOS++ reference frame as,

$$\vec{\gamma}_V = \{Y + Y_0, -X - X_0, Z + Z_0\}. \quad (3.15)$$

Finally, the angle θ between the momentum vector of the emitting ion and the emitted gamma-ray needed for the Doppler correction is obtained through Eq. (3.12). The calculated angle is depicted in Fig. 3.46.

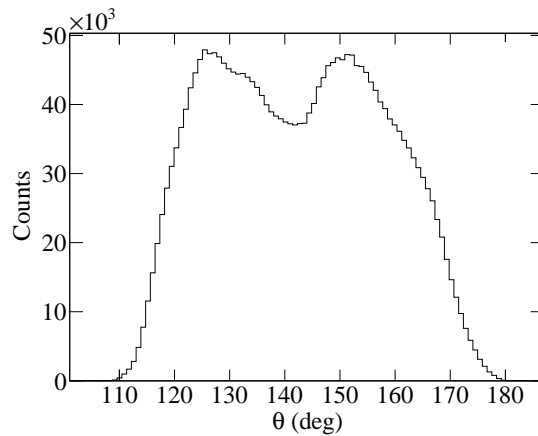


FIGURE 3.46: Angular distribution between the recoil direction and the emitted gamma-ray direction.

3.3.1.3. Tracked gamma-rays

Once the optimization of the parameters used in the Doppler correction is performed, the tracked gamma-rays can be identified using Eq. (3.11). As an example, the tracked gamma-ray spectra of ^{92}Mo populated in this reaction is shown in Fig. 3.47 without (top) and with (bottom) the Doppler correction

As explained in Chapter 2, the reaction used in the experiment was $^{92}\text{Mo}+^{92}\text{Mo}$ and the grazing angle of the reaction in the laboratory frame is around 23° (see Fig. 2.6). The ions identified at VAMOS++, which were ejected at 23° , emitted gamma-rays in flight. Its reaction partners were ejected at almost 67° being stopped inside the target material and, thus, emitting the gamma-rays at rest. The contributions of both types of gamma-ray emission are clearly illustrated in Fig. 3.47 for ^{92}Mo . In this case, both reaction partners are the same. Therefore,

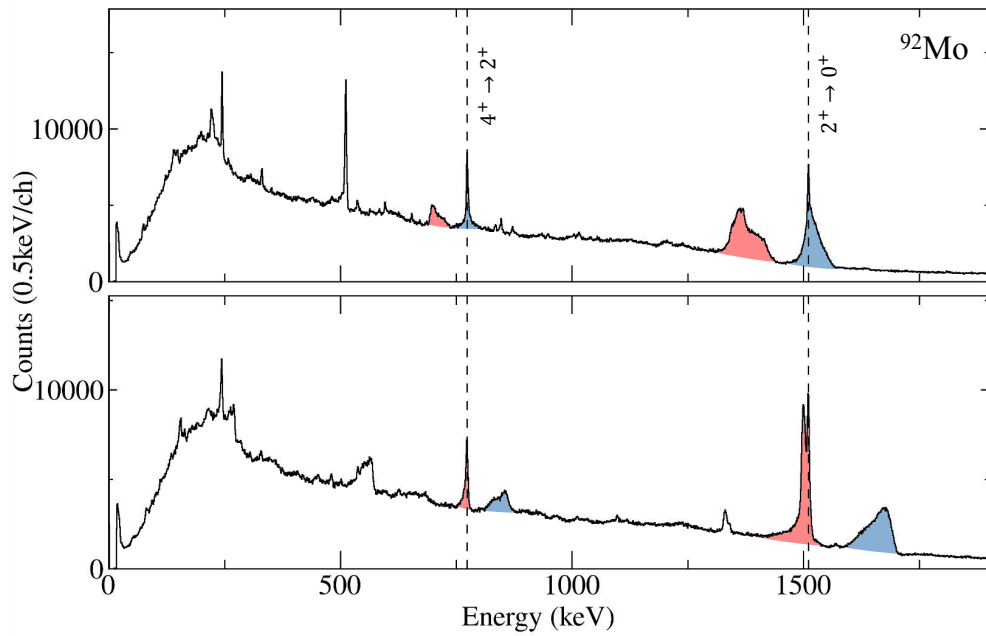


FIGURE 3.47: Comparison of the tracked gamma-ray energy detected after the degrader in ^{92}Mo without (top) and with (bottom) the Doppler correction. The counts of the first two yrast transitions of these nuclei are indicated in red and blue. The former correspond to the gamma-rays emitted in flight, which display a double peak structure due to the usage of the plunger device for the lifetime measurement. The latter, to the gamma-rays emitted at rest. These spectra correspond to the measurement with the shortest target-to-degrader distance: 19.3(9) μm .

the main transitions of this nucleus can be identified at the correct energy without (gamma-ray emitted at rest, in blue on the top panel) and with the Doppler correction (gamma-rays emitted in flight, in red on the bottom panel).

If one plots the spectra in Fig. 3.47 as a function of the angle between the ions direction and the gamma-rays direction one should observe that the dependency

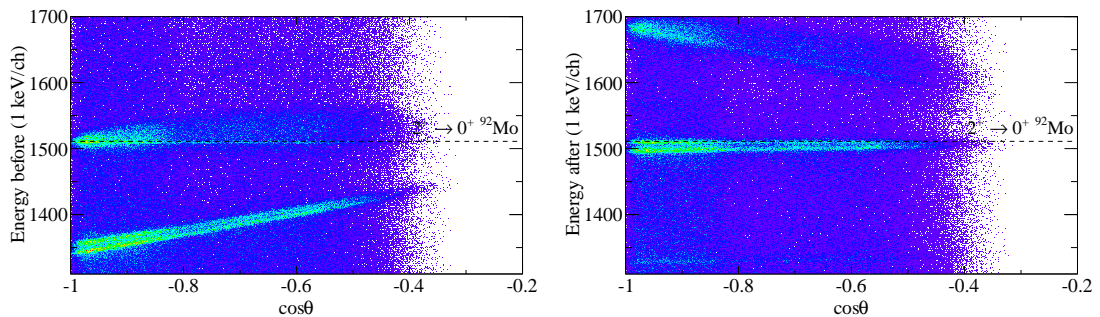


FIGURE 3.48: Comparison of the gamma-ray energy detected after the degrader in ^{92}Mo as a function of the angle without (left) and with (right) the Doppler correction. These matrices correspond to the measurement with the shortest target-to-degrader distance: 19.3(9) μm .

disappears for the unshifted component after the proper Doppler correction. This is depicted in Fig. 3.48. The example is shown for the $2^+ \rightarrow 0^+$ transition in ^{92}Mo . The two components, shifted and unshifted, due to the different velocities before and after the degrader can be appreciated without (left) and with (right)

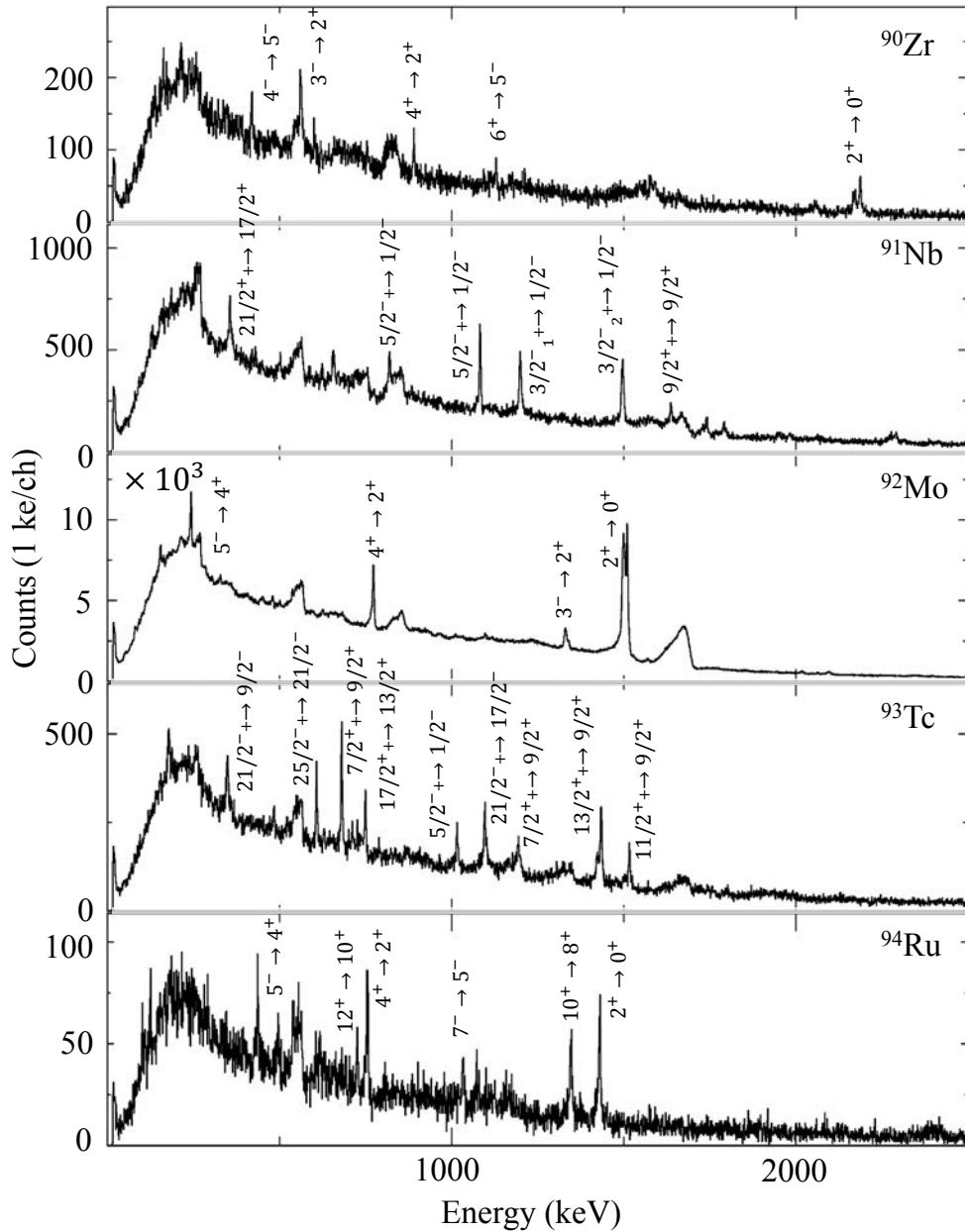


FIGURE 3.49: Tracked gamma-ray spectra obtained with AGATA in coincidence with VAMOS++ for the nuclei ^{90}Zr , ^{91}Nb , ^{92}Mo , ^{93}Tc and ^{94}Ru . The main transitions of these nuclei are reported. If not indicated the transitions shown correspond to the yrast transitions of the nucleus. It should be remarked that the visible double peak structure is due to the usage of the plunger for the lifetime measurement (see Section 2.4). These spectra correspond to the measurement with the shortest target-to-degrader distance: $19.3(9) \mu\text{m}$.

the Doppler correction.

Finally, by making several selection in the Z and A values (Figs. 3.39 and 3.42) the nuclei of interest are identified and their corresponding tracked gamma-rays are Doppler corrected. These spectra are presented in Fig. 3.49 and will be used to determine the lifetime of the transitions of excited nuclei of study. This will be shown in detail in Chapter 4.

3.3.2. Total Kinetic Energy Loss (TKEL) in MNT reactions

The consideration of level-feeding in the analysis is crucial for the reliable determination of the lifetime. In multi-nucleon transfer reactions states with angular momenta up to $10 \hbar$ can be excited. The advantage of using a spectrometer is that it permits to partially control the feeding (direct or from higher states) by means of a selection in the Q-value or TKEL [49]. In this way it is possible to limit or reduce the contribution of the feeding to our state of interest. Fig. 3.50 illustrates the correspondence between the TKEL selection values and the population of the excited states in the ^{92}Mo nucleus. The upper panel a) shows the

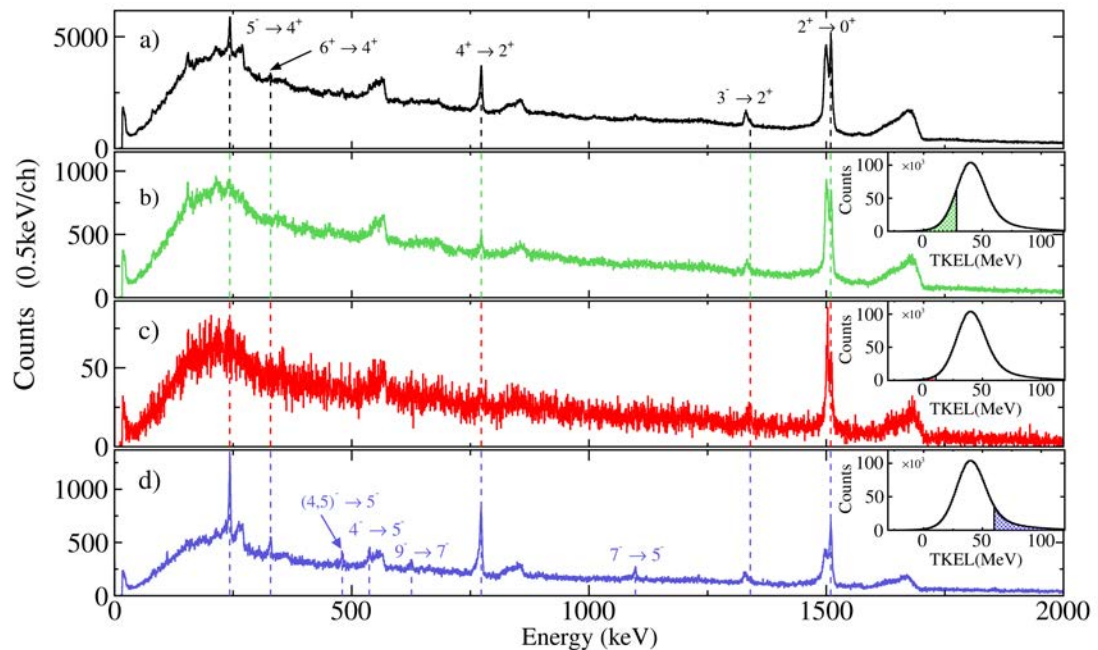


FIGURE 3.50: Example of different TKEL cuts in ^{92}Mo for the shortest target-to-degrader distance. a) Doppler-corrected spectrum of ^{92}Mo without gating on the TKEL. b) Gate on the low part of the TKEL. c) More restrictive gate on the low part of the TKEL. d) Gate on the high part of the TKEL.

Doppler corrected gamma-ray spectrum for ^{92}Mo without any TKEL gate and the populated states. For low values of the TKEL the population of the higher states is reduced. With this condition in panel b) the $6^+ \rightarrow 4^+$ and $5^- \rightarrow 4^+$ transitions have vanished. In panel c), where the gate is further lowered, practically only the $2^+ \rightarrow 0^+$ transition remains. A high gate on the TKEL enhances the intensities of the higher excited levels. This is demonstrated in panel d), where transitions that were inappreciable in the first panel became visible now. This is clearly appreciated in the intensity variation of the two components of the $2^+ \rightarrow 0^+$ transition, which is a short-lived transition (0.35(2)ps [83]). Low TKEL values enhance the shifted component, while high TKEL values tend to increase the unshifted component due to the extra contribution from the feeders.

In summary, this method has been shown to be convenient in order to avoid systematic uncertainties in the final lifetime value due to side-feeding from higher excited levels [49]. Therefore, it will be consistently applied to the data of this experiment, as described in Chapter 4.

Chapter 4

Lifetime determination

The lifetime determination through the RDDS technique is discussed in this Chapter. Firstly, a brief description of the analysis methodology is given together with the approach followed to treat the feeding contributions. Afterwards, an experimental validation of the implemented methodology is presented, which is based on well known lifetime values of ^{93}Tc and ^{94}Mo . Finally, lifetime results are obtained for the states of interest in ^{90}Zr , ^{92}Mo and ^{94}Ru . In order to study the structure of these atomic nuclei, the reduced transition probabilities, $B(E2)$, are determined from the lifetime values using the definitions described in Refs. [84, 85].

4.1. RDDS data analysis

As it was explained in Chapter 2, Section 2.4.1, the RDDS technique is a well established method for the determination of lifetimes in the range of picoseconds to hundreds of picoseconds. In this experiment, the standard technique using a stopper after the target was modified by replacing it with a degrader. This enabled to measure the reaction products in the magnetic spectrometer. The degrader slows down the reaction products yielding two components in the gamma spectrum due to the different velocities (before and after the degrader) of the emitted nuclei (Fig. 4.1, see also Fig. 2.17 for more details), but it is still possible to detect the out-coming ions with a magnetic spectrometer as VAMOS++. Afterwards, the lifetime can be derived from the ratio of the intensities of the two components shifted I_s (before the degrader) and unshifted I_u (after the degrader) as a function of the target-to-degrader distance d .

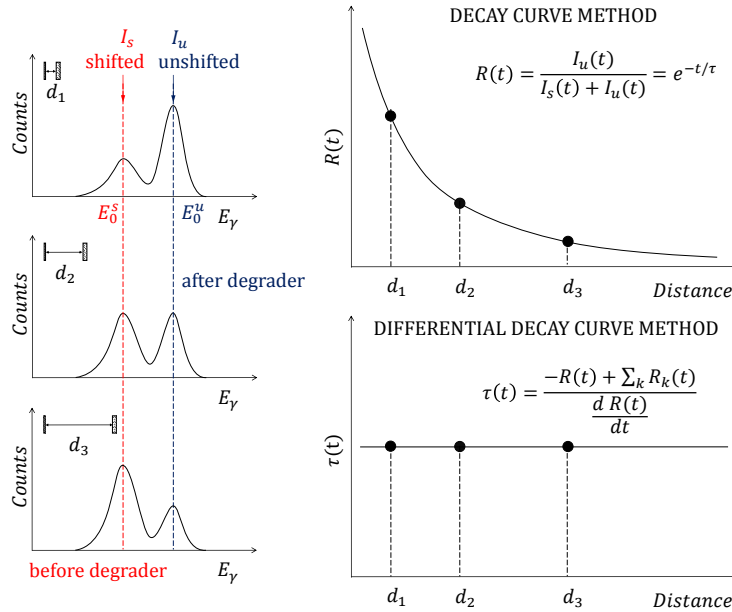


FIGURE 4.1: Left panel: Schematic drawing of the RDDS technique using the differential plunger showing the variation of the two components in the peak for 3 different distances. Right panel: Simplified drawing and formulas of the methods that can be used to determine the lifetime from the intensities of the two components in the gamma-ray spectrum, I_s and I_u . For more details see Sections 4.1.1 and 4.1.2

Two analysis methods can be used to extract the lifetime of excited states in nuclei: the decay curve method and the differential decay curve method. The two methods are schematically illustrated in the top and bottom panels of Fig. 4.1, respectively. The procedure and the formulation of these methods for the lifetime determination is given for a general level-feeding pattern in the following subsections. The treatment of the feeding observed in the transitions of interest is also described.

4.1.1. Decay Curve Method (DCM)

The traditional method to extract the lifetime is the Decay Curve Method (DCM), which derives the lifetime from the ratio of the intensities of the shifted and unshifted components as a function of the distance. With these intensities is possible to construct the decay curve:

$$R(t) = \frac{I_u(t)}{I_s(t) + I_u(t)}, \quad (4.1)$$

with $t = d/v$ being the time of flight of de ion to cover the distance target-to-degrader d with a velocity $v = v_{bef}$ (see Section 2.4.1 and Section 3.3.1).

If the nuclear state of interest is populated directly by a nuclear reaction at $t=0$, the decay curve obeys the simple equation,

$$R(t) = e^{-t\lambda}, \quad (4.2)$$

where λ is the exponential decay constant of the level of interest, which is related with the lifetime τ or the half-life $t_{1/2}$ as,

$$\lambda = \frac{1}{\tau} = \frac{\ln 2}{t_{1/2}}. \quad (4.3)$$

Since states with medium to low angular momenta can be excited in the multi-nucleon transfer reaction, the nuclear states of interest may be populated also by the de-excitation of other higher-lying states that have been populated at $t = 0$. Thus, one should consider a more general case where different levels are involved in the gamma-decay. The feeding terms in the system of differential equations that describes the radioactive decay need to be taken into account.

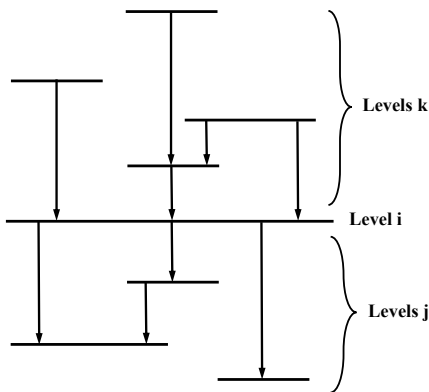


FIGURE 4.2: Schematic level-feeding pattern. The level i is the level of interest which is populated by the levels k and deexcites to the levels h via gamma-ray transitions.

Considering a complex level-feeding pattern as the one shown in Fig. 4.2 for a level i with N levels k feeding it, the number of nuclei in the level i at time t , $n_i(t)$, obeys the differential system of Bateman equations,

$$\frac{dn_i(t)}{dt} = -\lambda_i n_i(t) + \sum_{k=i+1}^N \lambda_k n_k(t) b_{ki}, \quad (4.4)$$

where $n_k(t)$ is the number of nuclei in level k , λ_i and λ_k are the decay constants of the levels and b_{ki} is the branching ratio from the level k to level i . The solution of the differential equation with respect to the experimentally determinable decay curve is [47],

$$R_i(t) = P_i e^{-t\lambda_i} + \sum_{k=i+1}^N M_{ki} \left[(\lambda_i/\lambda_k) e^{-t\lambda_k} - e^{-t\lambda_i} \right], \quad (4.5)$$

where

$$M_{ki}(t)(\lambda_i/\lambda_k - 1) = b_{ki} P_k - b_{ki} \sum_{m=k+1}^N M_{mk} + \sum_{m=i+1}^{k-1} M_{km} b_{mi} (\lambda_m/\lambda_k) \quad (4.6)$$

and P_i and P_k are the direct feeding intensities of each level. The function $R_i(t)$ is fitted to the experimental data curve, Eq. (4.1), in order to obtain the lifetime of the excited state of interest i . This is schematically depicted on the top panel in Fig. 4.1 for a the simplest case of a decay without feeding transitions.

With this method the determination of the lifetime for excited states with complex feeding patterns becomes very difficult since not all the feeding contributions can be observed. In addition, the fit involves a significant number of parameters which hinders the disentanglement of systematic errors. Another drawback is related to the distance between target and degrader, which needs to be accurately known.

4.1.2. Differential Decay Curve Method (DDCM)

The Differential Decay Curve Method (DDCM) is an alternative approach to determine lifetimes [47]. This method has been developed to avoid the aforementioned limitation related with the determination of the absolute value of the distance of the standard analysis. The major advantages of this method are the following:

- Only measurable quantities are used.
- Only relative distances target-to-degrader are required.

- More reliable treatment of the systematic uncertainties.
- Independent lifetime determinations per distance are feasible.

Both singles and coincidence gamma-ray spectra may be used to obtain lifetimes using the DDCM method. In the present experiment, the statistics of the nuclei of interest were not high enough to enable coincidence analysis. For this reason, only the DDCM for the singles case has been used following the formulation given in [47]. Starting from the differential system of Bateman equations, Eq. (4.4), for a level i with N levels k feeding it (Fig. 4.2), and integrating, one obtains,

$$\int_t^\infty \frac{dn_i(t)}{dt} dt = -\lambda_i \underbrace{\int_t^\infty n_i(t) dt}_{N_i(t)} + \sum_{k=i+1}^N b_{ki} \lambda_k \underbrace{\int_t^\infty n_k(t) dt}_{N_k(t)}, \quad (4.7)$$

where $N_i(t)$ and $N_k(t)$ are the decay functions of the levels i and k respectively. One can rewrite Eq. (4.7) as,

$$n_i(\infty) - n_i(t) = -N_i(t) + \sum_{k=i+1}^N b_{ki} N_k(t). \quad (4.8)$$

Using $n_i(\infty) = 0$ (from the assumption of finite lifetimes) and the derivative of the decay function $N_i(t)$ the equation of the lifetime of the level i reads,

$$\tau_i(t) = 1/\lambda_i = \frac{-N_i(t) + \sum_{k=i+1}^N b_{ki} N_k(t)}{\frac{dN_i(t)}{dt}}. \quad (4.9)$$

The experimentally determinable decay curves are proportional to the decay functions, and thus, the lifetime can be written as,

$$\tau_i(t) = \frac{-R_i(t) + \sum_{k=i+1}^N b_{ki} \alpha_{ki} R_k(t)}{\frac{dR_i(t)}{dt}}. \quad (4.10)$$

The proportionality factor, α_{ki} , is determined from the detector efficiencies, $\varepsilon(E_{\gamma_j})$, and the angular distributions, $\omega_j(\theta)$, of the depopulating gamma-ray transitions of the levels $j = i, k$ as follows,

$$\alpha_{ki} = \frac{\omega_k(\theta)\varepsilon(E_{\gamma k})}{\omega_i(\theta)\varepsilon(E_{\gamma i})}. \quad (4.11)$$

Thus the lifetime can be individually extracted for each measured distance. As it is shown schematically on the bottom panel in Fig. 4.1, the lifetime is determined fitting the obtained values per distance to a constant function $\tau_i(t)$. Each value is calculated from the ratio of two values. The numerator, which is measured experimentally and the denominator, which is obtained from the derivative of the fitted function to the ratio of the shifted and unshifted intensities. The sensitive region of the method is the region where the measuring accuracy for the level lifetime is highest, i.e. where the fitted function $R_i(t)$ has a large gradient.

In summary, the DDCM technique allows for a consistent interpretation of the interplay between the different experimental effects affecting the lifetime determination, which is an important aspect for the reliable treatment of the involved systematic uncertainties.

4.1.3. Feeding treatment

The consideration of level-feeding in the analysis is crucial for the correct determination of the lifetime. In multi-nucleon transfer reactions states with angular momenta up to $10\hbar$ can be excited. The advantage of using a spectrometer is that it permits to partially control the feeding (direct or from higher states) by means of a selection in the TKEL (see Section 3.3.2). In this way it is possible to reduce the number of feeding terms to be included in the decay equations described in the previous sections.

Fig. 3.50 illustrated the correspondence between the TKEL selection values and the population of the excited states in the ^{92}Mo nucleus, revealing that for low TKEL values the population of the higher states is reduced, while for high TKEL values the intensities of the higher excited levels are enhanced.

This method has been consistently applied to the data of this experiment in order to avoid systematic uncertainties in the final lifetime value due to side-feeding from higher excited levels [49]. Nevertheless, due to the very exotic nature of the ^{94}Ru under study the accumulated statistics were rather limited and thus an alternative

method had to be implemented. In the ^{92}Mo and ^{94}Ru cases, the existence of long-lived states, with half-lives of 1.5 and 0.5 ns respectively, contributes to the biased feeding of both the shifted and unshifted components. This occurs because the gamma-ray emission is produced at a long distance after the target, and the angle θ between the ion direction and the emitted gamma-ray is increased compared to the angle of gamma-ray emission at the degrader position for a given first interaction position of the gamma-ray. Therefore, after doing the Doppler correction, although the state has a long lifetime, it appears a Doppler-shifted gamma-ray energy observed at a given detection position and reduced for the emission at a long distance. This effect, illustrated in Fig. 4.3, is used for the so call geometrical DSAM [86].

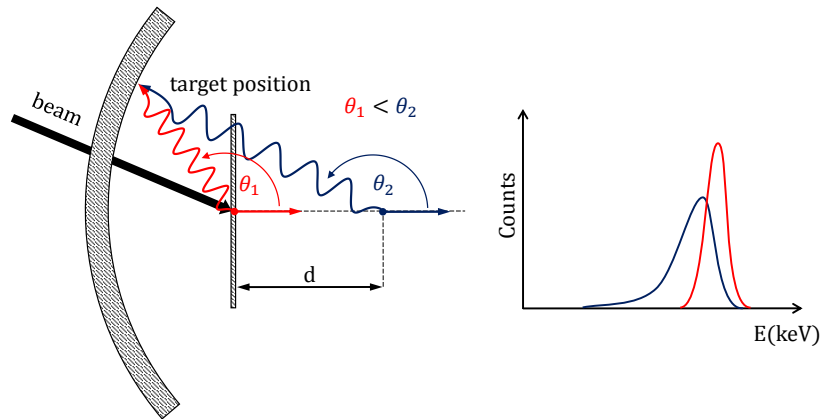


FIGURE 4.3: Effect of the long-lived transitions in RDDS technique. For long-lived transitions the gamma-ray emission occurs at a distance d after the target. Thus the Doppler correction is producing a lineshape since it depends on the detection angle and it is not possible to know the emission point.

In the case of ^{94}Ru it is compulsorily to use what we have called the subtraction method, i.e. the intensities of the shifted and unshifted components have been obtained with the subtraction of the contribution of the high-lying long-lived transitions as depicted in Fig. 4.4 for the shortest target-to-degrader distance. In panels a) and b) the shape of the long-lived transitions ($5^- \rightarrow 4^+$ and $6^+ \rightarrow 4^+$, respectively) due to the solid-angle effects can be appreciated. The subtraction of the two contributions to the 4^+ state is illustrated in red in panel c). To this aim, the corresponding spectra of the long-lived feeders have been reconstructed at the proper $4^+ \rightarrow 2^+$ transition energy taking into account corrections for efficiency and angular distributions.

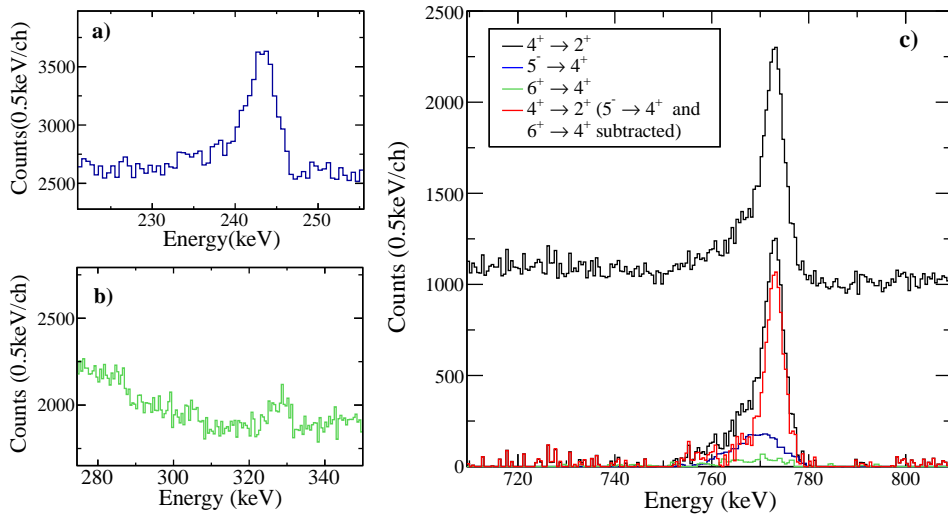


FIGURE 4.4: Example of subtraction in ^{92}Mo for the shortest target-to-degrader distance. a) Intensity of the contribution of the 5^- state to the 4^+ state before the background subtraction. b) Intensity of the contribution of the 6^+ state to the 4^+ state before and after the background subtraction. c) In black, the intensity of the $4^+ \rightarrow 2^+$ transition before and after the background subtraction. In red, the same transition after the subtraction of the intensities of the feeding components, 5^- state (blue line) and 6^- state (green line). For the subtraction of the contribution of the high-lying long-lived transitions the correction in efficiency and angular distribution have been taken into account.

4.1.4. Deorientation

The deorientation effect impacts the nuclear alignment during the flight of the recoils in vacuum [47]. Usually the spins of the nuclei are aligned with respect to the beam axis after a nuclear reaction. During the reaction and the flight of the nuclei through the target the electron configurations are distorted. This configurations are rearranged into energetically more favourable states when leaving the target creating strong magnetic hyperfine fields. The interaction of the nuclear spin with these fields changes the spin orientation with the flight time in vacuum. Consequently the intensities measured may change as the angular distributions vary over time. This needs to be quantified and eventually taken into account for the lifetime analysis. If present, neglecting these effects would lead, for example in the case of stretched E2-transitions, to apparently shorter lifetimes [47].

In order to identify and quantify the magnitude of this effect in this experiment, the low-spin states (where the effect is expected to be more pronounced) have been studied in ^{92}Mo . To this aim, the position sensitivity detector of AGATA becomes a remarkable advantage versus other systems, because it allows to perform

a detailed study of the deorientation effect as a function of the gamma-ray angle. In this work, the ratio of intensities for the unshifted component in two angles subtended by AGATA has been determined as a function of different flight times or target-to-degrader distances. The results are shown in Fig. 4.5, which displays the evolution in time of the gamma-ray intensities at 125° and 155° with $\Delta = 10^\circ$ for the $4^+ \rightarrow 2^+$ in ^{92}Mo . The corresponding flight time for the distances used for the analysis can be calculated using the velocity of the ^{92}Mo ions (Table 3.6), which is $35.5(10) \mu\text{m}/\text{ps}$. Eventually, the flat distribution indicates that no significant deorientation influence is appreciated per angle when increasing the flight time. Therefore, it can be concluded that the deorientation effect is negligible for the present lifetime analysis. It should be remarked that this evaluation should be done for each nucleus. However due to the lack of statics to separate the gamma-ray intensity per angles in the other nuclei, we assume that the results would be analogous since the nature of the nuclei, the states and the lifetimes are relatively similar.

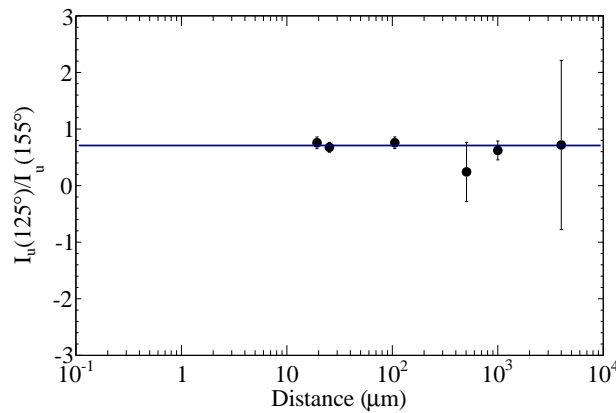


FIGURE 4.5: Measured intensities from the ratio of the unshifted component at 125° and 155° of $4^+ \rightarrow 2^+$ transition in ^{92}Mo (773.0 keV) as a function of several target-to-degrader distances. The blue line is the fitted curve to illustrate the absence of dependency with the angles.

4.2. Verification of methodology: lifetime in ^{93}Tc and ^{94}Mo

The accurate analysis of the lifetimes of interest involves the treatment of the feeding from higher states. For $4^+ \rightarrow 2^+$ transitions the feeding has been reduced as much as possible in order to use the simplest formulation for the DCM and DDCM

methods. This allows for a twofold validation, where the systematic uncertainties ascribed to each analysis methodology can be independently quantified. For the $2^+ \rightarrow 0^+$ the lifetime of higher-lying states has been included in the formulation. In summary, two validation analysis have been performed to probe both methods, thereby using nuclear states with known lifetimes as a reference. The seven target-to-degrader distances used for the lifetime determination were already shown in Table 2.12. As indicated in Section 2.4.3, the measurement with the 505 μm distance has limited statistics due to the short measurement time. In addition, two measurements were taken with the 2000 μm .

4.2.1. Verification with ^{93}Tc

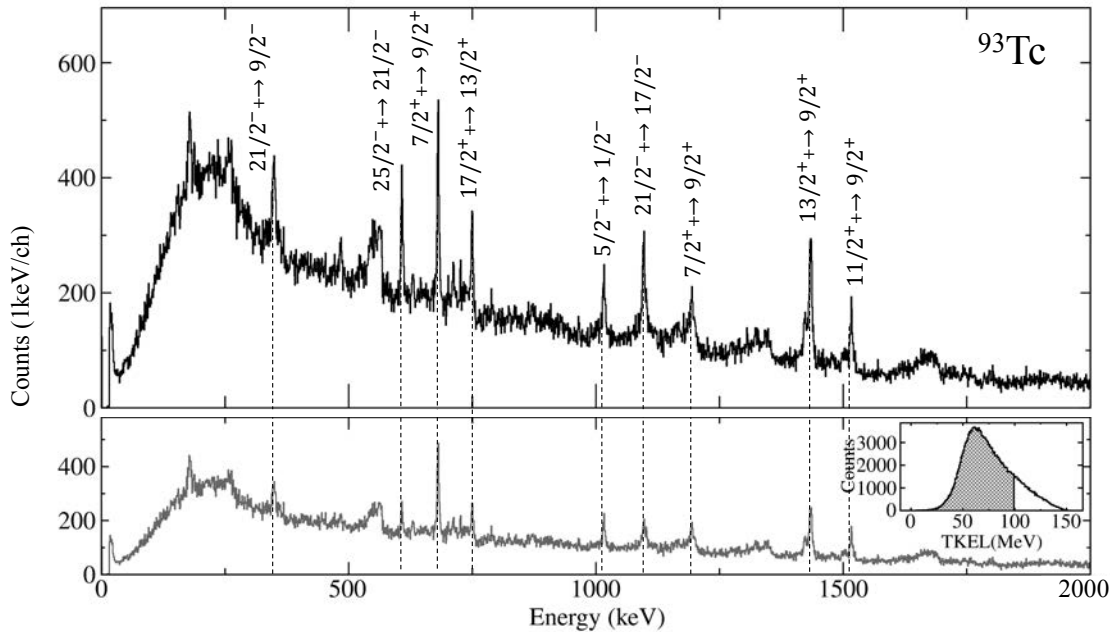


FIGURE 4.6: Doppler corrected gamma-ray energy spectrum for ^{93}Tc for the shortest target-to-degrader distance. Top: Full spectrum without gating on the TKEL. Bottom: Spectrum with a gate on the low part of the TKEL.

The simplest case corresponds to a situation where the nuclear state of interest is populated directly by a nuclear reaction at time $t = 0$. This has been investigated using the lifetime of the $25/2^-$ state in ^{93}Tc . The Doppler corrected gamma-ray spectrum of ^{93}Tc is shown in Fig. 4.6 together with the transitions identified. No feeders were identified in the gamma-ray spectrum for the test transition, $25/2^- \rightarrow 21/2^-$. Hence, the simplest level decay is assumed in the analysis, Fig. 4.7.

Fig. 4.8 shows the variation of the two components in the peak used to extract the lifetime. To this aim, the spectra were analysed separately for each distance by extracting in each case the areas of the gamma-ray of interest emitted before and after the degrader. For fitting the peaks the spectra-analysis program *Tv* [87] was used. The FWHM of the unshifted and shifted components were fixed for all the distances after getting its value with the shortest distance (in the case of the unshifted component) and with the longest distance (for the shifted component).

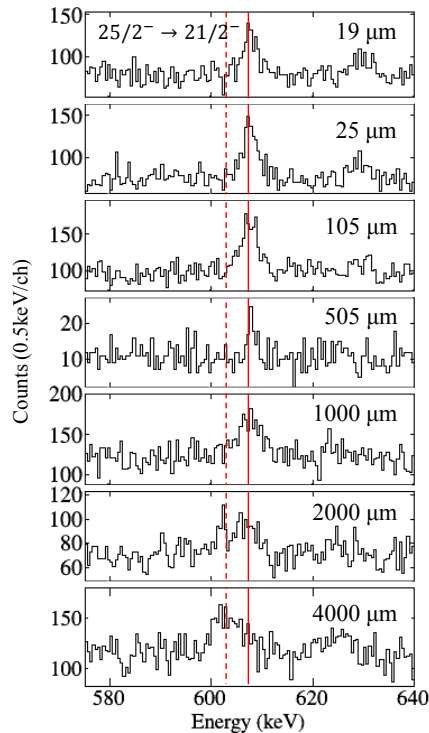


FIGURE 4.8: Doppler corrected spectra of ^{93}Tc in the $25/2^- \rightarrow 21/2^-$ (607.5 keV) transitions region for the seven distances measured with the TKEL cut illustrated in Fig. 4.6. The red solid line indicates the unshifted component (after the degrader) and the red dashed line, the shifted component (before the degrader).

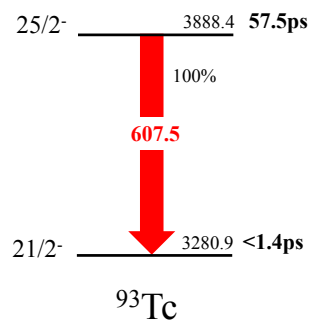


FIGURE 4.7: Transition of study in ^{93}Tc .

After that, knowing the target-degrader distance, d (Table 2.12), and the velocity of the ions, v_{bef} (Table 3.6), one can determine the lifetime by means of two different methods. These are discussed in the following.

For the DCM case, the experimental curve has been fitted using the simplest equation,

$$R(t) = Ae^{-t/\tau}, \quad (4.12)$$

with $t = d/v_{bef}$. The parameter A should be 1 if the nuclear state has been directly populated in the nuclear reaction. In the case of the $25/2^-$ state no feeders are observed in the energy spectrum of ^{93}Tc . In addition, a gate in the TKEL (see bottom panel in Fig. 4.6) has been applied to avoid possible unobserved feeding contributions. The parameter A obtained from the fit is equal to 0.99(3) thus confirming a direct population of the state of interest. In the DDCM case, Eq. (4.10) is simplified to,

$$\tau(t) = \frac{-R(t)}{\frac{dR(t)}{dt}}. \quad (4.13)$$

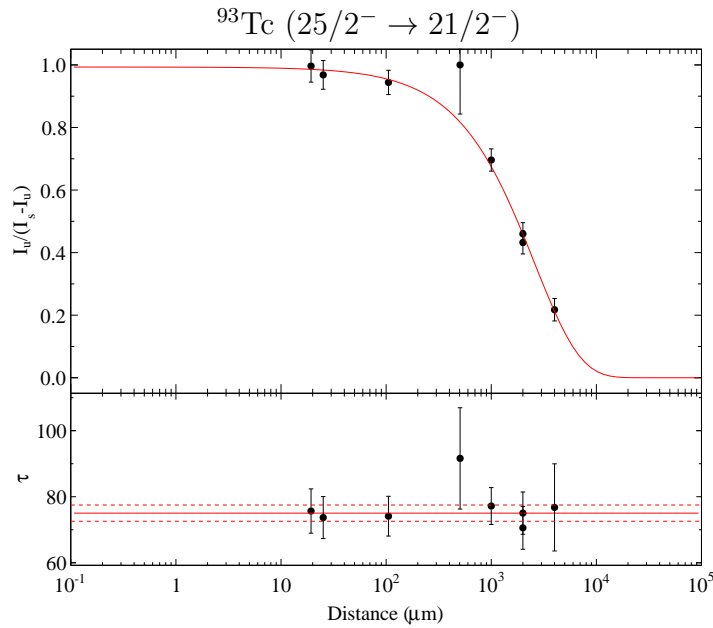


FIGURE 4.9: Decay curve for the $25/2^- \rightarrow 21/2^-$ transition in ^{93}Tc . On the top panel the conventional DCM method has been applied. The bottom panel shows the DDCM implemented within the region of sensitivity. The solid red lines represent the corresponding fits for each method. The dashed lines represents the experimental uncertainty to the one standard deviation level. The error bars of the of the distances (x-axis) are not visible because they are smaller than the symbols.

The fitted curves are shown in Fig. 4.9 for both methods. The resulting lifetime is $\tau=75(6)\text{ps}$ ($t_{1/2} = 52(4)\text{ps}$) for the DCM method and $\tau = 75(3)\text{ps}$ ($t_{1/2} = 52.0(17)\text{ps}$) for the DDCM method. These results are in agreement with the half-life $t_{1/2} = 57.5(21)\text{ps}$ given in [88], thereby confirming the correctness of the analysis methodology.

4.2.2. Verification with ^{94}Mo

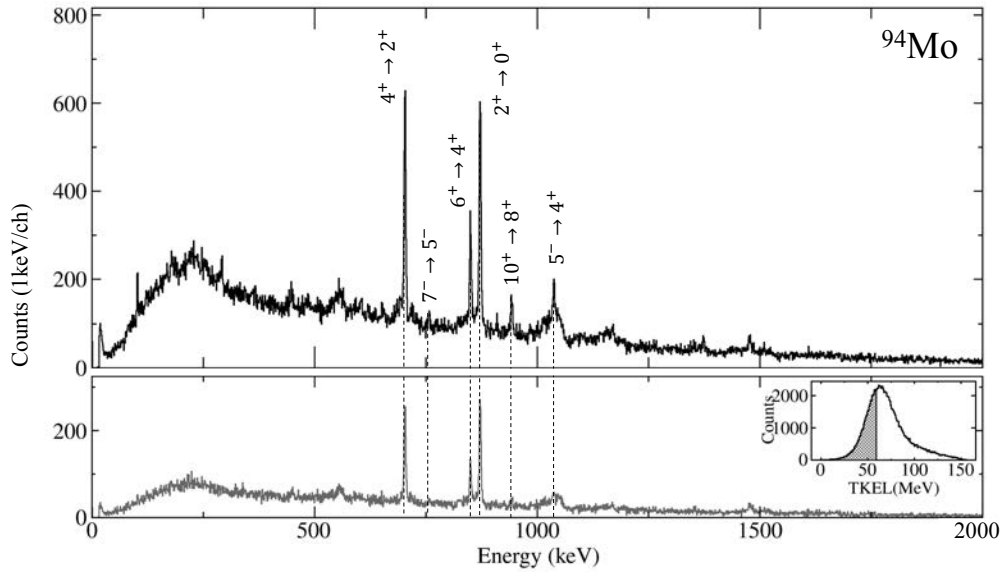


FIGURE 4.10: Doppler corrected gamma-ray energy spectrum for ^{94}Mo for the shortest target-to-degrader distance. Top: Full spectrum without gating on the TKEL. Bottom: Spectrum with a gate on the low part of the TKEL.

As it can be understood from the transitions identified in Fig. 4.10 the validation approach with ^{94}Mo included the feeding of the higher states $6^+ \rightarrow 4^+$ and $5^- \rightarrow 4^+$ to determine the known lifetime of the $4^+ \rightarrow 2^+$ transition. This simplified level-feeding pattern is shown in Fig. 4.11. In this analysis the TKEL gate was again used to avoid any side-feeding and reduce as much as possible the feeders observed as in the case of $5^- \rightarrow 4^+$ transition (bottom panel in Fig. 4.10). The spectra from which the lifetime is extracted are shown in Fig. 4.12.

Using Eqs. (4.5) and (4.10) for a state fed with one state above (6^+), the experimental curves are fitted, as shown in Fig. 4.13. The determined lifetimes of $\tau=7.1(17)\text{ps}$ ($t_{1/2}=4.9(1.2)\text{ps}$) for the DCM method and $\tau=7.1(10)\text{ps}$ ($t_{1/2}=4.9(7)\text{ps}$) for the DDCM, agree well with the reference half-life value $t_{1/2}=5.0(7)$ from [89]. The lifetime of the 6^+ state has been also determined for the analysis of the 6^+ being $9.2(11)\text{ps}$.

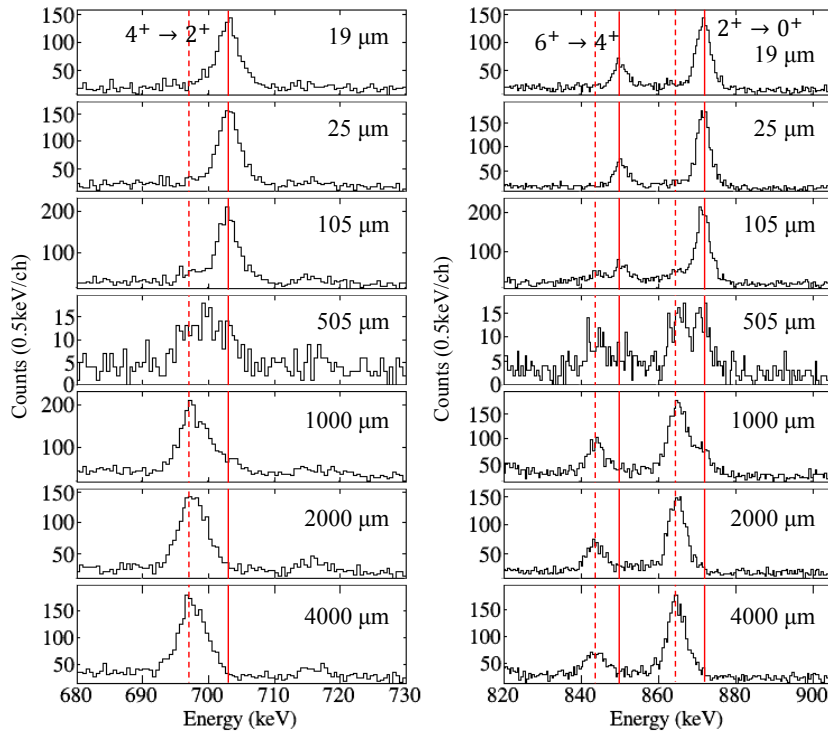


FIGURE 4.12: Doppler corrected spectra of ^{94}Mo showing the $2^+ \rightarrow 0^+$ (871.1 keV), $4^+ \rightarrow 2^+$ (702.6 keV) and $6^+ \rightarrow 4^+$ (849.7 keV) transitions region for the seven distances measured with the TKEL cut illustrated in Fig. 4.10. The red solid lines indicate the unshifted component (after the degrader) and the red dashed lines, the shifted component (before the degrader).

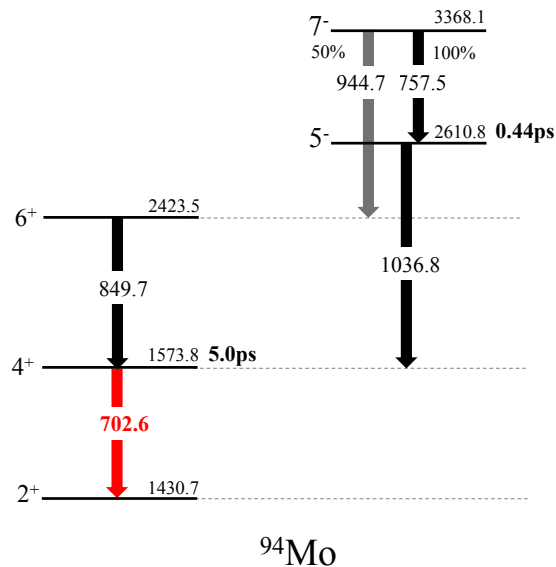


FIGURE 4.11: Simplified level scheme of ^{94}Mo showing the feeding levels and the transition of interest (in red). The gamma-ray transitions represented by grey lines have not been observed in the energy spectrum. The thickness of the transitions do not account for their observed intensity. Instead of that, the corresponding intensities taken from Ref. [89] are indicated with numbers. If no number is indicated the intensity is 100%.

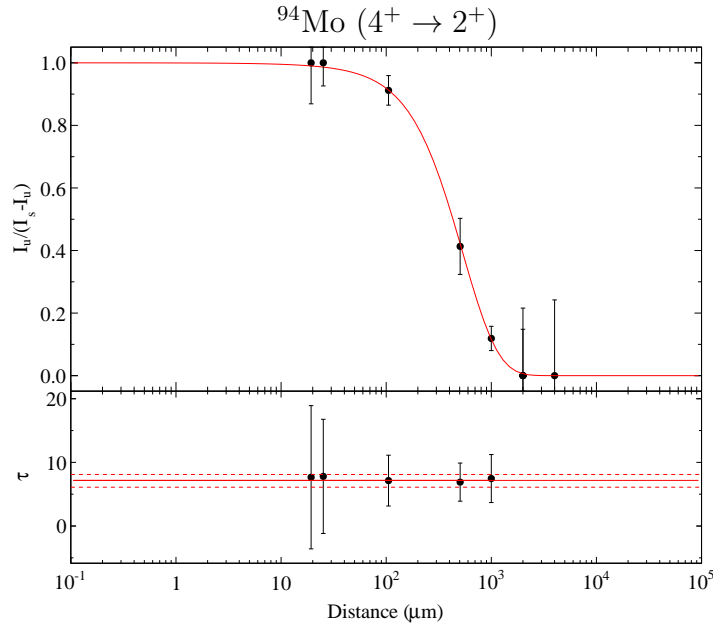


FIGURE 4.13: Decay curve for the $4^+ \rightarrow 2^+$ transition in ^{94}Mo . On the top panel the conventional DCM method has been applied. The bottom panel shows the DDCM implemented within the region of sensitivity. The solid red lines represent the corresponding fits for each method. The dashed lines represents the experimental uncertainty to the one standard deviation level. The error bars of the of the distances (x-axis) are not visible because they are smaller than the symbols.

4.3. Analysis of the Inelastic Channel: lifetime in ^{92}Mo

In Fig. 4.14 the Doppler corrected gamma-ray spectrum for ^{92}Mo is presented with the identified transitions. As mentioned before, in the ^{92}Mo nucleus the population of long-lived states with lifetimes at the limit of the RDDS technique, represents a bias in the feeding of the shifted component. In Fig. 4.15 the level scheme is shown schematically for the relevant transitions used in the analysis. The transition of interest, $4^+ \rightarrow 2^+$, is fed by two long-lived states, 6^+ and 5^- . The latter feedings have been effectively suppressed via two methods, as explained previously.

On one side, namely *method 1*, the intensities of the shifted and unshifted components have been obtained with a condition in the TKEL using the VAMOS++ spectrometer (see bottom panel in Fig. 4.14).

On the other side, the intensities of the shifted and unshifted components in the $4^+ \rightarrow 2^+$ transition have been obtained from the subtraction of the contribution of the intensities of the $5^- \rightarrow 4^+$ and $6^+ \rightarrow 4^+$ transitions. This approach has been indicated as *method 2*. The resulting ratio of intensities can be treated as

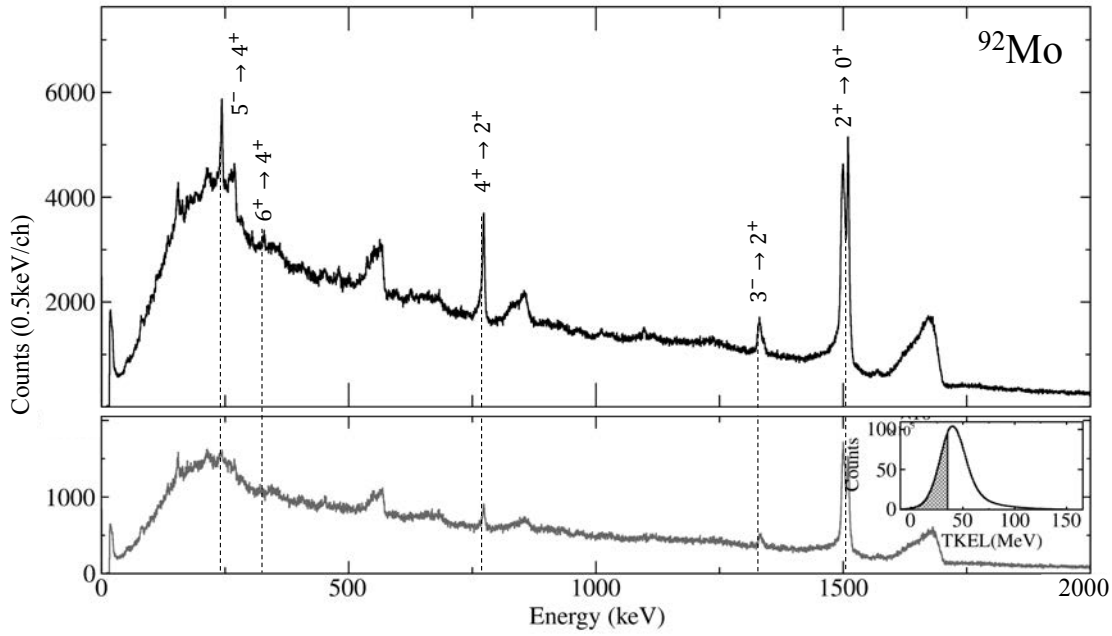


FIGURE 4.14: Doppler corrected gamma-ray energy spectrum for ^{92}Mo for the shortest target-to-degrader distance. Top: Full spectrum without gating on the TKEL. Bottom: Spectrum with a gate on the low part of the TKEL.

the ratio of a state directly populated using Eqs. (4.12) and (4.13) for the DCM and DDCM methods, respectively.

A further verification can be done with the measurement of the $2^+ \rightarrow 0^+$ transition, which is also well known. For this, Eqs. (4.5) and (4.10), with a state fed with two states above (4^+ and 3^-), have been applied utilizing the spectra obtained after the TKEL condition.

The variation of the two components in the peaks for the two transitions is shown in Fig. 4.16. The experimental curves for the DCM and DDCM methods are represented together with their corresponding fits, in Figs. 4.17 to 4.19. Figs. 4.17 and 4.18 are the analysis of the lifetime for the $4^+ \rightarrow 2^+$ and $2^+ \rightarrow 0^+$ transitions, respectively, using the TKEL condition. The analysis presented in Fig. 4.19 corresponds to the long-lived subtraction method for the $4^+ \rightarrow 2^+$. The lifetimes values resulting from the two methods for the $4^+ \rightarrow 2^+$ are shown in Table 4.1. In Table 4.2 the measured lifetime for the $2^+ \rightarrow 0^+$ is given and compared with the previous measured value.

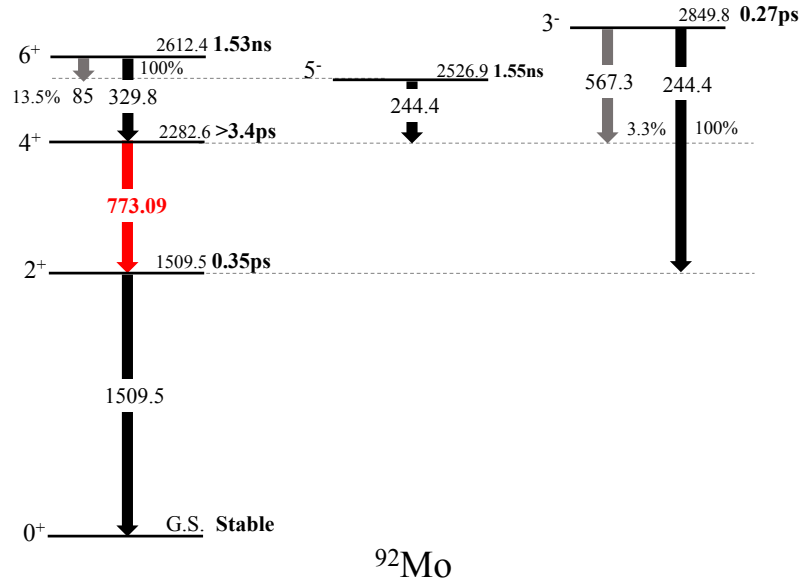


FIGURE 4.15: Simplified level scheme of ^{92}Mo showing the feeding levels for the transition of interest (in red). The gamma-ray transitions represented by grey lines have not been observed in the energy spectrum. The thickness of the transitions do not account for their observed intensity. Instead of that, the corresponding intensities taken from Ref. [89] are indicated with numbers. If no number is indicated the intensity is 100%.

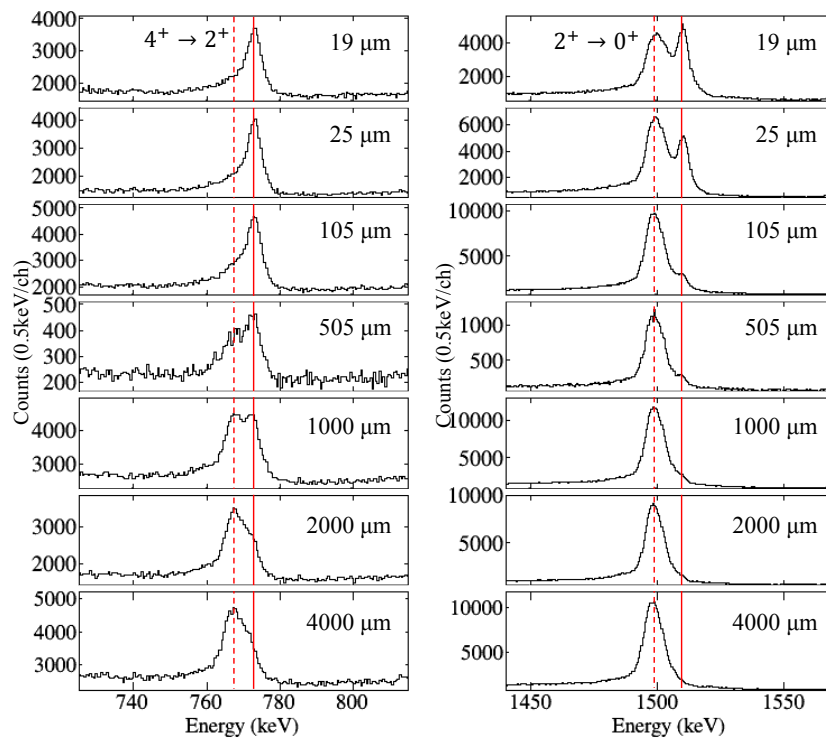


FIGURE 4.16: Doppler corrected spectra of ^{92}Mo showing the $4^+ \rightarrow 2^+$ (773.09 keV) and $2^+ \rightarrow 0^+$ (1509.5 keV) transitions region for the seven distances measured. The red solid lines indicate the unshifted component (after the degrader) and the red dashed lines, the shifted component (before the degrader).

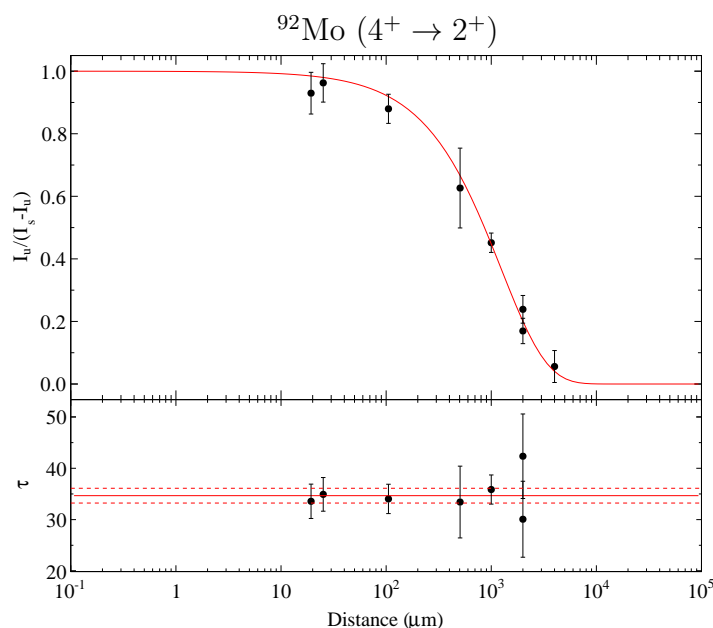


FIGURE 4.17: Decay curve for the $4^+ \rightarrow 2^+$ transition in ^{92}Mo . The data have been processed to subtract the contribution of the $5^- \rightarrow 4^+$ and $6^+ \rightarrow 4^+$ transitions with a selection in the TKEL. On the top panel the conventional DCM method has been applied. The bottom panel shows the DDCM implemented within the region of sensitivity. The solid red lines represent the corresponding fits for each method. The dashed lines represents the experimental uncertainty to the one standard deviation level. The error bars of the of the distances (x-axis) are not visible because they are smaller than the symbols.

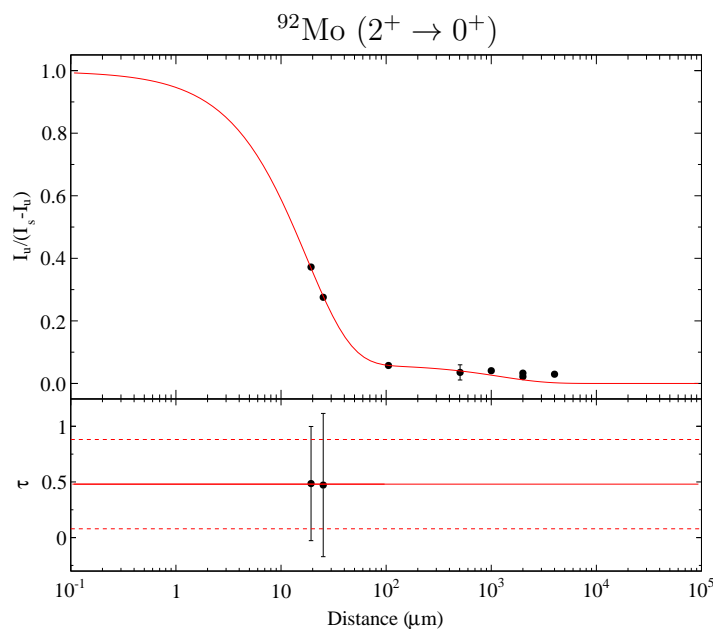


FIGURE 4.18: Decay curve for the $2^+ \rightarrow 0^+$ transition in ^{92}Mo . The data have been processed to subtract the contribution of the $5^- \rightarrow 4^+$ and $6^+ \rightarrow 4^+$ transitions with a selection in the TKEL. On the top panel the conventional DCM method has been applied. The bottom panel shows the DDCM implemented within the region of sensitivity. The solid red lines represent the corresponding fits for each method. The dashed lines represents the experimental uncertainty to the one standard deviation level. The error bars of the of the distances (x-axis) are not visible because they are smaller than the symbols.

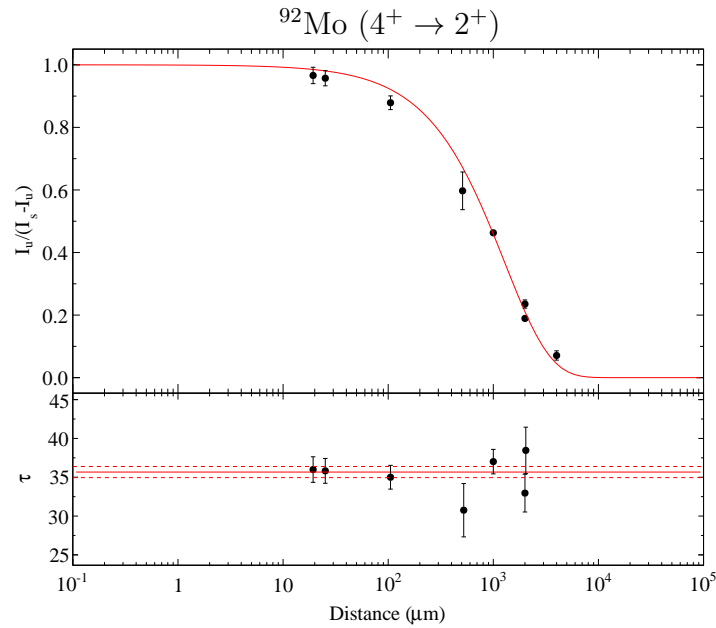


FIGURE 4.19: Decay curve for the $4^+ \rightarrow 2^+$ transition in ^{92}Mo . The data have been processed to subtract the contribution of the $5^- \rightarrow 4^+$ and $6^+ \rightarrow 4^+$ transitions. On the top panel the conventional DCM method has been applied. The bottom panel shows the DDCM implemented within the region of sensitivity. The solid red lines represent the corresponding fits for each method. The dashed lines represents the experimental uncertainty to the one standard deviation level. The error bars of the of the distances (x-axis) are not visible because they are smaller than the symbols.

TABLE 4.1: Half-life ($t_{1/2}$), lifetime (τ) and reduced transition probability ($B(E2)$) for the ^{92}Mo $4^+ \rightarrow 2^+$ transition at 773 keV. 1 and 2 indicate the method used.

Method	$t_{1/2}$ (ps)	τ (ps)	$B(E2)$ ($e^2\text{fm}^4$)
Literature	>3.4 [89]		
1-DCM	24.6(18)	35.5(24)	83(5)
1-DDCM	24.0(10)	34.6(14)	85.4(3)
2-DCM	25.4(9)	36.6(13)	80.7(19)
2-DDCM	24.7(5)	35.7(7)	82.8(1.6)

TABLE 4.2: Half-life ($t_{1/2}$), lifetime (τ) and reduced transition probability ($B(E2)$) for the ^{92}Mo $2^+ \rightarrow 0^+$ transition at 1510 keV.

Method	$t_{1/2}$ (ps)	τ (ps)	$B(E2)$ ($e^2\text{fm}^4$)
Literature	0.35(2) [83]		
DCM	0.33(14)	0.47(20)	221(90)
DDCM	0.34(12)	0.49(18)	212(78)

4.4. Analysis of the Two-Proton Transfer Channel: lifetimes in ^{90}Zr and ^{94}Ru

4.4.1. Analysis of ^{90}Zr

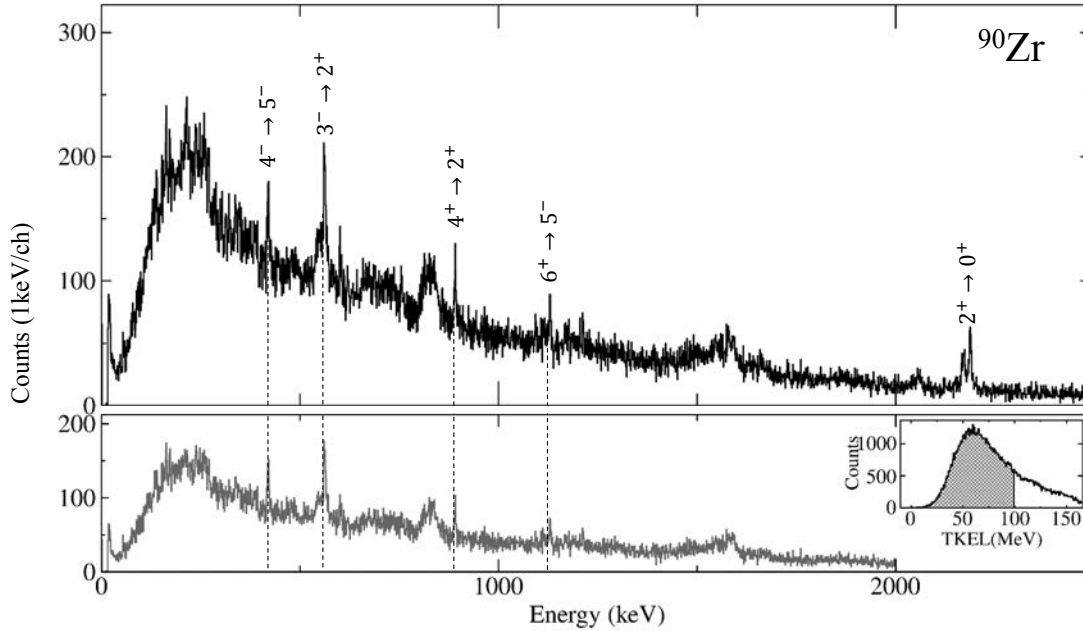


FIGURE 4.20: Doppler corrected gamma-ray energy spectrum for ^{90}Zr for the shortest target-to-degrader distance. Top: Full spectrum without gating on the TKEL. Bottom: Spectrum with a gate on the low part of the TKEL.

The Doppler corrected gamma-ray spectrum for ^{90}Zr with the identified transitions is depicted in Fig. 4.20. In Fig. 4.21, the level scheme for the ^{90}Zr nucleus is shown. The transition of interest, $4^+ \rightarrow 2^+$, is marked in red.

None of the feeders for the yrast 4^+ state are observed in the gamma-ray spectrum. As indicated in Fig. 4.21, the $6^+ \rightarrow 4^+$ transition has an intensity 1.95(7)% [89], while the $6^+ \rightarrow 5^-$ has an intensity of 100.0(5)% [89]. Therefore, comparing the intensities of our measured spectrum (top panel in fig4:90Zrspec) the latter transition appears with an intensity of around 70% related to the $4^+ \rightarrow 2^+$ transition, which implies a negligible contribution of 1% for the $6^+ \rightarrow 4^+$ transition (371 keV) as compared with the $4^+ \rightarrow 2^+$ transition.

The TKEL condition has been applied to avoid this possible, although negligible, contribution and any possible unobserved feeding. Therefore, as in the case of the

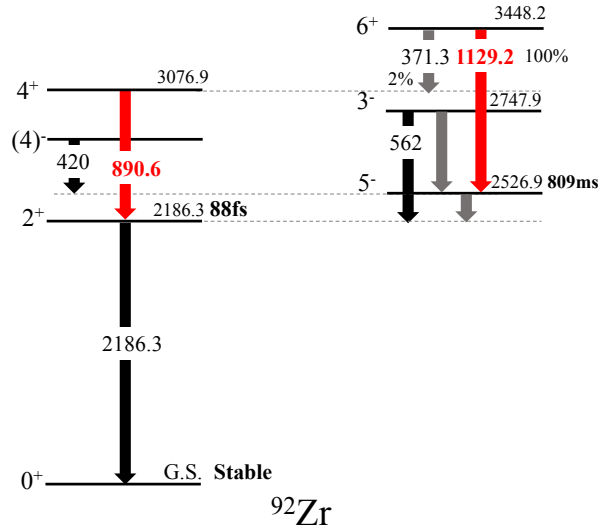


FIGURE 4.21: Simplified level scheme of ^{90}Zr showing the feeding levels for the transitions of interest (in red). The gamma-ray transitions represented by grey lines have not been observed in the energy spectrum. The thickness of the transitions do not account for their observed intensity. Instead of that, the corresponding intensities taken from Ref. [89] are indicated with numbers. If no number is indicated the intensity is 100%.

4^+ state in ^{92}Mo , the analysis has been done considering that the state is directly populated at time $t = 0$ using Eqs. (4.12) and (4.13) for the DCM and DDCM methods, respectively.

The half-life of the $2^+ \rightarrow 0^+$ is known to be 88(3)fs [89], which lies outside the limits of the RDDS sensitivity. The measurement of the $6^+ \rightarrow 5^-$ allows to determine the lifetime of the 6^+ state and, hence, to calculate the reduced transition probability of the $6^+ \rightarrow 4^+$ via the corresponding branching ratio correction deduced from the aforementioned intensities taken from Ref. [89]. This measurement is also useful for the completion of the systematics of the $N=50$ isotones collectivity in the $g_{9/2}$ for the $6^+ \rightarrow 4^+$. The same cut in the TKEL loss is used in this case and no feeders are considered for the lifetime determination.

The variation of the two components in the peak for the $4^+ \rightarrow 2^+$ and $6^+ \rightarrow 5^-$ transitions is shown in Fig. 4.22. In the spectra of the latter transition, a contribution of another transition is observed in a similar energy (1122 keV). This corresponds to the second 2^+ state decaying to the yrast 2^+ state, which has a known half-life of 91(6) fs [89]. Therefore, only one component will appear fully shifted. This is illustrated with the dashed blue line in Fig. 4.22. For the shortest distances, where the 6^+ decays mainly after the degrader the shifted component of the second 2^+ is appreciated clearly, while for the longer distances this contribution

is masked by part of the 6^+ decaying before the degrader. This has been included in the analysis by doing a three peaks fit of the line components for the different distances.

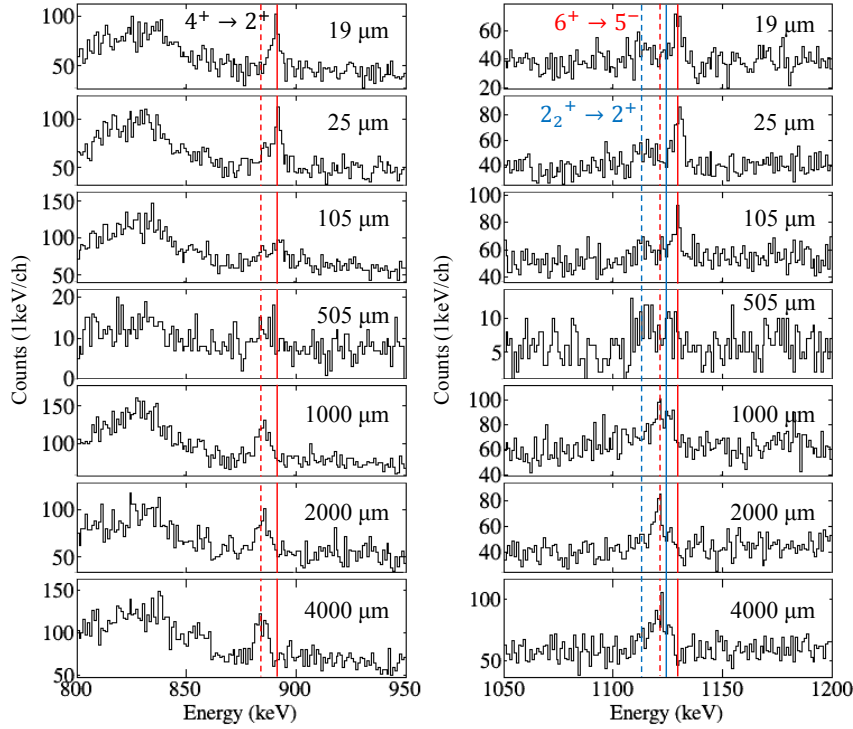


FIGURE 4.22: Doppler corrected spectra of ^{90}Zr showing the $4^+ \rightarrow 2^+$ (890.7 keV) and $6^+ \rightarrow 5^-$ (1129.2 keV) transitions region for the seven distances measured with the TKEL cut illustrated in Fig. 4.20. The solid lines indicate the unshifted component (after the degrader) and the red dashed lines, the shifted component (before the degrader). The red lines account for the transitions of study. The contribution from the $2_2^+ \rightarrow 2^+$ lying in a similar gamma-ray energy as the $6^+ \rightarrow 5^-$ transition is shown in blue (see text for details).

The DCM and DDCM curves are represented in Figs. 4.23 and 4.24 and the measured values are listed in Tables 4.3 and 4.4. Due to these difficulties regarding the peak areas extraction the lifetime determination using the $6^+ \rightarrow 5^-$ transition, and consequently, the reduced transition probabilities for the $6^+ \rightarrow 4^+$ transition are considered tentative.

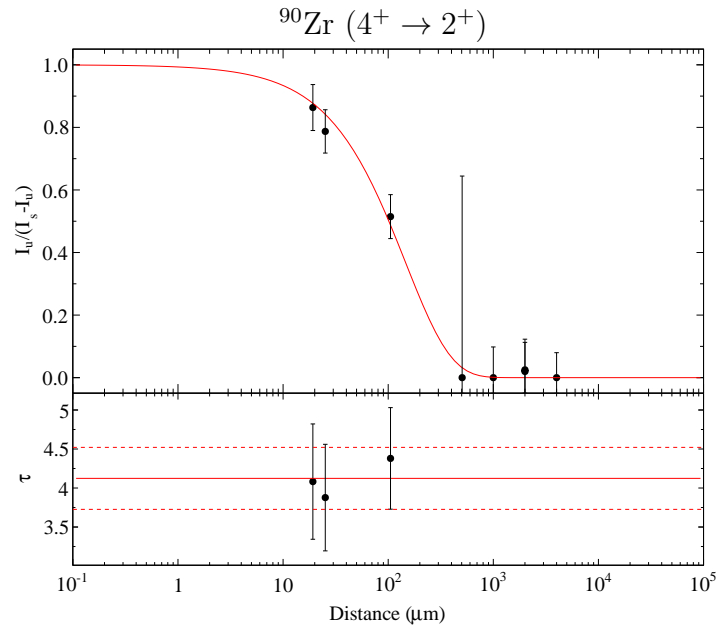


FIGURE 4.23: Decay curve for the $4^+ \rightarrow 2^+$ transition in ^{90}Zr . On the top panel the conventional DCM method has been applied. The bottom panel shows the DDCM implemented within the region of sensitivity. The solid red lines represent the corresponding fits for each method. The dashed lines represents the experimental uncertainty to the one standard deviation level. The error bars of the of the distances (x-axis) are not visible because they are smaller than the symbols.

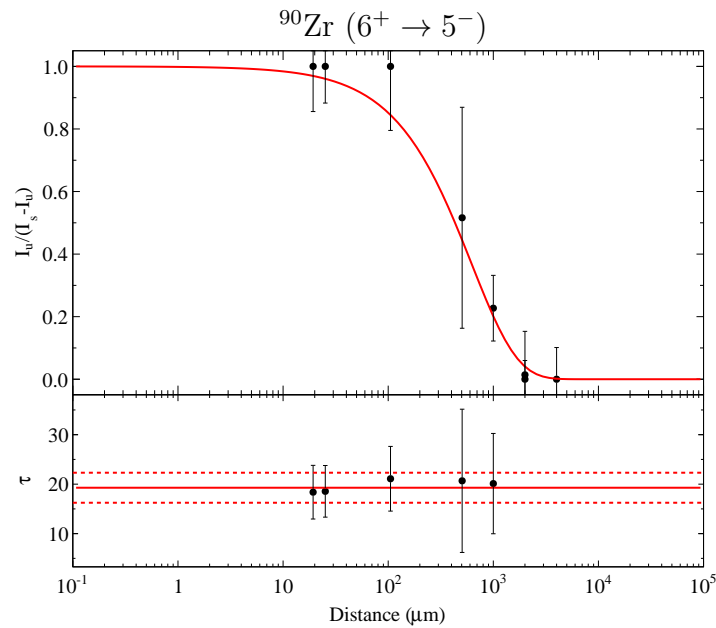


FIGURE 4.24: Decay curve for the $6^+ \rightarrow 5^-$ transition in ^{90}Zr . On the top panel the conventional DCM method has been applied. The bottom panel shows the DDCM implemented within the region of sensitivity. The solid red lines represent the corresponding fits for each method. The dashed lines represents the experimental uncertainty to the one standard deviation level. The error bars of the of the distances (x-axis) are not visible because they are smaller than the symbols.

TABLE 4.3: Half-life ($t_{1/2}$), lifetime (τ) and reduced transition probability ($B(E2)$) for the $^{90}\text{Zr } 4^+ \rightarrow 2^+$ transition at 890 keV.

Method	$t_{1/2}$ (ps)	τ (ps)	$B(E2)$ ($e^2\text{fm}^4$)
DCM	3.0(5)	4.3(7)	297(50)
DDCM	2.9(3)	4.2(4)	304(30)

TABLE 4.4: Tentative half-life ($t_{1/2}$), lifetime (τ) for the $^{90}\text{Zr } 6^+ \rightarrow 5^-$ transition at 1129 keV and reduced transition probability ($B(E2)$) for the $6^+ \rightarrow 4^+$ transition at 371 keV.

Method	$t_{1/2}$ (ps)	τ (ps)	$B(E2)$ ($e^2\text{fm}^4$)
DCM	12(7)	18(5)	120(30)
DDCM	13(3)	19(4)	115(24)

4.4.2. Analysis of ^{94}Ru

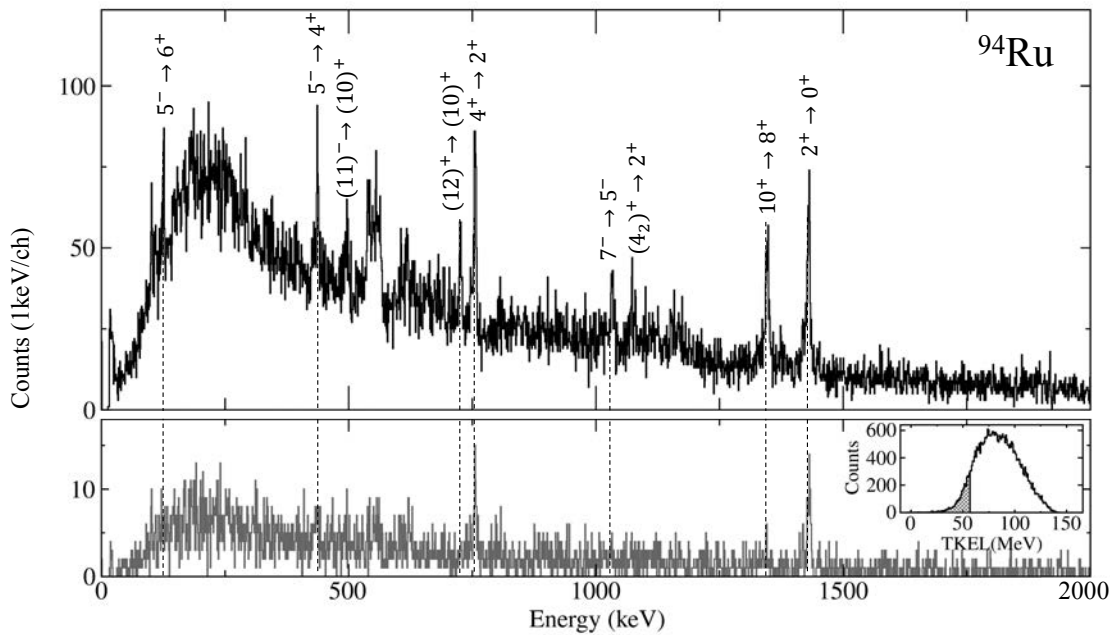


FIGURE 4.25: Doppler corrected gamma-ray energy spectrum for ^{94}Ru for the shortest target-to-degrader distance. Top: Full spectrum without gating on the TKEL. Bottom: Spectrum with a gate on the low part of the TKEL.

The transitions identified in ^{94}Ru are shown in the gamma-ray spectrum in Fig. 4.25. In order to take into account the long-lived feeder existing in this nucleus for the yrast 4^+ state, the same procedure as in the inelastic case has been implemented. As seen in the bottom panel of Fig. 4.25, the TKEL cut is necessary to avoid the high lying feeding levels of the yrast 4^+ state. However, it reduces drastically the statistics in the energy spectrum. An accurate lifetime measurement cannot be

achieved with such limited statistics, hence, only the *method 2* has been used to extract the lifetime. This method consisted of the subtraction of the contribution from the long-lived state to the intensities of the state of interest.

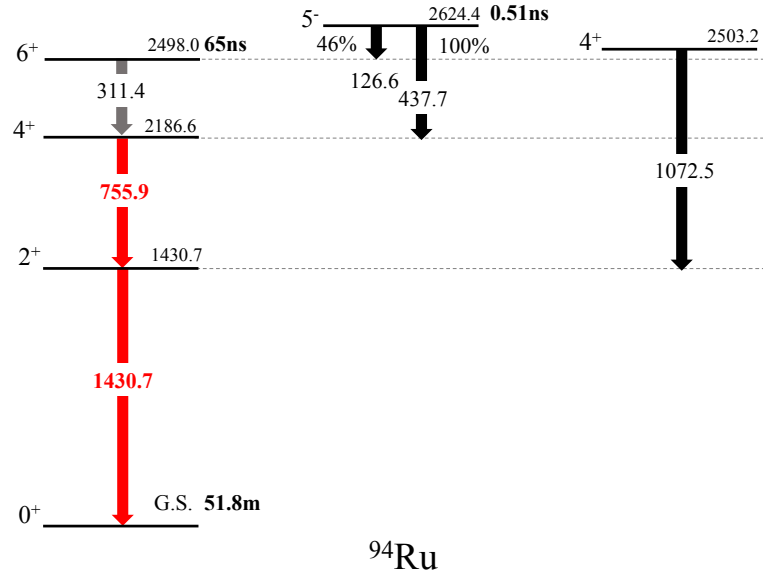


FIGURE 4.26: Simplified level scheme of ^{94}Ru showing the feeding levels for the transitions of interest (in red). The gamma-ray transitions represented by grey lines have not been observed in the energy spectrum. The thickness of the transitions do not account for their observed intensity. Instead of that, the corresponding intensities taken from Ref. [89] are indicated with numbers. If no number is indicated the intensity is 100%.

In Fig. 4.26 the level-feeding pattern for the transitions of interest in ^{94}Ru is schematically depicted. After the subtraction of the 5^- state contribution, the 4^+ state was analysed as a directly populated state using Eqs. (4.12) and (4.13) for the DCM and DDCM methods, respectively. For the 2^+ state analysis (after the subtraction) the general formulas Eqs. (4.5) and (4.10) were used for a state populated by two levels above (4^+ and 4_2^+). The contributions of the observed feeding have been estimated to be 51% from the yrast 4^+ state and 7% from the 4_2^+ state.

The lifetime of the latter has been also analysed to be included in the decay equations and corresponds to 12(8)ps. The variation of the two components in the peaks of the transitions of interest for the different distances is shown in Fig. 4.27. The decay curves and the resulting lifetime values are shown in Figs. 4.28 and 4.29 and Tables 4.5 and 4.6 for the $4^+ \rightarrow 2^+$ and $2^+ \rightarrow 0^+$ transitions, respectively.

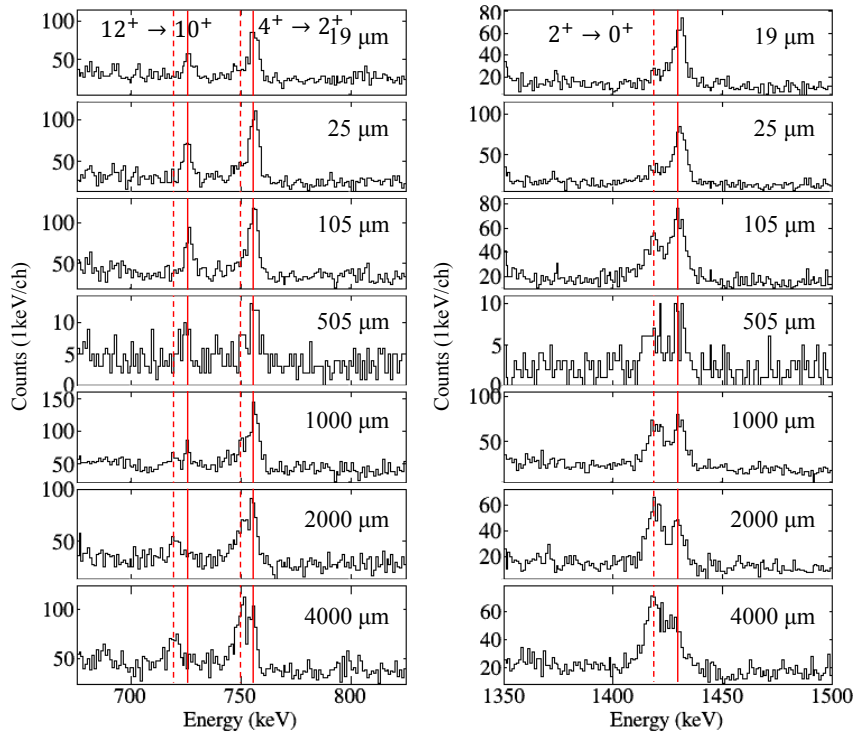


FIGURE 4.27: Doppler corrected spectra of ^{94}Ru showing the $4^+ \rightarrow 2^+$ (755.5 keV) and $2^+ \rightarrow 0^+$ (1430.7 keV) transitions region for the seven distances measured. The red solid lines indicate the unshifted component (after the degrader) and the red dashed lines, the shifted component (before the degrader).

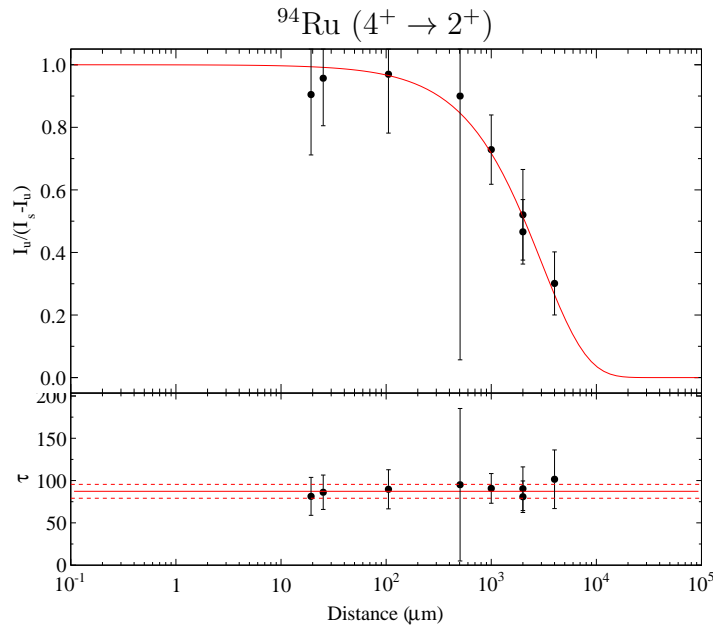


FIGURE 4.28: Decay curve for the $4^+ \rightarrow 2^+$ transition in ^{94}Ru . The data have been processed to subtract the contribution of the $5^- \rightarrow 4^+$ transition. On the top panel the conventional DCM method has been applied. The bottom panel shows the DDCM implemented within the region of sensitivity. The solid red lines represent the corresponding fits for each method. The dashed lines represents the experimental uncertainty to the one standard deviation level. The error bars of the of the distances (x-axis) are not visible because they are smaller than the symbols.

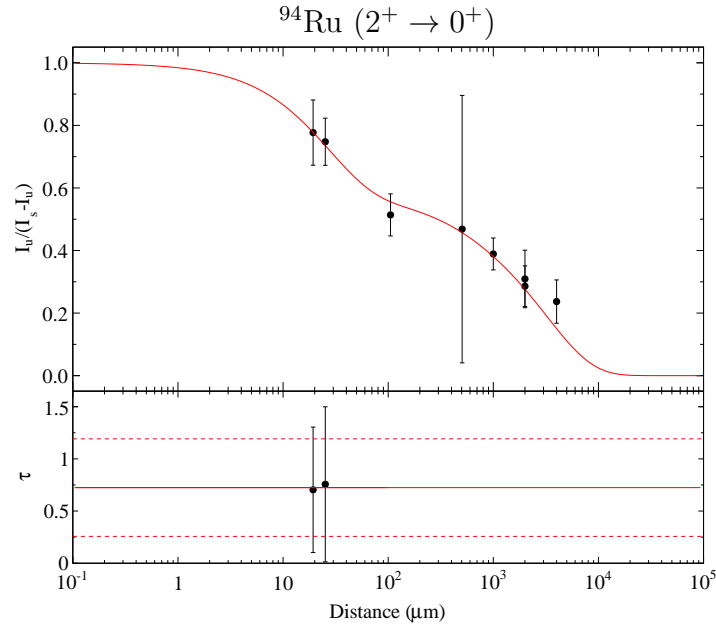


FIGURE 4.29: Decay curve for the $2^+ \rightarrow 0^+$ transition in ^{94}Ru . The data have been processed to subtract the contribution of the $5^- \rightarrow 4^+$ transition. On the top panel the conventional DCM method has been applied. The bottom panel shows the DDCM implemented within the region of sensitivity. The solid red lines represent the corresponding fits for each method. The dashed lines represents the experimental uncertainty to the one standard deviation level. The error bars of the of the distances (x-axis) are not visible because they are smaller than the symbols.

TABLE 4.5: Half-life ($t_{1/2}$), lifetime (τ) and reduced transition probability ($B(E2)$) for the ^{94}Ru $4^+ \rightarrow 2^+$ transition at 755 keV.

Method	$t_{1/2}$ (ps)	τ (ps)	$B(E2)$ ($e^2\text{fm}^4$)
Literature	≤ 50 [11]		
DCM	61(11)	89(16)	37(7)
DDCM	66(6)	87(8)	38(4)

TABLE 4.6: Half-life ($t_{1/2}$), lifetime (τ) and reduced transition probability ($B(E2)$) for the ^{94}Ru $2^+ \rightarrow 0^+$ transition at 1430 keV.

Method	$t_{1/2}$ (ps)	τ (ps)	$B(E2)$ ($e^2\text{fm}^4$)
Literature	≤ 10 [11]		
DCM	0.49(21)	0.7(3)	194(83)
DDCM	0.49(4)	0.7(5)	194(139)

Chapter 5

Theoretical interpretation and Conclusions

As explained in Chapter 1 the main goal of this experiment is the study of the collectivity along the $N=50$ isotones to probe the seniority conservation in $g_{9/2}$ shell for protons, as predicted by shell-model calculations. In the previous chapter the lifetime results obtained for the ^{90}Zr , ^{92}Mo and ^{94}Ru were discussed and used to determine the reduced transition probabilities. This chapter will deal with the shell-model description of these nuclei. These calculations, based on realistic effective interactions, were performed by the theoretical group from INFN, Complesso Universitario di Monte S. Angelo (Napoli, Italy), in particular by A. Gargano and L. Coraggio, in the context of the collaboration performing this study. Eventually, the conclusions and perspectives for this work will be presented.

5.1. The nuclear shell-model

The nuclear shell-model has demonstrated over the years to be a crucial tool for the understanding of nuclear structure. This model simplifies the nuclear many-body problem to only a few active nucleons (the so-called valence nucleons which can be particles or holes) outside a core made up of filled shells, and the shell-model Hamiltonian, composed of a one-body term and a two-body residual interaction, is defined and diagonalized in a truncated space. The physical observables must be calculated within an effective theory, namely the shell-model Hamiltonian has

to take into account all the degrees of freedom that are not considered explicitly [90, 91].

Different types of effective shell-model Hamiltonian exist that can be divided essentially in the following three categories [92]:

- **Empirical interactions.** The optimum values for the single-particle (SP) energies of the one-body term and the two-body matrix elements (TBME) of the residual interaction are obtained from a least-squares fit to the experimental data.
- **Realistic interactions.** The shell-model Hamiltonian, or only the TBME, are obtained by means of many-body techniques starting from the free nucleon-nucleon (NN) potentials, without any empirical adjustment.
- **Schematic interactions.** The two-body term is given by an analytical expression with few adjustable parameters.

For this work a realistic effective interaction is used and its derivation will be discussed briefly in the following section.

5.1.1. Realistic effective Hamiltonian

The nuclear Hamiltonian for a system of A nucleons interacting via two-body forces, can be written as,

$$H = \sum_{i=1}^A \frac{p_i^2}{2m} + \sum_{i<j=1}^A V_{ij} = T + V, \quad (5.1)$$

where T is the kinetic energy and V is the two-body interaction potential. Introducing an auxiliary one-body potential U the Hamiltonian of Eq. (5.1) can be rearranged as,

$$H = (T + U) + (V - U) = H_0 + H_{\text{res}}, \quad (5.2)$$

H_0 being the single particle Hamiltonian, which describes the independent motion of the nucleons, and H_{res} , the residual interaction.

Since it is impossible to solve exactly the full, $H\psi = E\psi$, except for very few nucleon systems, an effective Hamiltonian is defined, as mentioned above, within a reduced Hilbert space, the model space, written in terms of eigenvectors of H_0 . Then, the realistic effective Hamiltonian is defined through the model-space eigenvalue problem,

$$H_{\text{eff}}P|\psi_\alpha\rangle = (H_0 + V_{\text{eff}})P|\psi_\alpha\rangle = E_\alpha P|\psi_\alpha\rangle, \quad (5.3)$$

where the operator P projects from the complete Hilbert space onto the model space, being E_α and the corresponding $|\psi_\alpha\rangle$ a subset of the eigenvalues and eigenfunctions of the original Hamiltonian, respectively.

In the present approach, we derive the shell-model effective interaction V_{eff} in the framework of the many-body perturbation theory [90, 91] starting from the high-precision CD-Bonn NN potential [93]. This potential, due to its strong short range repulsive behaviour, must be renormalized to be used. To this aim, a low momentum potential $V_{\text{low-}k}$ is constructed within a cutoff momentum, $\Lambda = 2.6 \text{ fm}^{-1}$ [93], preserving the on-shell properties of the original one. The $V_{\text{low-}k}$ potential is then used as the two-body interaction term (V) of the Hamiltonian in Eq. (5.1).

The next step to derive V_{eff} is done by the \hat{Q} -box folded-diagram expansion [93], where the \hat{Q} -box is defined as a function of the unperturbed ϵ energy of the valence particles:

$$\hat{Q}(\epsilon) = PH_{\text{res}}P + PH_{\text{res}}Q \frac{1}{\epsilon - QHQ} QH_{\text{res}}P, \quad (5.4)$$

where $Q = 1 - P$. In the present calculations the \hat{Q} -box is obtained by using its perturbative diagrammatic expansion and including one- and two-body diagrams up to third order in the interaction. The folded-diagram series is then summed up to all orders using the Lee-Suzuki iteration method. A detailed description of the derivation of the \hat{Q} -box can be found in [93] and references therein.

With this approach, V_{eff} is derived for systems with two valence nucleons and therefore it is made up of one- and two-body terms. The theoretical SP energies of the shell-model effective Hamiltonian are obtained and the TBME from the two-body contributions of V_{eff} . However, a subtraction procedure can be used, as

done in this work, so as to retain only the two-body terms of V_{eff} , while the SP energies are taken from experiment.

5.1.2. Transition operators

The most common transition operators are the electric quadrupole (E2), the magnetic dipole (M1) and Gamow-Teller (GT) operators. These one-body effective operators are subject to considerable renormalization depending on the shell-model space used [94]. In the particular case of this Thesis the effective electric quadrupole operator $\mathcal{O}_{\text{eff}}(E2)$ is used in order to obtain the corresponding strength on the reduced transition probabilities, which is given by [92]:

$$B(EL; J_i \rightarrow J_f) = \frac{\langle J_f || \mathcal{O}_{\text{eff}}(EL) || J_i \rangle^2}{2J_i + 1}, \quad (5.5)$$

with L being the multipolarity ($L = 2$ for the electric quadrupole), J_i and J_f are initial and final states and $\langle J_f || \mathcal{O}(EL) || J_i \rangle^2$ are the reduced matrix elements, which depends on the coupling constants for protons and neutrons, the electric charges e_π and e_ν , respectively. In a similar way, as for the interaction, the single matrix elements of the one-body effective operator, and hence the effective charges e_{eff} , can be deduced by applying a fitting procedure to the experimental data or using microscopic calculations.

The most reliable data on e_{eff} are obtained from the fit to measured quadrupole moments of high-spin isomers in nuclei near closed shells, since they have relatively pure shell-model character [95].

Alternatively, the effective operator can be given by extending the \hat{Q} -box formalism of Kuo et al. [96] developed for the derivation of H_{eff} to the problem of transition operators. The microscopic calculation of the $\mathcal{O}_{\text{eff}}(E2)$ and e_{eff} for this work follows the procedure described in [93, 96]. The effective transition operators, namely the reduced matrix elements of the effective quadrupole operator, are calculated consistently with the shell-model H_{eff} up to third order in perturbation theory.

Both approaches have been used in the shell-model calculations described in this work.

5.2. Evolution of collectivity along the $\pi g_{9/2}$

The doubly-magic nature of ^{100}Sn has attracted great interest in the last years. Magic numbers represent indeed a key feature of fermionic systems, and reflect the underlying mean field. In particular, the structure of this nucleus and its neighbours are excellent benchmark cases to test state-of-the-art shell-model calculations. The study of the collectivity of the low-lying states along the $N=50$ isotones towards ^{100}Sn can shed light on the seniority scheme validity. Furthermore, it can help to understand the similarities and differences in the properties with the another emblematic region of the nuclear chart: the Ni isotopes near the doubly-magic ^{78}Ni , which are valence-mirror symmetry partners.

5.2.1. Experimental results

The new lifetimes, τ , measured in this work and the corresponding reduced transition probabilities $B(E2)$ values are summarized in Table 5.1. Since the extracted values using the DCM and DDCM methods (discussed in the previous chapter) are in good agreement, the adopted lifetimes have been taken from the value with smaller uncertainty. In the case of the $4^+ \rightarrow 2^+$ in ^{92}Mo a weighted average has been done between the two DDCM values obtained from the different methods of long-lives states subtraction. It should be noticed that the result for the $6^+ \rightarrow 4^+$ transition in ^{90}Zr is written in parenthesis, because of the difficulties found in the lifetime extraction (see Section 4.4.1). The previously measured reduced probability transitions are also reported in Table 5.1.

TABLE 5.1: Adopted lifetimes (τ), half-lives ($t_{1/2}$) and reduced transition probabilities ($B(E2)$).

Nucleus	Transition	τ (ps)	$t_{1/2}$ (ps)	$B(E2)_{exp}$ (e^2fm^4)	$B(E2)_{exp-prev}$ (e^2fm^4)
^{90}Zr	$4^+ \rightarrow 2^+$	4.2(4)	2.9(3)	304(29)	-
	$6^+ \rightarrow 4^+$	(19(4))	(13(3))	(115(24))	-
^{92}Mo	$2^+ \rightarrow 0^+$	0.49(18)	0.34(12)	212(75)	206(12)[89]
	$4^+ \rightarrow 2^+$	35.0(6)	24.3(4)	84.3(14)	<304[89]
^{94}Ru	$2^+ \rightarrow 0^+$	0.7(3)	0.49(21)	194(83)	≥ 9.5 [11]
	$4^+ \rightarrow 2^+$	87(8)	60(6)	38(3)	≥ 46 [11]

The present lifetime results allowed to estimate reduced transition probabilities that were never measured before (only a limit on the lifetime was measured in some cases) for the neutron magic nuclei in this region. In general, the $B(E2)$ strengths are in good agreement with the values and limits measured in previous experiments. The large uncertainty of 35% in the $B(E2; 2^+ \rightarrow 0^+)$ of ^{92}Mo arises from the method used to determine its lifetime. This short lifetime was outside of the range of sensitivity of the RDDS technique and only the values for two distances of the seven measured ones contributed to the lifetime determination. To achieve a systematic uncertainty of the order of the previous measurement safe Coulomb excitation or DSAM techniques should be used [83, 97]. Similarly occurs for the $2^+ \rightarrow 0^+$ lifetime measurement in the case of ^{94}Ru . Regarding the previously quoted limits on the lifetime, the new values are in perfect agreement with the measured limits, except for the $4^+ \rightarrow 2^+$ yrast transition in ^{94}Ru , where the new measured value lies below the upper limit defined. This discrepancy could come from the lifetime measurement technique used in Ref. [11]. The ultrafast-timing method is typically used for lifetimes in the range of tens of picoseconds to microseconds or more [98, 99]. Therefore, the lifetime is in the limit of the sensitivity of this technique and, nevertheless, is appropriated for the measurement with the RDDS technique.

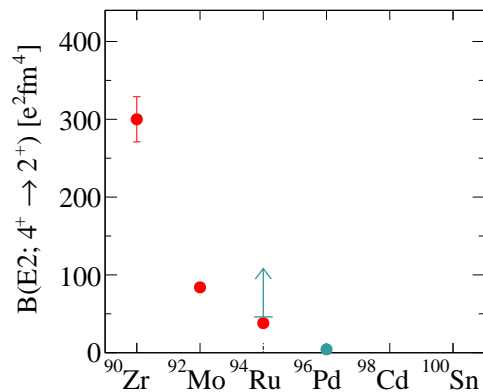


FIGURE 5.1: Experimental collectivity along $N = 50$ of the $4^+ \rightarrow 2^+$ transition. The red symbols are the experimental results of this work. The turquoise symbols are the experimental values from previous experiments, [11].

The evolution of collectivity along the $N = 50$ isotones in the $g_{9/2}$ shell for the $4^+ \rightarrow 2^+$ yrast transition is depicted in Fig. 5.1. The overall trend of the $N=50$

isotones towards ^{100}Sn (excluding the ^{94}Ru limit) confirms the seniority conservation behaviour described in Chapter 1. In the following section the comparison with theoretical models and a complete seniority scheme will be presented.

5.2.2. Theoretical calculations

Shell-model calculations for ^{90}Zr , ^{92}Mo and ^{94}Ru have been performed within the $f_{5/2}$, $p_{3/2}$, $p_{1/2}$, $g_{9/2}$ model space for protons. All the SP energies are derived from ^{59}Cu except for the $g_{9/2}$ orbital that is not yet observed and an estimated energy of 3.2 MeV is used [9]. The residual two-body interaction is obtained starting with the CD-Bonn NN potential as described previously. All the contributions up to third order have been included in the perturbative expansion, using the Q-box folded-diagram method. For the $E2$ transition probabilities, results are presented by using both empirical and microscopic effective charges of the electric quadrupole operator. The first one, indicated as *th1*, uses an empirical effective of charge of $e_{\pi}=1.5e$. The second one, namely *th2*, corresponds to the microscopic derivation of the effective charges [93, 96].

The results for both approaches (*th1* and *th2*) and experimental values for the low-lying excited states and $B(E2)$ transition rates are shown in Tables 5.2 to 5.4, for the ^{90}Zr , ^{92}Mo and ^{94}Ru nuclei, respectively. The agreement between theory and experiment can be considered more satisfactory when using the microscopic effective $E2$ operator, *th2*. Figs. 5.2 to 5.4 illustrate the comparison between the calculated and experimental excitation energies for the ^{90}Zr , ^{92}Mo and ^{94}Ru nuclei, respectively. The numbers between the levels and the thickness of the arrows are proportional to the $B(E2)$ values. In the three figures, the accordance between theoretical and experimental low-energy spectra and $B(E2)$ strengths is excellent. In Fig. 5.2 (^{90}Zr), small discrepancies are found in the energies, while the experimental $B(E2)$ s are satisfactorily reproduced by the theory. For the most interesting case ^{94}Ru , which is the middle of the shell (Fig. 5.4), the pattern observed is consistent with the pattern discussed in Chapter 1 for a seniority conserving interaction in a $(g_{9/2})^4$ system (see Fig. 1.2). The $B(E2; 4^+ \rightarrow 2^+)$ value is very small in comparison with the $B(E2; 2^+ \rightarrow 0^+)$, which is typical of $E2$ transitions between $v = 2$ states in nuclei near mid shell [5].

TABLE 5.2: Experimental and calculated $B(E2)$ strengths of ^{90}Zr . The subindex $th1$ and $th2$ account for the shell-model calculation with empirical and microscopic effective charges, respectively (see text for details).

^{90}Zr			
State	E_{exp} (MeV)	E_{th} (MeV)	
2^+	2.19	2.11	
4^+	3.08	2.94	
6^+	3.45	2.26	
Transition	$B(E2)_{exp}$ (e^2fm^4)	$B(E2)_{th1}$ (e^2fm^4)	$B(E2)_{th2}$ (e^2fm^4)
$2^+ \rightarrow 0^+$	129(4)[89]	148	176
$4^+ \rightarrow 2^+$	304(29)	249	303
$6^+ \rightarrow 4^+$	(115(24))	172	211

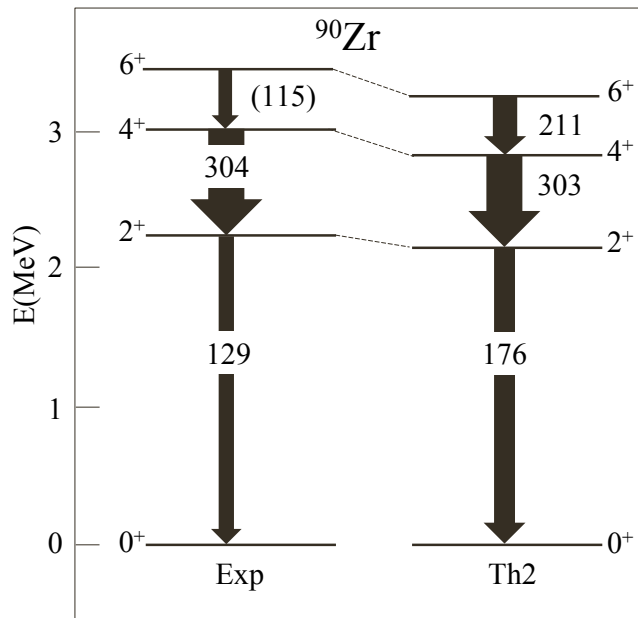


FIGURE 5.2: Experimental and theoretical energy spectra of ^{90}Zr . The numbers and the thickness of the arrows are proportional to the $B(E2)$ strength in e^2fm^4 units. The theoretical values reported correspond to realistic shell-model calculations with microscopic charge. The $B(E2; 2^+ \rightarrow 0^+)$ value is taken from Ref. [89]

TABLE 5.3: Experimental and calculated $B(E2)$ strengths of ^{92}Mo . The subindex $th1$ and $th2$ account for the shell-model calculation with empirical and microscopic effective charges, respectively (see text for details).

^{92}Mo			
State	E_{exp} (MeV)	E_{th} (MeV)	
2^+	1.51	1.54	
4^+	2.28	2.19	
Transition	$B(E2)_{exp}$ (e^2fm^4)	$B(E2)_{th1}$ (e^2fm^4)	$B(E2)_{th2}$ (e^2fm^4)
$2^+ \rightarrow 0^+$	212(75)	194	200
$4^+ \rightarrow 2^+$	84.3(14)	105	100

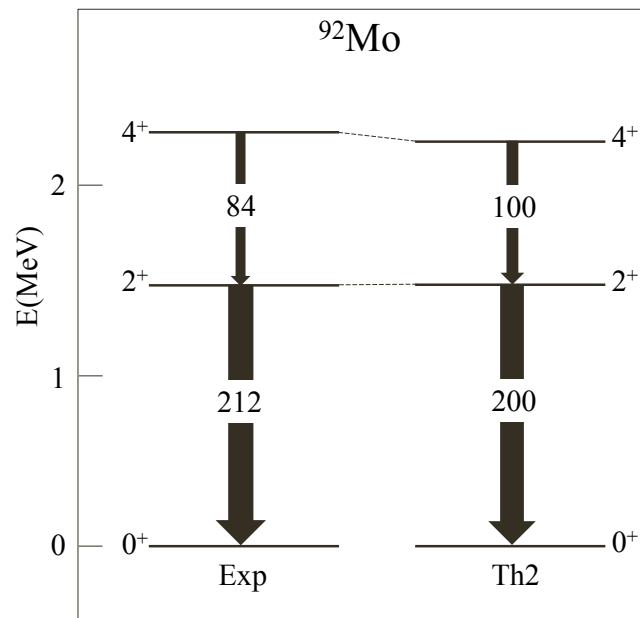


FIGURE 5.3: Experimental and theoretical energy spectra of ^{92}Mo . The numbers and the thickness of the arrows are proportional to the $B(E2)$ strength in e^2fm^4 units. The theoretical values reported correspond to realistic shell-model calculations with microscopic charge.

TABLE 5.4: Experimental and calculated $B(E2)$ strengths of ^{94}Ru . The subindex $th1$ and $th2$ account for the shell-model calculation with empirical and microscopic effective charges, respectively (see text for details).

^{94}Ru			
State	E_{exp} (MeV)	E_{th} (MeV)	
2^+	1.43	1.45	
4^+	2.19	2.08	
Transition	$B(E2)_{exp}$ ($e^2\text{fm}^4$)	$B(E2)_{th1}$ ($e^2\text{fm}^4$)	$B(E2)_{th2}$ ($e^2\text{fm}^4$)
$2^+ \rightarrow 0^+$	194(83)	225	220
$4^+ \rightarrow 2^+$	38(3)	6	10

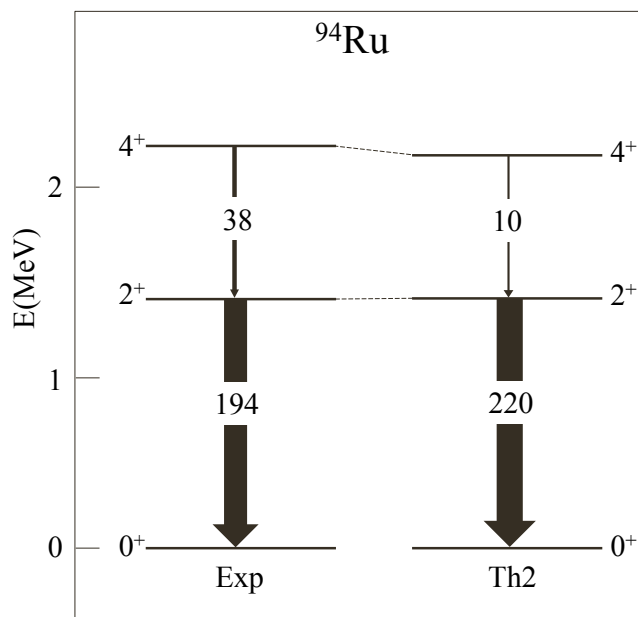


FIGURE 5.4: Experimental and theoretical energy spectra of ^{94}Ru . The numbers and the thickness of the arrows are proportional to the $B(E2)$ strength in $e^2\text{fm}^4$ units. The theoretical values reported correspond to realistic shell-model calculations with microscopic charge.

5.2.2.1. Seniority scheme

In order to evaluate the seniority scheme along the $N = 50$ isotones towards the doubly-magic nucleus ^{100}Sn , a review of the existent experimental $B(E2)$ strengths has been reported in Fig. 5.5 for the 2^+ , 4^+ , 6^+ and 8^+ states in nuclei from $Z = 40$ to 50.

The $B(E2)$ values from this work are depicted in red. The turquoise symbols are the experimental values from previous experiments [11, 89, 100]. Moreover the theoretical calculations are depicted for the evaluation of the seniority conservation. In green, the realistic shell-model calculations performed by the Naples group for this work are shown. The green dashed lines and empty squared symbols indicate the calculations with an empirical charge of $e_\pi=1.5e$. The green solid lines and filled squared symbols correspond to calculations with microscopic charges.

For the sake of completeness, apart from aforementioned shell-model calculations, the theoretical calculations corresponding to the model marked as SMCC in [11] (see section III.A) are also presented in the figure. These calculations are also performed in the $f_{5/2}$, $p_{3/2}$, $p_{1/2}$, $g_{9/2}$ model space for protons using a shell-model effective interaction derived from the CD-Bonn potential, but the TBME are calculated in the hole formalism taking ^{100}Sn as core and the empirical effective proton charge is $e_\pi=1.35e$. The black dashed lines account for these calculations.

Finally, the theoretical approaches account very well for all the transitions in the $N=50$ isotones and, in particular, for the $4^+ \rightarrow 2^+$ transition. Thus, the obtained results on the $B(E2; 4^+ \rightarrow 2^+)$ strengths confirm the expected trend and the conservation of seniority.

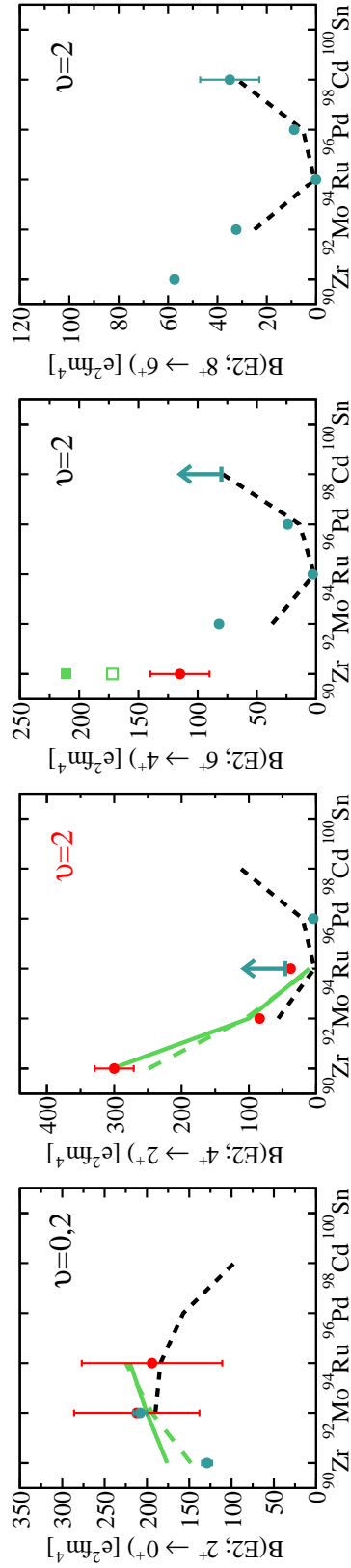


FIGURE 5.5: Evolution of collectivity along $N=50$. Experimental and theoretical $B(E2; 4^+ \rightarrow 2^+)$, $B(E2; 6^+ \rightarrow 4^+)$ and $B(E2; 8^+ \rightarrow 6^+)$ values for $N = 50$ isotones with $A = 90 - 100$. The red symbols are the experimental results of this work. The turquoise symbols are the experimental values from previous experiments, $B(E2; 2^+ \rightarrow 2^+)$ [89], $B(E2; 4^+ \rightarrow 2^+)$ [11], $B(E2; 6^+ \rightarrow 4^+)$ [11, 89] and $B(E2; 8^+ \rightarrow 6^+)$ [89, 100]. The black dashed lines correspond to the shell-model calculation reported in Ref. [11] as SMCC. The green dashed (solid) lines or empty (filled) square are the shell-model predictions for the approach using empirical charges, *th1* (microscopic charges, *th2*) [9]. See text for details. Note that the value of the $6^+ \rightarrow 4^+$ in ^{90}Zr is tentative.

5.3. Summary and conclusions

The evolution of collectivity along the $N = 50$ isotones towards ^{100}Sn has been experimentally studied in this Thesis. To this aim, lifetime measurements for the yrast low-spin states in the $N=50$ isotones ^{90}Zr , ^{92}Mo and ^{94}Ru were performed.

The measurements were realized at the GANIL installation, where the proton-rich region close to $N = Z = 50$ closure shell was successfully populated via a multi-nucleon transfer reaction. This reaction allowed to populate low-lying states in the presence of long-lived feeding by high-spin isomers. The reaction products were uniquely identified by the VAMOS++ magnetic spectrometer, and the gamma-ray in coincidence were measured using the AGATA tracking array. The plunger device was used to determine the lifetimes of the excited states in this region through the Recoil Distance Doppler Shift (RDDS) method. Seven distances, at 19, 25, 100, 500, 1000, 2000 and 4000 μm , were used.

The validity of the setup and methodology has been tested with the lifetime measurement, via two different methods (DCM and DDCM), of the $25/2^-$ excited state in ^{93}Tc and the first 4^+ state in ^{94}Mo . Their results are compatible with the values reported in literature.

The results obtained for the lifetimes and reduced transition probabilities for the yrast $4^+ \rightarrow 2^+$ and $2^+ \rightarrow 0^+$ and $6^+ \rightarrow 4^+$ transitions in ^{94}Ru and ^{92}Mo and ^{90}Zr have been shown. The publication of this results is in preparation and is intended to be published in a *Physical Review Letters*. The measured values for the reduced transition probabilities are in good agreement with realistic shell-model calculations (red symbols in top panel of Fig. 5.6). These calculations (green lines in top panel of Fig. 5.6) for the zero-particle, two-particle and four-particle $\pi g_{9/2}$ nuclei have been performed by the Naples group in the $f_{5/2}, p_{3/2}, p_{1/2}, g_{9/2}$ proton valence space ($\pi(fpg)$) using a realistic effective interaction based on the CD-Bonn NN potential. For the quadrupole operator the effective charge has been deduced fitting to experimental ($e_\pi = 1.5e$) data or from a microscopic calculation. The complete theoretical study along $N = 50$ will be carried out for the publication of the results. Here, the shell-model calculations named SMCC ($\pi(fpg)$, CD-Bonn, $e_\pi = 1.35e$) of H. Mach and coworkers [11] have been included for the sake of completeness along $N=50$ (black dashed lines in top panel of Fig. 5.6).

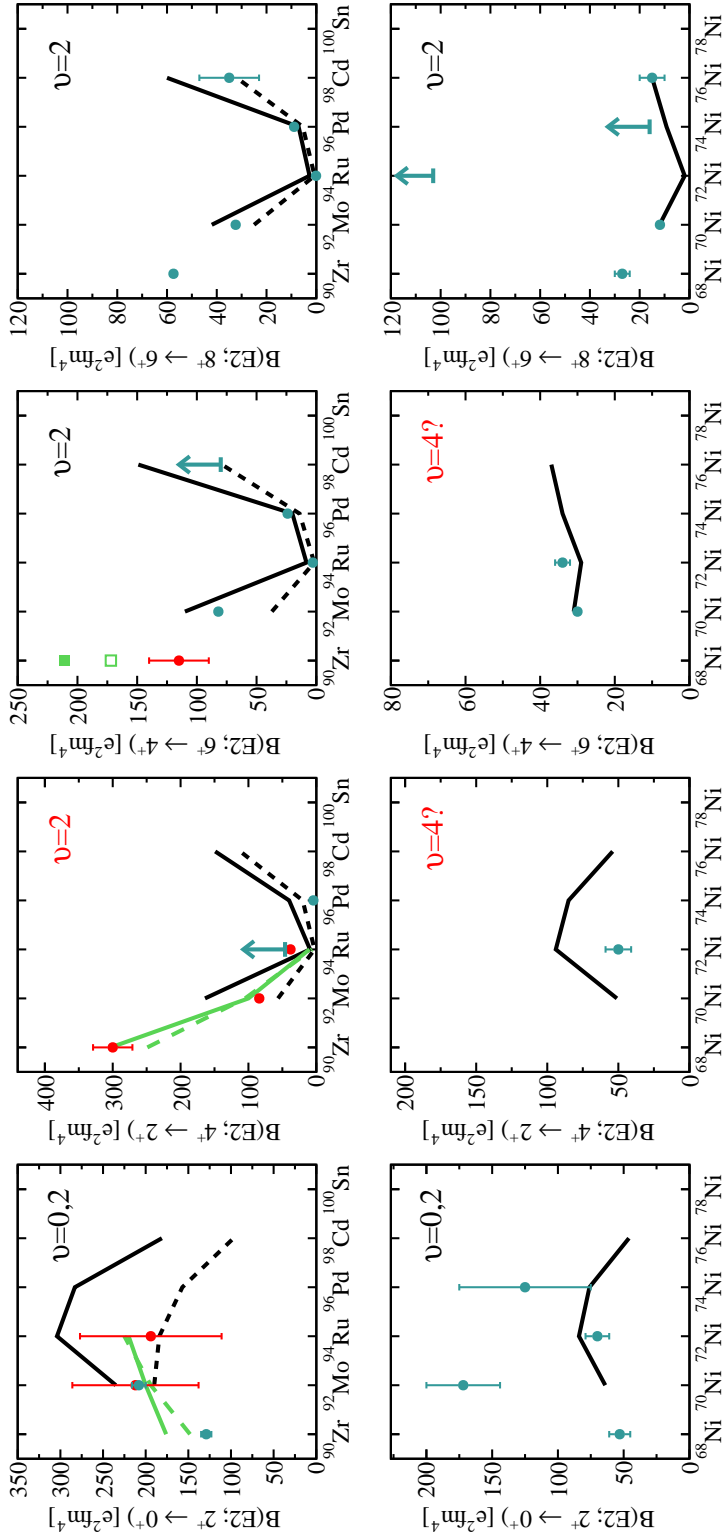


FIGURE 5.6: Evolution of collectivity along the $g_{9/2}$ orbital for the VMS partners with different seniority schemes. Experimental and theoretical $B(E2; 2^+ \rightarrow 0^+)$, $B(E2; 4^+ \rightarrow 2^+)$, $B(E2; 6^+ \rightarrow 4^+)$ and $B(E2; 8^+ \rightarrow 6^+)$ values for $N = 50$ isotones with $A = 90 - 100$ (top) and the $Z = 28$ isotopes with $A = 68 - 78$ (bottom). The red symbols are the experimental results of this work. The turquoise symbols are the experimental values from previous experiments. For the $N = 50$ isotones: $B(E2; 2^+ \rightarrow 0^+)$ [89], $B(E2; 4^+ \rightarrow 2^+)$ [11], $B(E2; 6^+ \rightarrow 4^+)$ [11, 89] and $B(E2; 8^+ \rightarrow 6^+)$ [89, 100]. For the $Z = 28$ isotopes: $B(E2; 2^+ \rightarrow 0^+)$ [101, 102], $B(E2; 4^+ \rightarrow 2^+)$ [102], $B(E2; 6^+ \rightarrow 4^+)$ [103, 104] and $B(E2; 8^+ \rightarrow 6^+)$ [89, 105, 106]. The black solid lines belong to the shell-model calculations discussed in Ref. [8]. The black dashed lines correspond to the shell-model calculation reported in Ref. [11] as SMCC. The green dashed (solid) lines or empty (filled) square are the shell-model predictions for the approach using empirical charges, $th1$ (microscopic charges, $th2$) [9]. Note that the value of the $6^+ \rightarrow 4^+$ in ^{90}Zr is tentative.

The measured $B(E2; 4^+ \rightarrow 2^+)$ values follow the expected trend for $\Delta v = 0$ transitions in the seniority scheme (top panel in Fig. 5.6). Therefore, it can be concluded that the conservation of seniority along $\pi g_{9/2}$ at $N = 50$ is confirmed.

These results allow also for the comparison of the nuclear structure trends between the valence-mirror symmetry (VMS) partners ^{78}Ni - ^{100}Sn $N = 50$ isotones and $^{56-78}\text{Ni}$ $Z = 28$ isotopes. The measured and expected transition probabilities along the $g_{9/2}$ orbital for the VMS partners with different seniority schemes are depicted in Fig. 5.6 for protons (top panels, from ^{90}Zr to ^{100}Sn) and neutrons (bottom panels, from ^{68}Ni to ^{78}Ni). A.F. Lisetskiy and coworkers studied for the first time the calculated structures between this VMS partners [8]. In their calculations, black solid lines in Fig. 5.6, the interactions are derived from a fit to experimental data ($\pi - \nu(fpg)$, Bonn-C, $e_\pi = 2.0e$, $e_\nu = 1.0e$). The different effective two-body interaction observed between the two chains of VMS partners changes some of the nuclear structure features in the middle of the shell as comparing both partners. The main features are summarized in Table 5.5. The effective interaction might not preserve the seniority for the $Z=28$ isotopes towards ^{78}Ni .

TABLE 5.5: VMS partners nuclear structure features comparison in the $g_{9/2}$ mid shell.

^{94}Ru - ^{96}Pd	^{72}Ni - ^{74}Ni
8_1^+ isomer	8_1^+ not isomer
6_1^+ $v = 2$	6_1^+ $v = 4$
4_1^+ $v = 2$	4_1^+ $v = 4$
2_1^+ $v = 2$	2_1^+ $v = 2$

However, as the bottom panel of Fig. 5.6 illustrates, the existing experimental results are inconclusive for the known $Z = 28$ isotopes with valence nucleons in the $g_{9/2}$. For the yrast $8^+ \rightarrow 6^+$ transition, the results are consistent with the absence of 8^+ seniority isomers in ^{72}Ni - ^{74}Ni [104–106]. Nevertheless, recent measurements [104], not observing the isomer, suggest that the normal seniority ordering is recovered at low spins in opposition to the shell-model predictions. Therefore, the measurement of lifetimes of the yrast 4^+ states along the $Z = 28$ isotopes towards ^{78}Ni would help to shed light on the seniority scheme validity in the $(\nu g_{9/2})^n$ configurations and would allow to understand the differences and similarities between the VMS partners in this two emblematic region of the nuclei chart.

Chapter 6

Performance of AGATA

In Chapter 3 the data treatment of the AGATA spectrometer through the series of source measurements performed before and after our experiment was described. In these measurements the same conditions as for the experiment regarding the VAMOS++ electronics and trigger were used. This fact allows us to investigate the performance figures of AGATA in realistic conditions, which is mandatory in order to assess the success and optimal performance of the experiments.

This chapter presents the AGATA performance evaluated on the basis of sources measurements using quantities such as energy resolution, photo-peak efficiency and peak-to-total. Furthermore the performance expectations for in-beam measurements will be discussed.

6.1. AGATA configuration

The early sub-arrays of AGATA, with a limited number of crystals, can be used in nominal or in compact position, i.e. reducing the distance between the target or gamma source and the detectors by displacing one of them along the beam axis [15, 52]. Since AGATA is geometrically designed for the nominal distance, such displacements have sizeable consequences, as for example to unbalance the contribution of the individual detectors to the total efficiency. The selection of the configuration is fundamental for the success of an experiment.

In our measurement, the AGATA sub-array was composed by 8 triple clusters (ATC) organized in a packed geometry to optimize the performance of the tracking

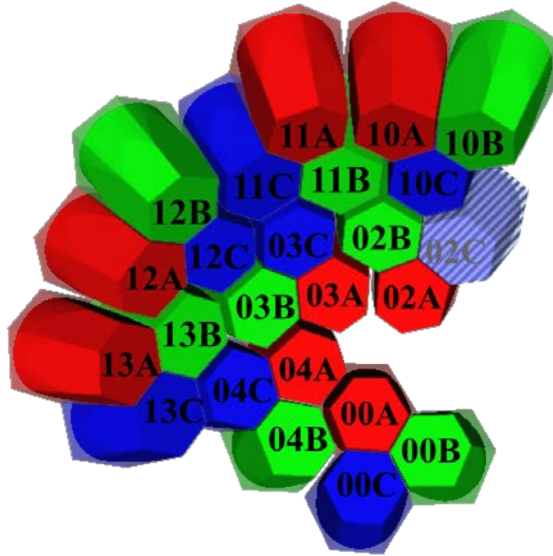


FIGURE 6.1: Configuration of the 24 AGATA crystals as seen from the reaction chamber at GANIL during the E682 experiment in the first AGATA-VAMOS++ campaign. AGATA triples are shown in red (type A), green (type B) and blue (type C), for more information see Section 2.5 . The detector coloured with strips (position 02C) was physically present but not operational.

array. The AGATA clusters were grouped at backward angles with respect to the target position and were set at the target-array distance of 22.8 cm (very close to the AGATA nominal target detector distance) ensuring a good energy resolution for the in-beam Doppler corrected gamma-ray spectra. In Fig. 6.1 the arrangement of the 24 AGATA detectors in ATCs, seen from the center of the reaction chamber, is shown. Only 23 detectors were used for the analysis because the detector in position 02C was not operational. The clusters, the crystals and the positions of the AGATA arrangement are summarized in Table 6.1.

TABLE 6.1: Crystal look up table for the 24 capsules present in the set-up, although only 23 were used for the measurement. *Capsule in position 02C was not operational.

Cluster	Crystal A	Crystal B	Crystal C	Position Array
ATC6	A001	B004	C010	00
ATC8	A009	B005	C008*	02
ATC5	A005	B002	C009	03
ATC1	A008	B001	C003	04
ATC2	A003	B003	C005	10
ATC7	A006	B013	C006	11
ATC3	A002	B010	C001	12
ATC4	A007	B007	C007	13

6.2. Measurement and methodology description

The analysis of experimental data requires the determination of the response of the spectrometer by measuring energy resolution, efficiency and P/T after the corresponding calibrations. It is also relevant for the optimization of the signal processing from individual AGATA crystals. With this purpose, a series of measurements were conducted with calibration sources ^{60}Co and ^{152}Eu before and after the in-beam experiment. The characteristics of radioactive sources used are listed in Table 6.2. The AGATA set-up described in Section 6.1 was comprised of 23 36-fold segmented AGATA crystals positioned at the target-array distance of 22.8 cm. During the in-beam experiments, the target is hold by the VAMOS++ spectrometer reaction chamber, so that the emitted gamma-rays are detected by the surrounding array and the reaction products are identified by the spectrometer. A detailed description of the set-up is given in Chapter 2.

TABLE 6.2: Radioactive calibration sources used for the performance measurement.

Source	Activity(T_0) (Bq)	T_0
^{152}Eu	22296(445)	17/01/2013
^{60}Co	12822(256)	17/01/2013

VAMOS++, as a complementary instrument for AGATA working with common dead-time VME electronics, its front-end electronics and data acquisition systems were coupled to AGATA by the time-stamp and the trigger distributed by the GTS system [13] via the VME AGAVA board. With the aforementioned radioactive sources it is not possible to get signals in the VAMOS++ detectors. Therefore, to simulate the experimental conditions and control the dead-time of the detection system, it was used the *OR* of gammas detected in AGATA, already used in coincidence with the VAMOS++ detectors in experimental conditions. This allows to simulate a VAMOS++ trigger on the front-end electronics and data acquisition system. In our particular case, the Cologne Plunger device was settled inside the chamber for the lifetime measurement (for more information see Chapter 2). With the purpose of keeping the same experimental conditions, each source was centred between the target and the degrader of the Plunger in the VAMOS++ spectrometer reaction chamber (Fig. 6.2(a)).

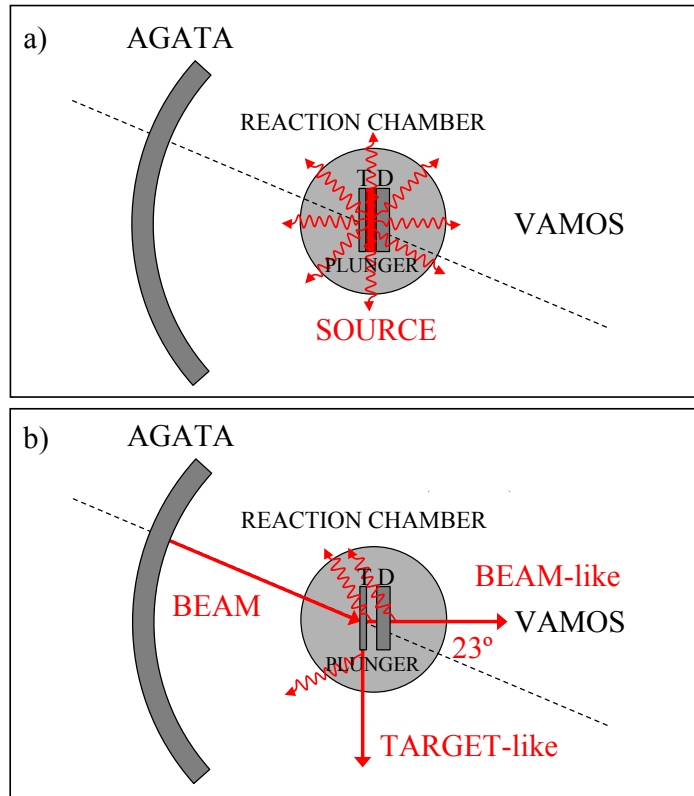


FIGURE 6.2: Schematic view of the detectors configuration from the top. a) Measurement with gamma-ray sources: ^{152}Eu and ^{60}Co . The sources were centred between the target (T, ^{92}Mo) and the degrader (D, ^{24}Mg). b) In-beam measurement. In our experiment the reaction was ^{92}Mo into ^{92}Mo , thus the beam-like and the target-like for the inelastic reaction channel were the same: ^{92}Mo .

In the experiment, a ^{92}Mo beam with an energy of 716.9 MeV impinged in the stretched ^{92}Mo target of the Plunger, while a ^{24}Mg foil was used to degrade the energy of the reaction products. For the efficiency measurement in-beam, the inelastic reaction channel has been used, which, for the reaction mentioned, is the ^{92}Mo . Since the beam and the target are the same (^{92}Mo), the binary partner of the inelastic reaction channel will be also ^{92}Mo . Thus, an approximated efficiency will be measured for the $2^+ \rightarrow 0^+$ transition at 1509 keV in the inelastic channel ^{92}Mo ions going into VAMOS++ i.e. close to 0° in our reference system and for the same transition in its reaction binary partner, again ^{92}Mo but close to 90° from the target position (this is schematically represented in (Fig. 6.2(b))).

In the following sections the AGATA performance for the calibrated gamma-ray sources will be evaluated. We will also estimate the in-beam efficiency to discuss additional effects to be taken into account in experimental conditions. The most

important AGATA performance characteristics to be analysed are the energy resolution, the efficiency and the peak-to-total of the gamma spectroscopy detector array.

6.2.1. Energy Resolution

The *energy resolution* is a measure of the width of a single gamma-ray peak at a specific energy and indicates the capability of a detector to separate two gamma-ray peaks that are close to each other. The most common figure used to express detector resolution is full width at half maximum (FWHM). This is the width of the gamma-ray peak at half of the highest point on the peak distribution (Fig. 6.3).

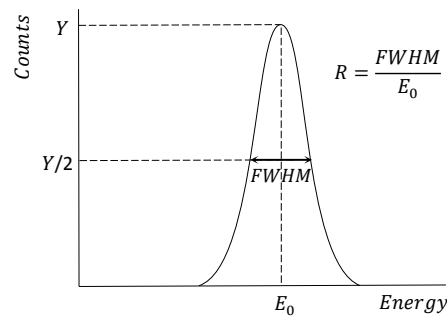


FIGURE 6.3: Detector resolution.

If a standard Gaussian shape is assumed for the photo-peak, the FWHM is given by $2\sigma\sqrt{\ln 2}$, where σ is the Gaussian width parameter.

Better resolution (lower FWHM value) enables the system to more clearly separate the peaks within a spectrum, therefore increasing the sensitivity of the instrument. The HPGe detectors have an excellent resolution -of the order of 2 per mil at 1 MeV- permitting the observation of fine details in the gamma energy spectrum. In particular, a big improvement in the accuracy of the determination of the lifetimes by means of Doppler techniques -that require high resolution- is achieved with the use of arrays of HPGe detectors, which provide large efficiencies at similar angles, with the detectors located symmetrically around the axis defined by the reaction product trajectories. This is very important in order to distinguish the two components in a lifetime measurement using RDDS technique with a Differential Plunger. The presence of a degrader in the plunger device generates large counting rates in the germanium detectors when the necessary beam intensity is used to achieve the required statistics in time coincidence with the magnetic spectrometer. As mentioned previously in Chapter 2, the material of the degrader is chosen such

that the reactions on it do not produce triggers in the magnetic spectrometer, but nevertheless the counting rate in the Ge detectors due to the reactions on this material is unavoidable. In Fig. 6.4 an example is shown for the counting rates reached with a source of ^{152}Eu (~ 550 Hz per crystal with 19650 Bq) and in-beam conditions (~ 50 kHz per crystal at 1pA). The best energy resolutions are

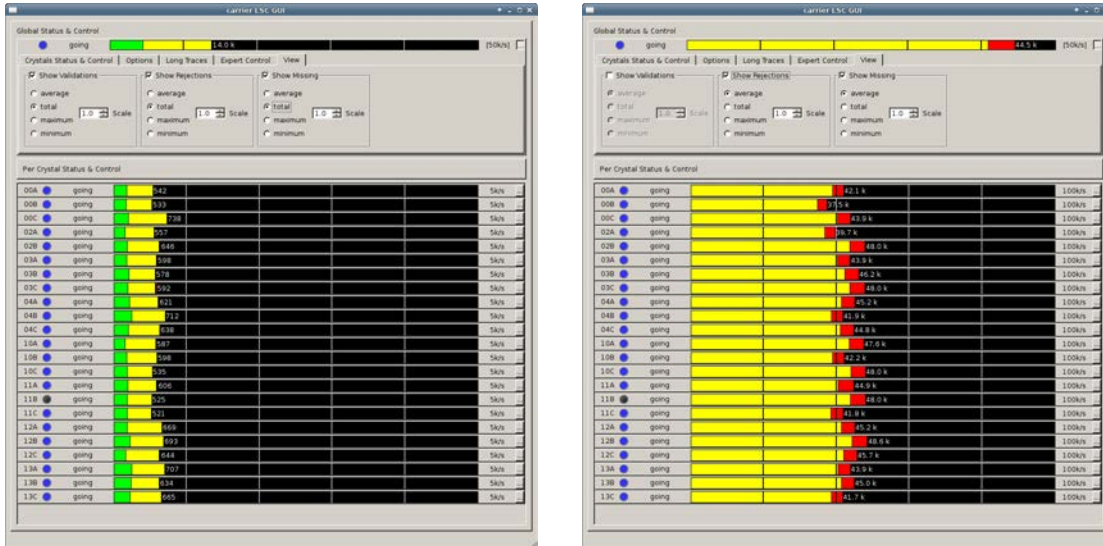


FIGURE 6.4: Counting rate per detector registered in the Carrier GUI. On the left, counting rates generated by the ^{152}Eu calibration source with an activity of 19650 Bq. On the right, counting rates produced in-Beam with an intensity of $\sim 1\text{pA}$.

achieved when the germanium detector operates at low counting rates and large shaping times (MWD-risetime, see Chapter 2). Hence, both energy resolution and efficiency suffer losses when operating at experimental conditions (low shaping times and high rates) [55]. In particular the efficiency losses are due to the pile-up protection. The higher are the rate and the MWD-risetime, the bigger are the so called pile-up losses. Fig. 6.5, taken from reference [55], shows the efficiency as a function of the counting rate and the MWD-risetime selected. The efficiency decreases as the counting rate increases, decaying faster for the largest MWD-risetimes. Concerning our experimental case, the counting rates are around 40 to 50 kHz, which implies a loss of 60% in efficiency for a MWD-risetime 10 μs .

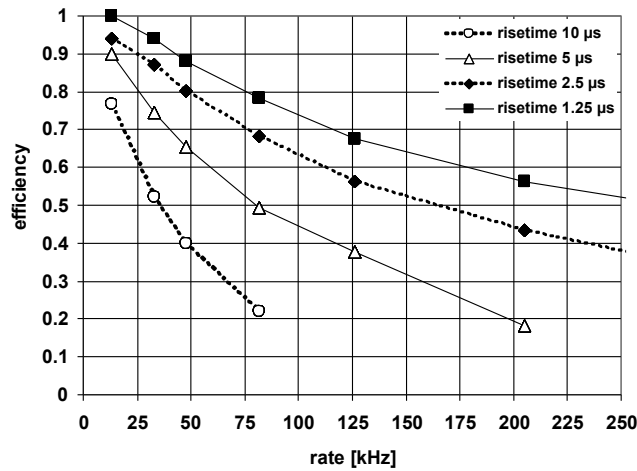


FIGURE 6.5: Efficiency as a function of the counting rate for different MWD-risetimes [55].

In order to avoid a huge loss of efficiency the MWD-risetime chosen for the experiment was $2.5 \mu\text{s}$. The energy resolution is slightly affected by the selection of a low MWD-risetime, but still good enough to distinguish the two components of the lifetime measurement. In Fig. 6.6 an example is shown for the energy resolution behaviour as function of different MWD-risetimes ($10 \mu\text{s}$, $5 \mu\text{s}$ and $2.5 \mu\text{s}$) for the calibration source ^{60}Co of one of the AGATA triple clusters.

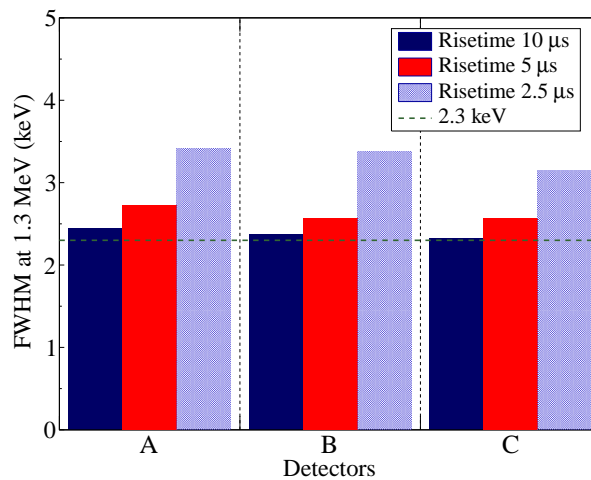


FIGURE 6.6: FWHM at 1.332 MeV (^{60}Co) of the central contact for different MWD-risetimes (see legend) for detectors at position 13. The MWD-risetime used in the experiment was $2.5 \mu\text{s}$.

Resolution values in Fig. 6.6 are given respect to the 1332 keV gamma ray energy.

6.2.2. Efficiency and Peak-to-Total

Since gamma-rays can travel a large distance between interactions and not all the gamma-rays that pass through the detector will deposit all the energy, in order to determine the intensity of the transitions, it becomes necessary to have a precise figure for the detector efficiency. The detector efficiency is the probability that an emitted gamma-ray interacts with the detector and produces a count at the full absorption energy peak. This can be classified as *absolute efficiency* and *intrinsic efficiency*,

$$\varepsilon_{abs} = \frac{\text{number of } \gamma \text{ recorded}}{\text{number of } \gamma \text{ emitted by the source}}, \quad (6.1)$$

$$\varepsilon_{int} = \frac{\text{number of } \gamma \text{ recorded}}{\text{number of } \gamma \text{ incident on the detector}}. \quad (6.2)$$

Both efficiencies are dependent on the detector properties, but while in the intrinsic efficiency the detector geometry is not included as a implicit factor, the absolute efficiency depends on it. Then, the two efficiencies are related by,

$$\varepsilon_{int} = \varepsilon_{abs} \frac{4\pi}{\Omega}, \quad (6.3)$$

where Ω is the solid angle subtended by the detector from the source position. Moreover, the detector efficiency can be classified in other two categories related to the type of the event recorded: The *total efficiency*, ε_{total} , where all the pulses from the detector are accepted and the aforementioned *photo-peak efficiency*, ε_{peak} , where only the full-energy peak pulses are taken into account. The ratio of these efficiencies is known as the *peak-to-total* ratio.

$$P/T = \frac{\varepsilon_{peak}}{\varepsilon_{total}}. \quad (6.4)$$

Another kind of efficiency definition commonly used for gamma-ray detectors is the *relative efficiency* which is the efficiency of one detector relative to another. Typically the relative efficiency of a germanium detector is specified at 1332 keV (^{60}Co) as a percent of the of the efficiency of a 3 in \times 3 in NaI detector at 25cm distance from the source and the same gamma-ray energy (known to be 1.2×10^{-3}).

6.2.2.1. Methodology of Analysis

To measure the detector efficiency a calibrated source is placed at a determined distance from the detector. Comparing the counts detected in the spectrum from a source of known activity with the counts expected to be emitted one can obtain the absolute photo-peak efficiency (following the Eq. (6.1)),

$$\varepsilon_{peak}(E) = \frac{N_{\gamma}(E) / (1 - D_t)}{A \cdot I_R(E) \cdot \Delta t}, \quad (6.5)$$

where A is the activity of the source, $I_R(E)$ the relative intensity of the gamma transition E , D_t the dead-time of the system, Δt the time interval of the measurement and $N_{\gamma}(E)$ the number of counts in the peak with energy E . The number of counts $N_{\gamma}(E)$ is obtained by integrating the total area under the peak after background subtraction. More details about the procedure are explained in the section of results. This approach corresponds to the measurement of the photo-peak efficiency *in singles* (left part in Fig. 6.7).

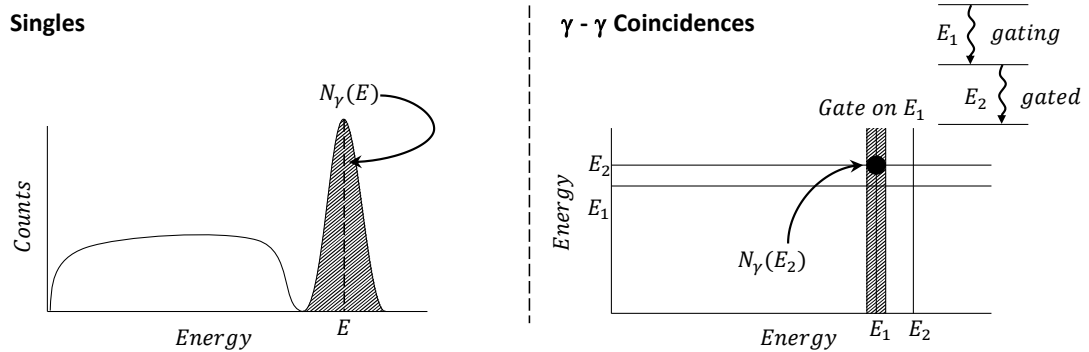


FIGURE 6.7: Schematic illustration for the two approaches used to obtain the absolute photo-peak efficiency.

An alternative to this method is the efficiency *in coincidences* (right part in Fig. 6.7) of two gamma-rays from the same cascade (Fig. 6.8), which consists of setting a gate on the events in which the transition above (with gamma energy E_1) have been detected in time coincidence with the transition below (with gamma energy E_2). Using Eq. (6.5) and the equivalence $I_T = I_R \cdot (1 + \alpha_T)$, the number of counts detected in singles for the energy of the transition above is,

$$N_{\gamma,sing}(E_1) = S \cdot I_T(E_1) / (1 + \alpha_T(E_1)) \cdot \varepsilon_{peak}(E_1), \quad (6.6)$$

where,

$$S = A \cdot (1 - D_t) \cdot \Delta t \quad (6.7)$$

and $I_T(E_1)$ and $\alpha_T(E_1)$ are, respectively, the total intensity and the total internal conversion coefficient of the transition energy E_1 . On the other hand, the number of counts detected in coincidence after gating on the transition above is given by,

$$\begin{aligned} N_{\gamma,coinc}(E_2) &= S \cdot W(\theta) \\ &\times I_T(E_1)/(1 + \alpha_T(E_1)) \cdot \varepsilon_{peak}(E_1) \\ &\times I_T(E_2)/(1 + \alpha_T(E_2)) \cdot \varepsilon_{peak}(E_2), \end{aligned} \quad (6.8)$$

where the sub-index 1 corresponds to the transition above (gating), sub-index 2 corresponds to the transition below (gated) and $W(\theta)$ is the angular correlation correction between the two transitions.

As shown in Fig. 6.8, in a two gamma-rays cascade an intermediate state j is formed from an initial state of spin j_1 via multipolarity λ_1 and decays to a final state of spin j_2 via multipolarity λ_2 .

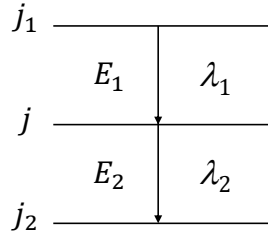


FIGURE 6.8: Example of the level scheme for two gamma-rays cascade via pure transition.

The angular correlation of two successive gamma-rays is expressed as a Legendre polynomial series of the angle between the two direction given by the two gamma-rays multiplied by a coefficient,

$$W(\theta)^1 = \sum_{k=0,2,..} A_k(j_1\lambda_1j\lambda_2j_2) P_k(\cos\theta), \quad (6.9)$$

¹ In the in beam angular correlation the direction of the beam is also involved which implies a more complicated expression (see [107, 108]). Some hints about the in-beam angular correlations can be inferred from the results in Section 6.3.2.2.

with $k_{max} = \min \{2\lambda_1, 2\lambda_2, 2j\}$. If we assume that each decay has been produced via pure transition the coefficients are given by [84],

$$A_k(j_1\lambda_1j\lambda_2j_2) = F_k(j_1\lambda_1j) F_k(j_2\lambda_2j),^2 \quad (6.10)$$

Coming back to the efficiency in coincidences, from Eqs. (6.6) and (6.8) and knowing that the $I_T(E_2) = 1$ (the second transition is measured through a gate on the first transition therefore its intensity will be 100% since, in the cases of study, the first transition is fully decaying to the second one) the following equation is extracted,

$$\varepsilon_{peak}(E_2) = \frac{N_{\gamma,coinc}(E_2)}{N_{\gamma,sing}(E_1) \cdot W(\theta) \cdot 1/(1 + \alpha_T(E_2))}, \quad (6.11)$$

with this method we avoid the dependencies on the source activity and the dead-time of the system, which makes the measurement more reliable.

6.3. Results

As described in Chapter 3 the raw data have been treated with the chain of Narval actors before the analysis. The signals of the AGATA crystals have been processed in two levels. Firstly, each crystal data are processed individually (local level processing) in order to obtain the interaction points using the Pulse Shape Analysis techniques [13]. Afterwards, the data from the separately treated crystals are built together into a global event (global level processing) to perform the gamma-ray tracking [109].

Although AGATA is a tracking array, it can be also used as the conventional arrays utilizing the signals from the central contacts. Then, depending on the type of spectra generated at the different stage of analysis, the performance figures have been evaluated through the following modes of analysis:

- The *core common* mode is the sum of the individual energy histograms for the central contacts.

² The F_k coefficients can be found in the Tab. 2A.2 from the reference [84] for all possible combinations of angular momenta.

- The *calorimeter* mode is the total sum of energies of all the central contacts of the whole AGATA array. Note that is meaningful only when a single gamma-ray is being detected by the array. Coincident gamma-rays will artificially reduce the peak efficiency in calorimetric mode.
- The *tracked* mode is the reconstructed energy by the tracking algorithm which uses the information given by the PSA. Depending on the origin of the energy sent to the tracking, two modes can be used: *tracked from the sum of the segments* (its energy is reconstructed by using the sum of the energy of the segments) and *tracked from the core* (its energy is built making the energy of the segments equal to the energy of the central contact (core) using the option "ForceSegtoCore" (see Chapter 3 for more details).

The reconstruction of the gamma-ray path has been performed using the Orsay Forward Tracking (OFT) algorithm. The evaluation of the OFT parameters have been done previously in Chapter 3, concluding that the set of parameters $\sigma_\theta = 0.8$, $prob_{sing} = 0.02$ and $prob_{track} = 0.05$ provides the best combination of peak-to-total and efficiency figures.

In this section the performance figures will be presented, firstly, for the sets of data with the calibrated sources and later for the in-beam data set.

6.3.1. Performance with sources

The different modes of AGATA analysis explained in the section above are illustrated in Fig. 6.9 using the ^{152}Eu spectrum. The blue spectrum in Fig. 6.9 corresponds to the core common mode, the red spectrum, to the calorimeter mode and the green one, to the tracked mode using the parameters described in the figure.

As described earlier, two sets of data have been evaluated for the tracking. Fig. 6.10 shows a comparison between two tracking modes. The blue spectrum corresponds to a tracking mode where the segments energies are forced (set) to the central contact value. The red line spectrum results from the energy sum of all segments. It should be observed that due to the physics of the segmented germanium detector, the sum energy of the segments contains a number of events with a deficit in the

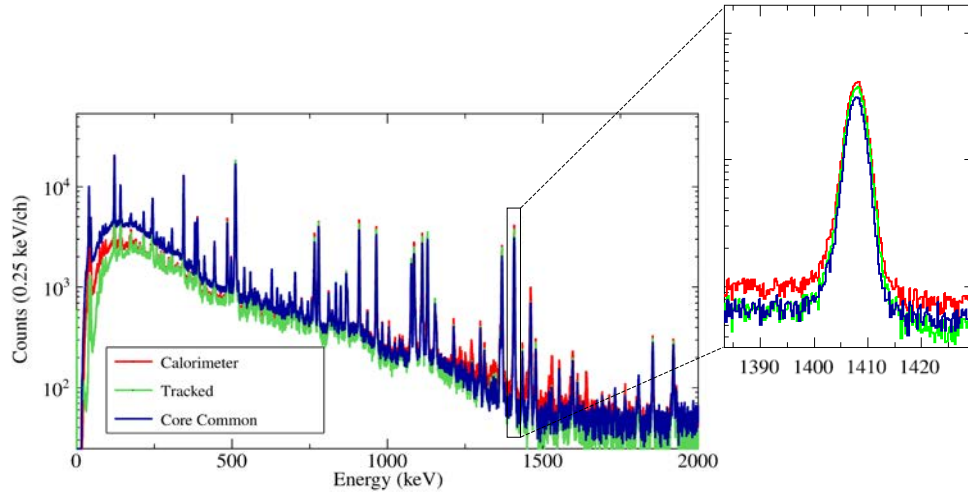


FIGURE 6.9: Comparison of the spectra of ^{152}Eu using the different operational modes of AGATA. The OFT parameters used for the tracking are $\sigma_\theta = 0.8$, $prob_{sing} = 0.02$ and $prob_{track} = 0.05$. In this example is shown the spectrum for the case of tracked data using the core energy.

evaluated energy that results in a large tail in the left part of the peak (red line in the zoomed spectrum in Fig. 6.10).

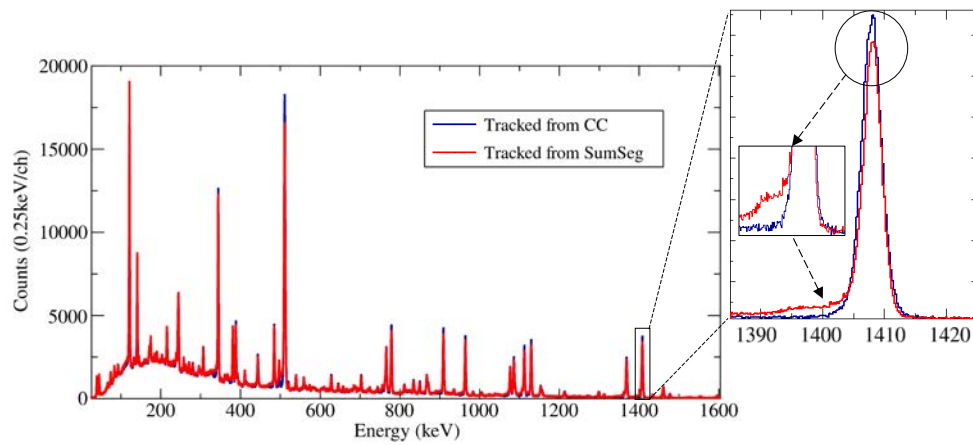


FIGURE 6.10: Comparison between the tracked spectra regarding the nature of the energy sent to the tracking. OFT parameters used in both cases: $\sigma_\theta = 0.8$, $prob_{sing} = 0.02$ and $prob_{track} = 0.05$

Each of the AGATA analysis modes, described before, have been used to estimate the performance values of the AGATA sub-array with calibrated sources, which will be a reference for the in beam experiments.

6.3.1.1. Energy Resolution

As described in Section 6.2.1 high counting rates critically affect the efficiency and requires a low MWD-risetime, which degrades the energy resolution of the germanium detectors. The MWD-risetime chosen for the experiment was 2.5 μ s, which avoided a huge loss in efficiency at the cost of only small losses on energy resolution.

Another important factor influencing the quality of energy resolution is the neutron damage. After the detectors have been exposed to fast neutrons produced in deep inelastic collisions, fission and fusion evaporation reactions during the previous experiments in the campaign at GANIL in 2015, some AGATA crystals were damaged by the charge traps created by neutron radiation damage in the germanium crystal. These traps are lattice defects, that lead to a reduction of the charge collection efficiency. The latter appears as a low energy tail on the energy line shape (red line in Fig. 3.17). In position sensitive Ge detectors, like the AGATA ones, it is possible to apply an empirical correction to the neutron damage effect, based in a constant density of trapping defects and the travel distance of the charges being collected [63]. Section 3.1.1 describes the neutron damage correction applied to the affected detectors (04B, 04C, 11A, 11C, 12A, 12C, 13A) in order to recover a good energy resolution. Fig. 6.11 displays the resolutions for the central contacts (core) and sum of segments for the used detectors at 1.3 MeV. The figure shows that segments are more sensitive to neutron induced traps than the core.

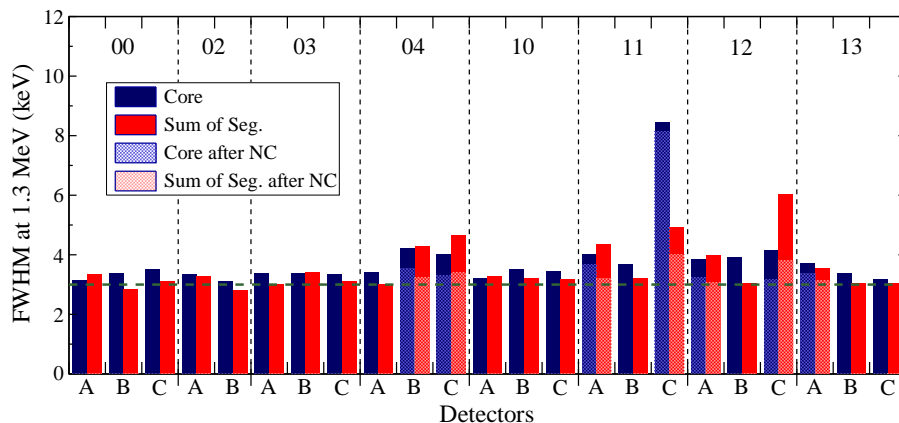


FIGURE 6.11: FWHM at 1.332 MeV (^{60}Co) of the central contact (blue) and the sum of segments (red) before (dark colours) and after (light colours) the neutron damage correction for the 23 capsules individually named with its position label. The green dashed line is drawn to guide the eye.

In general, all measured FWHM resolutions for the crystals are within the range 2.8-3.2 keV, except for the detector 11C. The latter, apart from being neutron damaged was having a resolution problem in both core (especially) and segments, due to electronic noise. In the case of the cores the average FWHM excluding detector 11C is ~ 3.5 keV, while in the case of the sum of the segments the average FWHM becomes better, ~ 3.2 keV. Fig. 6.12 shows the resolution as a function of the energy. As expected from the individual resolutions, the global sum of segments (empty circles) presents a better resolution than the core common one (filled circles). The tracking resolutions (triangles) get worse compared to each corresponding analysis modes (see labels in Fig. 6.12). The calorimeter resolution (squares) is slightly higher in comparison with the tracking from the core energy.

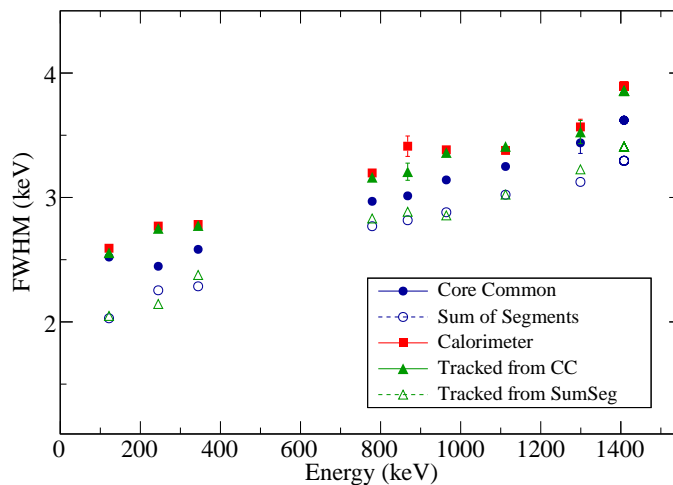


FIGURE 6.12: FWHM as a function of the energy for the different modes of analysing the AGATA data.

A good energy resolution is very important in order to distinguish the two components in a lifetime measurement using the Differential Plunger Technique. For this reason the tracking, with the energy coming from the sum of segments, is the suitable option for our experiment.

6.3.1.2. Efficiency and Peak-to-Total

As mentioned before, two approaches have been used to analyse the efficiency of the different AGATA modes: the efficiency in singles and the efficiency in coincidences, which can be compared after the dead-time evaluation of the system.

The efficiencies in singles were obtained by comparing the detected peak areas to the expected intensities given the source activity, the time of measurement and the electronics dead-time (Eq. (6.5)). To extract the peak areas a Gaussian fit with background subtraction has been done using the Radware software package [110]. In addition, the radioactivity due to the activation of the chamber during the in-beam measurement was still present. As can be seen in Fig. 6.13, five of the peak lines of the ^{152}Eu source are contaminated (down triangles) and thus the efficiency values extracted (Fig. 6.14 blue line). Therefore, for the efficiency in singles, the background radiation must be subtracted from the actual measurement. For that, a measurement without source was taken immediately just after the measurement with source. In this way, the subtraction of the background could be done normalizing to the timestamps that provide the time interval measured. Fig. 6.14 illustrates how the background radiation subtraction gives rise to the recovery of the efficiency curve shape for the energy lines affected in the ^{152}Eu spectrum (red line).

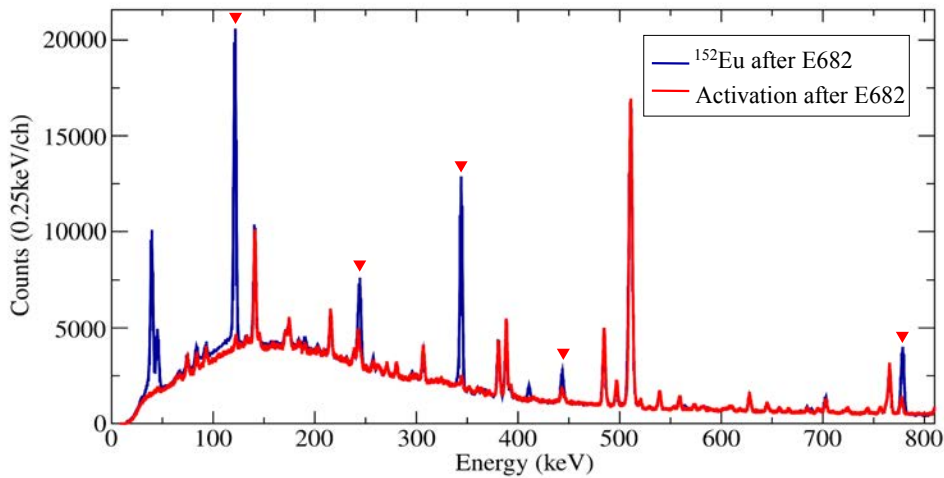


FIGURE 6.13: Core common energy spectrum of ^{152}Eu source in comparison with the background when no source is present. Down triangles point out the energy lines of ^{152}Eu affected by the background.

The efficiencies in coincidences were determined by comparing the detected peak areas in cascades of two gamma-rays, Eq. (6.11), within a coincidence time window selected: the area in coincidences, from the gated transition, and in singles, from the gating transition. For that, the following pairs of gamma-rays cascades have been evaluated: 121 keV-1408 keV, 121 keV-244 keV and 344 keV-778 keV from the ^{152}Eu source and 1332 keV-1173 keV from the ^{60}Co source. The total internal conversion coefficients for the gamma-rays of interest are summarized in Table 6.3.

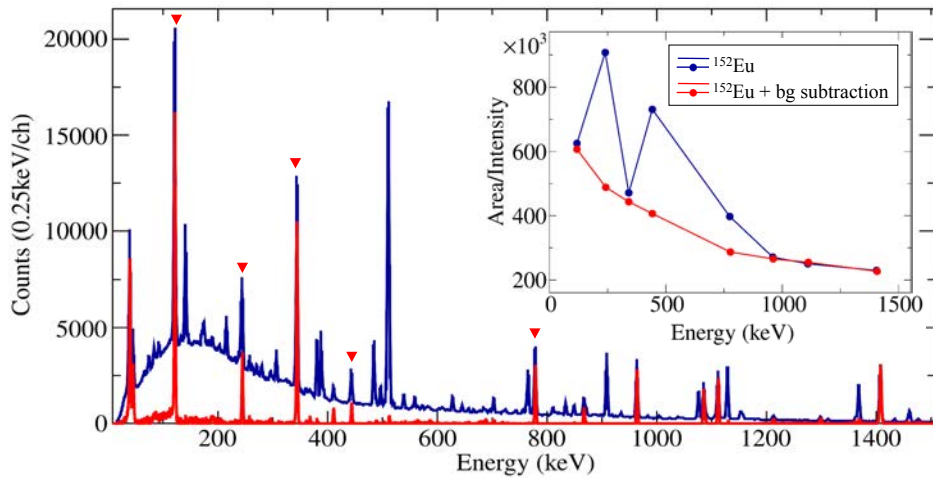


FIGURE 6.14: Core common energy spectrum of ^{152}Eu and the corresponding efficiency curve before (in blue) and after (in red) the background subtraction. Down triangles mark out the energy lines of ^{152}Eu affected by the background.

The angular correlation correction of the two successive gamma-rays have been applied on a event by event basis for each one of the cascades analysed using Eq. (6.9) with the corresponding angular correlation coefficients calculated in Table 6.4. To extract the area in coincidences (peak area of the gated energy) in addition of the Gaussian fit with background, the background coming from the gating energy was subtracted by evaluating the correlated background in both sides of the gating energy.

TABLE 6.3: Total internal conversion coefficient for different nuclei and different gamma-ray energies [111].

Nuclei	E (keV)	α_T
^{60}Ni	1332.5	0.0001625(23)
^{152}Sm	121.8	1.155(17)
^{152}Gd	344.3	0.0398(6)

The calculated A_k coefficients from the reference [84] are listed in Table 6.4 for the gamma-ray cascades, which are of interest in connection with our experiments.

It should be pointed out that when using the modes core common or calorimeter in the coincidences method, the events are identified from the transition above detected in one of the array's crystals. For that reason the gating crystal is excluded from the counts contributing to the events in coincidence for the core common or calorimeter spectra. The exclusion of one crystal is taken into account by adding a correction factor to Eq. (6.11) $N/N - 1$, where N is the number of crystals.

Moreover, the time window of coincidences is performed using the timing of the

TABLE 6.4: Angular correlation coefficients for different cascades of two gamma-rays calculated from the F_k coefficients of the Table 2A.2 in [84]. The initial state of spin j_1 decays to an intermediate state of spin j emitting a gamma-ray of multipolarity λ_1 , which in turn decays to the final state of spin j_2 via a gamma-ray multipolarity λ_2 . *The first transition in the $2^- \rightarrow 2^+ \rightarrow 0^+$ (1408 keV, 121 keV) cascade is of mixed multipole (E1+M2) but is assumed pure for simplicity since the mixing ratio is $\delta=+0.043$ [89].

Nuclei	$j_1 \rightarrow j \rightarrow j_2$	λ_1	λ_2	A_2	A_4
$^{60}\text{Ni}, ^{152}\text{Sm}$	$4 \rightarrow 2 \rightarrow 0$	E2	E2	0.1020	0.0091
^{152}Sm	$2 \rightarrow 2 \rightarrow 0$	E1*	E2	0.2499	0
^{152}Gd	$3 \rightarrow 2 \rightarrow 0$	E1	E2	-0.0714	0

cores in both cases, while in the tracked option it is made with the timing of the tracked gammas.

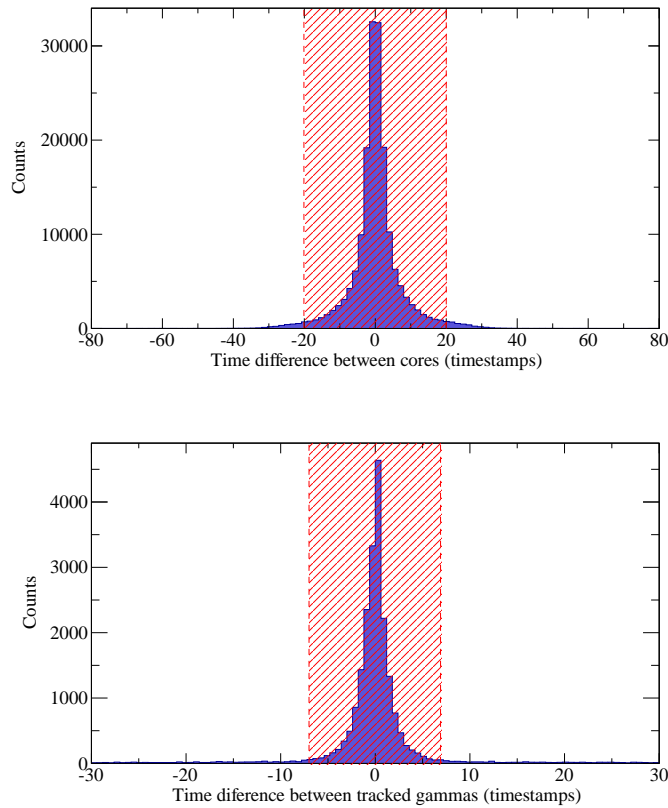


FIGURE 6.15: Time window gamma-gamma coincidence.

The coincidence time windows selected for the gamma-gamma coincidence method are represented in Fig. 6.15. For the cores a time window of 400 ns (top figure) has been selected, while for the tracked gammas a time window of 140 ns (bottom figure).

The photo-peak efficiency has been calculated for each detector in order to know the functioning of each detector individually. The relative core efficiency at 1.3 MeV for each detector at nominal position is shown in Fig. 6.16. The mean value is around 80% of efficiency.

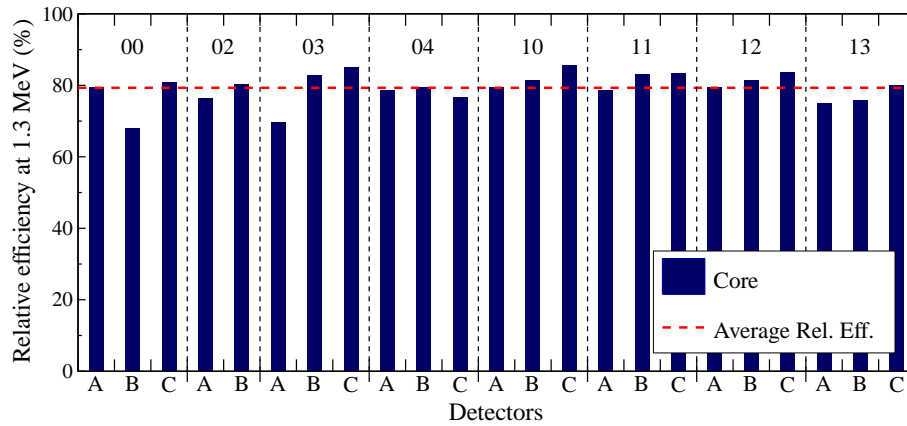


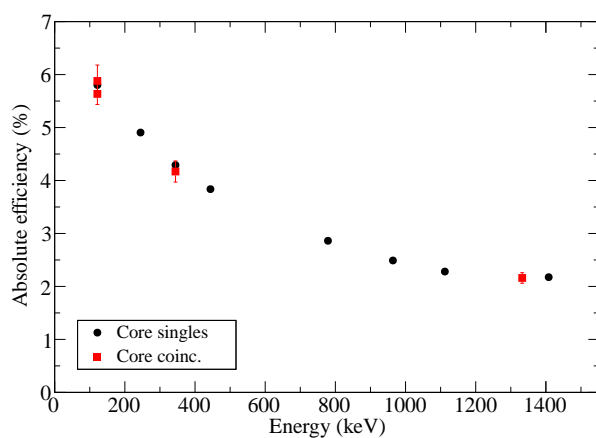
FIGURE 6.16: Relative core efficiency at 1.3MeV (^{60}Co) for the 23 capsules individually named with its position label. The red line is the average relative core efficiency.

In general all the relative efficiencies agree within the mean value, thereby ensuring no losses in the global efficiency.

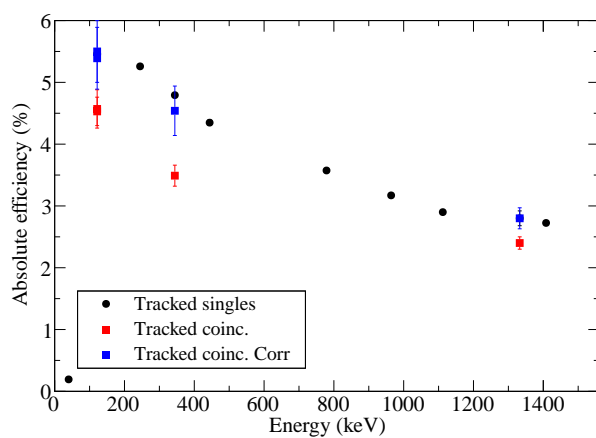
Regarding the global efficiency, the values have been obtained for several of the evaluations mentioned in the introduction to Section 6.3, i.e., core common, tracked forcing the energy of the segments to the central contact and tracked taking the energies of the individual segments.

The absolute photo-peak efficiency for the whole array, composed of 23 operational crystals, is presented in Fig. 6.17 for the nominal position of AGATA. The values obtained by the method in singles are compared with the results in coincidences for the core common and tracked methods.

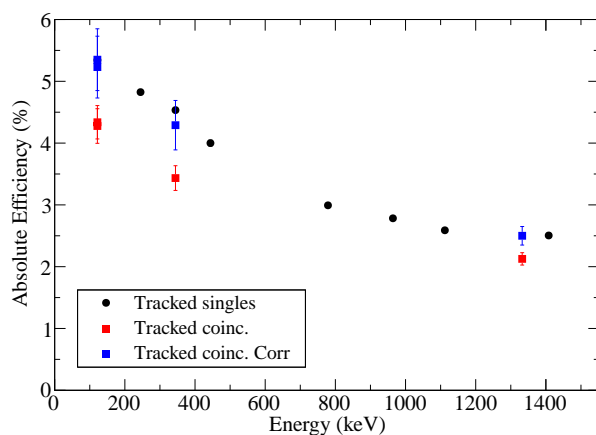
The efficiencies obtained in coincidences (red squares) agree with the efficiency curve in singles for the core common mode (Fig. 6.17(a)). Comparing both methods the dead-time of the electronic system can be estimated and contrasted with the dead-time measured by the VAMOS++ scalers. This was needed since in the measurements we are triggering the VAMOS++ data acquisition using the OR of the gammas detected in AGATA to simulate the experimental conditions, Table 6.5.



(a) Core Common efficiency.



(b) Efficiency for Tracked gamma-rays with core energies.



(c) Efficiency for Tracked gamma-rays with segment energies.

FIGURE 6.17: Absolute efficiency for the 23 capsules of the AGATA sub-array at 22.8 cm distance target position to detectors obtained with the data from ^{152}Eu and ^{60}Co . The different modes of analysis are presented in singles (black circles) and in coincidences (red squares). The tracking efficiency in coincidences has been corrected by the losses due to the angular correlation correction (blue squares, see text for more details). The OFT parameters used for the tracking are $\sigma_\theta = 0.8$, $prob_{sing} = 0.02$, $prob_{track} = 0.05$. The rate per crystal at this position was around 500 Hz.

TABLE 6.5: Electronics dead-time estimation.

Measurement	D_t from Scalers (%)	D_t estimated (%)
^{152}Eu	66	69
^{60}Co	64	61

By contrast, for tracked gamma-rays with both energy determination methods, even after applying the corresponding dead-time corrections to each data set, sizeable discrepancies are obtained comparing the results of the efficiency in singles and the one in coincidences (red squares, Figs. 6.17(b) and 6.17(c)). These discrepancies might be related to the fact that the tracking algorithms cluster together interactions within a given solid angle. Consequently, they are not able to recognize two gamma-rays, which appear inside the same cluster as individual ones. This fact is clearly reflected in the angular correlation measurements from the tracked data.

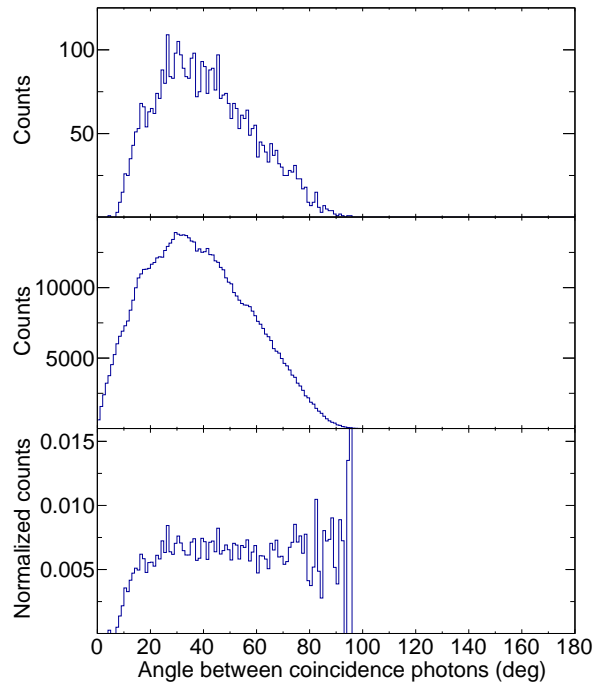


FIGURE 6.18: Angular distributions: on top, correlated gamma-rays; in the middle, uncorrelated gamma-rays; and, down, normalized events. Example for the ^{60}Co source, $4^+ \rightarrow 2^+ \rightarrow 0^+$ cascade.

In order to correct for these deficiencies and restore the real efficiency in coincidences (blue squares, Figs. 6.17(b) and 6.17(c)), the angular correlation has been built as shown in Fig. 6.18, following the procedure described in [112]. On the top panel, the angular distribution for correlated events is presented. This shows the angle between the first interaction points for two gamma-ray in the cascade

of interest per event. In the middle, the angular distribution for uncorrelated events is shown, the latter is built from angles between the first interaction points of two gamma-rays in the cascade of interest corresponding to different events. By normalizing the correlated events with the uncorrelated events (i.e. correcting by the geometrical effects) the angular correlation is extracted as illustrated on

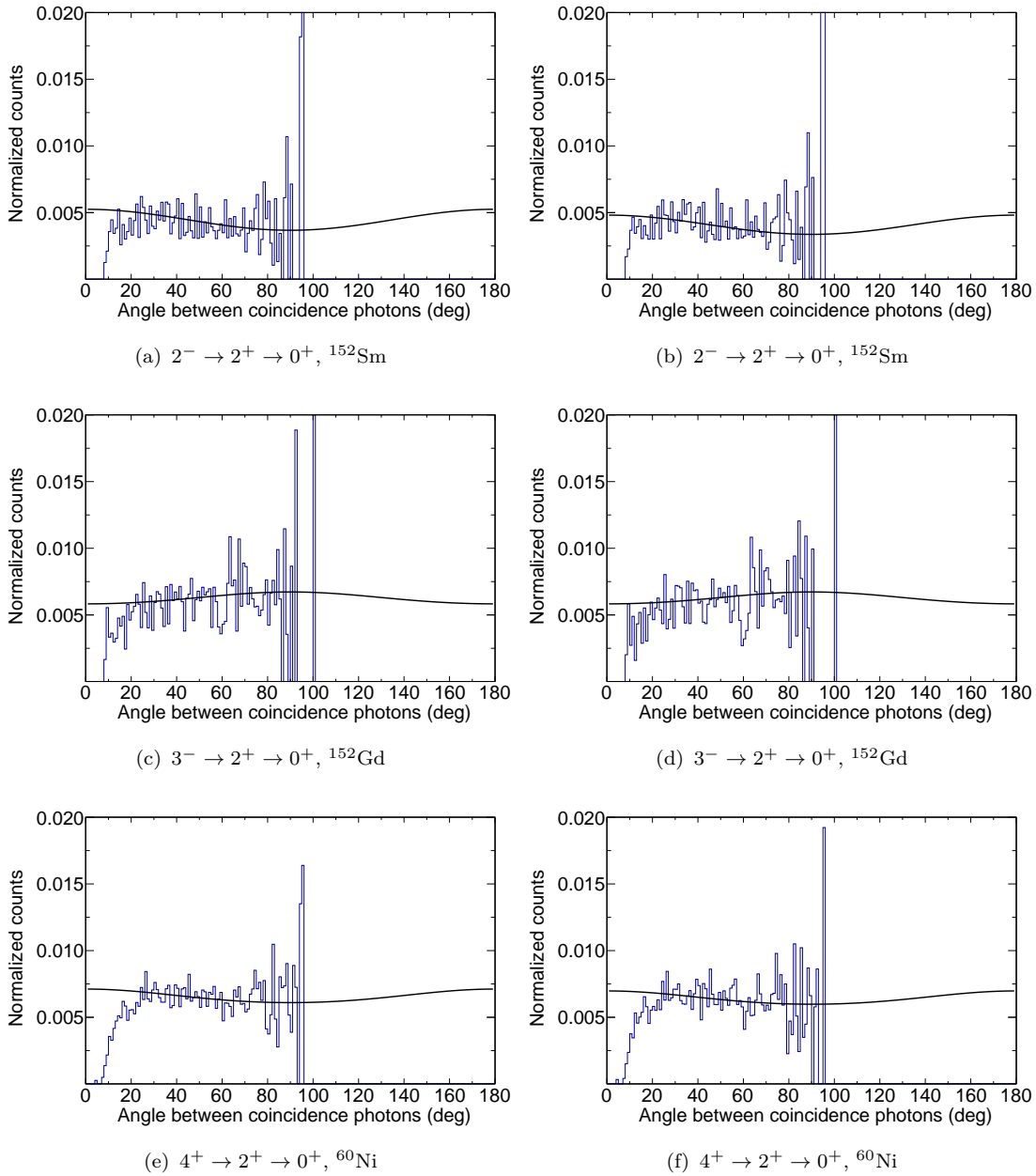


FIGURE 6.19: Angular correlation from the tracked data with OFT parameters $\sigma_\theta = 0.8$, $prob_{sing} = 0.02$ and $prob_{track} = 0.05$ for the different cascades of two gamma-rays used in the analysis with sources. The black line is the best adjustment found of the theoretical curves to the data (in blue). The left column (a),(c),(e) corresponds to the tracked data from the core energy and the right column (b),(d),(f) to the tracked data from the sum energy of the segments.

the bottom plot. The impact of the tracking can be appreciated by extracting the angular correlation of the different gamma-ray cascades studied. The angular correlations in Fig. 6.19 show that the solid angle covered in the AGATA setup is about 95 degrees and the tracking efficiency vanishes for gamma-rays with an angular separation of less than about 10 degrees. These losses at small angles arise because the tracking algorithm is not able to separate the points corresponding to two photons in the same detector. Moreover, as expected, a dependency of the losses has been observed, due to correlations, with the tracking parameter σ_θ [18].

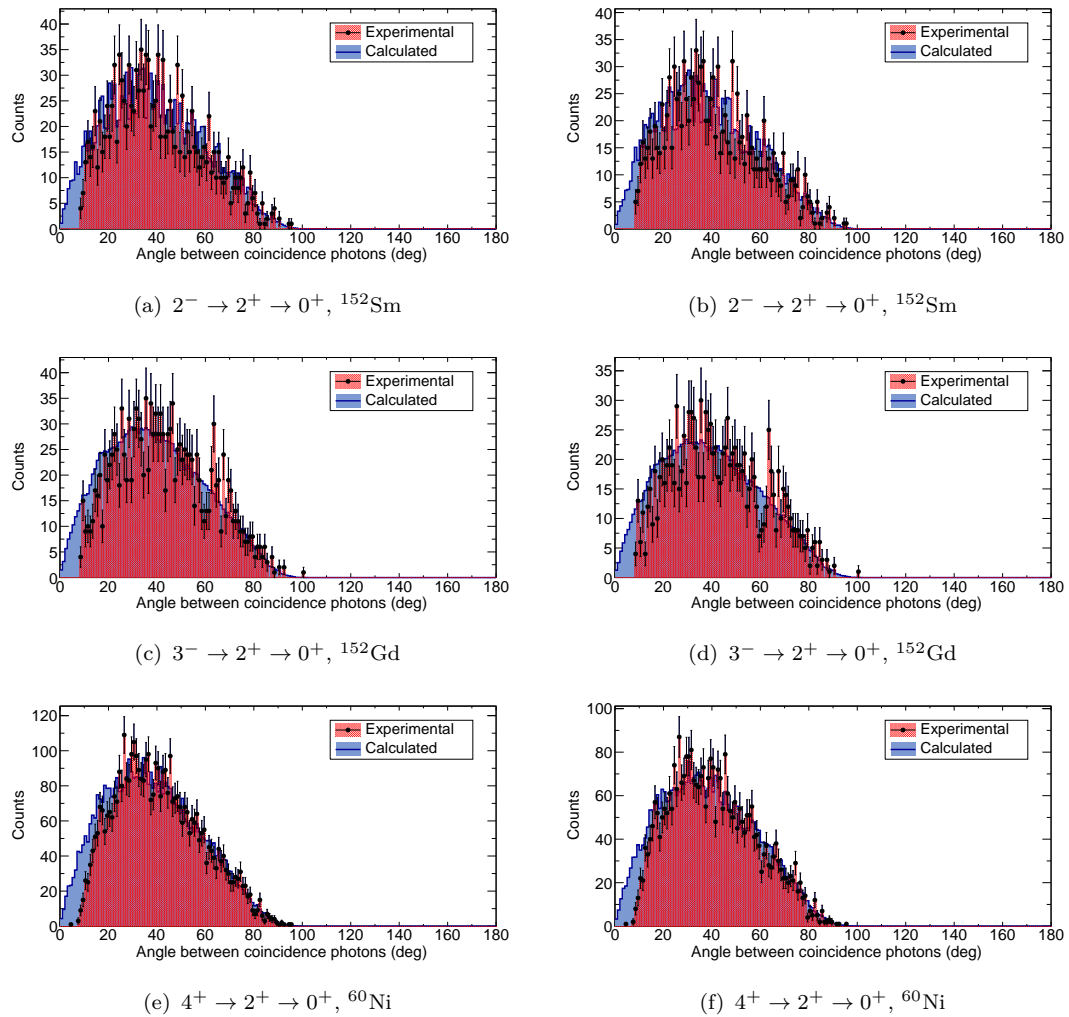


FIGURE 6.20: Angular correlation distribution from the studied two gamma-rays cascade. The left column (a),(c),(e) corresponds to the tracked data from the core energy and the right column (b),(d),(f) to the tracked data from the sum energy of the segments.

After fitting the experimental angular correlation using Eq. (6.9) the angular distribution for correlated events has been deduced and the coincidence efficiency has

been corrected by the missing fraction of the experimental angular correlation distribution compared to the theoretical angular correlation distribution calculated. The comparison of the theoretical and experimental angular distribution for the tracking analysis is presented in Fig. 6.20 for both tracking methods. The losses range from 10 to 15 %.

The final results for the efficiency as a function of the gamma-ray energy, of the mentioned AGATA configuration, measured with the calibration sources and for the different analysis modes, are represented in Fig. 6.21, with the fitted curve for each case. In the case of the calorimetric mode (red square), only the efficiency in coincidences at 1332 keV is shown as reference for the ideal efficiency that could be reached with the system. For the rest of modes to use AGATA, the results are presented in singles for the energies of the ^{152}Eu source and in coincidences at 1332 keV. The drop in the tracking efficiency at low energies is related in part to the

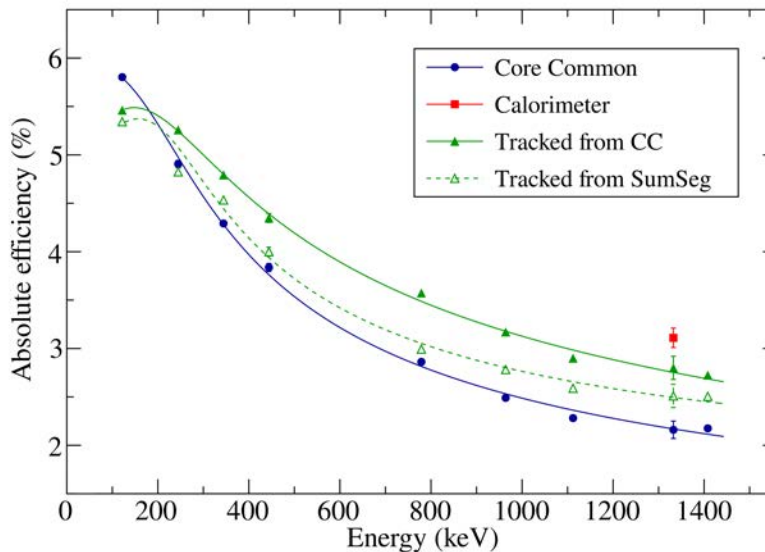


FIGURE 6.21: Absolute efficiency comparison of the different modes of analysis for the 23 capsules AGATA sub-array at 22.8 cm distance target position to detectors obtained with the data from ^{152}Eu and ^{60}Co in singles. The rate per crystal at this position was around 500 Hz. The different lines are the corresponding fit curves for each mode of analysing AGATA.

treatment of single interactions and in part to the Ge-sphere approximation made for calculating distances travelled in Ge from the source to the various interaction points in the OFT algorithm. This approximation overestimates the distance travelled by photons which is penalizing for low energy photons. A new method has been developed to improve the low energy efficiency in the OFT algorithm by calculating the distances given the exact geometry of the AGATA detectors and

by the single-interaction-point evaluation procedure [18, 113]. This new method is only available since few months ago and could not be implemented for the present analysis that was completed before.

The expression used for the fit is [110],

$$\varepsilon_{peak}(E_\gamma) = \exp[(A + Bx + Cx^2)^{-G} + (D + Ey + Fy^2)^{-G}]^{-1/G}, \quad (6.12)$$

where the fit calibration parameters go from A to G, $x = \log(E_\gamma/100\text{keV})$ describes the efficiency at low energies and $y = \log(E_\gamma/1000\text{keV})$, at high energy. The fitted values for the calibration parameters are presented in Table 6.6 for each mode of analysis.

TABLE 6.6: Fit parameters of the efficiency curves for different methods of analysis. The parameter C was kept fixed to 0 in all the cases.

Analysis mode	A	B	D	E	F	G
Core Common	1.789(10)	0.00(15)	0.911(4)	-0.487(15)	0.038(15)	10.1(5)
Tracked from CC	1.705(10)	0.13(11)	1.141(4)	-0.442(13)	-0.01(3)	10(3)
Tracked from SG	1.660(5)	0.10(3)	1.017(4)	-0.379(14)	0.077(14)	11.51(16)

Table 6.7 shows the results for the absolute photo-peak efficiency and P/T at 1.3 MeV in a configuration of 23 capsules. These efficiency values are the ones derived from the method in coincidences. The P/T has been calculated with the gated area of 1332 MeV line over the total counts in the gated spectra. The significant differences in the values presented in the table come from the mode of treating the energy extracted from the AGATA array. Using AGATA as a conventional detector, the so called core common, give rise to the lower values in efficiency and peak-to-total at 1.3 MeV, 2.15(8)% and 18.3(2)%, respectively. The use of AGATA as a calorimeter produces an increment in both quantities efficiency and peak-to-total, being the former 3.11(9)% and the later 29.9(4)%.

TABLE 6.7: Efficiency and P/T at 1332 keV obtained for different modes of analysis in the data treatment.

Analysis mode	Efficiency (%)	P/T (%)
Core Common	2.15(8)	18.3(2)
Calorimeter	3.11(9)	29.9(4)
Tracked from CC	2.84(12)	31.8(3)
Tracked from SG	2.51(13)	31.0(3)

Lastly, the efficiency to track a 1.3 MeV with 23 capsules is found to be 2.84% and 2.50% for the energy of the cores and sum of segments respectively. This

corresponds to an add-back factor with respect the efficiency of the 23 detectors taken individually (core common) of 1.32 and 1.16 respectively for each tracked case. Note that the use of the array in calorimetric mode works only in ideal conditions with sources and only one gamma-ray being detected. Therefore, that value rather represents an upper limit for the efficiency of the system. This is not the case for the P/T ratio because there is no capability to reject partially absorbed gammas in such mode.

The Peak-to-total found for the tracking cases at 1.3 MeV is smaller than the one found at GSI at 1.1 MeV [17] due to the way the single interactions are treated in OFT with respect to MGT. As mentioned before, a new method to treat the single interactions has been developed recently for the OFT tracking algorithm to improve the peak-to-total ratio and the efficiency at low energy [18, 113].

6.3.2. Discussion on the in-beam performance with the inelastic reaction channel

In this section, we will make an attempt to evaluate the AGATA sub-array performance figures under the extreme experimental conditions of our measurement. To this aim, the inelastic reaction channel of the main reaction in the experiment was used to study the effect of the in-beam measurements in tracking arrays. It should be pointed out that this experiment is not ideal for such measurements, since a plunger device has been used which leads to double peaks in the measured spectra.

As described in Section 6.2 the in-beam experiment was performed with the set-up shown in Fig. 6.22 (top left). There are two sets of data coming from the inelastic reaction for the efficiency studies. In the first one the ejectile of ^{92}Mo (beam-like) is going at 23° with respect to the beam direction and therefore entering VAMOS++ at 0° (in red in Fig. 6.22). At the same time, the reaction partner of ejectile (target-like or recoil), which is ^{92}Mo too, is going to 66.91° with respect to the beam direction that corresponds to $\sim 90^\circ$ with respect to the VAMOS++ axis (second set of data, in blue in Fig. 6.22). It should be remarked that in this reaction the kinematics of both partners is exchangeable, if the ejectile (beam-like) goes into de target (66.91°) the recoil (target-like) will go into VAMOS++ at 23° with the same energy. In the first case the Doppler correction has been done since

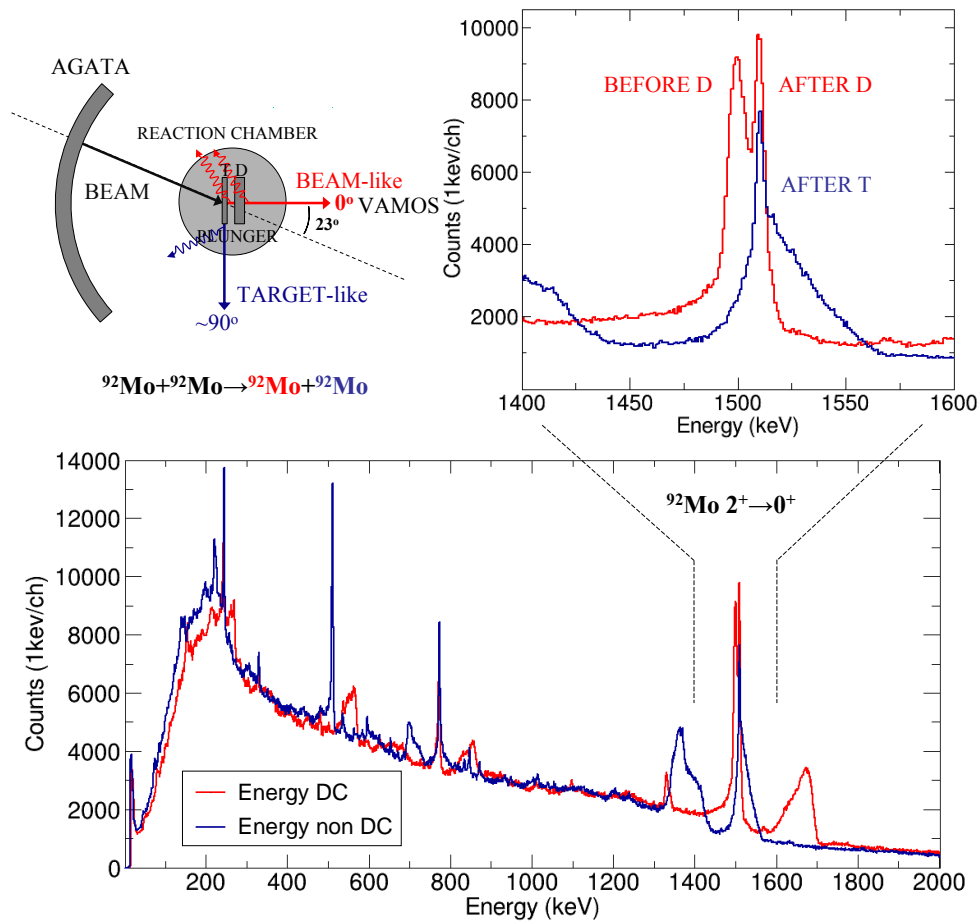


FIGURE 6.22: In-beam measurement for the inelastic reaction channel ^{92}Mo . On the top left, scheme of the reaction products direction: the beam of ^{92}Mo was impinging on a target (T) of ^{92}Mo and a degrader (D) of ^{24}Mg was set after the target to slow down the velocity of the reaction products for the lifetime measurement. The beam-like reaction products are ejected at 0° (red) and the target-like ones at around 90° (blue) in the VAMOS++ reference frame, both being ^{92}Mo . On the bottom, energy spectrum for mass 92 and z element 42 before (blue) and after the Doppler correction (red), which corresponds target-like and beam-like respectively. On the top right, zoom of the energy spectrum for the inelastic reaction channel for the $2^+ \rightarrow 0^+$ yrast transition.

the reaction products are measured with a speed of around $30 \mu\text{m}/\text{ps}$. On the other hand, in the second case, gamma-rays were emitted at rest. In the zoomed part of the spectra, the two components before and after degrader and the one after the target for the $2^+ \rightarrow 0^+$ transition in ^{92}Mo are better appreciated.

In experimental conditions the spectroscopic quality depends critically on the knowledge, on an event-by-event basis, of the position and the velocity of emitting nuclei, since the capability of Doppler correction depends on these quantities [52]. In Chapter 3, the ion-identification analysis in the VAMOS++ magnetic spectrometer was shown, aiming at highest possible Z and A/Z resolution, and

the best accuracy in the determination of the recoil position, recoil velocity direction and recoil speed.

Fig. 6.23 illustrates the quality of the final Doppler corrected 3 spectra for different types of AGATA analysis, similarly as it was shown with the measurement with sources. In blue, the core common spectrum, and in green, the tracked spectrum.

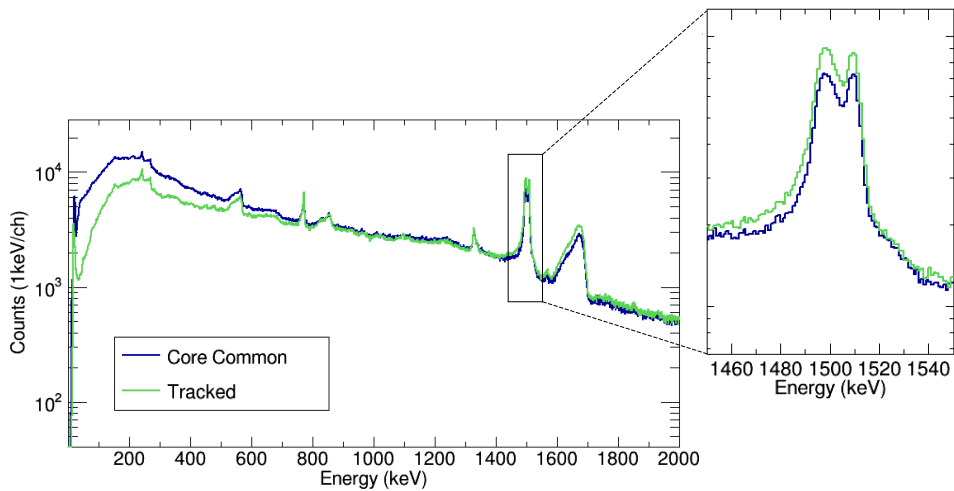


FIGURE 6.23: Comparison of the Doppler corrected spectra using the different operational modes of AGATA. The OFT parameters used for the tracking are $\sigma_\theta = 0.8$, $prob_{sing} = 0.02$ $prob_{track} = 0.05$. In this example is shown the spectrum for the case of tracked data using the core energy.

If we compare the two sets of data that have been evaluated for the tracking it is evident that at high counting rates, we do not note the deficit in the evaluated energy of the sum energy of the segments observed in the source data taken at very low counting rates (see Fig. 6.10 for the comparison). In addition, it can be appreciated that in the case of the tracking using the sum energy of the segments (red line in Figs. 6.24 and 6.25) the resolution and the counts in the peaks are better than in the tracking derived from the cores (blue line) keeping the background at the same level. This can be related to issues in the base-line restoration, since the pile-up of the signals produce larger base-lines in the core signals than for the segments. For the latter the counting rate is much lower, since we have 36 segments for each single core.

³The Doppler correction approach have been described in Section 3.3.1. Notice that for the core common case the position information used for the Doppler correction is the highest PSA hit.

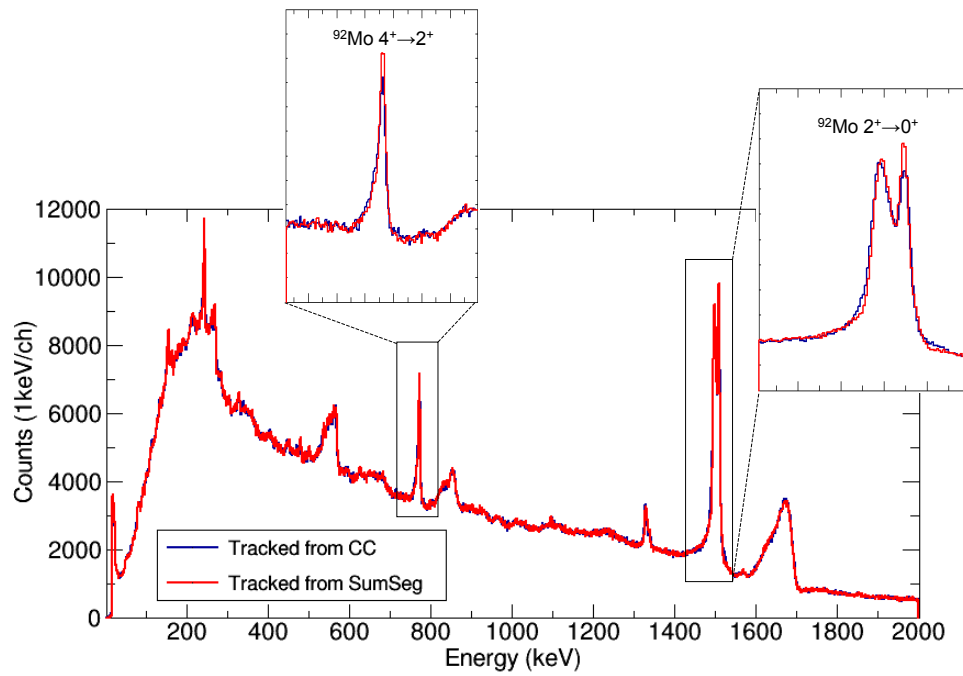


FIGURE 6.24: Comparison between the in beam Doppler corrected tracked spectra regarding the nature of the energy sent to the tracking. OFT parameters used in both cases: $\sigma_\theta = 0.8$, $prob_{sing} = 0.02$ and $prob_{track} = 0.05$.

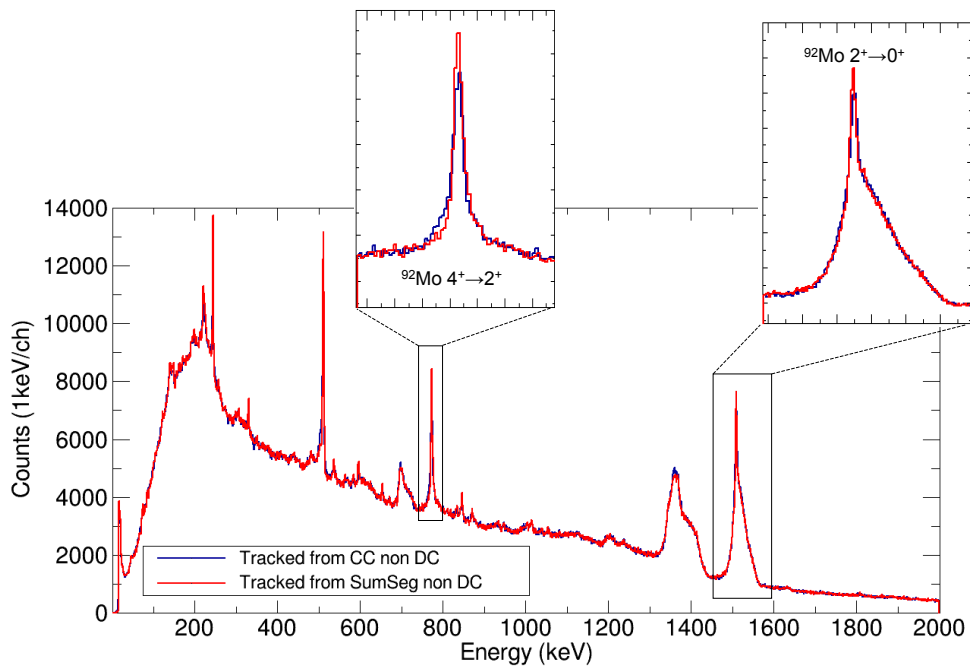


FIGURE 6.25: Comparison between the in beam non Doppler corrected tracked spectra regarding the nature of the energy sent to the tracking. OFT parameters used in both cases: $\sigma_\theta = 0.8$, $prob_{sing} = 0.02$ and $prob_{track} = 0.05$.

6.3.2.1. Energy Resolution

The effect of in-beam measurements in tracking arrays can affect to the energy resolution of the peaks considerably. In experimental conditions the emission point of the radiation depends not only on the trajectory and target thickness, but also on the beam-spot size and the half-life of the populated level [52]. Therefore, the best resolution attainable with AGATA depends on the intrinsic resolution of the detector itself, but also on the accuracy of the quantities that provide the Doppler correction of the measured energy.

The VAMOS++ magnetic spectrometer uses a Dual Position Sensitive Multi-Wire Proportional Counter (DPS- MWPC) for measuring the scattering angle, the interaction position on the target and the velocity of reaction products with the high precision required in the AGATA array [41]. This ensures the good spectral quality after the Doppler correction.

Because the lifetime measurement comprises the plunger device the measured gamma-ray transitions typically show two components due to the different velocity before and after the degrader, depending on its lifetime and the distance between the target and degrader. This experimental effect complicates the estimation of the FWHM. The transition of interest, the $2^+ \rightarrow 0^+$ transition in ^{92}Mo , has a half-live of 0.35(2)ps and even for the shortest distance between target and degrader the two components are observed due to its short lifetime. Another channel

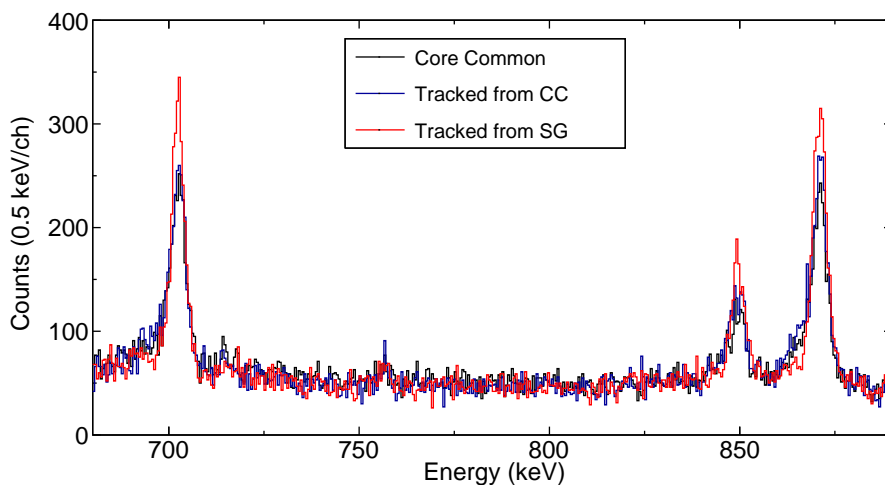


FIGURE 6.26: Comparison of the Doppler corrected spectra of ^{94}Mo using the different operational modes of AGATA in order to evaluate the resolution quality of the peaks. The OFT parameters used for the tracking are $\sigma_\theta = 0.8$, $prob_{sing} = 0.02$ $prob_{track} = 0.05$.

of the reaction have been selected which contained a gamma-ray transition with a longer lifetime and all its counts in the unshifted peak.

Fig. 6.26 shows the energy spectra of ^{94}Mo and illustrates the quality of the resolution after Doppler correction for the different types of data treatment in AGATA (see labels in Fig. 6.26). The use of the sum of the segments clearly improves the FWHM of the peaks in comparison with the other options. This effect was already observed with sources. With beam this effect is worsened due to the fact that the core signal suffers more pile-up of the signals than the segments at high counting rates.

6.3.2.2. Efficiency and Peak-to-Total

For the in-beam data, the only possible method to obtain the efficiency is the gamma-gamma time-coincidences technique. In this approach the efficiencies are determined by comparing the detected peak areas of the 1510-773 keV gamma-rays cascade, Eq. (6.11), in the inelastic channel reaction, ^{92}Mo . In Fig. 6.27 the coincidence time windows are shown for the core common case (top figure) and for the tracked gammas (bottom figure). Like in the sources, the former is 400 ns and the later 140 ns.

The bumps observed in the time spectrum of tracked gammas are the random coincidences with reactions produced by the ions of the previous or latter accelerator bunches. This bunches are separated a time of around 90 ns, that corresponds to the accelerator RF period. In the case of the core common time spectrum the bumps are not present due to the way that the spectra are built. It is a relative time spectrum, related to the discriminator that produces the local trigger and, therefore, the random coincidences are not observed because each gamma timing is referred to itself. On the other side the tracked time spectrum is related to the global trigger between the particle and the gammas. The extraction of the areas has been done by integrating the peaks of interest in the range that comprises the two components existing for each transition. Figs. 6.28 and 6.29 schematically show the procedure for gating and gated areas, for the Doppler corrected and non Doppler corrected energy spectra, respectively. The area in singles (from the gating transition of 773 keV) is obtained with an integral with background subtraction, as depicted in Figs. 6.28 and 6.29 (top). The area in coincidences (from the gated transition at 1510 keV) is extracted also with an integral after background

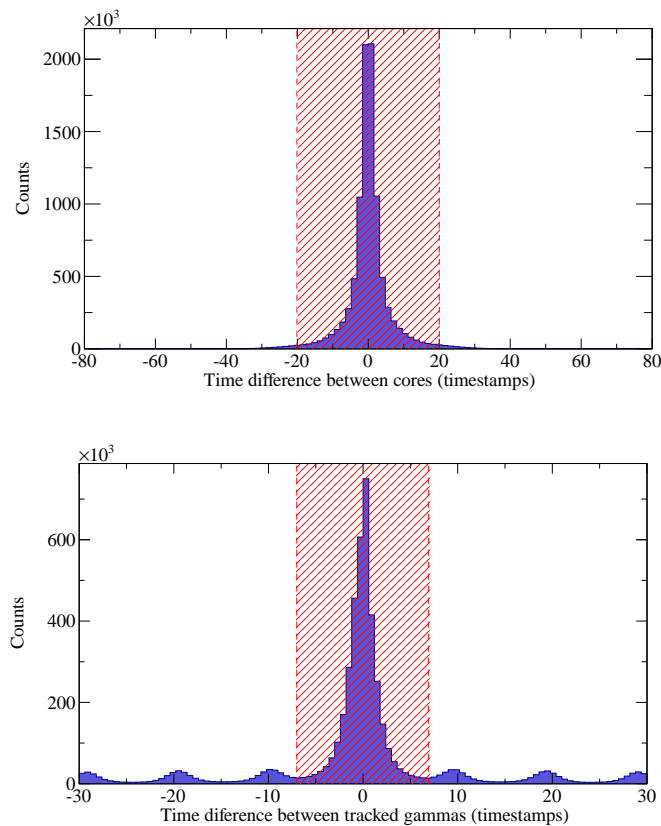


FIGURE 6.27: Time window gamma-gamma coincidence.

subtraction. The background at the gating energy is evaluated from the correlated background on both sides of the gating energy, bottom of Figs. 6.28 and 6.29 (light red and light blue spectra respectively). Finally, Figs. 6.28 and 6.29 demonstrate the quality of the peak-to-total ratio that is achieved with in-beam conditions.

The angular correlations introduce a further correction in the efficiency in coincidences as described by (Eq. (6.11)). In this case, as the beam is an oriented source, the gamma-gamma correlations have a triple correlation related to the beam direction and the two gamma-rays. Therefore, the simplest angular correlation described in Eq. (6.9) and the procedure sketched in Fig. 6.20 can not be applied to the in-beam data. The angular correlation function becomes more complicated if one accounts for the dependency not only on the angle between the emission direction of the two gamma-rays, but also for the angles of each gamma-ray with respect to the beam direction, as described in [85, 107, 108, 114]. Unfortunately, the low number of events measured in this experiment makes a detailed study of the in-beam angular correlation difficult.

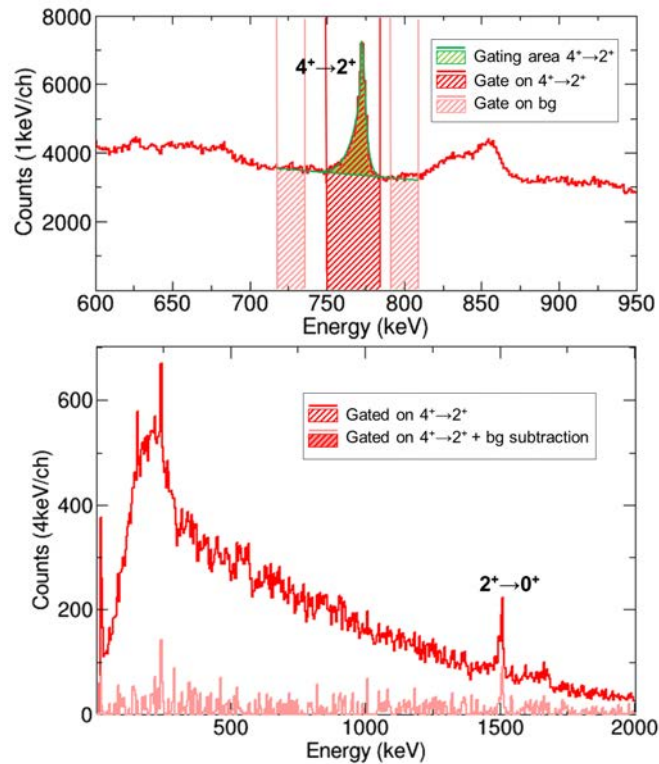


FIGURE 6.28: Gamma-gamma coincidences in-beam procedure for the ^{92}Mo nucleus going at 0° with respect to the VAMOS++ axis. On the top, the ^{92}Mo energy spectrum in singles with the integral plus background subtraction in green for the $4^+ \rightarrow 2^+$ yrast transition, the gating area in red and the gating area for the background in light red. On the bottom, ^{92}Mo energy spectrum after gating on the $4^+ \rightarrow 2^+$ yrast transition in red and the same with background subtraction in light red.

Table 6.8 shows the calculated efficiency taking only into account the areas subtracted, as explained above, and the total internal conversion coefficient, which for the 1510 keV energy transition in ^{92}Mo is 0.000408(6) [111].

TABLE 6.8: Raw efficiency at 1510 keV obtained for different modes to use AGATA.

Analysis mode	Raw Eff. 0° (%)	Raw Eff. 90° (%)
Core Common	1.39(15)	1.45(13)
Tracked from CC	1.45(12)	1.52(11)
Tracked from SG	1.50(12)	1.50(11)

One can observe very small differences ($\sim 4\%$ at most) between the two methods used for measuring the efficiency in-beam, the 0° and 90° recoil trajectories, which have a completely different angular distribution. In the case of the gammas emitted by the reaction products going towards VAMOS++, i.e., at 0° respect to VAMOS++ axis (see 6.22) the AGATA angular distribution varies from 60° to 120° , while for the gammas emitted by the recoils at 90° respect to VAMOS++

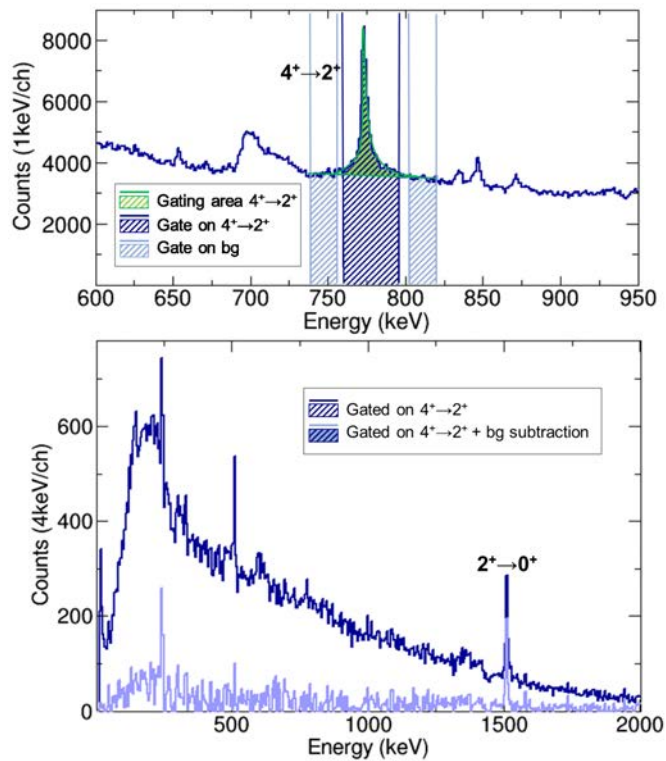


FIGURE 6.29: Gamma-gamma coincidences in-beam procedure for the ^{92}Mo nucleus going at 90° with respect to the VAMOS++ axis. On the top, the ^{92}Mo energy spectrum in singles with the integral plus background subtraction in green for the $4^+ \rightarrow 2^+$ yrast transition, the gating area in blue and the gating area for the background in light blue. On the bottom, ^{92}Mo energy spectrum after gating on the $4^+ \rightarrow 2^+$ yrast transition in blue and the same with background subtraction in light blue.

axis, the AGATA angular distribution varies from 60° to 120° . This indicates that the angular correlation correction will be small in both cases. In addition, the small add-back factor between the core common and the tracked values confirms that there are losses in the tracking when measuring the efficiency in coincidences. This effect was also observed in the sources (around 10%) and it can be ascribed to the tracking algorithm, which is not able to disentangle points corresponding to two photons in the same pre-defined cluster.

Apart from those losses, one needs to take into account losses due to the high counting rates. While with the sources the rates reached per crystal are of the order of hundreds of Hz, for the in-beam case the rates per crystal vary from 40 to 50 kHz (Fig. 6.4).

One of the effects caused by the high counting rates is the loss of efficiency due to pile-up rejection, as already mentioned in Section 6.2.1. As seen in Fig. 6.5

the higher are the rate and the MWD-risetime, the bigger are the so called pile-up losses in the efficiency. For the rates achieved in the experiment and the used MWD-risetime of 2.5 μs , the efficiency losses due to the pile-up rejection are about 15-20%.

Another effect, recently discussed in [115, 116], is the loss of trigger requests in the trigger processor when the requested rate exceeds 1 MHz. Fig. 6.30 shows the losses measured for different total rates in AGATA. The total rate estimated in this experiment is found between 920 and 1150 kHz, which corresponds to losses of 15% and 18%, respectively. The correction due to the losses in the trigger processor in the experimentation with AGATA have been performed in 2014, 2015, 2016 since the idle period of the GTS was set by default to 9 MHz. This fact provoked the saturation of the GTS fiber bandwidth to the trigger processor at high request rate. From 2017, it is a free parameter with the new release of the GTS firmware (including epics) from Padova.

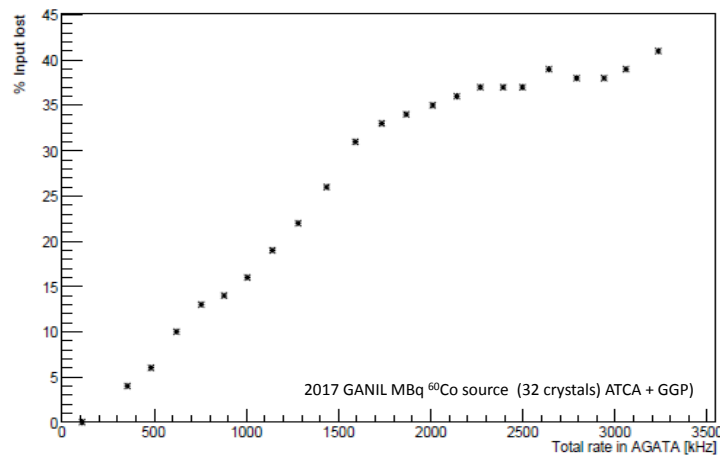


FIGURE 6.30: Measured losses of requests in the trigger processor as a function of total rates in AGATA [115, 116].

Although, other minor effects may be found in further investigations, the corrections applied in Table 6.9 certainly account for the main losses. It should be remarked that the average raw efficiency has been calculated for simplicity but before this step the small factor due to angular correlation needs to be calculated for each case. The main losses taken into account for this evaluation are the following:

- $\sim 18\%$ due to pile-up losses.
- $\sim 17\%$ from trigger processor losses.

- $\sim 10\%$ in the tracking case due to the angular correlation losses as seen in the sources at low angles mainly.

In Table 6.9, the corrected values are confronted with the ones expected from the sources curve trend, that was calculated in Section 6.3.1.2. The experimental results with the corresponding estimation of losses agree within the error with the expected values at 1509 keV, which shows that they are consistent in terms of losses.

TABLE 6.9: Average efficiency estimation at 1510 keV for different modes of analysis in the data treatment compared with the expected efficiency derived from the sources (see text for details).

Analysis mode	Raw Eff. (%)	Corrected Eff.(%)	Expected Eff. (%)
Core Common	1.42(14)	2.09(21)	2.047(17)
Tracked from CC	1.49(12)	2.43(20)	2.602(37)
Tracked from SG	1.50(12)	2.45(20)	2.395(18)

6.4. Summary

In this chapter the AGATA performance has been discussed using the same experimental conditions for calibrated gamma-ray sources as for the in-beam experiments. The set-up was a combination of the AGATA tracking array, the VAMOS++ magnetic spectrometer and the differential plunger device necessary for the level lifetime determination of the nuclei of interest, which is the purpose of this Thesis. As mentioned earlier, it should be remarked that the presence of the plunger device produces a double peak structure in the in-beam gamma-ray spectra, which is not the best scenario to evaluate the performance of AGATA. Nevertheless, the main performance characteristics have been analysed for 23 AGATA crystals and different analysis approaches for a comprehensive assessment of the systematic uncertainties.

The energy resolution has been presented for the AGATA detector itself using sources and evaluated qualitatively in experimental conditions, where the FWHM is dominated in most of the cases by the Doppler broadening. The latter arises from the accuracy attained on the determination of the position and velocity of the emitted nuclei on an event by event basis. In the present AGATA set-up, the evaluation of the energy resolution of each crystal showed better results using the sum energy of the segments after the correction for neutron damage effects.

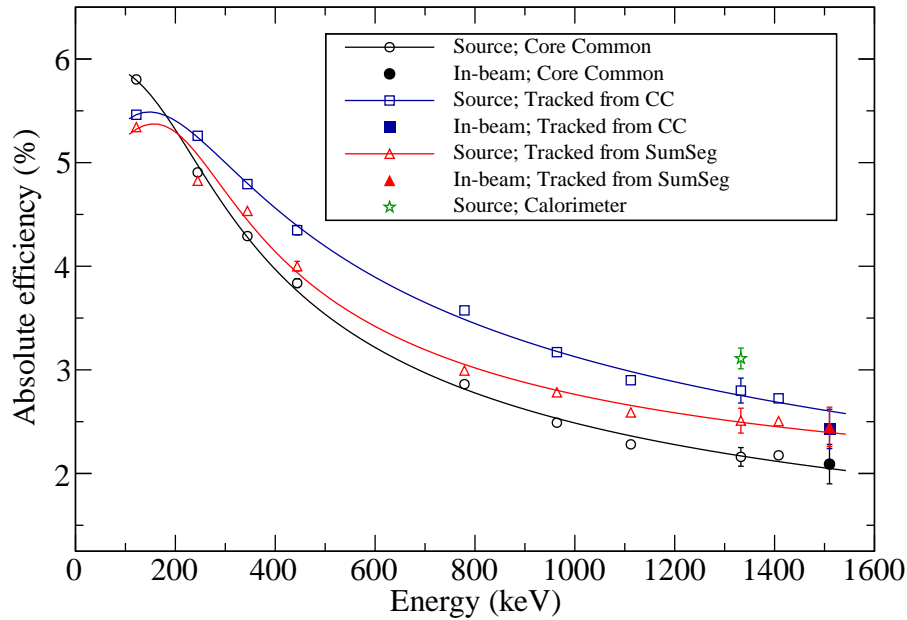


FIGURE 6.31: Absolute efficiency comparison of the different modes of analysis obtained from the measurements with sources and the in-beam measurements. The experimental curves are made with the data from ^{152}Eu in singles normalized to the efficiency at 121 keV in coincidences and compared with the 1332 keV efficiency in coincidences from the ^{60}Co . The lines are the corresponding fits for each method of analysis in the source case. The in-beam values correspond to the 1509 keV level in ^{92}Mo with the corrections mentioned in the text. The AGATA sub-array was composed of 23 capsules and was setted at a 22.8 cm distance (target position to detectors).

The absolute AGATA efficiency for different methods of data treatment have been experimentally determined by means of calibrated gamma-ray sources and compared with the in-beam gamma-ray efficiency for the $2^+ \rightarrow 0^+$ 1509 keV transition in ^{92}Mo . The rates per crystal were around 550 Hz for source measurements, while the rates in-beam were in the range of 40-50 kHz. The results and the fitted curves are presented together in Fig. 6.31.

For the efficiency in coincidences the angular correlations have been investigated. The angular correlations with the sources showed a loss of efficiency tracked data for small angles between the two gamma-rays. This correction was at around 10%. The AGATA collaboration have developed a method, that can be used to extend the angular correlation towards lower angles, based on the mixing of events with the total energy of the studied gamma-rays before tracking [18]. For the in-beam case, the angular correlations become more difficult to analyse because of the source momentum orientation and the relatively low number of events measured

in this experiment did not allow to go further in this aspects of the study. Nevertheless, with the low alignment in the inelastic channel the angular correlations do not have a strong relevance, as it was inferred from the only 4% differences for 0° and 90° trajectories (Table 6.8). As seen in Fig. 6.31, the final estimations of the in-beam efficiency are consistent with the curve trend of the efficiencies obtained with the sources. These estimations take into account the losses due to the high counting rates. The correction for the tracked efficiency losses at small angles has been also included, taking as a reference the value estimated for the source efficiency in coincidences. Regarding the mode used to analyse the experiment of this Thesis (tracking from the sum energy of the segments) the absolute efficiency calculated from the sources at 1509 keV is found to be 2.395(18)%, which is fully in agreement with 2.45(20)% at 1509 keV.

One can expect, that the analysis work presented in this chapter will be extended and improved in the future, when more AGATA crystals are included in the system, and when data with a setup more convenient for a performance study, like just a simple thin target, become available.

This studies together with the work performed in collaboration with the AGATA performance team at GANIL using 30 crystals are intended to be published in the review *Nuclear Instruments and Methods in Physics Research A*. The manuscript was submitted in May 2019 [18].

Chapter 7

Resumen de la Tesis

7.1. Introducción

El trabajo desarrollado en esta Tesis se centra en el estudio experimental de la evolución de la colectividad en la capa $g_{9/2}$ hacia el núcleo ^{100}Sn con metodología de espectroscopia gamma aplicada con el multi-detector AGATA.

El ^{100}Sn , siendo el núcleo doblemente mágico ligado más pesado con igual número de protones y neutrones, ha atraído un considerable interés desde el punto de vista experimental y teórico [1, 2]. La estructura de este núcleo y sus vecinos son excelentes referencias para probar los cálculos de los modelos de capas de última generación en esta región emblemática de la tabla nuclear. Además, el estudio de las propiedades de la capa $g_{9/2}$ a través de los isótopos con $N = 50$ en la vecindad del ^{100}Sn es de gran interés para entender las diferencias y similitudes con respecto a los isótopos con $Z = 28$ hacia el ^{78}Ni puesto que tienen los mismos nucleones de valencia para protones y neutrones, respectivamente. Esta situación se denomina simetría espejo de valencia (VMS). En este contexto, los modelos de capas predicen la conservación de *seniority* hacia la ocupación completa del orbital $g_{9/2}$ en el primer caso debido a una fuerza de *pairing* creciente a lo largo de los isótonos $N = 50$ [8], contrariamente a lo que sugieren para el segundo caso.

La espectroscopía gamma de alta resolución es una herramienta de investigación experimental fundamental en el estudio de la estructura de los núcleos atómicos. Esta experimentación se lleva a cabo con multi-detectores de semiconductores de germanio de alta pureza (HPGe) donde cada cristal de germanio es un diodo

que detecta la radiación gamma incidente. AGATA (Advanced Gamma Tracking Array) [13] es un multi-detector compuesto por cristales de germanio de alta pureza, con contactos eléctricamente segmentados, sensibles a la posición y con capacidad de trazar la absorción del fotón gamma dentro del detector. AGATA es el resultado de varios avances técnicos con el fin de obtener identificación de la posición de interacción, alta sensibilidad (eficiencia, relación de pico a total y corrección Doppler) en condiciones de medida difíciles (elevada tasa de conteo y alta tasa de fondo), como sucede en la segunda generación de instalaciones de haces radiactivos.

7.2. Detalles experimentales

Para probar experimentalmente la conservación de *seniority* en el orbital de protones con $N=50$, el multi-detector AGATA [13], instalado en el laboratorio GANIL, se utilizó, en combinación con el *plunger* diferencial de IKP, Colonia [47], con el objetivo de medir las probabilidades de transición reducidas para las transiciones *yrast* $4^+ \rightarrow 2^+$ y $2^+ \rightarrow 0^+$ en los núcleos de ^{94}Ru y ^{92}Mo (y por completitud el ^{90}Zr). El mecanismo de reacción usado para poblar los núcleos de interés, ricos en protones, fue la reacción de transferencia de varios nucleones [23] raramente usada para poblar dichos núcleos. Contrariamente a las reacciones de fusión- evaporación (típicamente usadas para producir núcleos ricos en protones), las reacciones de transferencia de varios de nucleones permiten que se pueblen directamente estados de momento angular medio o bajo, incluso en presencia de isómeros (que es el caso de los núcleos que nos ocupan), esto facilita la determinación directa, con métodos Doppler, de la vida media. En este experimento, un haz de ^{92}Mo con una energía de 716.9 MeV incidió en el blanco de ^{92}Mo ($0.775\text{mg}/\text{cm}^2$) del *plunger*, mientras que una lámina de ^{24}Mg con $1.9\text{ mg}/\text{cm}^2$ de espesor se usó para degradar la energía de los productos de reacción. Los productos de reacción de interés se identificaron con el espectrómetro magnético VAMOS++ [40]. Los rayos gamma en coincidencia con los productos de reacción identificados se midieron usando AGATA. El montaje experimental se muestra esquemáticamente en la Fig. 7.1. La posición de los detectores y la configuración del *plunger* con respecto al haz se pueden apreciar en la figura.

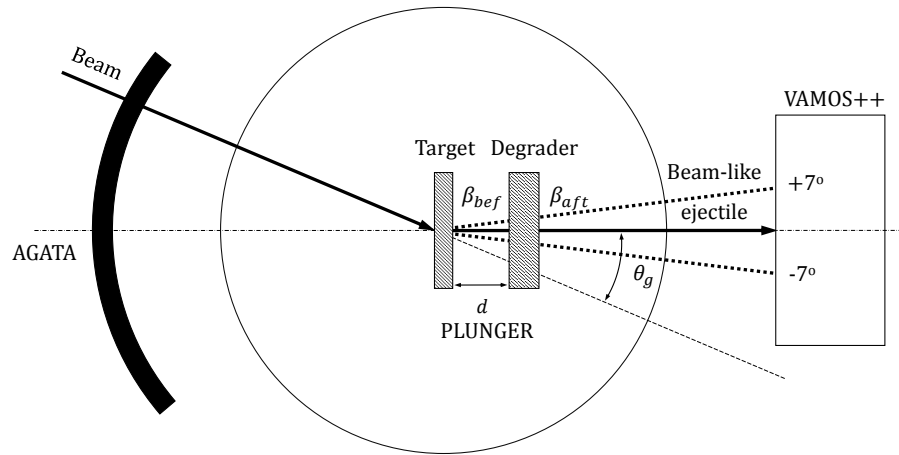


FIGURA 7.1: Dibujo esquemático del montaje experimental. El ángulo de *grazing*, θ_g , calculado aproximadamente, es 23° .

7.2.1. El espectrometro magnético VAMOS++

El sistema de detección de VAMOS++ [39–41] proporciona toda la información necesaria para la identificación completa de los iones en términos de la masa M , el número atómico Z y el estado de carga q . Ésta se realiza a través de la reconstrucción, evento por evento, de la trayectoria dentro de los elementos magnéticos del espectrómetro. Estos constan de dos cuadrupolos magnéticos de gran apertura en la entrada, para focalizar los iones vertical y horizontalmente y un gran dipolo magnético, para curvar la trayectoria de los iones según su rigidez magnética. El sistema de detección de VAMOS++ estaba compuesto por los siguientes detectores en la posición de entrada y en el plano focal. En la posición de entrada, se situaban dos detectores de trazado de alta resolución y sensibles a la posición (DPS-MWPC). Estos fueron incluidos para poder identificar mejor la trayectoria del ion en el espectrómetro y así optimizar el uso de la resolución angular superior del multi-detector AGATA [41]. Los detectores de trazado proporcionan la información del tiempo de inicio, la medida del ángulo de dispersión (θ) y el punto de interacción en el blanco (X_t, Y_t). En el plano focal, el MultiWirePPAC (MWPPAC) da el tiempo de parada para medir el tiempo del vuelo (TOF) del ion junto con el tiempo de inicio de el primer MWPC. Las cámaras de deriva (DC) proporcionan la posición en el plano focal (X_f, Y_f). Y la cámara de ionización (IC)

mide la pérdida de energía (ΔE) y la energía total (E) de los productos de la reacción. Dicha medida permite la identificación del número atómico Z del producto de reacción. En este experimento, el espectrómetro VAMOS++ se colocó en el llamado ángulo de *grazing* (23° con respecto al eje del haz) donde la sección eficaz de producción para los canales cuasi-elásticos es mayor [26]. El campo magnético del dipolo de VAMOS++ se seleccionó para que la rigidez magnética central fuese $B\rho = 0.91\text{Tm}$. Todos los detectores operaban con gas isobutano a una presión de 6 mb, excepto la IC que usaba una presión de 60 mb. En la Fig. 7.1 se indica la aceptación horizontal de VAMOS++ ($\pm 7^\circ$).

7.2.2. El espectrometro AGATA

AGATA es un multi-detector de última generación para la espectroscopía de radiación gamma [13]. La instalación de AGATA usada en este experimento estaba compuesta por 23 cristales HPGe segmentados eléctricamente en 36 partes y colocados en ángulos hacia atrás en una configuración nominal (a 22.8 cm de distancia del blanco). Dichos ángulos son más sensibles a las variaciones por el desplazamiento Doppler y, por lo tanto, al efecto del tiempo de vida. El detector de radiación gamma funcionaba con una *MWD-risetime* de 2.5 μs y operaba a 40-50 kHz por cristal aproximadamente. El análisis de forma de pulso (PSA)[14] se realizó *on-line* mientras que el trazado (tracking) de los rayos gamma [109] se realizó *near-line* y los trazas (datos que contienen toda la información sin procesar desde el inicio de su medida) se almacenaron para optimizaciones y correcciones posteriores. El análisis de datos de AGATA implicó el uso de GRID [117] para un preprocesamiento y una clasificación eficiente del gran volumen de datos tomados, que incluyen un tratamiento detallado de varios efectos experimentales, como correcciones de segmentos que no funcionaban, correcciones de los efectos del daño de neutrones, etc.

7.2.3. El plunger diferencial

El *plunger* diferencial es un dispositivo complejo, desarrollado por la Universidad IKP de Colonia, que permite medir el tiempo de vida de los núcleos excitados en el rango de picosegundos mediante la técnica de desplazamiento Doppler de distancia de retroceso (RDDS). El *plunger* diferencial se colocó en el centro geométrico de la

cámara de reacción y perpendicular al eje óptico del espectrómetro. El degradador se colocó a diferentes distancias, d , para determinar la vida útil utilizando la técnica RDDS. Para cubrir el rango de vida útil esperado para los isótonos de interés (desde 1 ps hasta cientos de ps), se midieron siete distancias diferentes: 19, 25, 100, 500, 1000, 2000 y 4000 μm . Siete días de tiempo de haz (24 UT) fueron necesarios para medir las siete distancias entre el degradador y el blanco.

7.3. Procesado de datos

El procesado de datos de AGATA se lleva a cabo en dos niveles: el nivel local, donde todos los cristales se manejan por separado; y el nivel Global, donde los datos procesados de los cristales tratados individualmente se ensamblan en base al *timestamp* de cada evento y se procesan posteriormente como eventos que se fusionarán con datos de detectores complementarios. Todas las operaciones en los datos se llevan a cabo con la cadena de actores NARVAL representados en la Fig. 3.1. En ella se presenta un resumen esquemático del procesado a nivel local y global. Cada actor es aplicado secuencialmente desde el primero hasta el último en el procesado del flujo de datos, tal como se define en un archivo de topología [72]. El procesado de los datos AGATA comienza a partir de las trazas de las señales del contacto central (core) y los segmentos de cada uno de los 23 cristales del multi-detector durante el experimento. A partir de esta información, la posición y la energía de cada interacción se deducen mediante el análisis de forma de pulso (PSA) a nivel local. Los resultados obtenidos en el volumen del detector se analizan con el algoritmo de trazado (*tracking*), que proporciona un archivo que contiene los rayos gamma reconstruidos y los datos de los detectores complementarios (VAMOS++) combinados a nivel global. La preparación adecuada de los datos es crucial para el correcto funcionamiento del algoritmo de PSA. Con este objetivo, la amplitud de la señal sin procesar debe calibrarse, las trazas de los segmentos deben alinearse adecuadamente en el tiempo y todos los segmentos deben funcionar correctamente. Además, los efectos debidos a la diafonía entre segmentos deben ser corregidos. También antes de poder realizar la reconstrucción de los rayos gamma, el efecto del daño de neutrones debe ser corregido. AGATA es básicamente un instrumento para espectroscopía gamma de alta resolución y, por lo tanto, una buena resolución energética es el objetivo fundamental del instrumento. Además, una buena resolución energética es de gran

importancia para observar claramente los dos componentes de una transición de rayos gamma causada por el *plunger* diferencial.

El espectrómetro VAMOS++ se utiliza para la identificación de los productos de reacción en términos de número atómico (Z), número de masa (A) y estado de carga (q) según cada evento. La identificación de partículas evento por evento basada en la reconstrucción de su trayectoria [42] se realiza a través de los pasos ilustrados esquemáticamente en Fig. 3.28. Las posiciones medidas en el DPS-MWPC permiten determinar las posiciones vertical y horizontal, X_t y Y_t , y los ángulos, θ_t y ϕ_t . Estos parámetros definen la trayectoria del ión en la posición del blanco. Con las posiciones vertical y horizontal medidas en las cámaras de deriva, X_f y Y_f , y los ángulos, θ_f y ϕ_f , se determina la trayectoria del ión en el plano focal. Esta información, en combinación con la información angular en la posición del blanco, permite la reconstrucción de cada trayectoria del ión. Este último se define por la rigidez magnética, $B\rho$, y la longitud de la trayectoria, D (parámetros en los cuadros con líneas discontinuas en Fig. 3.28). Después de esto, la velocidad v de los iones después del degradador se puede calcular a partir de los ToF medidos y los D reconstruidos, usando $v = D/ToF$. Por otro lado, la energía depositada en la cámara de ionización da la pérdida de energía parcial, ΔE , y la energía total, E , del ion que permite la identificación del número Z . El número A se obtiene de los parámetros medidos E y v . La relación masa sobre carga, A/q , se deriva de la información de trayectoria utilizando las ecuaciones del movimiento de la partícula cargada en el campo magnético del dipolo para finalmente deducir el estado de carga, q . Estos parámetros identifican de forma exclusiva los productos de reacción y se indican en cuadros rellenos grises Fig. 3.28. Además, la velocidad y los ángulos en la posición de destino (en rojo en Fig. 3.28) permiten la corrección Doppler de los rayos gamma detectados en coincidencia. Finalmente, el uso del espectrómetro magnético VAMOS++ en combinación con la técnica RDDS permite controlar parcialmente la alimentación desde estados superiores estableciendo condiciones en la pérdida de energía cinética total, TKEL (ver Section 3.3).

7.4. Determinación del tiempo de vida

7.4.1. Técnica RDDS

La técnica RDDS es un método bien establecido para la determinación de vidas medias de los estados nucleares excitados en el rango entre picosegundos y cientos de picosegundos. En el experimento realizado, para poder realizar medidas de RDDS y aun así poder detectar los productos de reacción se usó un degradador. El degradador permite ralentizar los productos de reacción para observar las dos componentes correspondientes en el espectro gamma debido a las diferentes velocidades (antes y después del degradador) de los núcleos emitidos (ver las Figs. 2.17 y 4.1 para más detalles). Posteriormente, el tiempo de vida se puede derivar de la relación de las intensidades de las dos componentes: *shifted* I_s (componente desplazada en energía, antes del degradador) y *unshifted* I_u (componente no desplazada, después del degradador) en función de la distancia entre el blanco y el degradador.

$$R(t) = \frac{I_u(t)}{I_s(t) + I_u(t)} \quad (7.1)$$

donde $t = d/v$ es el tiempo de vuelo de los iones durante la distancia del blanco al degradador d y con una velocidad v , que corresponde a la velocidad de los iones antes del degradador.

Dos métodos de análisis pueden ser usados dentro de la técnica RDDS para extraer el tiempo de vida de los estados excitados en los núcleos: el método de la curva de decaimiento y el método de la curva de decaimiento diferencial. Los dos métodos se ilustran esquemáticamente en los paneles superior e inferior de Fig. 4.1, respectivamente. Ambos métodos se utilizaron siguiendo la formulación general para el esquema de niveles general con alimentación proveniente de los estados de arriba descrito en [47].

Método de la curva de decaimiento (DCM)

La curva de decaimiento experimental derivada de las ecuaciones diferenciales de Bateman, para un nivel i con N niveles k que la alimentan, viene dada por,

$$R_i(t) = P_i e^{-t\lambda_i} + \sum_{k=i+1}^N M_{ki} \left[(\lambda_i/\lambda_k) e^{-t\lambda_k} - e^{-t\lambda_i} \right], \quad (7.2)$$

donde

$$M_{ki}(t)(\lambda_i/\lambda_k - 1) = b_{ki}P_k - b_{ki} \sum_{m=k+1}^N M_{mk} + \sum_{m=i+1}^{k-1} M_{km}b_{mi}(\lambda_m/\lambda_k), \quad (7.3)$$

y P_i y P_k son las intensidades de alimentación directa de cada nivel, λ_i y λ_k son las constantes de decaimiento de los niveles y b_{ki} es el *branching ratio* de los niveles k a i . La función $R_i(t)$ se ajusta a la curva de datos experimentales, Eq. (7.1), para obtener la vida útil del estado de interés excitado i (panel superior derecho de la Fig. 4.1).

Método de la curva de decaimiento diferencial (DDCM)

El tiempo de vida de un nivel i con N niveles k que lo alimentan, viene dada por,

$$\tau_i(t) = \frac{-R_i(t) + \sum_{k=i+1}^N b_{ki}\alpha_{ki}R_k(t)}{\frac{dR_i(t)}{dt}} \quad (7.4)$$

Y el factor α_{ki} está determinado por las eficiencias del detector, $\varepsilon(E_{\gamma j})$, y las distribuciones angulares, $\omega_j(\theta)$, de las transiciones de rayos gamma de los niveles $j = i, k$ de la siguiente manera,

$$\alpha_{ki} = \frac{\omega_k(\theta)\varepsilon(E_{\gamma k})}{\omega_i(\theta)\varepsilon(E_{\gamma i})} \quad (7.5)$$

Luego, el tiempo de vida se puede extraer individualmente para cada distancia medida. Como se muestra esquemáticamente en el panel inferior en Fig. 4.1, el tiempo de vida se determina ajustando los valores obtenidos por distancia a una función constante $\tau_i(t)$.

Alimentación desde estados superiores

La consideración de la alimentación de estados superiores en el análisis del nivel a estudiar es crucial para la determinación fiable de el tiempo de vida. En las reacciones de transferencia de varios nucleones, se pueden excitar estados con momentos angulares de hasta $10 \hbar$. La ventaja de utilizar un espectrómetro magnético de masas es que permite controlar parcialmente la alimentación, directa o indirecta, a través de estados con mayor energía de excitación [49]. De esta manera es posible limitar o reducir la contribución de la alimentación indirecta en el estado de interés. Este método se ha aplicado consistentemente a los datos de este experimento para evitar incertidumbres sistemáticas en el valor final de el tiempo de vida debido a la alimentación desde niveles excitados más altos. Sin embargo, debido a la exótica naturaleza del ^{94}Ru en estudio, las estadísticas acumuladas eran bastante limitadas y, por lo tanto, se tuvo que implementar un método alternativo. En los casos de los núcleos de ^{92}Mo y ^{94}Ru , la existencia de estados de largas vidas medias con periodos de semidesintegración entre 1.5 y 0.5 ns, contribuye a la alimentación sesgada tanto del componente desplazado como del no desplazado. Esto ocurre porque la emisión de rayos gamma se produce a una gran distancia después del blanco, y el ángulo θ (entre la dirección de iones y los rayos gamma emitidos) aumenta en comparación con el ángulo de emisión de rayos gamma en la posición del degradador. Por lo tanto, después de hacer la corrección Doppler, si el estado tiene una vida media larga, aparece a una energía gamma desplazada (reducida) por el efecto Doppler. Este efecto se usa para el método llamado DSAM geométrico [86]. En el caso de ^{94}Ru es obligatorio usar lo que hemos llamado el método de sustracción, es decir, las intensidades de los componentes desplazados y no desplazados se han obtenido con la resta de la contribución de las transiciones de vida media larga.

7.4.2. Verificación de la metodología

El análisis preciso de las vidas medias de interés implica el tratamiento de la alimentación de estados superiores. Para las transiciones $4^+ \rightarrow 2^+$, la alimentación se ha reducido lo máximo posible para utilizar la formulación más simple en los métodos DCM y DDCM. Esto permite una doble validación, donde las incertidumbres sistemáticas atribuidas a cada metodología de análisis pueden cuantificarse

independientemente. Para las transiciones $2^+ \rightarrow 0^+$, la vida media de los estados superiores se ha incluido en la formulación. En resumen, se han realizado dos análisis de validación para comprobar ambos métodos utilizando como referencia estados nucleares con vidas medias conocidas.

El caso más simple corresponde a una situación en la que el estado nuclear de interés está poblado directamente por una reacción nuclear en el momento $t = 0$. Esto se ha investigado utilizando la vida media del estado $25/2^-$ en ^{93}Tc . La vida media determinada es $\tau = 75(6)$ ps ($t_{1/2} = 52(4)$ ps) para el método DCM y $\tau = 75(3)$ ps ($t_{1/2} = 52,0(17)$ ps) para el método DDCM. Estos resultados están de acuerdo con el período de semidesintegración $t_{1/2} = 57,5(21)$ ps dado en [88], confirmando así la exactitud de la metodología de análisis.

La verificación de la metodología con ^{94}Mo incluyó la alimentación indirecta desde los estados, a mayor energía de excitación de los estados superiores $6^+ \rightarrow 4^+$ y $5^- \rightarrow 4^+$ para determinar la vida media conocida de la transición $4^+ \rightarrow 2^+$. En este análisis, se usó también una selección en la TKEL para evitar cualquier alimentación indirecta y reducir lo máximo posible la alimentación de los niveles observados como es el caso de la transición $5^- \rightarrow 4^+$ (ver panel inferior en Fig. 4.10). Los vidas medias determinadas $\tau = 7.1$ (17) ps ($t_{1/2} = 4.9$ (1.2) ps) para el método DCM y $\tau = 7.1$ (10) ps ($t_{1/2}=4.9(7)$ ps) para el DDCM, están de acuerdo con el valor de referencia de el período de semidesintegración en la Ref. [89], $t_{1/2} = 5.0$ (7).

El mismo análisis se aplicó a los núcleos de interés. Además, puesto que en caso del ^{94}Ru no era posible la aplicación de la selección en la energía de excitación, el método de la sustracción de las transiciones de vidas medias largas fue aplicado, previamente verificado con el ^{92}Mo .

7.4.3. Resultados

Las nuevas vidas medias, τ , medidas en este trabajo y las correspondientes probabilidades de transición reducida $B(E2)$ se resumen en la Tabla 7.1. Dado que los valores extraídos utilizando los métodos DCM y DDCM están en buen acuerdo, las vidas adoptadas han sido tomadas del valor con menor incertidumbre. En el caso de la transición $4^+ \rightarrow 2^+$ en ^{92}Mo se ha hecho la media ponderada entre los dos valores DDCM obtenidos de los diferentes métodos de sustracción de estados

usados para eliminar la contribución de los estados de de vida media larga. Nótese que el resultado de la transición $6^+ \rightarrow 4^+$ en ^{90}Zr se escribe entre paréntesis, debido a las dificultades encontradas en la extracción de la vida media (ver Section 4.4.1).

TABLA 7.1: Vidas medias (τ), períodos de semidesintegración ($t_{1/2}$) y probabilidades de transición reducidas ($B(E2)$).

Núcleo	Transición	τ (ps)	$t_{1/2}$ (ps)	$B(E2)_{exp}$ ($e^2\text{fm}^4$)	$B(E2)_{exp-prev}$ ($e^2\text{fm}^4$)
^{90}Zr	$4^+ \rightarrow 2^+$	4.2(4)	2.9(3)	304(29)	-
	$6^+ \rightarrow 4^+$	(19(4))	(13(3))	(115(24))	-
^{92}Mo	$2^+ \rightarrow 0^+$	0.49(18)	0.34(12)	212(75)	206(12)[89]
	$4^+ \rightarrow 2^+$	35.0(6)	24.3(4)	84.3(14)	<304[89]
^{94}Ru	$2^+ \rightarrow 0^+$	0.7(3)	0.49(21)	194(83)	≥ 9.5 [11]
	$4^+ \rightarrow 2^+$	87(8)	60(6)	38(3)	≥ 46 [11]

Los presentes resultados de la vida media han permitido estimar, por primera vez, las probabilidades de transición reducidas nunca antes medidas para los núcleos mágicos de neutrones en esta región. En general, las $B(E2)$ están de acuerdo con los valores y límites medidos en experimentos anteriores.

7.5. Interpretación Teórica y Conclusiones

7.5.1. Evolución de la colectividad en la capa $\pi g_{9/2}$

Los cálculos del modelo de capas para los núcleos de ^{90}Zr , ^{92}Mo y ^{94}Ru se han realizado dentro del espacio de valencia del protón $f_{5/2}$, $p_{3/2}$, $p_{1/2}$ y $g_{9/2}$. Todos las energías SP se derivan del ^{59}Cu , excepto para el orbital $g_{9/2}$ aún no observado experimentalmente y para el que se usa una energía estimada de 3.2 MeV [9]. Estos cálculos del modelo de capas para la interpretación de los núcleos de interés están basados en interacciones realistas [93]. Éstos fueron realizados por el grupo teórico del INFN, Complesso Universitario di Monte S. Angelo (Nápoles, Italia), en particular por A. Gargano y L. Coraggio, en el contexto de la colaboración que realiza este estudio.

La interacción residual de dos cuerpos se obtiene empezando con el potencial CD-Bonn de nucleón-nucleón como se describe en la Ref. [93]. Todas las contribuciones

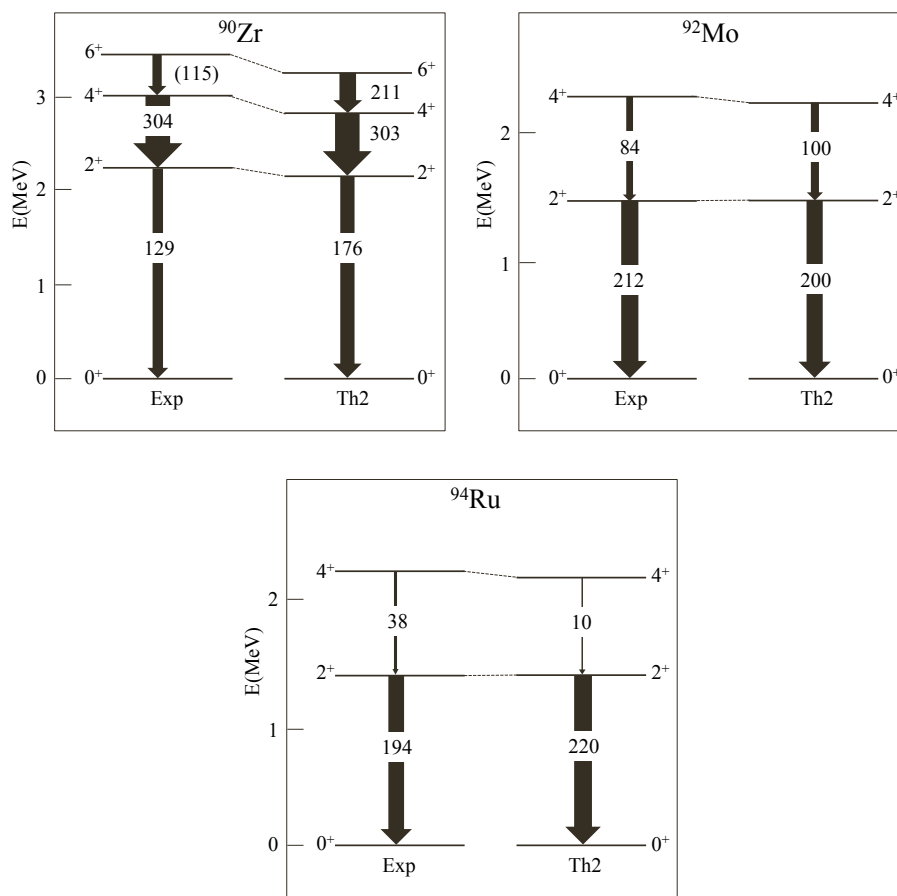


FIGURA 7.2: Espectros de energía experimentales y teóricos para los núcleos ^{90}Zr , ^{92}Mo y ^{94}Ru . Los números y el grosor de las flechas son proporcionales a la probabilidad de transición reducida $B(E2)$ en unidades de $e^2\text{fm}^4$. Los valores teóricos presentados corresponden a cálculos realistas del modelo de capas con carga microscópica. El valor $B(E2; 2^+ \rightarrow 0^+)$ para ^{90}Zr ha sido tomado de la Ref. [89].

hasta el tercer orden se han incluido en la expansión perturbativa, utilizando el método Q-box. Para el cálculo de las probabilidades de transición, la carga efectiva del operador del cuadrupolo eléctrico se puede obtener ajustando a los datos experimentales o mediante cálculo microscópico. Por lo tanto, en este trabajo se presentan dos resultados que utilizan cálculos realistas del modelo de capas en función de la carga efectiva utilizada para los protones. El primer resultado, indicado como *th1*, usa una carga efectiva empírica de $e_\pi = 1.5e$. El segundo, nombrado *th2*, corresponde a la derivación microscópica de la carga efectiva[93, 96].

El cálculo teórico para ambos resultados (*th1* y *th2*) y los valores experimentales de las $B(E2)$ para los estados de excitación baja se muestran en las Tablas 5.2, 5.3 y 5.4, para los núcleos ^{90}Zr , ^{92}Mo y ^{94}Ru , respectivamente. El acuerdo entre la teoría y el experimento puede considerarse más satisfactorio para el resultado

teórico utilizando la carga efectiva microscópica, *th2*. La Fig. 7.2 ilustra la comparación entre los cálculos realizados con esta carga efectiva y el experimento para los núcleos ^{90}Zr , ^{92}Mo y ^{94}Ru , respectivamente. Esto demuestra la fiabilidad del modelo de capas realista utilizando operadores microscópicos.

7.5.1.1. Esquema de *seniority*

Para evaluar el esquema de *seniority* a lo largo de los isótonos con $N = 50$ hacia el núcleo doblemente mágico ^{100}Sn , se ha realizado un estudio exhaustivo de las probabilidades de transición reducidas $B(E2)$ experimentales conocidas en la Fig. 7.3 para los estados 2^+ , 4^+ , 6^+ y 8^+ de esos isótonos. Los valores $B(E2)$ de este trabajo se representan en rojo. Los símbolos turquesa son los valores experimentales de experimentos previos [11, 89, 100]. Además, los cálculos teóricos se representan para la evaluación de la conservación de *seniority*. En verde, se muestran los cálculos realistas del modelo de capas realizados por el grupo de Nápoles para este trabajo. Las líneas discontinuas verdes y los símbolos cuadrados vacíos indican los cálculos con una carga empírica de $e_\pi = 1.5 e$. Las líneas continuas verdes y los símbolos cuadrados rellenos corresponden a cálculos con cargas microscópicas.

Por completitud, además de los cálculos del modelo de capas mencionados, los cálculos teóricos correspondientes al modelo indicado como SMCC en la Ref. [11] (ver sección III.A) también se presentan en la figura. Estos cálculos también se realizan en el espacio de valencia del protón $f_{5/2}$, $p_{3/2}$, $p_{1/2}$ y $g_{9/2}$ utilizando una

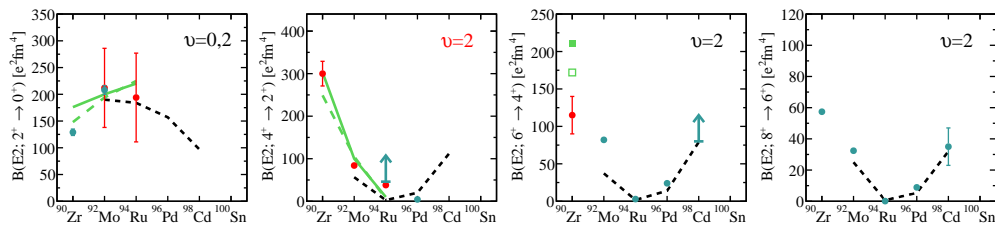


FIGURA 7.3: Evolución de la colectividad a lo largo de los isótonos con $N = 50$. Probabilidades de transición reducida experimentales y teóricas $B(E2; 2^+ \rightarrow 0^+)$, $B(E2; 4^+ \rightarrow 2^+)$, $B(E2; 6^+ \rightarrow 4^+)$ y $B(E2; 8^+ \rightarrow 6^+)$ para los isótonos $N = 50$ con $A = 90 - 100$. Los símbolos rojos son los resultados experimentales de este trabajo. Los símbolos turquesas son los valores experimentales de experimentos anteriores, $B(E2; 2^+ \rightarrow 0^+)$ [89], $B(E2; 4^+ \rightarrow 2^+)$ [11], $B(E2; 6^+ \rightarrow 4^+)$ [11, 89] y $B(E2; 8^+ \rightarrow 6^+)$ [89, 100]. Las líneas negras discontinuas corresponden al cálculo del modelo de capas reportado en la Ref. [11] como SMCC. Las líneas verdes discontinuas (continuas) y el cuadrado vacío (relleno) son las predicciones del modelo de capas para el cálculo utilizando cargas empíricas, *th1* (cargas microscópicas, *th2*) [9]. Ver el texto para más detalles. Téngase en cuenta que el valor de $6^+ \rightarrow 4^+$ en ^{90}Zr es tentativo.

interacción realista con el potencial de CD-Bonn y una carga de protones efectiva empírica, en este caso, de $e_\pi = 1.35 e$. Las líneas discontinuas negras representan estos cálculos.

Finalmente, los resultados teóricos explican muy bien todas las transiciones en los isótonos $N = 50$ y, en particular, la transición $4^+ \rightarrow 2^+$. Por lo tanto, los resultados obtenidos para los valores $B(E2; 4^+ \rightarrow 2^+)$ confirman la tendencia esperada y la conservación de *seniority*.

7.5.2. Conclusiones

En esta Tesis se ha estudiado la evolución de la colectividad a lo largo de los isótonos con $N = 50$ hacia ^{100}Sn . Para ello, se realizaron medidas de la vida media de los estados de espín *yrast* en los isótonos con $N = 50$ ^{90}Zr , ^{92}Mo y ^{94}Ru .

Las medidas fueron llevadas a cabo en las instalaciones de GANIL, donde la región rica en protones cerca a las capas cerradas $N = Z = 50$ fue poblada satisfactoriamente con una reacción de transferencia de varios nucleones. Esta reacción permitió poblar estados de bajo momento angular en presencia de alimentación con vidas medias largas por isómeros de alto espín. Los productos de la reacción fueron unívocamente identificados por el espectrómetro magnético de VAMOS++, y los rayos gamma en coincidencia fueron medidos usando el multi-detector de trazado AGATA. El *plunger* fue usado para determinar las vidas medias de los estados excitados en esta región con el método RDDS.

La validez de la instalación experimental y de la metodología fue probada, usando dos métodos diferentes (DCM y DDCM) con las medidas de la vida media del estado excitado $25/2^-$ en ^{93}Tc y con el primer estado 4^+ en ^{94}Mo . Dichos resultados son compatibles con los valores reportados en la literatura.

Los resultados de las vida media obtenidas y de las probabilidades de transición reducidas para las transiciones *yrast* $4^+ \rightarrow 2^+$, $2^+ \rightarrow 0^+$ y $6^+ \rightarrow 4^+$ en ^{94}Ru , ^{92}Mo y ^{90}Zr han sido determinados y comparados con los cálculos del modelo de capas realistas en espacio de valencia del protón $f_{5/2}$, $p_{3/2}$, $p_{1/2}$ y $g_{9/2}$.

Los valores $B(E2; 4^+ \rightarrow 2^+)$ medidos siguen la tendencia esperada para las transiciones con $\Delta v = 0$ en el esquema de *seniority*. Por ello, se puede concluir que se

confirma la conservación del *seniority* a lo largo del orbital $\pi g_{9/2}$ en núcleos con $N = 50$.

Estos resultados permitirán también comparar la tendencia de la estructura nuclear entre los isótonos ^{78}Ni - ^{100}Sn con $N = 50$ y los isótopos $^{56-78}\text{Ni}$ con $Z = 28$, núcleos de simetría espejo de valencia (VMS). Contrariamente a lo se ha comprobado para los isótonos con $N = 50$ en esta Tesis, las predicciones del modelo de capas indican que las interacciones efectivas podrían no conservar *seniority* para los isótopos con $Z = 28$ hacia ^{78}Ni .

7.6. Rendimiento de AGATA

El rendimiento de AGATA ha sido evaluado con fuentes radiactivas de rayos gamma usando las mismas condiciones experimentales que en experimentos con haz. Nótese que la presencia del *plunger* diferencial en el montaje (Section 7.2) provoca una estructura doble en todos los picos de los espectros gamma que provienen de la medida con haz. Aunque este no es el mejor escenario para evaluar el funcionamiento del multi-detector, las principales características de su rendimiento han sido analizadas usando diferentes enfoques de análisis para una evaluación exhaustiva de las incertidumbres sistemáticas.

7.6.1. Resolución en energía

La resolución energética de AGATA se ha presentado utilizando fuentes radiactivas (ver Fig. 6.11) y se ha evaluado cualitativamente en condiciones experimentales (ver Fig. 6.26), donde el FWHM está dominado en la mayoría de los casos por la corrección Doppler. Ésta depende de la precisión alcanzada en la determinación, evento por evento, de la posición y la velocidad de los núcleos emitidos. Para la configuración de AGATA usada en este experimento, la evaluación de la resolución de la energía de cada cristal muestra mejores resultados utilizando la energía de la suma de los segmentos después de ser corregidos por los efectos del daño de neutrones.

7.6.2. Eficiencia

La eficiencia absoluta de AGATA para diferentes métodos de tratamiento de datos se ha determinado experimentalmente por medio de fuentes radiactivas de rayos gamma calibradas y se ha comparado con la eficiencia estimada para la medida con haz usando la transición gamma $2^+ \rightarrow 0^+$ (1509keV) del ^{92}Mo . Para las medidas con fuente, las tasas de conteo por cristal eran alrededor de 550 Hz, mientras que para las medidas con haz estaban en el rango de 40-50 kHz. Los resultados y las curvas ajustadas se presentan en la Fig. 6.31.

Para la eficiencia en las coincidencias, se han investigado las correlaciones angulares. Las correlaciones angulares usando fuentes radiactivas muestran una pérdida de eficiencia del 10% para ángulos pequeños entre los dos rayos gamma en los datos analizados con el algoritmo de *tracking*. Para la medida con haz, las correlaciones angulares se vuelven más difíciles de analizar debido a la orientación del momento del haz. Además el número relativamente bajo de cuentas en el espectro en este experimento no ha permitido ir más lejos en este aspecto del estudio.

Como se ve en la Fig. 6.31, las estimaciones finales de la eficiencia de medidas con haz son consistentes con la tendencia de la curva de las eficiencias obtenidas con las fuentes radiactivas. Estas estimaciones tienen en cuenta las pérdidas debidas a las altas tasas de conteo en medidas con haz. También se han incluido las correcciones para las pérdidas de eficiencia para ángulos pequeños con el método de *tracking*, tomando como referencia el valor estimado para la eficiencia en coincidencias de las fuentes. Con respecto al modo utilizado para analizar el experimento de esta Tesis (*tracking* usando la suma de la energía los segmentos), se encuentra que la eficiencia absoluta calculada a partir de las fuentes a 1509 keV es 2.395(18)%, lo cual está totalmente de acuerdo con 2.45(20)% a 1509 keV.

7.7. Sumario

La presente Tesis se centra en el estudio experimental de la evolución de la colectividad alrededor de del núcleo doblemente mágico ^{100}Sn . En particular, se ha investigado la conservación de *seniority* a lo largo del orbital $g_{9/2}$.

La medida fue realizada con éxito en el laboratorio de GANIL. Para poblar los núcleos de interés ricos en protones se usó el mecanismo de reacción de transferencia de varios nucleones: un haz de ^{92}Mo con una energía de 716.9 MeV incidido en el blanco de ^{92}Mo del *plunger* de IKP de Colonia, mientras que se usó una lámina ^{24}Mg para degradar la energía de los productos de reacción para medir la vida media con la técnica RDDS. Los productos de reacción de interés se han identificado con el espectrómetro magnético VAMOS ++, mientras que los rayos gamma se han medido con AGATA. Se midieron siete distancias diferentes: 19, 25, 100, 500, 1000, 2000 y 4000 μm .

La validez de la instalación experimental y de la metodología fue probada, usando dos métodos diferentes (DCM y DDCM) con las medidas de la vida media del estado excitado $25/2^-$ en ^{93}Tc y con el primer estado 4^+ en ^{94}Mo . Dichos resultados son compatibles con los valores reportados en la literatura.

De este experimento, las probabilidades de transición reducidas para las transiciones $4^+ \rightarrow 2^+$ y $2^+ \rightarrow 0^+$ yrast en ^{92}Mo y ^{94}Ru y para los $4^+ \rightarrow 2^+$ y $6^+ \rightarrow 4^+$ yrast transiciones en ^{90}Zr han sido determinadas. Esto hizo posible un estudio completo del esquema de *seniority* en $\pi g_{9/2}$.

Los resultados de las probabilidades de transición reducidas obtenidas se han interpretado sobre la base de predicciones realistas del modelo de shell en $f_{5/2}$, $p_{3/2}$, $p_{1/2}$, $g_{9/2}$ espacio de valencia de protones, lo que permite también la comparación de las tendencias de la estructura nuclear entre los núcleos de simetría de espejo de valencia.

La publicación de estos resultados está en preparación y se pretende enviar a la revista *Physical Review Letters*.

Además, parte de esta Tesis está dedicada al rendimiento del detector de espectroscopía de rayos gamma de alta resolución de última generación utilizado en el experimento.

La caracterización de AGATA se muestra en base al análisis de los datos tomados con fuentes radiactivas y con haz usando 23 cristales HPGe segmentados. Cabe esperar que el trabajo presentado en este parte podrá ser ampliado y mejorado en el futuro, usando una configuración experimental más conveniente para el estudio del rendimiento, como por ejemplo un blanco simple de poco espesor, y un mayor número de cristales de AGATA .

El artículo para la publicación de estos estudios en combinación con el trabajo realizado en colaboración con el equipo de *performance* de AGATA en GANIL con 30 cristales ha sido enviado a la revista *Nuclear Instruments and Methods in Physics Research A* recientemente, en mayo de 2019.

Bibliografía

- [1] C. Hinke et al. Superallowed Gamow-Teller decay of the doubly magic nucleus ^{100}Sn . *Nature*, 486(7403):341–345, 2012.
- [2] B. A. Brown et al. Gamow-Teller strength in the region of ^{100}Sn . *Physical Review C*, 50(R2270(R)), 1994.
- [3] G. Racah. Theory of Complex Spectra. III. *Physical Review*, 63:367, 1943.
- [4] P. Van Isacker. Partial Conservation of Seniority in Nuclei. *International Journal of Modern Physics E*, 20(2):191–198, 2011.
- [5] P. Van Isacker and S. Heinze. Partial Conservation of Seniority and Nuclear Isomerism. *Physical Review Letters*, 100(052501), 2008.
- [6] A. Escuderos and L. Zamick. Seniority conservation and violation in the $g_{9/2}$ shell. *Physical Review C*, 73(044302), 2006.
- [7] P. Van Isacker. Seniority isomers in nuclei. *Journal of Physics: Conference Series*, 322(012003), 2011.
- [8] A. F. Lisetskiy et al. New $T = 1$ effective interactions for the $f_{5/2} p_{3/2} p_{1/2} g_{9/2}$ model space: Implications for valence-mirror symmetry and seniority isomers. *Physical Review C*, 70(044314), 2004.
- [9] A. Gargano and L. Coraggio. Private communication.
- [10] A.F. Lisetskiy et al. Exotic nuclei near ^{78}Ni in a shell model approach. *European Physical Journal A*, 25(s01):95–96, 2005.
- [11] H. Mach et al. Ultrafast-timing lifetime measurements in ^{94}Ru and ^{96}Pd : Breakdown of the seniority scheme in $N = 50$ isotones. *Physical Review C*, 95(014313), 2017.

- [12] H. Grawe. Experimental approach towards shell structure at ^{100}Sn and ^{78}Ni . *Nuclear Physics*, A704:211c–222c, 2002.
- [13] S. Akkoyun et al. AGATA-Advanced GAMMA Tracking Array. *Nuclear Instruments and Methods in Physics Research A*, 668:26–58, March 2012. And references therein.
- [14] A. Gadea et al. Conceptual design and infrastructure for the installation of the first AGATA sub-array at LNL. *Nuclear Instruments and Methods in Physics Research A*, 654:88–86, October 2011.
- [15] C. Domingo-Pardo et al. Conceptual design and performance study for the first implementation of AGATA at the in-flight RIB facility of GSI. *Nuclear Instruments and Methods in Physics Research A*, 694:297–312, 2012.
- [16] E. Clément et al. Conceptual design of the AGATA 1π array at GANIL. *Nuclear Instruments and Methods in Physics Research A*, 855:1–12, May 2017.
- [17] N. Lalović et al. Performance of the AGATA γ -ray spectrometer in the PreS-PEC set-up at GSI. *Nuclear Instruments and Methods in Physics Research A*, 806:258–266, 2016.
- [18] J. Ljungvall, R.M. Pérez-Vidal, et al. Performance of The Advanced GAMMA Tracking Array (AGATA) at GANIL. Submitted May 2019.
- [19] <http://pro.ganil-spiral2.eu/users-guide/accelerators/available-stable-ion-beams-at-ganil/view>.
- [20] <http://pro.ganil-spiral2.eu/users-guide/accelerators/spiral1newbeams>.
- [21] O. Kamalou et al. Stable and exotic beams produced at GANIL. *Proceedings of Cyclotrons 2016*, 2016.
- [22] D. Lunney G. Audi and H.J. Kluge, editors. *Atomic Physics at Accelerators: Mass Spectrometry: Proceedings of the APAC 2000, held in Cargese, France, 19-23 September 2000*, volume 132. Kluwer Academic Publishers, 2001.
- [23] R. Broda et al. Collisions between ^{106}Cd and ^{54}Fe at 30 MeV above the Coulomb barrier by high resolution $\gamma\gamma$ coincidences. *Physical Review C*, 49, 1994.

- [24] P. Sortais et al. ECR ion source developments at GANIL. *Nuclear Physics News*, 6(4):6–8, 1996.
- [25] L. Corradi, G. Pollarolo, and S. Szilner. Multinucleon transfer processes in heavy-ion reactions. *Journal of Physics G: Nuclear and Particle Physics*, 3(113101), 2009.
- [26] K.E. Rehm. Quasi-elastic heavy-ion collisions. *Annu. Rev. Nuc. Part. Sci.*, 41:429–468, 1991.
- [27] K. S. Krane. *Introductory Nuclear Physics*. 1988.
- [28] G. Pollarolo. Multinucleon transfer reactions. *Pramana – Journal of Physics*, 53(3), 1999.
- [29] <http://lise.nscl.msu.edu/lise.html>.
- [30] <http://lise.nscl.msu.edu/doc/tutorial.pdf>.
- [31] M.P. Kuchera, O.B. Tarasov, D. Bazin, B. Sherril, and K.V. Tarasova. LISE⁺⁺ Software Updates and Future Plans. *Journal of Physics: Conference Series*, 664(072029), 2015.
- [32] <http://personalpages.to.infn.it/nanni/grazing/>.
- [33] A. Winther. Dissipation, polarization and fluctuation in grazing heavy-ion collisions and the boundary to the chaotic regime. *Nuclear Physics A*, 594(2):203–245, 1995.
- [34] A. Winther. Grazing reactions in collisions between heavy nuclei. *Nuclear Physics A*, 572(1):191–235, 1994.
- [35] T. Mijatović et al. Multinucleon transfer reactions in the $^{40}\text{Ar}+^{208}\text{Pb}$ system. *Physical Review C*, 94(064616), 2016.
- [36] G. Pollarolo. Private communication.
- [37] S. Szilner. Private communication.
- [38] Vogt et al. Light and heavy transfer products in $^{136}\text{Xe}+^{238}\text{U}$ multinucleon transfer reactions. *Physical Review C*, 92(024619), 2015.

- [39] S. Pullanhiotan et al. Improvement in the reconstruction method for VAMOS spectrometer. *Nuclear Instruments and Methods in Physics Research B*, 266, 2008.
- [40] M. Rejmund et al. Performance of the improved large acceptance spectrometer: VAMOS++. *Nuclear Instruments and Methods in Physics Research A*, 646:184–191, 2011.
- [41] M. Vandebrouck et al. Dual Position Sensitive MWPC for tracking reaction products at VAMOS++. *Nuclear Instruments and Methods in Physics Research A*, 812:112–117, 2016.
- [42] S. Pullanhiotan et al. Performance of VAMOS for reaction near Coulomb barrier. *Nuclear Instruments and Methods in Physics Research A*, 593:343–352, 2008.
- [43] <http://pro.ganil-spiral2.eu/laboratory/experimental-areas/g1-vamos/beam-optics/vamos-optics/view>.
- [44] H. Savajols. VAMOS: A variable mode high acceptance spectrometer. *Nuclear Instruments and Methods in Physics Research B*, 204:146–153, 2003.
- [45] A. Lemasson. <<Analysis at GANIL>> AGATA@VAMOS. In *EGAN-3rd Data Analysis School 2014*, 2014.
- [46] C. Fransen. Exploring exotic nuclei using the Cologne compact plunger with AGATA and VAMOS. In *AGATA Week Madrid*, 2014.
- [47] A. Dewald et al. Developing the recoil distance doppler-shift technique towards a versatile tool for lifetime measurements of excited nuclear states. *Progress in Particle and Nuclear Physics*, 67(3):786–839, 2012.
- [48] F.J. Karasek. Fabrication of target foils by rolling techniques. *Nuclear Instruments and Methods*, 102(3):457–458, 1972.
- [49] D. Mengoni. Lifetime measurements of neutron-rich nuclei around ^{48}Ca with the CLARA-PRISMA setup. *The European Physical Journal A*, 42:387–391, 2009.
- [50] R.M. Lieder et al. *Nucl. Phys. A*, 682:279c, 2001.
- [51] M. A. Deleplanque et al. GRETA: utilizing new concepts in γ -ray detection. *Nuclear Instruments and Methods in Physics Research A*, 430(2-3), 1999.

- [52] E. Farnea et al. Conceptual design and Monte Carlo simulations of the AGATA array. *Nuclear Instruments and Methods in Physics Research A*, 621:331–343, 2010.
- [53] A. Georgiev and W. Gast. Digital Pulse Processing in High Resolution, High Throughput Gamma-Ray Spectroscopy. *IEEE Transactions on Nuclear Science*, 40(4), 1993.
- [54] V.T. Jordanov and G.F. Knoll. Digital synthesis of pulse shapes in real time for high resolution radiation spectroscopy. *Nuclear Instruments and Methods in Physics Research A*, 345:337–345, 1994.
- [55] F. Recchia et al. Efficiency and Energy Resolution of the AGATA Demonstrator at High Count Rate. *LNL Annual Report*, 2010.
- [56] B. Bruyneel, B. Birkenbach, and P. Reiter. Pulse shape analysis and position determination in segmented HPGe detectors: The AGATA detector library. *European Physical Journal A*, 52(70), 2016.
- [57] A. Korichi and T. Lauritsen. Tracking γ rays highhigh segmented HPGe detectors: A review of AGATA and GRETINA. *European Physical Journal A*, 55:121, 2019.
- [58] P.-A. Söderström et al. Interaction position resolution simulations and in-beam measurements of the AGATA HPGe detectors. *Nuclear Instruments and Methods in Physics Research A*, 638:96–109, 2011.
- [59] R. Venturelli and D. Bazzacco. Adaptive grid search as pulse shape analysis algorithm for gamma-tracking and results. *LNL Annual Report*, 220, 2004.
- [60] L. Lewandowski et al. Pulse-Shape Analysis and position resolution in highly segmented HPGe AGATA detectors. Submitted to European Physical Journal.
- [61] B. Bruyneel et al. Crosstalk properties of 36-fold segmented symmetric hexagonal HPGe detectors. *Nuclear Instruments and Methods in Physics Research A*, 599:196–208, February 2009.
- [62] B. Bruyneel, P. Reiter, and G. Pascovici. Characterization of large volume HPGe detectors. Part II: Experimental results. *Nuclear Instruments and Methods in Physics Research A*, 569:774–789, 2006.

- [63] B. Bruyneel et al. Correction for hole trapping in AGATA detectors using pulse shape analysis. *The European Physical Journal A*, 49:61, 2013.
- [64] G.F. Knoll. *Radiation Detection Measurement*. John Wiley & Sons, third edition, 2000.
- [65] G. J. Schmid et al. A γ -ray tracking algorithm for the GRETA spectrometer. *Nuclear Instruments and Methods in Physics Research A*, 430:69–83, 1999.
- [66] J. van der Marel and B. Cederwall. Backtracking as a way to reconstruct Compton scattered γ -rays. *Nuclear Instruments and Methods in Physics Research A*, 437:538–551, 1999.
- [67] A. López-Martens, K. Hauschild, A. Korichi, J. Roccaz, and J-P. Thibaud. γ -ray tracking algorithms: a comparison. *Nuclear Instruments and Methods in Physics Research A*, 533(3):454–466, 2004.
- [68] D. Bazzacco. The Advanced Gamma Ray Tracking Array AGATA. *Nuclear Physics A*, 746:248c–254c, 2004.
- [69] G. Wittwer et al. Merging several separate data acquisition systems at GANIL. *14th Conference on Real Time (RT2005), Jun 2005, Stockholm, Sweden.*, (in2p3-00105175):pp.427–428, 2006.
- [70] M. Bellato. Private communication.
- [71] X. Grave et al. NARVAL a Modular Distributed Data Acquisition System with Ada 95 and RTAI. In *Real Time Conference 14th IEEE-PSS*, 2005.
- [72] https://atrium.in2p3.fr/nuxeo/nxdoc/default/878272cd-bb33-4b35-aa30-227c1a38e8d1/view_documents.
- [73] ROOT - A Data Analysis Framework. <https://root.cern.ch/drupal>.
- [74] GammaWare - Agata Data Analysis. <http://agata.in2p3.fr>.
- [75] R.M. Pérez-Vidal. AGATA Analysis. <https://atrium.in2p3.fr/nuxeo/nxpath/default/Atrium/sect>.
- [76] M. Kaci and V. Mendez. The AGATA GRID computing model for data management and data processing., 2011.
- [77] <https://home.cern/science/computing/worldwide-lhc-computing-grid>.

- [78] I. Foster and C. Kesselman. *The GRID Blueprint for a New Computing Infrastructure*. Morgan Kaufmann Publishers, Inc., San Francisco, USA, ISBN 1-55860-475-8.
- [79] <http://wlcg-public.web.cern.ch/tier-centres>.
- [80] M. Kaci. <http://ns.ph.liv.ac.uk/EGAN/files/wednesday/GRID-HOWTO.pdf>.
- [81] R. M. Pérez-Vidal. AGATA Analysis on the GRID. [https://atrium.in2p3.fr/nuxeo/nxpath/default/Atrium/sections/Public/AGATA/DataProcessing/AGATA Analysis workshops/AGATA Analysis workshop.1548153669115@view_documents?tabIds=%3A&conversationId=0NXMAIN2](https://atrium.in2p3.fr/nuxeo/nxpath/default/Atrium/sections/Public/AGATA/DataProcessing/AGATA%20Analysis%20workshops/AGATA%20Analysis%20workshop.1548153669115@view_documents?tabIds=%3A&conversationId=0NXMAIN2).
- [82] The Lustre file system: <http://www.lustre.org>.
- [83] P. H. Stelson et al. Coulomb Excitation of States in ^{92}Mo and ^{119}Sn . *Bull. Am. Phys. Soc.*, 9(4):484, 1964.
- [84] H. Morinaga and T. Yamazaki. *In-beam gamma-ray spectroscopy*. North-Holland, 1976.
- [85] W.D.Hamilton, editor. *Nuclear Spectroscopy*. North-Holland, 1975.
- [86] C. Stahl et al. APCAD - Analysis program for the continuous-angle DSAM. *Computer Physics Communications*, 214:174–198, 2017.
- [87] A. Fitzler. Tv User-Manual, July 2000.
- [88] M. Hausmann et al. Lifetime study of particle-hole excitations in the semi-magic nucleus ^{93}Tc . *Physical Review C*, 68(024309), 2003.
- [89] [https://www.nndc.bnl.gov/ensdf - xundl](https://www.nndc.bnl.gov/ensdf/xundl).
- [90] L. Coraggio, A. Covello, A. Gargano, N. Itaco, and T. T. S. Kuo. Shell-model calculations and realistic effective interactions. *Prog. Part. Nucl. Phys.*, 62:135, 2009.
- [91] L. Coraggio et al. Effective shell-model hamiltonians from realistic nucleon–nucleon potentials within a perturbative approach. *Annals of Physics*, 327:2125–2151, 2012.

- [92] P.J. Brussaard and P.W.M. Glaudemans. *Shell-model applications in nuclear spectroscopy*. North-Holland, 1977.
- [93] L. Coraggio et al. Renormalization of the Gamow-Teller operator within the realistic shell model. *Physical Review C*, 100(014316), 2019. And references therein.
- [94] J.S. Al-Khalili and E. Roeckl, editors. *The Euroschool Lectures on Physics with Exotic Beams Vol. I*. Springer, 2004.
- [95] I.P. Johnstone and I.S. Towner. Effective charges for ^{88}Sr and ^{90}Zr closed-shell cores. *European Physical Journal A*, 2:263–268, 1998.
- [96] K. Suzuki and R. Okamoto. Effective Operators in Time-Independent Approach. *Progress of Theoretical Physics*, 93(5), 1995.
- [97] F.R. Metzger. Lifetimes of excited states of ^{92}Mo . *Physical Review C*, 1977.
- [98] M. Moszyński and H. Mach. A method for picosecond lifetime measurements for neutron-rich nuclei: (2) Timing study with scintillation counters. *Nuclear Instruments and Methods in Physics Research A*, 277:407–417, 1989.
- [99] L. Fraile et al. Fast timing study of a CeBr₃ crystal: Time resolution below 120 ps at ^{60}Co energies. *Nuclear Instruments and Methods in Physics Research A*, 701:235–242, 2013.
- [100] A. Blazhev et al. Observation of a core-excited E4 isomer in ^{98}Cd . *Physical Review C*, 69(064304), 2004.
- [101] T. Marchi et al. Quadrupole Transition Strength in the ^{74}Ni Nucleus and Core Polarization Effects in the Neutron-Rich Ni Isotopes. *Physical Review Letters*, 113(182501), 2014.
- [102] K. Kolos et al. Direct Lifetime Measurements of the Excited States in ^{72}Ni . *Physical Review Letters*, 116(122502), 2016.
- [103] C.J. Chiara et al. Seniority, collectivity, and B(E2) enhancement in ^{72}Ni . *Physical Review C*, 84(037304), 2011.
- [104] A.I. Morales et al. Is seniority a partial dynamic symmetry in the first $\nu g_{9/2}$ shell? *Physical Letters B*, 781:706–712, 2018.

-
- [105] M. Sawicka et al. Low energy levels in ^{72}Ni . *Physical Review C*, 68(044304), 2003.
- [106] A.I. Morales et al. Low-lying excitations in ^{72}Ni . *Physical Review C*, 93(034328), 2016.
- [107] J.A.M. Cox and H.A. Tolhoek. ON THE THEORY OF ANGULAR CORRELATION OF 2 SUCCESSIVE GAMMA QUANTA EMITTED BY ORIENTATED NUCLEI. *Physica*, 18:1262–1263, 1952.
- [108] J.A.M. Cox and H.A. Tolhoek. DIRECTIONAL CORRELATION OF 2 SUCCESSIVE RADIATIONS EMITTED BY ORIENTED NUCLEI. *Physica*, 19:1178–1186, 1953.
- [109] A. López-Martens et al. γ -ray tracking algorithms: a comparison. *Nuclear Instruments and Methods in Physics Research A*, 533:454–466, 2004.
- [110] D.C. Radfore. ESCL8R and LEVIT8R: Software for interactive graphical analysis of HPGe coincidence data sets. *Nuclear Instruments and Methods in Physics Research A*, 1995.
- [111] <http://bricc.anu.edu.au/index.php>.
- [112] T. Lauritsen et al. Characterization of a gamma-ray tracking array: A comparison of GRETINA and Gammasphere using a ^{60}Co source. *Nuclear Instruments and Methods in Physics Research A*, 836:46–56, 2016.
- [113] A. López-Martens. Improving tracking at low energies and tracking efficiency. In *18th AGATA Week*, 2017.
- [114] P.S. Jastram et al. Angular Correlation of Gamma Radiations from Oriented Nuclei. *Physical Review*, 101(4):1381–1388, 1956.
- [115] E. Clément. Efficiency studies. In *18th AGATA Week*, 2017.
- [116] E. Clément. Performance of the DAQ system. In *19th AGATA Week*, 2018.
- [117] V. Mendez and M. kaci. Status Report :Deployment and development of specific Grid Services and Applications for AGATA, 2011.